NANOSCIENCE AND NANOMATERIALS FOR THE KNOWLEDGE AND CONSERVATION OF CULTURAL HERITAGE

EDITED BY: Luca Tortora, Gabriella Di Carlo, Maria Jesus Mosquera and Gabriel Maria Ingo

frontiers Research Topics

About Frontiers

Frontiers is more than just an open-access publisher of scholarly articles: it is a pioneering approach to the world of academia, radically improving the way scholarly research is managed. The grand vision of Frontiers is a world where all people have an equal opportunity to seek, share and generate knowledge. Frontiers provides immediate and permanent online open access to all its publications, but this alone is not enough to realize our grand goals.

Frontiers Journal Series

The Frontiers Journal Series is a multi-tier and interdisciplinary set of open-access, online journals, promising a paradigm shift from the current review, selection and dissemination processes in academic publishing. All Frontiers journals are driven by researchers for researchers; therefore, they constitute a service to the scholarly community. At the same time, the Frontiers Journal Series operates on a revolutionary invention, the tiered publishing system, initially addressing specific communities of scholars, and gradually climbing up to broader public understanding, thus serving the interests of the lay society, too.

Dedication to Quality

Each Frontiers article is a landmark of the highest quality, thanks to genuinely collaborative interactions between authors and review editors, who include some of the world's best academicians. Research must be certified by peers before entering a stream of knowledge that may eventually reach the public - and shape society; therefore, Frontiers only applies the most rigorous and unbiased reviews.
Frontiers revolutionizes research publishing by freely delivering the most outstanding research, evaluated with no bias from both the academic and social point of view. By applying the most advanced information technologies, Frontiers is catapulting scholarly publishing into a new generation.

What are Frontiers Research Topics?

Frontiers Research Topics are very popular trademarks of the Frontiers Journals Series: they are collections of at least ten articles, all centered on a particular subject. With their unique mix of varied contributions from Original Research to Review Articles, Frontiers Research Topics unify the most influential researchers, the latest key findings and historical advances in a hot research area! Find out more on how to host your own Frontiers Research Topic or contribute to one as an author by contacting the Frontiers Editorial Office: researchtopics@frontiersin.org

NANOSCIENCE AND NANOMATERIALS FOR THE KNOWLEDGE AND CONSERVATION OF CULTURAL HERITAGE

Topic Editors:
Luca Tortora, Roma Tre University, Italy
Gabriella Di Carlo, Consiglio Nazionale delle Ricerche Italiano (CNR), Italy
Maria Jesus Mosquera, University of Cádiz, Spain
Gabriel Maria Ingo, National Research Council (CNR), Italy

Table of Contents

Editorial: Nanoscience and Nanomaterials for the Knowledge and Conservation of Cultural Heritage

Luca Tortora[1,2]*, Gabriella Di Carlo[3], Maria Jesus Mosquera[4] and Gabriel Maria Ingo[3]

[1]LASR3 Surface Analysis Laboratory, National Institute for Nuclear Physics (INFN) Roma Tre Division, Rome, Italy, [2]Department of Sciences, Roma Tre University, Rome, Italy, [3]Institute for the Study of Nanostructured Materials (ISMN), National Research Council (CNR), Rome, Italy, [4]Departamento de Quimica Fisica, Facultad de Ciencias, Universidad de Cadiz, Cadiz, Spain

Editorial on the Research Topic

Nanoscience and Nanomaterials for the Knowledge and Conservation of Cultural Heritage

"To protect and to serve" is the motto of the Los Angeles Police Department, adopted also by other law enforcement agencies; it underlines the necessity of protecting citizens from criminal acts and at the same time serving the community. Well, considering that works of art constitute a priceless good and they should be protected as such, this motto could be associated even to scientists working in the cultural heritage field. In fact, it is possible to safeguard the cultural heritage working for example on the development of innovative materials as protective agents or explaining degradation mechanisms occurring in artworks by using innovative materials and methods like those based on the nano-technologies science.

In the last decade, emerging organic and inorganic nanomaterials have been designed, synthesized, and characterized for the really non-invasive and selective cleaning, the reliable consolidation, and the long-lasting reliable conservation also under unsuitable climate conditions. At the same time, sophisticated analytical techniques are more frequently combined to understand the nano and micro-chemical and structural features of artworks for the comprehensive knowledge of their "material" nature and the deciphering of manufacturing processes.

The structure of this special issue reflects these two aspects. It is composed of six original research articles dealing with the application of innovative nanomaterials for the protection of different substrates (archeological wood, steel, and stone material) and cleaning techniques for the disinfection of historical leather and selective removal of polymeric material. In addition, this special topic collection presents seven research articles describing the application of combined advanced analytical techniques to unveil different degradation mechanisms.

For what concerns the nanomaterials for the conservation of cultural heritage, Antonelli et al. report an article where they tested three different nanoscale consolidants to protect waterlogged archaeological wood samples. Lignin nanoparticles, bacterial nanocellulose, and cellulose nanocrystals were used on wood samples coming from two Italian archaeological sites. Problems related to color changing and differences in penetration of the nano-consolidants were extensively discussed. The paper proposed by Giuliani et al. shows a new generation of smart materials able to release the loaded inhibitor depending on the chemical environmental

conditions. Three inhibitors containing a carboxylic moiety, such as p-aminobenzoic, succinic, and caffeic acids were studied as protective agents of corrosion in simulated concrete pore solutions containing chloride ions; p-aminobenzoic acid was then used for the functionalization of silica nanoparticles and LDHs, adopted as nanocarriers for the inhibitors.

Seems to be a great deal of interest for the consolidant products used for stone. In fact, Ruggiero et al. propose a coating composed of a tetraethoxyorthosilicate matrix (TEOS), an elasticiser [hydroxyl-terminated polydimethylsiloxane (PDMS-OH)] and a non-ionic surfactant (n-octylamine). This TEOS-based composite coating was then functionalized with two different silica nanofillers with antifouling properties: commercial TiO$_2$ nanoparticles and two different silica nanocontainers, loaded with the commercial biocide 2-mercaptobenzothiazole. In the same collection, Kapetanaki et al. reported a procedure for eco-friendly and one-pot synthesis of a consolidant incorporating in TEOS, PDMS, and nanoparticles of synthesized calcium oxalate. Cement mortars treated with this colloidal solution exhibited well-preserved aesthetic surface parameters and significant maintenance of the treatment.

Particular attention was also ~~payed~~ paid to cleaning methods. X-ray beams were used by Vadrucci et al. for the sterilization of leather wallpaper fragments dating back to the 1700s. The disinfection treatment permitted to eliminate the biofilms present on the leather and produced by the following microorganisms: *B. cereus* and *M. timonae*. On the other hand, a chemical approach for the removal of aged or detrimental polymeric coatings from artworks was investigated by Baglioni et al. The interaction between nanostructured fluids (NSFs), usually adopted by restorers for cleaning procedures, and four different kinds of acrylic and vinyl polymer films deposited onto glass, marble, and polystyrene substrates was studied.

Integrated methodological approaches based on the combined use of complementary surface, interfaces, and bulk analytical techniques were applied on different heritage objects and materials as like inks, gilded copper-based buckles, historical metal plates, gilded diadem fragments, gilded plaques, and ancient brass wind instruments. Saviello et al. analyzed blue and black writing inks. Results coming from Raman spectroscopy and surface enhanced Raman scattering (SERS) revealed that all analyzed writing inks are composed of Crystal Violet and other triarylmethane dye mixtures, with, in some cases, the addition of phthalocyanine dyes. Raman and SERS were used even to investigate related aging processes due to the presence of light and high temperatures. Degradation processes were also studied by Graziani et al. In this case, time of flight secondary ion mass spectrometry (ToF-SIMS) depth profiling experiments and SEM-energy dispersive X-ray

spectroscopy (EDS) were combined to spatially locate corrosion products present in a fire gilded brooch dating back to 16th–17th century AD and found during the dredging of the Tiber river (Rome, Italy). On the contrary, based on a non-destructive alternative, Lins et al. proposed an analytical approach to determine the gilding thickness for a similar gilded copper-based buckle. An innovative algorithm was developed to measure thin metallic layers deposited on a sample surface taking advantage of differential X-ray attenuation in MA-XRF analysis. Even in the article of Albini et al., the protagonists are copper-based objects. Painted metal surfaces were fully characterized by a plethora of complementary spectroscopic techniques such as Fourier transform infrared spectroscopy (FTIR), energy-dispersive X-Ray fluorescence spectroscopy (EDXRF), high spatial resolution field emission scanning electron microscopy coupled with energy dispersive X-ray spectroscopy (EDS), and optical microscopy (OM). In particular, FTIR analysis revealed degradation products generated from the interaction between the organic binding media and metal substrates. A detailed study aimed to understand the manufacturing techniques used to give the gold or silver appearance in metal artifacts from ancient Peru was afforded by Ingo et al.. In the article, different metal objects, some of them dating back around 300–400 AD, found in the tombs of the Lords of Sipán (Lambayeque, Peru) and of the Lady of Cao (El Brujo, Peru) were characterized using complementary techniques as OM, SEM-EDS, X-ray diffraction (XRD), and X-ray photoelectron spectroscopy (XPS). The abovementioned combined analytical approach permitted to the authors to have a detailed picture of the degradation process resulting from interactions between soil species and Ag-Cu-Au ternary alloys.

What happens when the surface of a brass comes in contact with saliva? Can be the saliva considered a potential corrosion agent? The problem was addressed by Fantauzzi et al. In the article, artificial saliva was placed in contact with brass surfaces, and the composition and morphology of the film formed after the chemical interaction ~~were~~ was investigated by XPS, SEM, and electrochemical impedance spectroscopy (EIS). Finally, the paper from Grottoli et al. shows the potentialities of the metagenomics applied to the cultural heritage conservation. A micro-invasive sampling method that involves the use of a simple adhesive tape followed by DNA extraction and PCR amplification permitted to identify the microbial communities colonizing the surface of the hypogeum of the Basilica di San Nicola in Carcere Church in Rome.

In conclusion, as you will appreciate, this special issue contains several hints and suggestions that fall in different fields of application strictly related to the cultural heritage. We hope that it can be a useful tool for conservation scientists, restorers, curators, or simply art lovers.

AUTHOR CONTRIBUTIONS

All authors contributed equally to this article and have made a substantial, direct and intellectual contribution to the work, and approved it for publication.

ACKNOWLEDGMENTS

Raman Spectroscopy and Surface Enhanced Raman Scattering (SERS) for the Analysis of Blue and Black Writing Inks: Identification of Dye Content and Degradation Processes

Daniela Saviello[1], Maddalena Trabace[2], Abeer Alyami[1], Antonio Mirabile[3], Piero Baglioni[2], Rodorico Giorgi[2] and Daniela Iacopino[1]*

[1] Nanotechnology Group, Tyndall National Institute, University College Cork, Cork, Ireland, [2] Department of Chemistry & CSGI, University of Florence, Florence, Italy, [3] Mirabile, Paris, France

Raman spectroscopy and Surface Enhanced Raman Scattering (SERS) were applied to the analysis of blue and black writing inks. SERS was performed by application of plasmonic nanopastes constituted by Ag nanoparticles and Au nanorods directly on inks deposited on paper substrates under laser irradiation of 514 nm. It was found that SERS spectra were largely enhanced compared to Raman spectra and that Ag nanopastes produced much larger enhancements than Au nanopastes, due to a combination of plasmonic resonance, charge transfer, and molecular resonance effects. All analyzed writing inks resulted constituted by Crystal Violet and other triarylmethane dye mixtures, to which sometimes phthalocyanine dyes were also added (for example in Bic pens). SERS was also used for the identification of degradation processes occurring in artificially aged blue pens deposited on paper substrates. It was found that color alteration changed from ink to ink and varied from darkening to discoloration to slight fading, depending on the initial chemical composition. For inks containing Crystal Violet, two mechanisms associated to de-methylation and photo-reduction of excited dye to colorless leuco forms were identified.

Keywords: ballpoint pens, dyes, Raman, plasmonic nanopastes, SERS, degradation

INTRODUCTION

Modern commercial inks are a complex mixture of several dyes and/or pigments constituting up to the 50% of the total ink formulation, carried either in a glycol-based solvent or benzyl alcohol (Bell, 2008; Houck and Siegel, 2010; Houck et al., 2013). Analysis of commercial writing inks is usually carried out in the context of forensic examination in order to assess dating and originality of documents and to correctly assess cases of crimes like falsification, questioned signatures and threatening letters. Accordingly, a vast number of publications in the last 20 years have focused on characterization of writing pens (i.e., identification of dyes and pigment contents in ballpoint and gel pens) and also on discrimination between inks. Therefore a number of techniques such as Thin Layer Chromatography (TLC) and mass spectrometry (MS) often coupled with optical analysis (ink absorption and luminescence) or image analysis have been routinely applied to

the analysis, differentiation, and classification of writing inks (Weyermann et al., 2007; Djozan et al., 2008; Gallidabino et al., 2011; Sauzier et al., 2015). Recently, visible, Raman, and infrared spectroscopies have also gained popularity as techniques for providing rapid information on the chemical content of the ink mixtures and are increasingly pursued for their rapidity of analysis, little sample preparation and non-destructive analysis. Such approaches are also particularly amenable to the investigation of ink-based paper works, whereby the identification of dyes and pigment ink constituents is important to assess dating, originality and to implement correct conservation procedures thus ensuring long-term preservation. Among spectroscopic methods, Raman and Surface Enhanced Raman Scattering (SERS) spectroscopies have been widely used for identification of colorants in artworks and have shown as promising techniques for the identification of dye components in commercial inks (Mazzella and Buzzini, 2005; Bráz et al., 2014; Calcerrada and García-Ruiz, 2015). In particular, SERS revealed very effective in quenching the interference strong fluorescence emission sometimes accompanying the direct Raman illumination of writing inks thus enabling generation of high intensity spectra even under visible laser irradiation (Jeanmaire and Van Duyne, 1977; Geiman et al., 2009; Luo et al., 2013). However, the majority of SERS results suffer from poor reproducibility arising from the use of randomly aggregated Ag colloidal solutions, usually dropped on extracted samples (Seifar et al., 2001; White, 2003). In contrast, in order to guarantee reproducibility of analysis, SERS requires the use of reliable and robust plasmonic probes ideally applicable directly on the paper substrate. Recently, our group has developed plasmonic probes comprising Ag and Au nanopastes and nanoinks and has used SERS in combination with UV-vis spectroscopy for the analysis of blue and colored Bic pens, increasingly used for artistic purposes (Alyami et al., 2016, 2017, 2018).

Another important consideration in the field of artwork preservation is the aging of the ink deposited on a substrate (usually, but not necessary, paper). As soon as an ink line is deposited on a substrate, compositional changes occur rapidly due to loss of volatile components, photodegradation of dyes or polymerization of resins. All these processes happen concomitantly and they all contribute to significantly alter the aesthetic of paper works exposed to environmental conditions. Photofading of ballpoint pens has been traditionally performed by laser desorption/ionization (LDI) and matrix-assisted laser desorption/ionization (MALDI) mass spectrometry (Weyermann et al., 2006). However, in light of the need to preserve the integrity of analyzed objects, non-destructive techniques are nowadays preferred for ink-based artworks. Accordingly, Raman spectroscopy has been successfully used for the investigation of dye aging dynamics in writing inks and SERS was successfully applied by Cesaratto et al. to the tracking of triarylmethane dyes photodegradation on nineteenth century woodblock Japanese prints (Gorshova et al., 2016; Cesaratto et al., 2017).

In this work we propose the use of Raman and SERS spectroscopy for the analysis of a number of blue and black writing inks on paper substrates. The aim of the present study is to evaluate the ability and limitations of Raman spectroscopy for the analysis of writing inks and to assess the improvements brought about by the use of SERS. This includes routine chemical make-up identification as well as more complex analysis such as degradation assessments. The ability of SERS in overcoming fluorescence background limitations and increasing the sensitivity of Raman spectroscopy have been investigated already. However, results are contradictory as robust SERS probes for such type of analysis are missing. The novelty of the presented manuscript relies on the development of SERS metal nanopastes providing a reproducible method for the investigation of signal enhancement effects associated with the use of SERS compared to Raman spectroscopy. This is relevant for analysis of artworks whereby only small size samples are available for analysis. Moreover, the ability to synthesize SERS nanopastes of different plasmonic properties (Ag, Au) widens the application of SERS spectroscopy to Raman instrumentations of different excitation wavelengths and also to portable/handheld instrumentation.

MATERIALS AND METHODS

Materials
Tetrachloroauric acid (99.5%), silver nitrate (ACS, 99%), sodium citrate (99 %), sodium borohydride (96%), ascorbic acid (CAS: 50817), cetyltrimethylammoniumbromide (CTAB, 99%), MeOH (CAS: 67561) were purchased from Sigma-Aldrich. All glassware was cleaned with *aqua regia* prior to nanopaste synthesis. Milli-Q water (resistivity > 18 MΩ cm^{-1}) was used throughout the experiments. Reference dye Crystal Violet (CAS: 548629) was also purchased from Sigma and used without further purification.

Synthesis of Plasmonic Nanopastes
Silver nanoparticle nanopastes were synthesized following the modification of the Lee and Meisel method reported by Polavarapu et al. (2014). Briefly, trisodium citrate solution (4.5 mL, 1.00 wt%) was added to an aqueous boiling solution containing AgNO$_3$ (200 mL, 42 mg) under vigorous stirring. The reaction was boiled for another 1 h and then cooled to room temperature. The obtained Ag nanoparticles in water (200 mL) were centrifuged at 7,000 rpm for 20 min and then re-dispersed in water (2 mL) to obtain Ag nanopaste (3 mg/mL). Au nanorod nanopastes were synthesized by a modification of the seed mediated growth reported by Polavarapu et al. (2014). Specifically, a seed solution was prepared by adding 0.3 mL of an ice-cold aqueous sodium borohydride (NaBH$_4$, 0.01 M) solution to an aqueous solution of 4.7 mL hexadecyltrimethylammonium bromide (CTAB, 0.1 M) and 25 µL of gold(III) chloride trihydrate (HAuCl$_4$, 0.05 M) at 30°C. An aliquot of 0.36 mL of the seed solution was added to a growth solution prepared by mixing 150 mL of CTAB (0.05 M), 1.5 mL HAuCl$_4$ (0.05 M), 0.225 mL of silver nitrate (AgNO$_3$, 0.01 M), and 5.0 mL of ascorbic acid (0.1 M) at 30°C. The solution color changed from colorless to brownish-bluish after the addition of the seed solution to the grown solution. The obtained aqueous solution of gold nanorods was centrifuged twice and re-dispersed in water (1 mL) to get the nanorod paste.
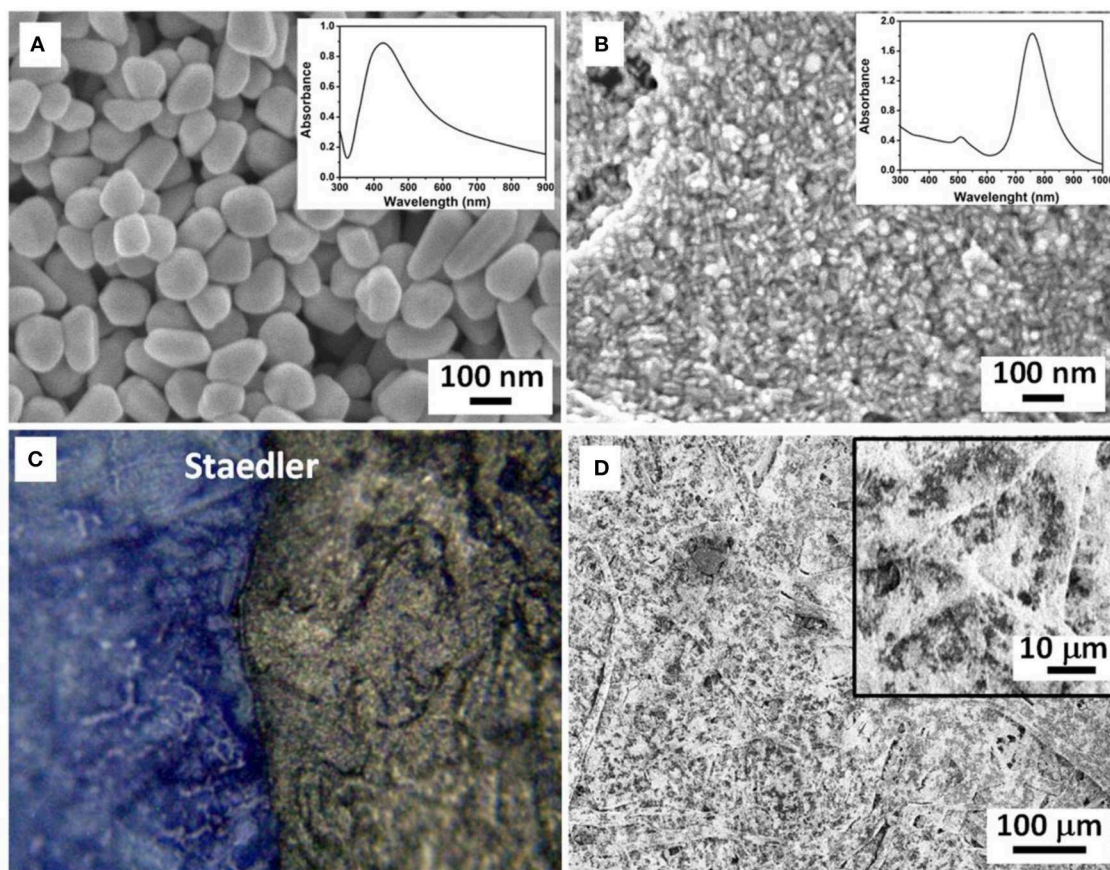
FIGURE 1 | SEM images of **(A)** Ag nanoparticle and **(B)** Au nanorod nanopaste deposited on SiO₂ support. Insets: UV-vis spectra of Ag nanoparticle and Au nanorod nanopaste in aqueous solution; **(C)** optical microscopy image of blue Stadler pen on paper with deposited droplet of Ag nanopaste; **(D)** SEM image of Ag nanopaste droplet on Stadler colored paper. Inset: high magnification SEM image showing even distribution of paste on the paper fibers.

Commercial Writing Pens

Commercial writing pens were purchased from local stores. Real pen artworks were made by French artist Anne-Flore Cabanis and were kindly donated by paper conservator Antonio Mirabile. Artworks were made by Bic blue and black pens on commercial paper.

Scanning Electron Microscopy

Scanning electron microscopy (SEM) images of nanoinks deposited on SiO₂ substrates were acquired using a field emission SEM (JSM-6700F, JEOL UK Ltd.) operating at beam voltages of 2 kV.

Thin Layer Chromatography

Thin layer chromatography was performed with silica plates 10 × 20 cm (Sigma-Aldrich). The writing inks and reference dye Crystal Violet were deposited as concentrated MeOH solutions. The TLC was developed in ethylacetate-ethanol-water (70:35:30 v/v) for 60 min.

Optical Characterization

UV-Vis spectra were acquired with an Agilent/HP 8453 UV-Vis Spectrophotometer (200 nm < λ < 1,100 nm). Raman spectra at 514 nm were obtained from a Renishaw inVia Raman system. An argon ion laser (1,800 l/mm grating) was employed as an excitation source. The laser beam was focused onto the sample through a Leica 20X objective with 0.4 N.A. Measured power at the sampling level was controlled at about 3 mW. Acquisition time was usually 10 s. Raman spectra at 785 nm were obtained from a Pelkin Elmer Raman station. The laser beam was focused onto the sample through a 50X objective (M Plan Achromat) with 0.75 N.A. The laser power was around 3.5 mW and typical acquisition time was 10 s. To obtain SERS spectra, 5 μL of plasmonic nanopastes were deposited on pen written lines on paper and left to evaporate for 30 min prior analysis.

Artificial Aging

Paper samples with written blue pen features were subjected to three artificial aging cycles as follows: thermo-hygrometric and photo-oxidative for a total duration of 88 days. Every cycle comprised three phases: an initial phase in humidity chamber with thermo-hygrometric control of temperature at 25.5°C and 80% relative humidity; a second phase of thermal degradation in oven at 80°C and a third phase of neon light exposure to the front and back of the paper sheet.

FIGURE 2 | Raman spectra of **(A)** blue Bic, Staedler, and Pilot inks on paper and **(B)** black Bic, Staedler inks on paper. Spectra were taken with 514 nm illumination wavelength.
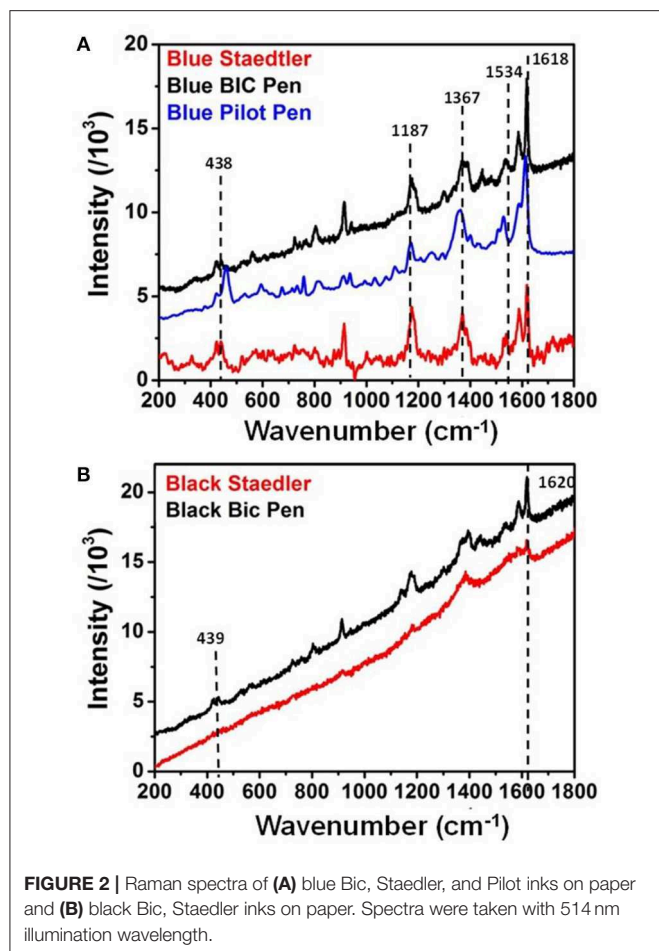
TABLE 1 | List of band positions found in Raman spectra of analyzed inks.

Blue Bic		Blue staedler	Blue pilot	Black Bic	Black stadler	Assignments*
1,618	A1	1,618	1,614	1,620	1,620	
1,583	E	1,587	1,583	1,585	1,584	
1,534	E	1,540	1,528	1,532		$\nu(C_{ring}N)\delta_s(CH_3)$
1,387	E			1,395		$\delta(CH)/\delta_s(CH_3)/\delta(CCC)_{ring}$
1,367	A1	1,369	1,359		1,382	$\nu_{as}(CC_{center}C)/\delta(CCC)_{ring}/\delta(CH)$
1,173	A1	1,170	1,168	1,174		$\nu_s(CC_{center}C)/\delta(CCC)_{breathing}/\rho_r(CH_3)$
913	E	914	911			$\delta(CC_{center}C)$
438	A1	440	438			$\delta(CNC)$
421	E	423	419	420		$\delta(CNC)/\delta(CC_{center}C)$

*ν, stretching (s, symmetric; as, asymmetric); δ, bending.

RESULTS AND DISCUSSION

Metal Nanopastes SERS Probes

Writing inks from 10 commercial pens (eight blue and two black) were analyzed. Details of used pens and optical microscopy images of deposited inks on paper are reported in **Figure S1**.

In order to perform SERS analysis directly on the pen lines, and therefore to avoid lengthy extraction processes,

it is necessary to use colloidal plasmonic solutions able to homogeneously cover the colored paper fibers, in order to ensure reproducibility of results and high density of hot spots necessary for generation of high intensity spectral features. Toward this end, Ag nanoparticle and Au nanorod nanopastes were synthesized by slight modification of the "pen-on-paper" method proposed by Polavarapu et al. (2014). **Figures 1A,B** show SEM images of the synthesized nanopastes deposited on n-doped conductive SiO_2 substrates. Ag nanopastes were mostly spherical in shape and had an average size of 65 ± 3 nm; the Au nanopastes displayed an elongated (rod-like) shape with average size of $13 \pm 2 \times 41 \pm 4$ nm. The absorbance spectra of synthesized nanopastes are reported as insets: the Ag nanopaste solution showed a relatively large plasmonic peak centered at 426 nm whereas the Au nanopaste solution was characterized by two peaks at 520 and 787 nm, associated to transversal and longitudinal plasmon resonances occurring in elongated nanoparticles (Johnson et al., 2002). **Figure 2B** shows a representative optical microscopy image of deposited Ag nanopaste on blue Staedler pen, showing formation of a well-defined SERS-active area on the analytical surface without smudging nor dissolution of the pen ink underneath. The representative SEM image showed in **Figure 1C** shows highly homogeneous distribution of plasmonic nanoparticles over large areas (>0.6 mm^2) of the colored paper fibers. Such high density of adsorbed Ag nanoparticles results in a high density of hot spots suitable for generation of high intensity SERS spectra.

Raman Spectroscopy and SERS of Writing Inks

Prior measurements of SERS spectra Raman spectra were recorded for five pens, in order to establish limitations of Raman spectroscopy and assess enhancement generated by subsequent application of SERS. All Raman spectra were recorded with 514 nm excitation wavelength and 3 mW laser power and are shown in **Figure 2** without background subtraction. Raman spectra of blue and black Bic and blue Staedler pens (**Figures 2A,B**) showed very similar bands (see **Table 1** for details) at 1,618, 1,587, 1,540 cm^{-1}, which were associated to the stretching of the benzene rings in triarylmethane compounds and 439, 420 cm^{-1} bands associated to bending of CNC bonds (Canamares et al., 2008). Based on previous findings by our group and others, the presence of crystal violet (CV, basic violet 3, C. I. 42555) was hypothesized for these pen inks (Alyami et al., 2016, 2017). It should be noted that previous analysis carried by our group on blue Bic pen ink whose components were separated by thin-layer chromatography (TLC) and subsequently identified by Raman/SERS spectroscopies showed also presence of a blue phthalocyanine component in the ink formulation. However, the phthalocyanine component did not give any Raman response at 514 nm excitation, confirming the results obtained in this work on the overall Bic pen ink showing only contribution from the CV component (Kunicki et al., 2013; Alyami et al., 2017). The Raman spectrum of blue Pilot pen (**Figure 2A**) showed good intensity bands centered at 1,614, 1,530, 1,359, 1,168, 438, and 419 cm^{-1}, which could also be attributed to the presence of a

FIGURE 3 | Comparison between Raman and SERS spectra for **(A)** blue Bic pen; **(B)** blue Staedler pen; **(C)** blue Pilot pen; **(D)** black Bic pen; and **(E)** black Staeadler pen. All spectra were taken with 514 nm illumination wavelength and laser power 3 mW.
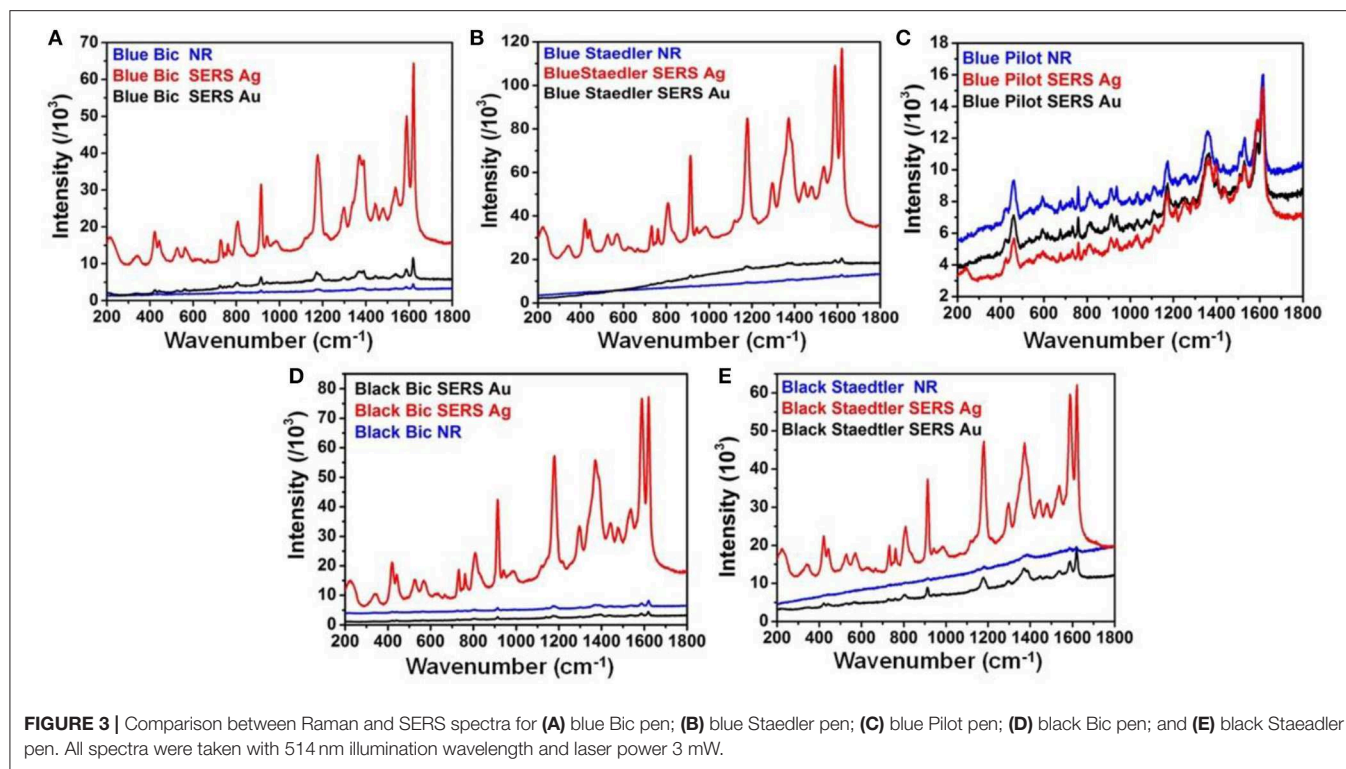
triarylmethane mixture but not specifically to CV. The Raman spectrum of black Staedler (**Figure 2B**) also indicated possible presence of CV, although the intensity of obtained Raman band was too low and affected by significant fluorescence interference to allow unequivocal peak assignment.

Figure 3 show SERS spectra recorded for each analyzed pen with both Ag and Au nanopastes. SERS spectra of additional blue writing inks are reported in **Figure S3**. The SERS spectra of each pen were plotted together with the corresponding Raman spectrum in order to give a straight forward visualization of the degree of enhancement obtained with both SERS probes compared to Raman conditions. In addition the blank Raman and SERS spectra of commercial Fabriano paper were also taken and are shown in **Figure S2**. The blank Raman spectrum was featureless; low intensity and broad peaks at 1,595, 1,519, and 1,407 cm^{-1} where observed with Ag nanopastes, one peak at 1,619 cm^{-1} peak was observed with Au nanopastes. The application of Ag nanopastes resulted in generation of high intensity SERS spectra for blue and black Bic and Staedler pens (**Figures 3A–E**). Specifically, spectra displayed intensities ca. 1 order of magnitude higher than intensities of corresponding Raman spectra (measured using the intensity of the 1,180 cm^{-1} band as reference) and showed all diagnostic peaks of CV. This enhancement was mainly attributed to an electromagnetic effect (EM), due to the use of an illumination wavelength in plasmonic resonance with the Ag nanopastes (**Figure 1C**). Details of the position of the bands found in all analyzed inks are reported in the SI (**Table S1**). The high intensity and clear formation of diagnostic bands allowed unequivocal identification of CV in

both Bic and Staedler blue and black pen inks. Closer observation of the Bic and Staedler blue and black SERS spectra showed a red shift of frequencies compared to the Raman spectra. This in turn was associated to a chemical effect (CE) due to the formation of a chemical bond, and consequent charge transfer (CT), between CV and Ag via the central C atom whereby CV acted as an electron donor and Ag as electron acceptor (Canamares et al., 2008). Specifically, the C=C ring frequency was shifted from 1,618 to 1,620 cm^{-1} for the above ink pens. Further proof of occurrence of a CE was found in the following observed shifts: for Bic blue the N-phenyl frequencies appearing at 1,367 and 1,387 cm^{-1} in the Raman spectrum were shifted to 1,371 and 1,392 cm^{-1}, respectively in the SERS spectrum; for blue Staedler shifts from 1,369 and 1,386 cm^{-1} to 1,371 and 1,389 cm^{-1} were measured; for Bic/Staedler black inks bands were located at 1,370/1,373 and 1,388/1,388 cm^{-1}, but resolution of the Raman spectrum was too low to measure bands positions, respectively. Further proof of the occurrence of a CT process was given by the predominant enhancement of the non-totally symmetric (E) modes compared to the totally symmetric (A1) modes (Canamares et al., 2008; Selvakannan et al., 2013). As well as a CE a molecular resonance (MR) effect occurred for these pen inks, being the excitation wavelength in resonance with the absorption maximum of CV (588 nm with shoulder at 548 nm). Therefore, the large enhancement observed was attributed to the joint play of three effects: MR, EM, and CE.

In contrast, much less pronounced enhancement was obtained with Au nanopastes. This was expected as the major longitudinal plasmonic band of Au nanopastes was centered at 787 nm, away

FIGURE 4 | Optical microscope images of artistic drawings realized with **(a,b)** blue pens on paper. Insets: photographs of the entire drawings under the Raman spectrograph objective; **(c)** Raman spectra of the artistic drawings shown in **(a,b)**.
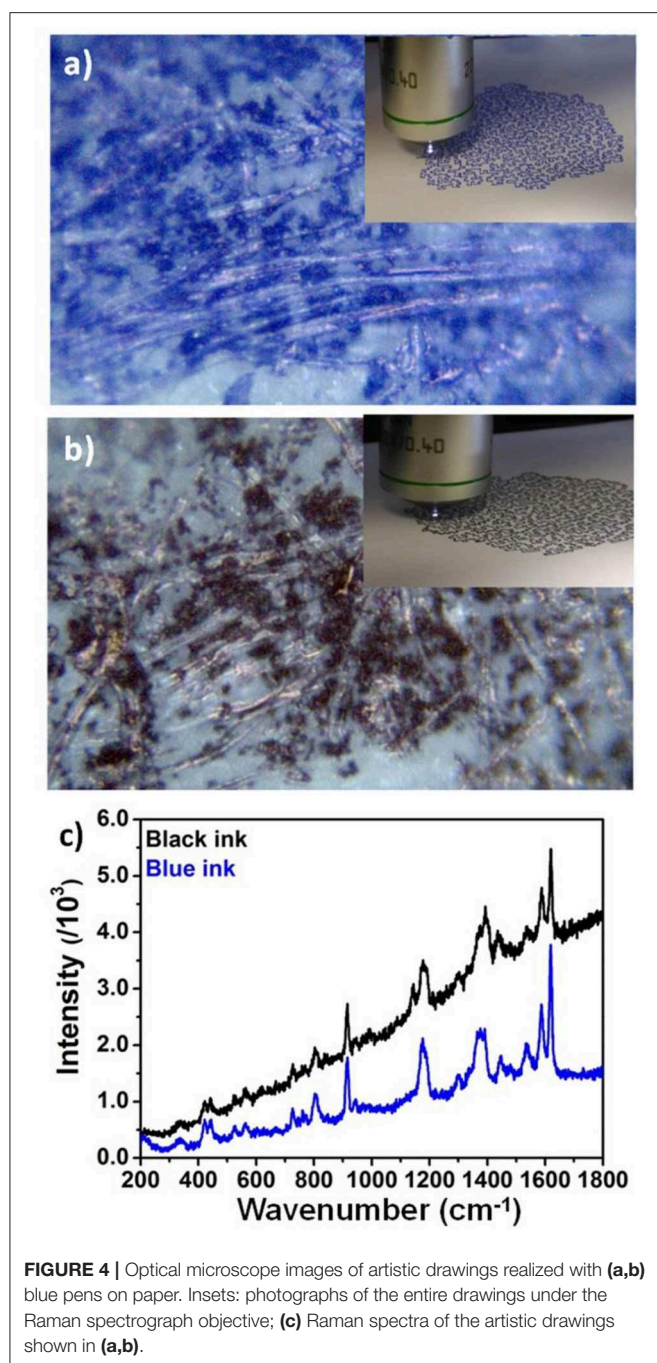
from the SERS excitation wavelength. The small enhancement observed could be attributed to a modest electromagnetic effect associated to the transversal band at 520 nm and to the ability of CV to form a CT complex with Au via the N groups (Selvakannan et al., 2013).

Presence of phthalocyanine in blue Bic pen was confirmed by SERS spectrum taken at 785 illumination wavelength with Au nanopastes (**Figure S4a**). In contrast SERS spectrum of blue Staedler taken at 785 nm with Au nanopastes (**Figure S4b**) showed bands in same positions as SERS bands recorded at

514 nm illumination, therefore proving no presence of additional dye components. Surprisingly, the application of both Ag and Au nanopastes resulted in no enhancement generation for the blue Pilot pen ink (**Figure 3C**), suggesting a marked different chemical composition compared to the Bic and Staedler ink mixtures. The presence of Victoria blue R component was hypothesized for this pen ink based on resemblance between the recorded spectrum at 785 nm (see **Figure S4c**) with the spectra of Pilot pens and reference dyes reported in literature (Ho et al., 2016). Specifically, bands at 1,611, 1,360, 1,178, 760, 732, 460, and 421 cm^{-1} overlapped the spectrum of Victoria R reference taken at 785 nm reported in literature.

Raman Spectroscopy of Real Artworks

In order to show the importance of database spectral collection for identification of inks used in artworks **Figure 4** shows Raman analysis performed on two artistic contemporary drawings made by writing blue and black pens. Specifically, **Figures 4a,b** shows optical microscopy images of the pen lines on the paper with areas of dense inks spots dis homogeneously distributed on the paper substrate, due to the dis homogeneous and fibrous morphology of the paper itself. **Figure 4b** shows Raman spectra of the blue and black drawings. Both spectra show bands associated to CV at 1,618, 1,586, 1,532, 1,445, 1,172, 916, 441, and 403 cm^{-1}. Careful comparison with Raman spectra of Bic pen (**Figure 2**) strongly suggested that this pen was used for the realization of the artistic drawing. As well as overlapping peak positions, the ratio of peaks 1,620/1,588 = 1.75 is equal to the ratio found in blue and black BIC pen Raman spectra.

SERS for Investigation of Writing Inks Aging Processes

As writing inks are increasingly used for the realization of drawings and mixed media artistic creations it is of paramount importance to carry out investigations on color changes brought upon exposure of ink-based objects to light as such exposure is known to induce severe color changes compromising the aesthetic, informational, and value of such objects. Moreover, the elucidation of mechanisms leading to color changes in ink dyes is important for characterization and identification of documents and objects, identification of ink-dye constituents and informative for the application of tailored conservation and exposure protocols.

Figures 5a,c,e show optical images of blue Bic, Staedler, and Pilot inks on paper taken after three cycles of artificial aging. Compared to unaged conditions minor color changes were observed for the Pilot pen whereas Bic and Staedler pens showed substantial color changes resulting in darkening of the Bic pen ink and a dramatic discoloration of the Staedler pen ink. Corresponding SERS spectra of aged inks are reported in **Figures 5b,d,f**. Spectra were obtained with Ag nanopaste and measured at 514 nm laser excitation wavelength. For easiness of comparison aged pen SERS spectra were plotted together as the equivalent SERS spectra (i.e., same laser power and exposure) of unaged pen inks. Spectra were background subtracted in order to allow more direct comparison of peak intensity changes. The SERS spectrum of aged Bic pen showed diagnostic bands of CV.
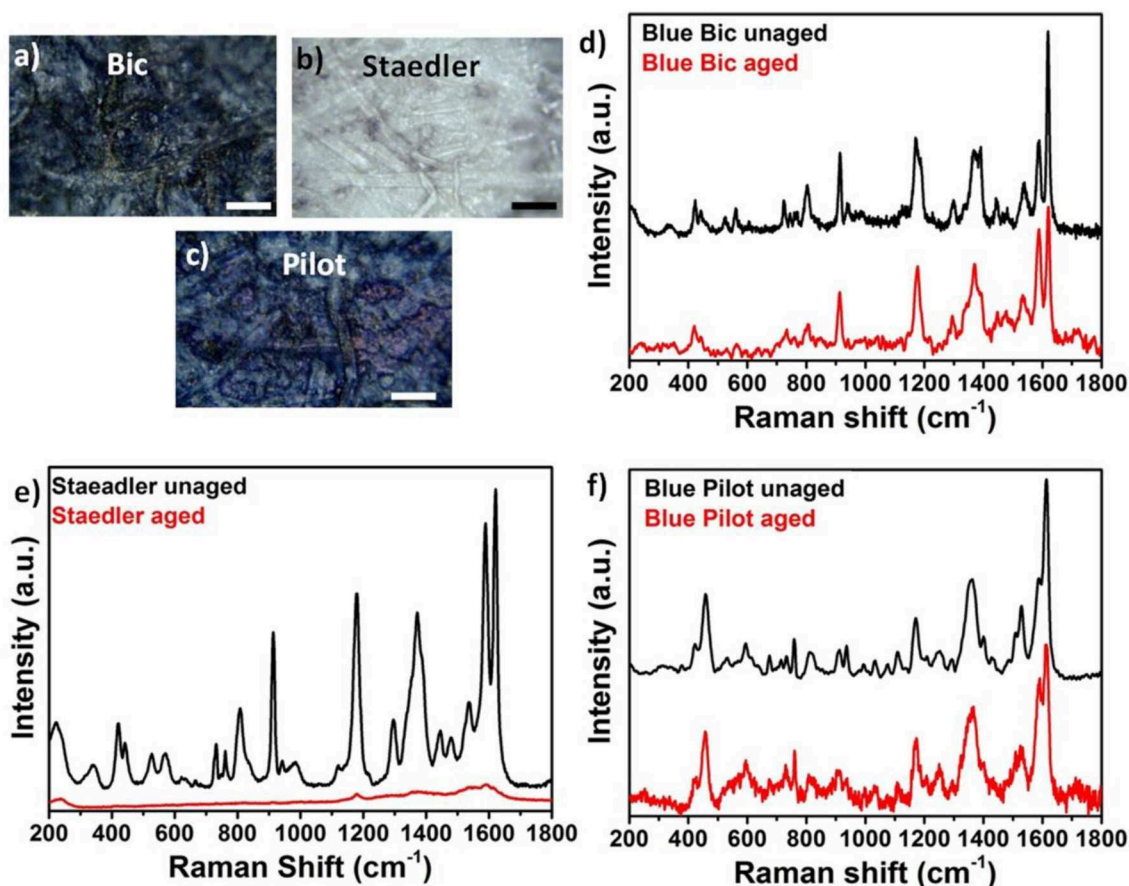
FIGURE 5 | (a–c) Optical microscopy images of artificially aged blue Bic, Staedler, and Pilot inks on paper; (d–f) Comparison between aged and unaged SERS spectra for blue Bic, Staedler, and Pilot inks on paper.

Compared to the unaged SERS spectrum, few key changes were observed. The ratio I_{1620}/I_{1587} decreased from the 2.21 value in the unaged sample to the 1.19 value in the aged samples, the CV peak at 723 cm^{-1} shifted to 732 cm^{-1}; the peaks at 744 and 771 cm^{-1} disappeared and the shoulders at 1,189 and 1,390 cm^{-1} disappeared. All these changes are in agreement with a mechanism of photo-induced N-demethylation already observed by Cesaratto et al. during their artificial aging studies on triarylmethylene dyes (Cesaratto et al., 2017). Specifically, the spectral changes observed in the Bic pen corresponded to what Cesaratto et al. observed at step 2 illumination, corresponding to a light dose of 0.12 MIx·h and associated to the occurrence of a N-demethylation process. Interestingly, faster degradation was observed for Staedler pen, as represented by the strong discoloration of exposed paper. Broad peaks were observed in the SERS spectrum of the aged pen centered at 1,613, 1,555, 1,536, 1,178, and 909 cm^{-1}.

Comparison of spectra showed strong resemblance with step 4 illumination (2.10 MIx·h) described by Cesaratto et al. and indicative of a chemical conversion from CV to fully N-demethylated pararosaniline. These results are in agreement with data reported by Weyermann et al. who found that degradation

kinetics of inks deposited on paper differed substantially from pen to pen (Weyermann et al., 2006). A few spectral changes also occurred for Pilot pen, although the uncertain dye mixture identification did not allow correlation with any specific degradation process. Specifically, peaks at 533, 937, and 1,073 cm^{-1} disappeared in the aged pen; also and the ratio I_{1616}/I_{1587} decreased from 1.97 to 1.29 following the artificial aging process.

The striking color difference between aged Bic and Staedler pens was ascribed to the chemical composition of their constituting ink. It is known that Bic ink formulations contain a mixture of blue phthalocyanine and triarylmethane dyes and that while the latter are extremely sensitive to photo- and thermal irradiation, phthalocyanine dyes degrade at a much lower rate compared to triarylmethane dyes. Interestingly and in contrast with common perception that aging induces color fading, our optical images showed a darker blue coloration in aged Bic pen inks, probably due to residual presence of phthalocyanine dye. In contrast, strong discoloration was observed in the Staedler pen, which further proves lack of phthalocyanine in the ink mixture. The discoloration could be ascribed to a degradation path involving photoreduction of the excited dye cation to a colorless leuco form, as reported by several authors, which may

occur in parallel with the described N-demethylation process (Gorshova et al., 2016).

CONCLUSION

Black and blue writing inks deposited on paper were investigated by Raman and SERS spectroscopies in order to identify major dye components. SERS measurements were performed *in situ* by deposition of a small droplet of plasmonic nanopaste on the analytical surface. Blue and black Bic and Staedler inks treated with Ag nanopastes gave SERS spectra of highly enhanced intensity compared to Raman spectra and SERS spectra taken at 514 nm illumination wavelength with Au nanopastes. The large enhancement was ascribed to a combination of EM, CT, and MR effects. SERS was also used to investigate the degradation process of blue writing inks through application of artificial aging processes involving light and high temperature exposure. Interestingly, in spite of the similar initial blue coloration, it was found that aged colored paper displayed very different colorations from each other. Specifically, the Bic paper displayed a darker blue color, the Staedler-colored paper displayed almost complete discoloration and the Pilot paper showed very small color changes. This was ascribed to the different chemical composition of the constituting inks, characterized by presence of phthalocyanine and triarylmethane dye in the case of Bic pen and only triarylmethane in the case of the Staedler pen. A degradation process involving N-demethylation of triarylmethane components was proposed based on spectral evidence. However, the intense discoloration observed for Staedler pen also suggested the concomitant formation of colorless leuco forms, due to photoreduction processes.

DATA AVAILABILITY STATEMENT

All datasets generated for this study are included in the article/**Supplementary Material**.

AUTHOR CONTRIBUTIONS

DS and AA performed the Raman, SERS measurements, SEMs, and synthesis of Ag nanopastes. MT and RG performed the aging of samples. AM provided the pens and set up the aging protocols. DI and PB wrote the manuscript.

FUNDING

SUPPLEMENTARY MATERIAL

The Supplementary Material for this article can be found online at: https://www.frontiersin.org/articles/10.3389/fchem. 2019.00727/full#supplementary-material

REFERENCES

Alyami, A., Barton, K., Lewis, L., Mirabile, A., and Iacopino, D. (2018). Identification of dye content in colored BIC ballpoint pen inks by Raman spectroscopy and Surface-Enhanced Raman Scattering. *J. Raman Spectrosc.* 50, 115–126. doi: 10.1002/jrs.5512

Alyami, A., Saviello, D., Mc Auliffe, M. A. P., Mirabile, A., Lewis, L., and Iacopino, D. (2017). Metal nanoinks as chemically stable surface enhanced scattering (SERS) probes for the analysis of blue BIC ballpoint pens. *Phys. Chem. Chem. Phys.* 19, 14652–14658. doi: 10.1039/C7CP01983A

Alyami, A., Saviello, D., McAuliffe, M. A. P., Cucciniello, R., Mirabile, A., Proto, A., Lewis, L., et al. (2016). Chemically stable Au nanorods as probes for sensitive surface enhanced scattering (SERS) analysis of blue BIC ballpoint pens. *AIP Conf. Proc.* 1873, 020003–020009. doi: 10.1063/1.4997132

Bell, S. (2008). *Encyclopedia of Forensic Sciences*. New York, NY: Infobase Publishing.

Bráz, A., López-López, M., and García- Ruiz, C. (2014). Studying the variability in the Raman signature of writing pen inks. *Forens. Sci. Intern.* 245, 38–44. doi: 10.1016/j.forsciint.2014.10.014

Calcerrada, M., and García-Ruiz, C. (2015). Analysis of questioned documents: a review. *Anal. Chim. Acta* 853, 143–166. doi: 10.1016/j.aca.2014.10.057

Canamares, M. V., Chenal, C., Birke, R. L., and Lombardi, J. R. (2008). DFT, SERS, and Single-Molecule SERS of Crystal Violet. *J. Phys. Chem. C* 112, 20295–20300. doi: 10.1021/jp807807j

Cesaratto, A., Lombardi, J. R., and Leona, M. (2017). Tracking photo-degradation of triarylmethane dyes with surface-enhanced Raman spectroscopy. *J. Raman Spectrosc.* 48, 418–424. doi: 10.1002/jrs.5056

Djozan, D., Baheri, T., Karimian, G., and Shahidi, M. (2008). Forensic discrimination of blue ballpoint pen inks based in thin layer chromatography and image analysis. *Forens. Sci Intern.* 179, 199–205. doi: 10.1016/j.forsciint.2008.05.013

Gallidabino, M., Weyermann, C., and Marquis, R. (2011). Differentiation of blue ballpoint pens by positive and negative mode LDI-MS. *Forens. Sci Intern.* 204, 169–178. doi: 10.1016/j.forsciint.2010.05.027

Geiman, I., Leona, M., and Lombardi, J. R. (2009). Application of Raman spectroscopy and Surface-Enhanced Raman Scattering to the analysis of synthetic dyes found in ballpoint pen inks. *J. Forensic Sci.* 54, 947–952. doi: 10.1111/j.1556-4029.2009.01058.x

Gorshova, K. O., Tumkin, I. I., Mymund, L. A., Tverjanovich, A. S., Mereshchenko, A. S., Panov, M. S., et al. (2016). The investigation of dye aging dynamics in writing inks using Raman spectroscopy. *Dyes Pigments* 131, 239–245. doi: 10.1016/j.dyepig.2016.04.009

Ho, Y. C., Lee, W. W. Y., and Bell, S. E. J. (2016). Investigation of the chemical origin and evidential value of differences in the SERS spectra of blue gel inks. *Analyst* 141, 5152–5158. doi: 10.1039/C6AN00972G

Houck, M. M., and Siegel, J. A. (2010). *Fundamentals of Forensic Science, 2nd Edn.* Burlington, MA: Academic Press.

Houck, M. M., Siegel, J. A., and Saucho, P. J. (2013). *Encyclopedia of Forensic Sciences, 2nd Edn.* Waltham: Academic Press. 375–379.

Jeanmaire, D. L., and Van Duyne, R. P. (1977). Surface raman spectroelectrochemistry: Part I. Heterocyclic, aromatic, and aliphatic amines adsorbed on the anodized silver electrode. *J. Electroanal. Chem. Interf. Electrochem.* 84, 1–20. doi: 10.1016/S0022-0728(77)80224-6

Johnson, C., Dujardin, C., Davis, S. A., and Murphy, C. J. (2002). Growth and form of gold nanorods prepared by seed-mediated, surfactant-directed synthesis. *Mater. Chem.* 12, 1765–1770. doi: 10.1039/b200953f

Kunicki, M., Fabianska, E., and Parczewski, A. (2013). Raman spectroscopy supported by optical methods of examination for the purpose of differentiating blue gel inks. *Problems Forens sci.* 95, 627–641.

Luo, Z., Smith, J. C., Goff, T. M., Adair, J. H., and Castleman. A. W., Jr. (2013). Gold cluster coating enhancing Raman Scattering from surfaces: ink analysis and document identification. *Chem. Phys.* 243, 73–78. doi: 10.1016/j.chemphys.2013.06.021

Mazzella, W. D., and Buzzini, P. (2005). Raman spectroscopy of blue gel pen inks. *Forens. Sci. Intern.* 152, 241–247. doi: 10.1016/j.forsciint.2004.09.115

Polavarapu, L., La Porta, A., Novikov, S. M., Coronado-Puchau, M., and Liz-Marzán, L. M. (2014). Pen-on-paper approach toward the design of Universal Surface Enhnanced Raman Scattering substrates. *Small* 10, 3065–3071. doi: 10.1002/smll.201400438

Sauzier, G., Giles, P., Lewis, S. W., and Van Bronswijk, W. (2015). *In situ* studies into the characterization and degradation of blue ballpoint inks by diffuse reflectance visible spectroscopy. *Anal. Methods* 7, 4892–4900. doi: 10.1039/C5AY00761E

Seifar, R. M., Verheul, J. M., Ariese, F., Brinkman, U. A. Th., and Gooijer, C. (2001). Applicability of Surface-Enhanced Resonance Raman Scattering for the direct discrimination of ballpoint pens inks. *Analyst* 126, 1418–1422. doi: 10.1039/b103042f

Selvakannan, P. R., Ramanathan, R., Plowman, B. J., Sabri, Y. M., Daima, H. K., O'Mullane, A. P., et al. (2013). Probing the effect of charge transfer enhancement in off resonance mode SERS via conjugation of the probe dye between silver nanparticles and metal substrates. *Phys. Chem. Chem. Phys.* 15, 12920–12929. doi: 10.1039/c3cp51646f

Weyermann, C., Kirsch, D., Costa-Vera, C., and Spengler,. B. (2006). Photofading of ballpoint pens studied on paper by LDI and MALDI MS. *J Am. Soc. Mass Spectrom.* 17, 297–306. doi: 10.1016/j.jasms.2005.11.010

Weyermann, C., Marquis, R., Mazzella, W., and Spiegler, B. (2007). Differentiation of blue ballpoint pen inks by laser desorption ionization mass spectrometry and high performance thin-layer chromatography. *J. Forens. Sci.* 52, 216–220. doi: 10.1111/j.1556-4029.2006.00303.x

White, P. C. (2003). *In situ* surface enhanced resonance Raman Scattering (SERRS) spectroscopy of biro inks–long-term stability of colloid treated samples. *Sci. Justice* 43, 149–152. doi: 10.1016/S1355-0306(03) 71762-6

Removing Polymeric Coatings With Nanostructured Fluids: Influence of Substrate, Nature of the Film, and Application Methodology

Michele Baglioni, Margherita Alterini, David Chelazzi, Rodorico Giorgi* and Piero Baglioni*

Department of Chemistry and CSGI, University of Florence, Sesto Fiorentino, Italy

Cleaning is one of the most important and delicate operations in the conservation of cultural heritage, and, if not correctly performed, may irreversibly damage works of art. The removal of aged or detrimental polymeric coatings from works of art is a common operation in conservation, and nanostructured fluids (NSFs), such as aqueous swollen micelles and oil-in-water (o/w) microemulsions, are used as an alternative to non-confined organic solvents, which pose a series of non-negligible drawbacks. NSFs effectiveness in removing polymeric coatings has been thoroughly demonstrated in the last decades, while their cleaning mechanism is still under investigation. The present work deepens the knowledge on the removal mechanisms of NSFs, studying the interaction of a four-component NSF with four different types of acrylic and vinyl polymer films cast from solutions or aqueous polymer latexes on three substrates (glass, marble, and polystyrene) with different hydrophilicity and wettability. NSFs were applied either as non-confined or confined in cellulose poultices (traditionally employed by conservators), or in highly retentive chemical gels, observing the influence of the confining matrix on the removal process. It was found that the NSF/polymer film interaction is greatly dependent on the film structure and composition. Films formed from solvent solutions can be swollen by water/organic solvents mixtures or dewetted when a surfactant is added to the cleaning fluid; films formed from polymer latexes, on the other hand, are generally swollen even just by water alone, but poorly dewet. The substrate also plays an important role in the removal of polymer films formed from solutions, for instance the removal of an acrylic polymer from polystyrene could be achieved only through highly selective cleaning using NSF-loaded chemical hydrogels. These results can be key for conservators, providing innovative solutions to face new challenges in art preservation.

Keywords: polymer coatings, cleaning, nanostructured fluids, acrylics, vinyls, non-ionic surfactants, hydrogels, dewetting

INTRODUCTION

Cleaning of works of art generally consists in the selective removal of materials that promote the degradation of the artifacts or alter their readability and appearance. Among these materials, aged or detrimental polymeric coatings are often found on works of art, and their removal is a common operation in art conservation. Synthetic polymers have been largely employed in the traditional restoration practice as varnishes, adhesives, protectives and consolidating agents. The presence of polymeric coatings on the surface of porous inorganic substrates (wall paintings, stone, mortars) drastically reduces water permeability and enhances the degradation induced by salts, up to consistent loss of the artifacts' surface layers (Carretti and Dei, 2004; Giorgi et al., 2010). Graffiti and vandalism are other well-known examples where selective removal of polymeric coatings must be carried out on artistic surfaces (Apostol et al., 2011; Sanmartín et al., 2014; Giorgi et al., 2017; Baglioni et al., 2018d). Other cases include the removal of aged pressure sensitive tapes from paper artworks (Bonelli et al., 2018), or of discolored and cracked varnishes from paintings (Burnstock and Kieslich, 1996; Baglioni et al., 2018a).

The vast amount of different solvent-sensitive materials found in classic and contemporary art poses continuous challenges to the safe removal of detrimental coatings (Kavda et al., 2017). Traditionally, restorers and conservators rely on the use of organic solvents to dissolve or swell unwanted materials. Solvents are typically applied either as non-confined, using cotton swabs, or thickened in viscous polymeric solutions and solvent gels (Burnstock and Kieslich, 1996; Burnstock and White, 2000; Baglioni et al., 2012c). However, these methods exhibit poor control and scarce selectivity, or involve the presence of residues from the cleaning system. In addition, health concerns arise from the toxicity of most solvents used in restoration.

Alternatively, nanostructured fluids (NSFs) such as aqueous swollen micelles and oil-in-water (o/w) microemulsions were proposed in the late 1980s for the removal of hydrophobic matter from porous inorganic substrates (Borgioli et al., 1995). Their effectiveness in removing polymeric coatings from different types of surfaces has been thoroughly demonstrated in the last decades (Carretti et al., 2003, 2007; Baglioni et al., 2010, 2012b, 2015a,b, 2016, 2018c). These NSFs are water-based systems where limited amounts of solvents are found either in the dispersed (as nano-sized droplets stabilized by surfactants) or in the continuous phase of the fluids. The large surface area developed by the nano-sized droplets, and the synergistic action of solvents and surfactants are responsible for enhanced cleaning power, while the presence of the continuous aqueous phase limits the re-deposition of detached hydrophobic matter on hydrophilic surfaces. Besides, being water-based, aqueous NSFs have reduced toxicity as opposed to traditional solvents. A further improvement was represented by the confinement of NSFs into retentive physical or chemical gels able to gradually release the fluids at the gel-artifact interface, maximizing control over the cleaning action (Baglioni et al., 2015c; Chelazzi et al., 2018).

While these systems represent the most advanced cleaning tools currently available to conservators, the interaction mechanism of NSFs with polymeric coatings is still being investigated.

The removal of high molecular weight macromolecules does not follow the rules of classical detergency. Studies performed on model samples, i.e., glass slides coated with an acrylate copolymer, have shown that dewetting takes place when water-based NSFs are put in contact with the polymeric coating (Raudino et al., 2015, 2017; Baglioni et al., 2017, 2018b). The film swells and detaches from the surface. This behavior was also observed on mortar samples coated with the same polymer (Baglioni et al., 2018b). The nature of both the organic solvents and the surfactant(s) included in the cleaning formulation was found to be of fundamental importance in the whole process. The solvents swell the polymer and lower its glass transition temperature, increasing the mobility of the polymer chains; the surfactant reduces the interfacial tension, kinetically promoting the detachment of the polymer film from the surface, and initiating the dewetting process that eventually breaks down the coating into separate polymer droplets.

Despite providing fundamental insights, previous studies on this subject depicted only a partial picture of the interaction mechanisms between NSFs and polymeric coatings. Namely, all the studies were conducted only on a single type of polymer, i.e., Paraloid B72® (poly(ethyl methacrylate/methyl acrylate) 70:30) cast from solution. Only glass or mortars were considered as substrates. Besides, simplified NSFs formulations were used to isolate the contribution of individual components in the system.

The present work aims to deepen the knowledge on the removal mechanisms of NSFs, studying the interaction of a four-component NSF with four different types of polymer films cast either from solutions or aqueous emulsions. In fact, it is well known that films of polymers cast from solutions have different physical structures than those cast from emulsions (Chevalier et al., 1992; Winnik, 1997; Steward et al., 2000), and polymers emulsions contain several additives; these can be crucial factors in determining the interaction process with the NSFs. For instance, hydrophilic additives in the polymer film might affect the interfacial tensions between the polymer, the substrate, and the NSF, which are key factors in wetting and dewetting processes. Three substrates were considered (glass, marble and polystyrene) with different hydrophilicity and wettability. At this stage, only laboratory samples and non-aged polymers were considered, so as to investigate simpler systems with controlled and known composition. Finally, NSFs were applied either as non-confined or confined in cellulose poultices (traditionally employed by conservators), or in highly retentive chemical gels, observing the influence of the confining matrix on the removal process in terms of controlled release and cleaning effectiveness. Our goal was to use a phenomenological approach to describe qualitatively the interaction between polymer films and NSFs, rather than providing a quantitative evaluation of polymer removal.

The NSF is composed of water, an alcohol ethoxylate nonionic surfactant, 2-butanol (BuOH), and 2-butanone (methyl ethyl ketone, MEK), and is representative of formulations actually employed in the conservation practice for the cleaning of real works of art.

The three selected substrates were coated with the four different polymers, obtaining a set of 12 samples, which were then exposed to the NSF, investigating the interaction mechanism for each combination. The effects of the NSF on the films were studied by means of optical microscopy and micro-reflectance infrared Fourier Transform spectroscopy 2D mapping of the areas of interest, which provides spatial resolution down to the micron-scale.

MATERIALS AND METHODS

Chemicals
$C_{9-11}E_{5,5}$ alcohol ethoxylate (Berol 266, AkzoNobel), sodium dodecylsulfate (SDS, Sigma-Aldrich, purity $\geq$ 99%), butanone (MEK, Sigma-Aldrich, purity 99%), 2-butanol (BuOH, Sigma-Aldrich, purity 99%), ethanol (EtOH, Fisher Chemical, purity $\geq$ 99%), white spirit (White Spirit, Fidea), D_2O (EurisoTop, 98%), and deuterated butanone (d-MEK, $C_4H_3D_5O$, Sigma-Aldrich, purity 98%) were used as received, without further purification. Water was purified with a Millipore Milli-Q gradient system (resistance > 18 MΩ cm).

Polymers Formulations
The four polymeric materials selected are widely used in the traditional restoration practice. They include: poly(vinyl acetate) (PVAc), commercially known as PVA K40®, dissolved in ethanol; PVAc as an aqueous emulsion, commercially known as Vinavil NPC®; poly(butyl methacrylate) (PBMA) dissolved in white spirit, commercially known as Plexisol P550®; poly(ethyl acrylate/methyl methacrylate) (PEA/PMMA) 40:60 as an aqueous emulsion, commercially known as Plextol B500®. **Table 1** reports the main properties of the formulations. All the products were applied on the substrates as a 10% (w/w) solution/emulsion.

Differential Scanning Calorimetry (DSC) for the Glass Temperature (Tg) Determination
DSC measurements were performed on a DSC Q1000 from TA Instruments on small samples (2–5 mg) of the four dry films, according to the following procedure: equilibration at −50°C; heating ramp from −50 to 60°C at 10°C/min; cooling ramp from 60 to −50°C at 10°C/min; heating ramp from −50 to 60°C at 10°C/min. The first heating/cooling ramp was used to equilibrate the sample, while the second heating ramp is the one used for the Tg determination. Each sample was run at least twice, in order to check for reproducibility of the measurement.

Substrates
The three different substrates selected for this work, i.e., glass, marble and polystyrene, were selected as they exhibit different wettability and are representative of artistic substrates frequently found in classic or contemporary art production. Glass slides of 5 × 5 × 0.3 cm³, marble tiles of 5 × 5 × 1 cm³, and polystyrene slides of 5 × 5 × 0.2 cm³ were used. The four different filming materials (polymers solutions or emulsions) were then laid manually on the top surfaces of each series of samples. 150 μl of each polymer formulation (V_S, V_E, A_S, A_E) was carefully spread using a pipette on a 4 × 5 cm² area on the surface of glass, marble and polystyrene samples. A reference area was thus left untreated. The specimens were left drying for 30 days, and then the dry mass of the films was evaluated. The density of the dry films was then measured, by drying for 4 days in a ventilated oven at 60°C weighed amounts of polymer solutions/emulsions that were poured into graduated vials. The results, reported in **Table 1**, made possible to calculate that the obtained films had an average thickness of ∼5–7 μm, assuming that they are homogeneously spread all over the treated surface.

Attenuated Total Reflectance Fourier-Transform Infrared Spectroscopy
ATR measurements were carried out with a Thermo Nicolet Nexus 870 spectrometer equipped with a liquid nitrogen-cooled MCT detector and a single reflection diamond crystal ATR unit. Spectra were recorded in the 4,000–650 cm^{-1} range (128 scans, 4 cm^{-1} resolution). ATR measurements were performed on small samples of spray-can paints' dried films, removed from the glass support.

NSF Preparation
The NSF selected for this work is composed as follows (w/w): H_2O, 65.9%; $C_{9-11}E_{5,5}$, 3.5%; BuOH, 9.7%; MEK, 20.9%. In order to better understand the role of each component in the interaction with the polymer coatings, other liquid systems were also used, obtained removing some of the components from the complete NSF formulation. Namely, a water/$C_{9-11}E_{5,5}$ surfactant solution, and a water/BuOH/MEK solvents mixture were used. In both systems, the ratio between each component was the same as in the complete NSF formulation. It is worth noting that both BuOH and MEK are partly water-miscible [12.5 and 24% at 20°C, respectively (Verschueren, 2001)] and this made possible to obtain a single-phase stable mixture of water and solvents even in the absence of surfactants.

Small-Angle Neutron Scattering
Small-angle neutron scattering (SANS) experiments were performed on the spectrometer V4 (Bensc-Helmholtz Zentrum Berlin). Two different configurations were employed (i.e., sample-to-detector distances, SD = 2 or 8 m) to cover a range of wave vectors q [$q = (4\pi/\lambda)\sin(\theta/2)$, where λ is the wavelength of the incident neutron beam and θ the scattering angle] from 0.007 to 0.28 Å^{-1}. For each configuration a 6 Å neutron wavelength was used and the wavelength resolution, $\Delta\lambda/\lambda$, was <10%. Samples were contained in 1 mm thick quartz cells and kept at 20 ± 2°C during the measurements. The scattering intensity was corrected for the empty cell contribution, transmission, and detector efficiency and was normalized to the absolute scale by direct measurement of the intensity of the incident neutron beam. The integration of the normalized 2D intensity distribution with respect to the azimuthal angle yielded the 1D scattering intensity distribution, $I(q)$, in cm^{-1}. The reduction of the data was performed using standard BENSC procedures for small-angle isotropic scattering. The background from the incoherent scattering coming from each sample was determined from analysis of the Porod asymptotic limit and subtracted from the normalized spectra. Experimental data normalized to absolute scale were fitted using Igor routines (NCNR_SANS_

TABLE 1 | Main properties and sample names of the four commercial polymers used.

Commercial name	Polymer nature	Physical appearance	Dry matter content	Applied as	Sample name[a]	Film density (g/cm^3)[b]	Tg (°C)[c]
PVA K40®	PVAc	Transparent grains	–	10% solution in EtOH	V_S	1.27	31
Vinavil NPC®	PVAc	Aqueous emulsion	52%	10% aqueous emulsion	V_E	1.05	16
Plexisol P550®	PBMA	40% solution in white spirit	40%	10% solution in white spirit	A_S	1.08	28
Plextol B500®	PEA/PMMA	Aqueous emulsion	50%	10% aqueous emulsion	A_E	1.03	30

[a] V, vinyl; A, acrylic; S, polymer applied as a solution; E, polymer applied as an emulsion.
[b] The density was calculated as described in section Substrates.
[c] The glass temperature (Tg) was measured by means of DSC analyses according to the procedure described in section Differential Scanning Calorimetry (DSC) for the Glass Temperature (Tg) Determination.

package_6.011) (Kline, 2006) available from NIST, National Institute for Standard and Technology, Gaithersburg, MD, running on Igor Pro© (Wavemetric Inc., Lake Oswego, Oregon; Version 6.22).

NSF/Polymer Interaction Experiments
Immersion Tests
The aim of these tests was to investigate the direct interaction between cleaning fluids and polymer films, without the influence of a medium (i.e., cellulose pulp poultice or gel). To this purpose, the coated specimens were partly immersed in about 30 ml of the selected fluids, i.e., the minimum amount of fluid needed to treat the samples. The area of the polymer film exposed to the fluid action was kept constant and fixed to 1×5 cm^2. At selected time intervals, up to 10 min, the specimens were extracted from the fluid and let dry, and then visual inspection of possible changes in the film was carried out. At $t = 0$ min and $t = 10$ min the superficial micromorphology of the films (after drying) was investigated by optical microscopy and FTIR 2D micro-reflectance mapping. Finally, after 10 min of incubation with each liquid system, a removal test was performed on all the samples, using a cotton swab soaked with water, in order to check the removability of the polymeric coatings.

Confocal Laser Scanning Microscopy (CLSM)
Confocal Microscopy experiments were performed on a Leica TCS SP8 confocal microscope (Leica Microsystems GmbH, Wetzlar, Germany) equipped with a 63× water immersion objective. The four polymers were stained with Coumarin 6, which was dissolved/dispersed in the liquid solutions or latexes. Then, 2–4 µm-thick polymer films were obtained by spin coating coverglasses for 60 s at 1,000 rpm. Coumarin 6 was excited with the 488 nm laser line of an argon laser. The emission of the dye was acquired with a PMT in the range 498–530 nm. CLSM experiments were performed to monitor the interaction of the different polymer films with the NSF. Briefly, 50 µl of the unlabeled liquid phase were put in contact with the coumarin 6-labeled polymer coated coverglass, and the morphological variations of the polymeric film were monitored over time.

Cleaning Tests
Two sets of cleaning tests were performed, in order to evaluate the influence on the application method of the NSF, and the effect of the supporting material (i.e., cellulose pulp poultice or chemical hydrogel) on the interaction between the NSF and the polymeric coating. Traditional cellulose pulp poultices were prepared by mixing 35 mg of cellulose pulp (Arbocel®, Zecchi, Firenze) and 160 µl of NSF. The obtained poultices were applied, interposing a Japanese paper sheet (Zecchi, Firenze) between the compress and the specimen surface, on 1 cm^2 areas of each sample for 15 min. After removing the poultices, a gentle mechanical action was performed on the treated surface, by means of wet cotton swabs. Poly(hydroxyethyl methacrylate/poly vinylpyrrolydone) semi-interpenetrated networks (pHEMA/PVP SIPNs) are highly retentive hydrogels, previously proposed in combination with NSFs for the cleaning of works of art (Baglioni et al., 2018a), and prepared as described elsewhere (Domingues et al., 2013a,b). Gels having a size of $1 \times 1 \times 0.2$ cm^3 were used, able to upload ca. 160 µl of NSF, i.e., the same amount of cleaning fluid loaded in the poultices. The gels were loaded with the NSFs by immersion for 24 h, so as to exchange water within the gel with the NSFs. The gel was applied for 15 min, and at the end of the treatment a gentle mechanical action was performed on the coating residues.

Contact Angle Measurements
The contact angle of 5 µL sessile droplets of Milli-Q water on the selected material surface was measured with a Rame-Hart Model 190 CA Goniometer. The three substrates and the four polymer films were investigated. The equilibrium contact angle was measured in at least eight different areas, and the average value and standard deviation was evaluated.

Optical Microscopy
A Reichert Zatopan 353–890 microscope was used to collect micrographs. The instrument was coupled with a Nikon Digital Sight DS-Fi2 camera. The NIS-ELEMENTS software was used to capture and edit images.

Fourier-Transform Infrared Spectroscopy−2D Micro-Reflectance Mapping
The Fourier transform infrared (FTIR) 2D imaging of the treated surfaces was carried out using a Cary 620–670 FTIR microscope, equipped with an FPA 128 × 128 detector (Agilent Technologies). The spectra were recorded directly on the surface of the samples in reflectance mode, with open aperture and

TABLE 2 | Contact angle of water droplets on the surface of the four selected polymeric coatings, and of the three types of substrates.

Sample	Contact angle	Substrate	Contact angle
V_S	57.8 ± 0.8°	glass	35.3 ± 3.1°
V_E	39.1 ± 1.9°	marble	61.7 ± 1.8°
A_S	78.2 ± 3.1°	polystyrene	77.0 ± 1.6°
A_E	62.5 ± 2.1°		

a spectral resolution of 8 cm^{-1}, acquiring 128 scans for each spectrum. Each analysis produces an IR map of 700 × 700 μm^2 (128 × 128 pixels), with a spatial resolution of 5.5 μm (i.e., each pixel has dimensions of 5.5 × 5.5 μm^2 and is associated to an independent spectrum). In each map, the intensity of a characteristic peak of each polymer, e.g., the C=O ester stretching typical of both acrylics and vinyls, at about 1,730 cm^{-1}, was shown with a chromatic scale, following the order red > yellow > green > blue.

RESULTS AND DISCUSSION

Polymer Films Characterization

The four polymeric coatings were characterized by means of FTIR-ATR and contact angle measurements. **Table 2** reports the values for the contact angle of water droplets laid on the surface of the polymer films, or of the selected substrates (glass, marble, polystyrene). The substrates exhibit a range of contact angles passing from hydrophilic (glass) to hydrophobic surfaces (polystyrene). Regarding the polymers, it can be noticed that the acrylics are more hydrophobic than the vinyls, and the films deriving from polymer latexes are more hydrophilic than those coming from solutions. This is likely due to the presence of surfactants, stabilizers, and other polar additives in the latexes emulsions, which affect the wettability of the film.

Figure 1 shows the FTIR-ATR spectra of the four polymer films. The spectra of the two vinyl films match closely, confirming that the same type of polymers is present in both films. The main bands were assigned as follows (Doménech-Carbó et al., 2001; Learner and Institute, 2004): C-H stretching (2,928 cm^{-1} and a shoulder at 2,972 cm^{-1}); C=O stretching (intense and narrow peak at 1,727 cm^{-1}); asymmetric stretching of the C–O group (1,222 cm^{-1}, distinctive of PVAc); C–H in-plane bending (1,428 cm^{-1} and 1,371 cm^{-1}); C–H out-of-plane bending (1,117 cm^{-1}); C–O symmetric stretching (1,018 cm^{-1}); C–C stretching (944 cm^{-1}); C–H rocking (792 cm^{-1}). Besides, the spectrum of V_E shows a broad band at 3,335 cm^{-1}, which is likely due to the OH stretching of poly(vinyl alcohol) (PVA), i.e., one of the main additives of the Vinavil NPC® aqueous latex.

The spectra of A_S and A_E show slightly different features in the fingerprint and CH stretching regions, as expected given the different type of acrylate polymers found in those films.

The main bands of the acrylic films were assigned as follows (Doménech-Carbó et al., 2001; Learner and Institute, 2004; Pintus and Schreiner, 2011): C–H stretching (A_S: peaks at 2,958, 2,933, 2,873 cm^{-1}; A_E: peaks at 2,887 cm^{-1} and 2,860 cm^{-1}); C=O stretching (1,720 cm^{-1}); C–H in-plane bending (1,465 and 1,380 cm^{-1}; A_E shows an additional peak is visible at 1,343
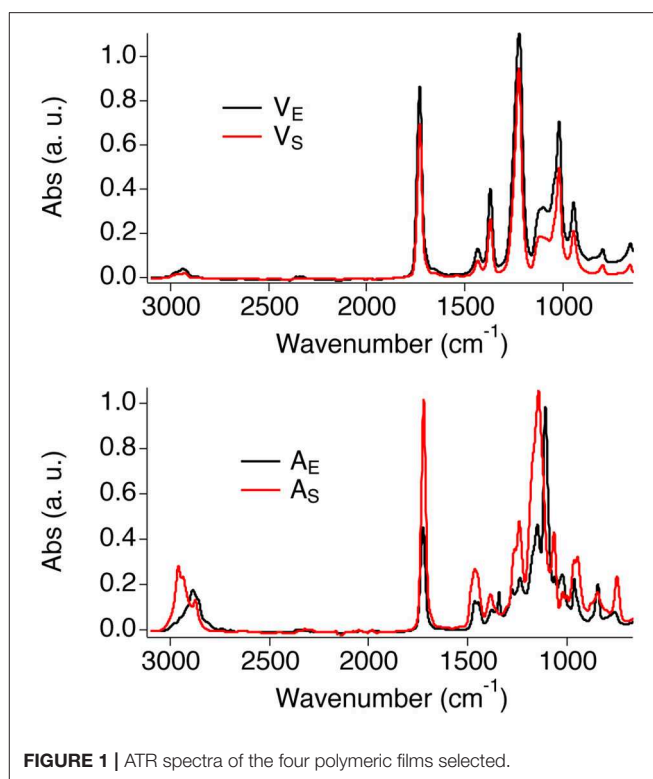
FIGURE 1 | ATR spectra of the four polymeric films selected.

cm^{-1}); C–O stretching (A_S: peaks at 1,240 and 1,065 cm^{-1}; A_E: peaks at 1,279, 1,241, 1,109, and 1,022 cm^{-1}); C–C stretching (965 and 946 cm^{-1}); C–H rocking (840 and 750 cm^{-1}).

NSF Characterization

The selected NSF for this work is composed of water, a nonionic surfactant and two solvents, i.e., BuOH and MEK, which are partly miscible with water. The structure of this NSF was never studied before, thus acquiring information on the micelles' size and shape, and on the location of each component in the NSF, was deemed a preliminary step to help understanding the interaction of the fluid with the polymeric films. To this aim, SANS measurements were performed on four D$_2$O based samples: (1) the D$_2$O/C$_{9-11}$E$_{5.5}$ binary mixture; (2) the D$_2$O/C$_{9-11}$E$_{5.5}$/BuOH ternary system; (3) the complete NSF formulation, i.e., D$_2$O/C$_{9-11}$E$_{5.5}$/BuOH/MEK; (4) the complete NSF formulation with deuterated d-MEK fully replacing the regular MEK. The analysis of samples 3 and 4 represents a contrast variation experiment, in which everything is kept constant from one sample to the other, except for its contrast, by changing the scattering length density (SLD) of one or more chemicals (in this case, exchanging MEK with d-MEK).

Figure 2-top shows the SANS profiles for the four samples analyzed. The data were fitted according to two different models. The supramolecular aggregates, in the case of the binary surfactant/water and the water/surfactant/BuOH systems, were modeled as non-interacting polydisperse core-shell spheres, defined by two contrasts, i.e., bulk/shell and shell/core. On the other hand, the best fitting for the complete NSF was obtained by modeling the micelles as non-interacting prolate core-shell
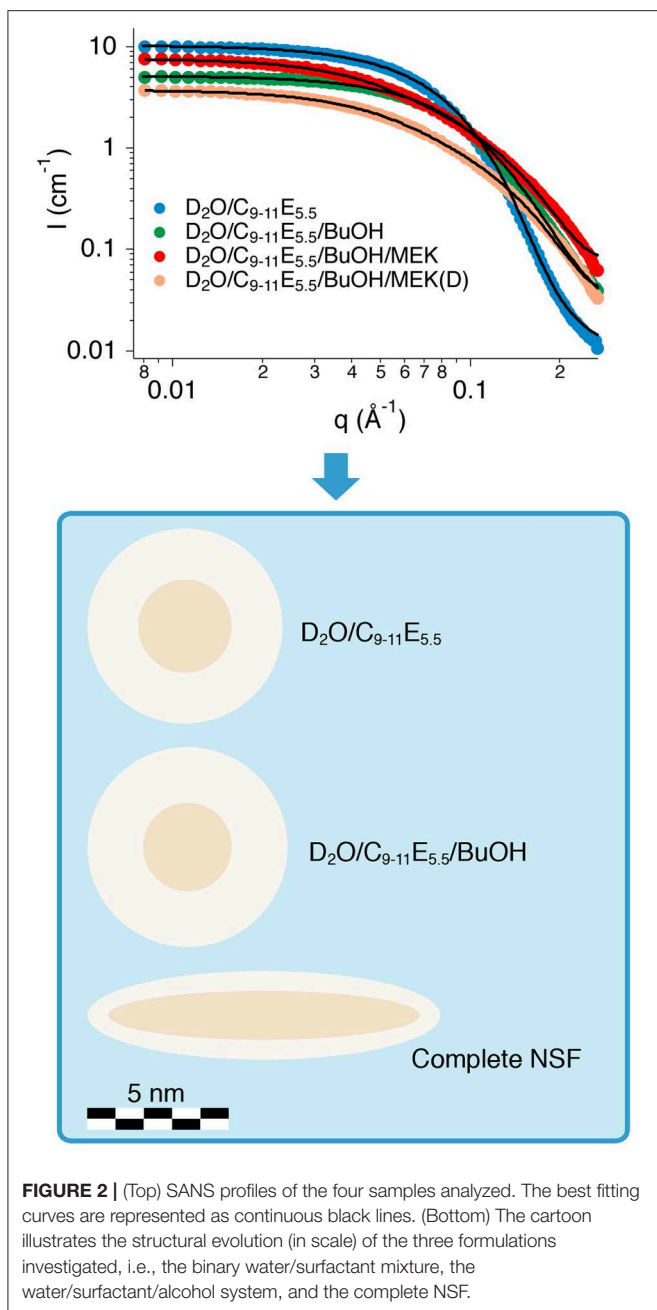
FIGURE 2 | (Top) SANS profiles of the four samples analyzed. The best fitting curves are represented as continuous black lines. (Bottom) The cartoon illustrates the structural evolution (in scale) of the three formulations investigated, i.e., the binary water/surfactant mixture, the water/surfactant/alcohol system, and the complete NSF.

TABLE 3 | SLD for neutrons scattering of the chemicals included in the NSF.

Chemical formula/structure	Compound/molecular group	SLD (10^{-6} Å^{-2})
D_2O	Heavy water	6.39
$CH_3(CH_2)_{8-10}(OCH_2CH_2)_{5.5}OH$	$C_{9-11}E_{5.5}^a$	0.37
$CH_3(CH_2)_{8-10}^a$	$C_{9-11}E_{5.5}$ apolar tail	−0.41
$HO(CH_2CH_2O)_{5.5}$	$C_{9-11}E_{5.5}$ polar head	0.97
$C_4H_{10}O$	BuOH	−0.33
$C_4H_3D_5O$	d-MEK	3.66
C_4H_8O	MEK	0.17

^{a}For the SLD calculation a C_{10} aliphatic chain was considered.

where N_p is the number density of the scattering particles (cm^{-3}), V_p is the volume (cm^3), $\Delta\rho$ is the contrast term (cm^{-2}), $P(q)$ is the form factor, and $S(q)$ is the structure factor. In this case $S(q) = 1$, as the particles were considered to be non-interacting. In the case of spherical core-shell aggregates, the particle scattering intensity is expressed as follows (Kline, 2006):

$$I(q) = \frac{\phi}{V_P}\left[(\rho_{core}-\rho_{shell})\frac{3V_c j(qr_c)}{qr_c} + (\rho_{shell}-\rho_{bulk})\frac{3V_P j(qr_s)}{qr_s}\right]^2 \tag{2}$$

where $j(x)$ is a spherical Bessel function and is expressed as:

$$j(x) = \frac{(\sin x - x\cos x)}{x^2} \tag{3}$$

and where φ is the volume fraction of the micellar phase, V_c is the core volume, r_c is the core radius, $r_s = r_c + t$ (t is the shell thickness). Since this model takes into account a polydisperse core, which follows the Schultz distribution, the form factor calculated in Equation (2) is normalized by the average particle volume:

$$\langle V \rangle = \frac{4\pi}{3}\langle r_c^3 \rangle \tag{4}$$

where:

$$\langle r_c^3 \rangle = \frac{(z+2)(z+3)}{(z+1)^2}\langle r_c \rangle \tag{5}$$

and z is the width parameter of the Schultz distribution (Degiorgio et al., 1985):

$$z = \frac{1}{\left(\frac{\sigma}{\langle r_c \rangle}\right)^2} - 1 \tag{6}$$

being σ^2 the variance of the distribution. The polydispersity index (PDI), reported in **Table 4** is defined as $\sigma/\langle r_c\rangle$ [see equation (6)] and its value is comprised between 0 and 1.

In the case of monodisperse non-interacting prolate ellipsoids, on the other hand, when modeling asymmetric micelles with a

ellipsoidal particles, again defined by a double contrast. The SLD of bulk, shell and core, i.e., respectively, ρ_{bulk}, ρ_{shell}, and ρ_{core}, were calculated according to the SLD for neutrons of each chemical included in the formulations, as reported in **Table 3**. For globular micelles of homogeneous scattering length density, the total scattered intensity $I(q)$ (cm^{-1}) is given by (Sheu and Chen, 1988; Liu et al., 1995):

$$I(q) = N_P V_P^2 \Delta\rho^2 P(q) S(q) + bkg_{inc} \tag{1}$$

TABLE 4 | Fitting results of the SANS data acquired on the NSF.

Fitting parameter	D$_2$O/C$_{9-11}$E$_{5.5}$	D$_2$O/C$_{9-11}$E$_{5.5}$/BuOH	Complete NSF
r (Å)	16.7 ± 0.3	15.7 ± 0.2	–
t (Å)	17.9 ± 0.1	19.6 ± 0.1	9.4 ± 0.4
PDI	0.20 ± 0.01	0.40 ± 0.02	–
a (Å)	–	–	53.0 ± 2.0
b (Å)	–	–	7.2 ± 0.3
P$_{BuOH}$	–	0.30 ± 0.03	0.28 ± 0.02
P$_{MEK}$	–	–	0.17 ± 0.01

core-shell scattering length profile, $P(q)$ included in Equation (1) is usually calculated as an orientationally-averaged normalized form factor, $\bar{P}(q)$. First, the orientation-dependent form factor $F(q, \mu)$, is defined as follows (where μ is the cosine between the direction of the symmetry axis of the ellipsoid and the Q vector):

$$F\left(q, \mu\right) = f\left(\rho\right)\frac{3j\left(u\right)}{u} + \left(1 - f\left(\rho\right)\right)\frac{3j\left(v\right)}{v} \qquad (7)$$

where $j(x)$ is the same spherical Bessel function defined in Equation (3) and u and v are expressed as:

$$u = q[\mu^2 a^2 + (1 - \mu^2)b^2]^{1/2} \qquad (8)$$

$$v = q[\mu^2 (a + t)^2 + (1 - \mu^2)(b + t)^2]^{1/2} \qquad (9)$$

which define the geometrical shape of the micelles, and where $f(\rho)$ contains the contrast calculation, and a, b, t are the geometrical parameters of the ellipsoid, i.e., the major semi-axis, the minor semi-axis, and the shell thickness, respectively.

$\bar{P}(q)$ is then calculated as follows (Kotlarchyk and Chen, 1983):

$$\bar{P}\left(q\right) = \int_0^1 d\mu \left|F(q, \mu)\right|^2 \qquad (10)$$

Even though the measured samples included D$_2$O instead of H$_2$O, the structural picture emerging from the analysis of SANS data can be safely transferred to the H$_2$O-based NSF, apart from possible slight changes (Baglioni et al., 2012a).

Table 4 shows the main fitting results, while **Figure 2**-bottom contains a cartoon depicting the size and shape evolution of micelles following the addition of each component to the formulation. The size of C$_{9-11}$E$_{5.5}$ micelles in D$_2$O was perfectly consistent with the length of the surfactant molecule and with the results of previous SAXS measurements performed on similar systems (Baglioni et al., 2017), where a $r + t$ total micelle radius of about 35 Å had been obtained. A polydispersity index of 0.2 for the size of the hydrophobic core fits such systems, which usually have a PDI in the 0.1–0.5 range. According to fitting results, the structure and size of the micelles do not change significantly after the addition of BuOH (see **Figure 2**-bottom). In fact, BuOH was found to be partitioned between the micellar and the aqueous bulk phase in a 30:70 ratio, meaning that most

of the solvent is mixed with water. The fraction solubilized in the micelles is preferentially located in the shell, replacing D$_2$O hydration molecules, and thus affects the micellar size and shape only slightly. The main effect of the inclusion of BuOH is to double the polydispersity of the core radius with respect to the binary water/surfactant system, even though the value is perfectly suitable for a micellar solution.

The results of the contrast variation experiments performed on the complete NSF formulation showed that the inclusion of a significant amount of MEK in the system completely alters both the size and shape of the aggregates (see **Figure 2**-bottom), as the result of a sphere-to-rod transition. This behavior was observed for similar systems containing the same surfactant (Baglioni et al., 2014) and is likely due to the system getting closer to its cloud point. In fact, micelles are known to grow and assume elongated shapes close to the clouding temperature, as observed in the present case. C$_{9-11}$E$_{5.5}$ has a cloud point of about 55–60°C, which is known to be lowered by the interaction of this surfactant with MEK (Baglioni et al., 2014). The inclusion of MEK in the system does not alter significantly the partition coefficient of BuOH (P$_{BuOH}$) between the micelles and the water phase, while MEK is mainly dissolved in the bulk phase (P$_{MEK}$ = 0.17).

Overall, SANS analysis clarified that the structure of the NSF is that of rod-like micelles, mainly composed of the sole surfactant, dispersed in a water/solvents mixture, indicating that the system is close to its cloud point. This structural information has relevant implications in terms of cleaning power of the NSF, as detergency is known to be maximized when these systems are close to the cloud point (Holmberg, 2002; Holmberg et al., 2002; Stubenrauch, 2008; Baglioni et al., 2014). Therefore, high cleaning effectiveness was expected from this NSF formulation.

NSF/Polymer Interaction

The interaction between the NSF and the four polymer films was initially investigated simply by immersing the coated specimens into four different liquid systems, i.e., water, water/surfactant, water/solvents, and the complete NSF. The micromorphology of the film was observed by optical microscopy at different times during the total 10 min of incubation of the specimens in the liquids, while 2D micro-FTIR mapping was performed on the polymer surface before exposure to the fluids and after 10 min of incubation. Finally, a removal test was performed on the polymers using wet cotton swabs, in order to check their removability.

Looking at the results of the immersion tests, illustrated in **Figures 3**–**6** and summarized in **Table 5**, a clear difference in the behavior of samples emerges, i.e., the polymer films deriving from latexes (V$_E$ and A$_E$) are preferentially swollen and only in few cases partly dewetted, whereas the films deriving from solutions are unaffected by just water, are swollen by the surfactant solution, and are partly or completely dewetted when solvents are included in the liquid systems. For instance, **Figures 3**, **5** show how for chemically identical polymers (both PVAc) the type of the film plays a key role in determining the behavior when the film is exposed to the same NSF. 2D microFTIR mapping was crucial to confirm the location and distribution of the polymers on the micron-scale. In particular, when a film is

FIGURE 3 | Immersion tests results for the V_S-coated glass **(A)**, marble **(B)**, and polystyrene **(C)** specimens. The frames, left to right, are taken at $t = 0$ s, 10 s, 30 s, 1 min, 5 min, 10 min. For $t = 0$ s and $t = 10$ min a representative 2D micro-reflectance FTIR map is reported, together with its relative micrograph in visible light. In each map, the intensity of the C=O ester stretching at about 1,730 cm^{-1} is shown with a chromatic scale, following the order red > yellow > green > blue. Visible light micrographs are approximately 1 cm^2 large; the FTIR mapping areas have a size of 400 μm × 550 μm. The blue boxes highlight areas of the samples, which were investigated by 2D FTIR mapping; the position of the blue frame in the lower magnification images does not correspond to the actual position of the investigated areas.

dewetted (see **Figures 3**, **4**) it was shown that no polymer residues are present (above the instrumental detection limit) outside the droplets on the substrate surface. In fact, it has been shown that the detection limit of an FPA detector is significantly lower than that of conventional mercury cadmium telluride (MCT)

detectors for the FTIR detection of trace amounts of materials. The heterogeneous distribution of analytes can result in small areas of localized high concentration, which can be detected thanks to the high spatial resolution of the FPA detector (Chan and Kazarian, 2006). For instance, for polyvinyl alcohol and

FIGURE 4 | Immersion tests results for the A_S-coated glass **(A)**, marble **(B)**, and polystyrene **(C)** specimens. The frames, left to right, are taken at $t = 0$ s, 10 s, 30 s, 1 min, 5 min, 10 min. For $t = 0$ s and $t = 10$ min a representative 2D micro-reflectance FTIR map is reported, together with its relative micrograph in visible light. In each map, the intensity of the C=O ester stretching at about 1,730 cm^{-1} is shown with a chromatic scale, following the order red > yellow > green > blue. Visible light micrographs are approximately 1 cm^2 large; the FTIR mapping areas have a size of 400 μm $\times$ 550 μm. The blue boxes highlight areas of the samples, which were investigated by 2D FTIR mapping; the position of the blue frame in the lower magnification images does not correspond to the actual position of the investigated areas.

polyvinyl acetate we verified that quantities < 1 pg/pixel (1 pixel = 5.5 × 5.5 μm) can be detected.

Polymer coatings formed from aqueous emulsions are significantly more sensitive to the action of water [a well-known issue when emulsion-based acrylic paint layers are exposed to aqueous cleaning fluids (Murray et al., 2002; Ormsby and Learner, 2009; Willneff et al., 2014)], and tend to be swollen. This is justified by the presence of a non-negligible amount of hydrophilic additives and surfactants in the polymer emulsions, which remain in the film after drying and are able to interact with

FIGURE 5 | Immersion tests results for the V_E-coated glass **(A)**, marble **(B)**, and polystyrene **(C)** specimens. For $t = 0\,s$ and $t = 10\,min$ a representative 2D micro-reflectance FTIR map is reported, together with its relative micrograph in visible light. In each map, the intensity of the C=O ester stretching at about 1,730 cm^{-1} is shown with a chromatic scale, following the order red > yellow > green > blue. Visible light micrographs are approximately 1 cm^2 large; the FTIR mapping areas have a size of 400 μm × 550 μm. The blue boxes highlight areas of the samples, which were investigated by 2D FTIR mapping; the position of the blue frame in the lower magnification images does not correspond to the actual position of the investigated areas.

water molecules, favoring the swelling of the film. The presence of hydrophilic additives can also explain why the swollen films tend to dewet less easily. The energetic balance of dewetting can be described by the spreading coefficient S, which for a polymer film on a glass surface, immersed in a liquid, is defined as (Baglioni and Chelazzi, 2013):

$$S = \gamma_{LG} - \gamma_{PG} - \gamma_{LP} \qquad (11)$$

where γ_{LG} is the interfacial tension between glass and the liquid, γ_{PG} is the interfacial tension between glass and the polymer, and γ_{LP} is the interfacial tension between the liquid and the polymer. When S is negative, dewetting is energetically favored and occurs spontaneously unless an activation energy barrier hinders the process kinetically. Hydrophilic additives in the

polymer film might lower the values of both γ_{PG} and γ_{LP}, making S less negative for a given liquid/polymer/glass set. On the other hand, the presence of surfactant additives may lower the glass transition temperature (T_g) of the polymer films (as in the case of V_E—see **Table 1**), making polymer chains more mobile, thus possibly decreasing the energy costs related to the formation of new interfacial regions during the detachment of the film, and lowering the activation energy necessary to initiate dewetting (Baglioni et al., 2017, 2018b; Montis et al., 2019).

Overall, in the case of the polymer films from emulsions investigated here, the films' thermodynamic stability seems to prevail on the kinetic drive of the dewetting process. However, the swollen films are softened and easily removable from glass and marble even with water and water/$C_{9-11}E_{5.5}$, meaning that the adhesion to the solid surface was sensibly reduced,
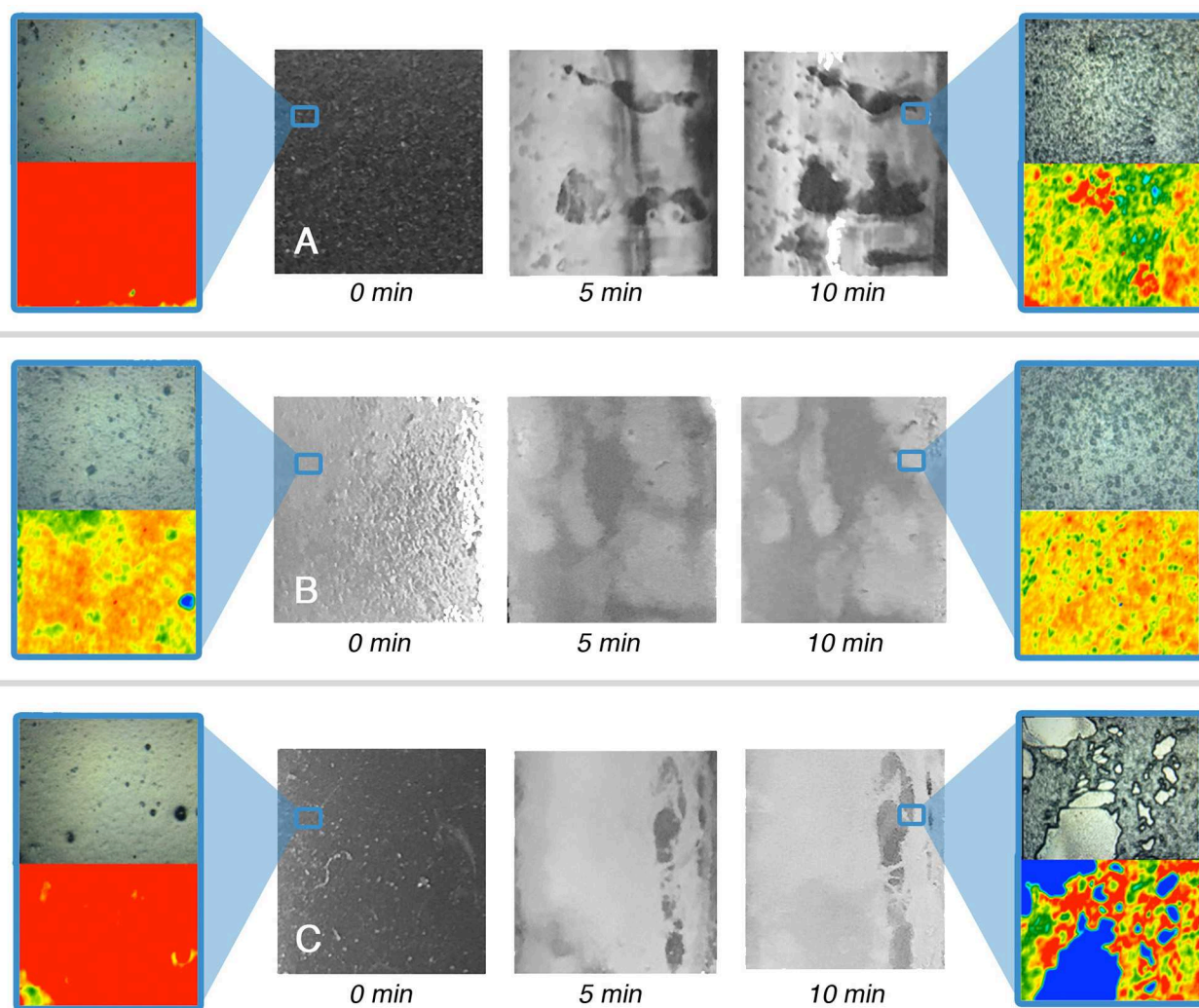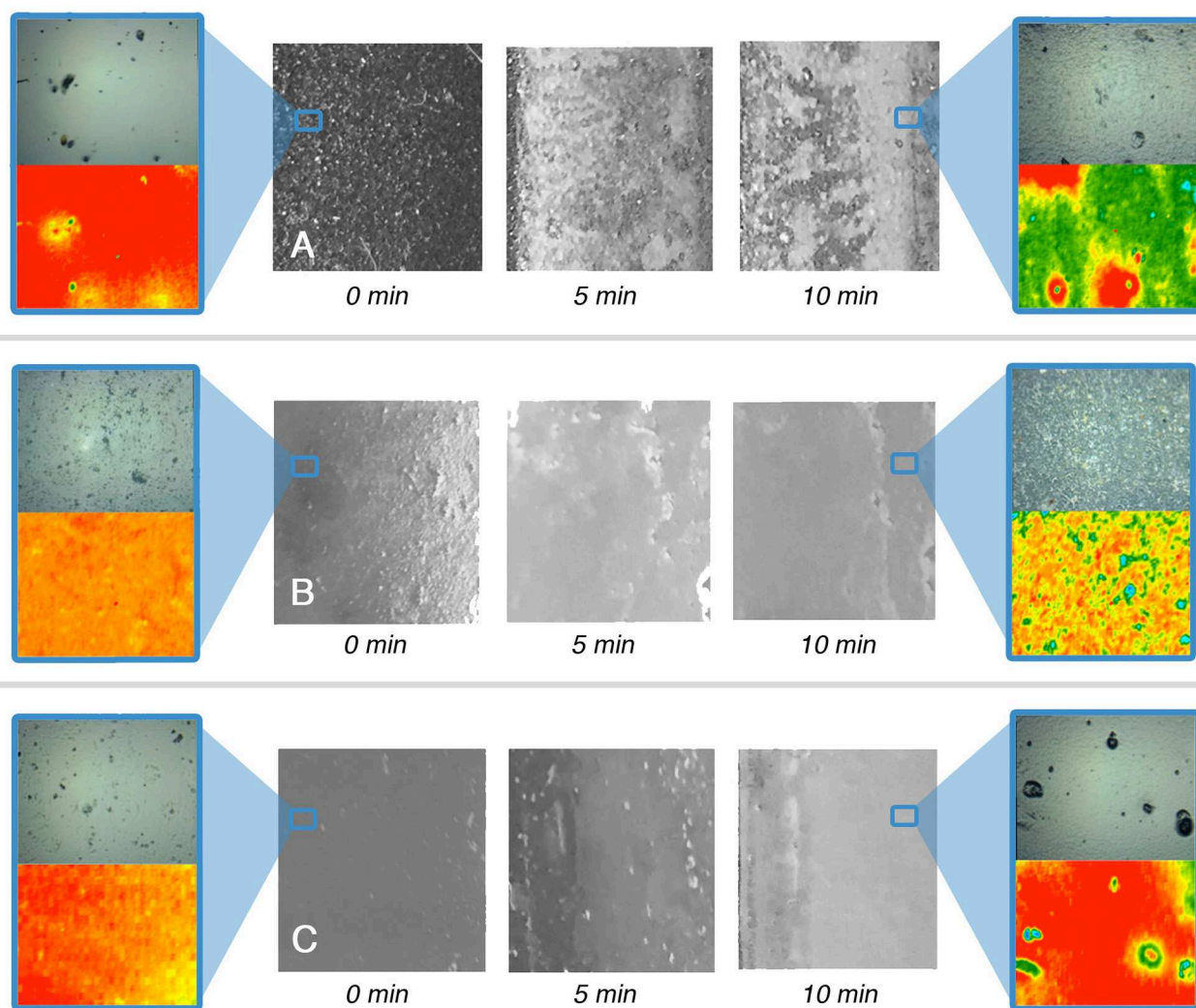
FIGURE 6 | Immersion tests results for the A_E-coated glass **(A)**, marble **(B)**, and polystyrene **(C)** specimens. For $t = 0$ s and $t = 10$ min a representative 2D micro-reflectance FTIR map is reported, together with its relative micrograph in visible light. In each map, the intensity of the C=O ester stretching at about 1,730 cm^{-1} is shown with a chromatic scale, following the order red > yellow > green > blue. Visible light micrographs are approximately 1 cm^2 large; the FTIR mapping areas have a size of 400 μm $\times$ 550 μm. The blue boxes highlight areas of the samples, which were investigated by 2D FTIR mapping; the position of the blue frame in the lower magnification images does not correspond to the actual position of the investigated areas.

while in the case of polystyrene the removal is slightly more difficult. When a polymer film formed from a solvent solution is exposed to a cleaning fluid, a more diversified behavior is observed. Water and water/C$_{9-11}$E$_{5.5}$ are partly or completely ineffective in removing the films. Instead, dewetting processes are induced by water/solvents mixtures or, more efficiently, by the synergistic action of solvents and surfactants (Gentili et al., 2012; Xu et al., 2012; Baglioni et al., 2017, 2018b). This is clearly exemplified by A$_S$ on marble, where water alone produces no visible effects on the polymer. The nonionic surfactant micellar solution is able to induce some swelling of the film, but not sufficient to grant its easy removal. A water/solvents mixture, on the other hand, produces a partial dewetting pattern, and the film can be partly removed using some mechanical action. This

means that solvents are able to swell the polymer to such an extent that the T_g is lowered below room temperature, starting the dewetting process. However, it is only with the synergistic action of a surfactant, which lowers the interfacial tension at the liquid/substrate and liquid/polymer interfaces, that dewetting proceeds further, leading to easy and complete polymer removal. The substrate's chemical nature is a key factor. Increasing the hydrophobicity of the substrate, the affinity of the polymer film with the substrate increases, leading to less efficient polymer removal, culminating with the limit case of A$_S$ on polystyrene, which resulted completely irremovable.

The interaction between the complete NSF and the four polymer films was also monitored through CLSM imaging, as described in section Confocal Laser Scanning Microscopy

TABLE 5 | Results of immersion tests performed on polymer-coated glass, marble and polystyrene specimens.

		Glass		Marble		Polystyrene	
		Film appearance	Removability[a]	Film appearance	Removability[a]	Film appearance	Removability[a]
V_S	H_2O	No change	±	No change	x	No change	x
	$H_2O/C_{9-11}E_{5.5}$	Swollen	o	Swollen	±	Swollen	±
	$H_2O/BuOH/MEK$	Dewetted	o	Dewetted	o	Dewetted	o
	NSF	Dewetted	o	Dewetted	o	Dewetted	o
A_S	H_2O	No change	x	No change	x	No change	x
	$H_2O/C_{9-11}E_{5.5}$	Swollen	o	Swollen	x	Swollen	x
	$H_2O/BuOH/MEK$	Dewetted	o	Partly dewetted	±	Swollen	x
	NSF	Dewetted	o	Dewetted	o	Swollen	x
V_E	H_2O	Swollen	o	Swollen	o	Partly dewetted	o
	$H_2O/C_{9-11}E_{5.5}$	Swollen	o	Swollen	o	Partly dewetted	o
	$H_2O/BuOH/MEK$	Swollen	o	Swollen	o	Swollen	±
	NSF	Swollen	o	Swollen	o	Partly dewetted	o
A_E	H_2O	Swollen	o	Swollen	o	Swollen	o
	$H_2O/C_{9-11}E_{5.5}$	Swollen	o	Swollen	o	Swollen	o
	$H_2O/BuOH/MEK$	Swollen	o	Swollen	o	Swollen	±
	NSF	Swollen	o	Swollen	o	Swollen	o

Both the film appearance and its removability after 10 min of incubation in the four different liquid systems are summarized in the table, following analysis with optical microscopy and 2D micro-FTIR mapping.

[a]After 10 min of incubation in the liquid systems, the removability of the coatings was checked performing a gentle mechanical action with a cotton swab soaked with water; x, no removal; ±, partial removal; o, complete removal.

(CLSM). Homogeneous and reproducible 2–4 μm thick films on coverglasses were obtained by spin coating. **Figure 7** summarizes the results of the investigation, which were in perfect agreement with what was observed during the immersion tests reported above. A_S and V_S, i.e., the polymer films cast from solutions, were completely and quickly dewetted by the NSF, while A_E and V_E, i.e., the films cast from polymer latexes, were just swollen. **Figure 7** shows that some small cracks and/or holes (of few microns) are visible in the V_E and A_E swollen films, which nonetheless maintain their overall coherence on a macro-scale. These holes possibly form in correspondence of previous film defects, which can be present on such thin films. Overall, the behavior of polymer films cast from aqueous latexes can be seen as if the physical process stopped at the very early stages of dewetting. This is in agreement with what observed during previous experiments, and seems to enforce the hypothesis that the amphiphilic additives in these films play a key role in inhibiting the dewetting process, which otherwise would likely occur.

The inhomogeneous aspect of the V_E and A_E films at $t = 0$ is due to the fact that the hydrophobic fluorescent dye was not evenly distributed in the aqueous polymer latex. As the films is swollen by the penetration of the organic solvents, the dye evenly spread through the film.

CLSM investigations, overall, allowed to confirm the results of the immersion tests on macroscopic samples, where the polymer thickness could not be directly measured and not accurately controllable.

Finally, the influence of the application methodology on the outcome of removal tests was evaluated. To this aim, the

same amount of NSF was uploaded, respectively, in traditional cellulose pulp poultices and in pHEMA/PVP chemical hydrogels. The latter have been characterized and assessed in the last years, and their use for the removal of unwanted materials from water-sensitive substrates has been thoroughly reported (Domingues et al., 2013a; Baglioni et al., 2018a; Bonelli et al., 2018). Recently, SAXS and rheology studies showed that these gels act as "sponges," able to load different NSFs without being altered or dramatically alter the properties of the fluids (Baglioni et al., 2018a).

The two systems were applied for 15 min on the surface of the films, and then micrographs of the treated area were taken before checking the coating removability via gentle mechanical action with a wet cotton swab. As visible in **Figure 8**, the areas treated with the NSF-loaded poultice are generally more inhomogeneous than the ones treated with the NSF-loaded hydrogel. Moreover, several cellulose fibers were spotted on the samples that were in contact with the poultice, indicating the permanence of paper or cellulose pulp residues on the treated areas. Dewetting patterns could be clearly highlighted in the areas of A_S on glass and marble treated with the NSF-loaded hydrogel, indicating a more controlled and reliable cleaning action. In any case, after the removal of either the compress or the gel, complete and easy removal could be obtained via a gentle mechanical action using wet cotton swabs, for all the specimens except A_S on polystyrene. In this case, the acrylic polymer could not be removed after 15 min of application of either the NSF-loaded poultice or hydrogel (**Figures 9A,B**). We hypothesized that in this case the application time was too long, causing the migration of solvents through the A_S coating up to the polymer/substrate interface,
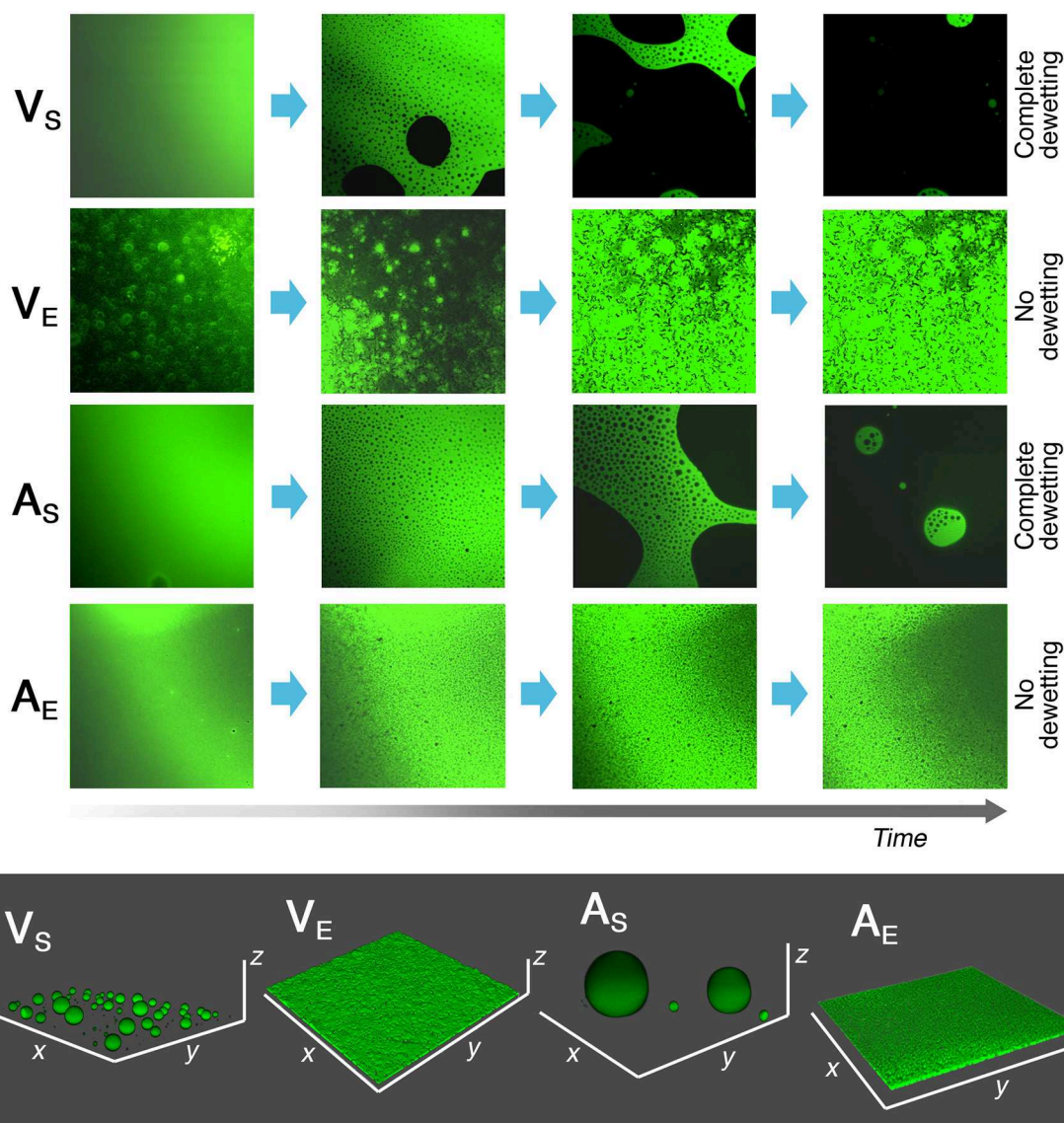
FIGURE 7 | Results of CLSM experiments on 2–4 μm thick spin-coated polymer films on coverglasses. The films were exposed to the action of 50 μl of the NSF, and their morphology was observed over time. The time scale is not the same for all samples, i.e., V_S and A_S completely dewetted from the coverglass in less than 10 s, while V_E and A_E films were still intact after 10 minutes of incubation with the NSF. In the bottom gray box, the 3D reconstruction of the four polymers' morphology after 10 min is reported. The different behavior between polymer films coming from solvent solutions or aqueous emulsions is clearly evidenced. Each side of the CLSM micrographs is 150 μm long. x and y axes in the 3D reconstructions have the same length.

where they interacted with polystyrene creating a sort of joint or adhesion layer between the polymer and the substrate. This issue is easily overcome by using multiple shorter applications, assuming that the confining matrix of the NSF is enough retentive to release gradually the uploaded fluid on short time scales, which is the case of the pHEMA/PVP gels. In fact, repeated shorter applications (2 +2 +2 min) of the NSF loaded in the hydrogel allowed complete removal of the coating (as confirmed by the 2D microFTIR mapping), while uneven polymer residues were left from the same application using cellulose poultices (see **Figures 9C–F**). The cartoon in **Figure 9** summarizes the removal

process in the two cases: using the highly retentive hydrogel it is possible to perform a gradual action, which proceeds layer by layer, controlling the interaction of the NSF with the substrate. This approach was recently used to perform highly selective removal of overpaintings and vandalism (Giorgi et al., 2017). It is worth noting that the pHEMA/PVP gels used for cleaning interventions do not leave detectable residues on the treated surfaces (as checked with FTIR), while the only non-volatile residues in the NSFs (i.e., the surfactants) can be feasibly removed with a rinsing steps using the gels simply loaded with water (Baglioni et al., 2016).

FIGURE 8 | Results of the cleaning tests performed comparing the effect of the same amount of NSF loaded respectively on a traditional cellulose pulp poultice and on an innovative highly retentive chemical hydrogel. (Top) Marble specimens during the tests. (Bottom) Selected representative micrographs taken before (*Pristine*, top-middle picture of each triad) and after 15 min of application of both the poultice (bottom-left picture of each triad) and the gel (bottom-right picture of each triad). Each micrograph is 1.2×1.6 mm^2 large.

FIGURE 9 | (A) The result of 15 min of application of the NSF-loaded poultice on A_S laid on polystyrene; **(B)** The result of 15 min of application of the NSF-loaded gel on A_S laid on polystyrene; **(C)** The result of 2 min + 2 min + 2 min of application of the NSF-loaded poultice on A_S laid on polystyrene; **(D)** The result of 2 min + 2 min + 2 min of application of the NSF-loaded gel on A_S laid on polystyrene. This is the only case that resulted in the complete removal of the polymer coating, as confirmed by the comparison between the micro-reflectance FTIR maps collected before **(E)** and after **(F)** the cleaning with the NSF-loaded hydrogel (the micro-picture is taken at the border between of the cleaned area, seen in blue). The cartoon on the right illustrates the mechanism proposed to explain the observed results. With the poultice (left), the solvents migrate through the polymer (1) and attack the polystyrene substrate, creating a junction or an enhanced adherence between the polymer film and the substrate (2). When a mechanical action is performed (3), an uneven layer of unremoved polymer layer is left stuck to the surface of polystyrene. Using the gel (right), the solvents migration is limited by the retention properties of the scaffold (1). The outer layers of the polymer coating are, then, slightly swollen (2) and easily removed by means of a gentle mechanical action (3). The gel is applied again (4) and the removal proceeds layer by layer, in a selective way, which allows for the complete and safe removal of the polymer film (5). Micrographs A, B, C, and D are 1.2 × 1.6 mm^2 large; micrographs E and F (and relative FTIR maps) have a size of 400 × 550 μm.

CONCLUSIONS

This study focused on unveiling some key aspects of the NSFs/polymer coatings interaction depending on several different factors: (i) the chemical nature and, thus, hydrophilicity of the substrate; (ii) the chemical nature and physical structure of the polymeric films to be removed; (iii) the influence of the application methodology on the cleaning outcome. A series of systematic tests was performed and a coherent and clear picture emerged. A water/C_{9-11}E5.5/BuOH/MEK NSF was selected for this study and was firstly characterized by means of SANS measurements, which showed that rod-like nonionic micelles are dispersed in a water/BuOH/MEK mixture close to the system cloud point. These features possibly make this NSF particularly effective in polymer removal. Then, glass, marble, and polystyrene specimens were coated with four different polymers, including two vinyls and two acrylics, each applied either as a solvent solution or as an aqueous emulsion. It was found that the NSF/polymer film interaction is greatly dependent on the film structure and composition. Films formed from solvent solutions can be swollen by water/organic solvents mixtures or dewetted when a surfactant is added to the cleaning fluid; films formed from polymer latexes, on the other hand, are generally swollen even just by water, but they tend not to dewet. This happens independently from the chemical nature of the polymer, and is a direct consequence of its structure and composition, which includes a significant amount of amphiphilic additives. These substances alter the energetic balance of the liquid/polymer/solid system and stabilize the film, which does not dewet. However, the films are easily removable from the substrates, meaning that the action of the cleaning fluid induces loss of adhesion, similarly to what happens during the first stages of the dewetting process that occurs for films cast from polymer solutions. The substrate also plays an important role in the removal of polymer films formed from solutions. In particular, the more the film is affine to the substrate, the harder its removal. In the limit case, the removal of an acrylic polymer from polystyrene could be achieved only through selective cleaning action using a NSF-loaded highly retentive chemical hydrogel, which grants significantly more controlled performances than traditional cellulose pulp poultices. These results have 2-fold relevance: they deepen the knowledge of the physico-chemical processes that underpin phenomena of daily conservation practice, and provide conservators with innovative solutions to face new challenges in art preservation.

DATA AVAILABILITY STATEMENT

The datasets generated for this study will not be made publicly available. The relevant data are already completely and clearly reported in the paper.

AUTHOR CONTRIBUTIONS

MB, MA, DC, and RG contributed to the conception and design of the work, to the acquisition, the analysis, and the interpretation of experimental data. PB and RG revised the work critically giving a substantial intellectual contribution, and ultimately provided the final approval for its publication.

FUNDING

ACKNOWLEDGMENTS

REFERENCES

Apostol, I., Damian, V., Garoi, F., Iordache, I., Bojan, M., Apostol, D., et al. (2011). Controlled removal of overpainting and painting layers under the action of UV laser radiation. *Opt. Spectrosc.* 111:287. doi: 10.1134/S0030400X110 80054

Baglioni, M., Bartoletti, A., Bozec, L., Chelazzi, D., Giorgi, R., Odlyha, M., et al. (2016). Nanomaterials for the cleaning and pH adjustment of vegetable-tanned leather. *Appl. Phys. A* 122:114. doi: 10.1007/s00339-015-9553-x

Baglioni, M., Berti, D., Teixeira, J., Giorgi, R., and Baglioni, P. (2012a). Nanostructured surfactant-based systems for the removal of polymers from wall paintings: a small-angle neutron scattering study. *Langmuir* 28, 15193–15202. doi: 10.1021/la303463m

Baglioni, M., Domingues, J. A. L., Carretti, E., Fratini, E., Chelazzi, D., Giorgi, R., et al. (2018a). Complex fluids confined into semi-interpenetrated chemical hydrogels for the cleaning of classic art: a rheological and SAXS study. *ACS Appl. Mater. Interfaces* 10, 19162–19172. doi: 10.1021/acsami. 8b01841

Baglioni, M., Giorgi, R., Berti, D., and Baglioni, P. (2012b). Smart cleaning of cultural heritage: a new challenge for soft nanoscience. *Nanoscale* 4:42–53. doi: 10.1039/C1NR10911A

Baglioni, M., Jàidar Benavides, Y., Berti, D., Giorgi, R., Keiderling, U., and Baglioni, P. (2015a). An amine-oxide surfactant-based microemulsion for the cleaning of works of art. *J. Colloid Interface Sci.* 440, 204–210. doi: 10.1016/j.jcis.2014.10.003

Baglioni, M., Jáidar Benavides, Y., Desprat-Drapela, A., and Giorgi, R. (2015b). Amphiphile-based nanofluids for the removal of styrene/acrylate coatings: cleaning of stucco decoration in the Uaxactun archeological site (Guatemala). *J. Cult. Herit.* 16, 862–868. doi: 10.1016/j.culher.2015.03.008

Baglioni, M., Montis, C., Brandi, F., Guaragnone, T., Meazzini, I., Baglioni, P., et al. (2017). Dewetting acrylic polymer films with water/propylene carbonate/surfactant mixtures – implications for cultural heritage conservation. *Phys. Chem. Chem. Phys.* 19, 23723–23732. doi: 10.1039/C7CP02608K

Baglioni, M., Montis, C., Chelazzi, D., Giorgi, R., Berti, D., and Baglioni, P. (2018b). Polymer film dewetting by water/surfactant/good-solvent mixtures: a mechanistic insight and its implications for the conservation

of cultural heritage. *Angew. Chem. Int. Ed. Engl.* 57, 7355–7359. doi: 10.1002/anie.201710930

Baglioni, M., Poggi, G., Ciolli, G., Fratini, E., Giorgi, R., and Baglioni, P. (2018c). A Triton X-100-based microemulsion for the removal of hydrophobic materials from works of art: SAXS characterization and application. *Materials* 11:E1144. doi: 10.3390/ma11071144

Baglioni, M., Poggi, G., Jaidar Benavides, Y., Martínez Camacho, F., Giorgi, R., and Baglioni, P. (2018d). Nanostructured fluids for the removal of graffiti – A survey on 17 commercial spray-can paints. *J. Cult. Herit.* 34, 218–226. doi: 10.1016/j.culher.2018.04.016

Baglioni, M., Raudino, M., Berti, D., Keiderling, U., Bordes, R., Holmberg, K., et al. (2014). Nanostructured fluids from degradable nonionic surfactants for the cleaning of works of art from polymer contaminants. *Soft Matter* 10, 6798–6809. doi: 10.1039/C4SM01084A

Baglioni, M., Rengstl, D., Berti, D., Bonini, M., Giorgi, R., and Baglioni, P. (2010). Removal of acrylic coatings from works of art by means of nanofluids: understanding the mechanism at the nanoscale. *Nanoscale* 2, 1723–1732. doi: 10.1039/c0nr00255k

Baglioni, P., Berti, D., Bonini, M., Carretti, E., Del Carmen Casas Perez, M., Chelazzi, D., et al. (2012c). Gels for the conservation of cultural heritage. *MRS Online Proc. Libr.* 1418. doi: 10.1557/opl.2012.97

Baglioni, P., Carretti, E., and Chelazzi, D. (2015c). Nanomaterials in art conservation. *Nat. Nanotechnol.* 10, 287–290. doi: 10.1038/nnano.2015.38

Baglioni, P., and Chelazzi, D. (2013). *Nanoscience for the Conservation of Works of Art.* Cambridge, UK: RSC Publishing. doi: 10.1039/9781849737630

Bonelli, N., Montis, C., Mirabile, A., Berti, D., and Baglioni, P. (2018). Restoration of paper artworks with microemulsions confined in hydrogels for safe and efficient removal of adhesive tapes. *Proc. Natl. Acad. Sci.* 115, 5932–5937. doi: 10.1073/pnas.1801962115

Borgioli, L., Caminati, G., Gabrielli, G., and Ferroni, E. (1995). Removal of hydrophobic impurities from pictorial surfaces by means of heterogeneous systems. *Sci. Technol. Cult. Herit. J.* 4, 67–74.

Burnstock, A., and Kieslich, T. (1996). *A Study of the Clearance of Solvent Gels Used for Varnish Removal From Paintings.* London: James & James, 253–262.

Burnstock, A., and White, R. (2000). A preliminary assessment of the aging/degradation of ethomeen C-12 residues from solvent gel formulations and their potential for inducing changes in resinous paint media. *Stud. Conserv.* 45, 34–38. doi: 10.1179/sic.2000.45.Supplement-1.34

Carretti, E., and Dei, L. (2004). Physicochemical characterization of acrylic polymeric resins coating porous materials of artistic interest. *Prog. Org. Coat.* 49, 282–289. doi: 10.1016/j.porgcoat.2003.10.011

Carretti, E., Dei, L., and Baglioni, P. (2003). Solubilization of acrylic and vinyl polymers in nanocontainer solutions. *Appl. Microemulsions Micelles Cult. Herit. Conserv. Langmuir* 19, 7867–7872. doi: 10.1021/la034757q

Carretti, E., Giorgi, R., Berti, D., and Baglioni, P. (2007). Oil-in-water nanocontainers as low environmental impact cleaning tools for works of art: two case studies. *Langmuir* 23, 6396–6403. doi: 10.1021/la700487s

Chan, K. L. A., and Kazarian, S. G. (2006). Detection of trace materials with Fourier transform infrared spectroscopy using a multi-channel detector. *Analyst* 131, 126–131. doi: 10.1039/B511243E

Chelazzi, D., Giorgi, R., and Baglioni, P. (2018). Microemulsions, micelles, and functional gels: how colloids and soft matter preserve works of art. *Angew. Chem. Int. Ed Engl.* 57, 7296–7303. doi: 10.1002/anie.201710711

Chevalier, Y., Pichot, C., Graillat, C., Joanicot, M., Wong, K., Maquet, J., et al. (1992). Film formation with latex particles. *Colloid Polym. Sci.* 270, 806–821. doi: 10.1007/BF00776153

Degiorgio, V., Corti, M., and Società italiana di fisica. (1985). *Physics of Amphiphiles–Micelles, Vesicles, and Microemulsions: Varenna on Lake Como, Villa Monastero, 19–29 July 1983.* Amsterdam: North-Holland Publishing.

Doménech-Carbó, M. T., Doménech-Carbó, A., Gimeno-Adelantado, J. V., and Bosch-Reig, F. (2001). Identification of synthetic resins used in works of art by fourier transform infrared spectroscopy. *Appl. Spectrosc.* 55, 1590–1602. doi: 10.1366/0003702011954152

Domingues, J., Bonelli, N., Giorgi, R., and Baglioni, P. (2013b). Chemical semi-IPN hydrogels for the removal of adhesives from canvas

paintings. *Appl. Phys. A* 114, 705–710. doi: 10.1007/s00339-013-8150-0

Domingues, J. A. L., Bonelli, N., Giorgi, R., Fratini, E., Gorel, F., and Baglioni, P. (2013a). Innovative hydrogels based on semi-interpenetrating p(HEMA)/PVP networks for the cleaning of water-sensitive cultural heritage artifacts. *Langmuir* 29, 2746–2755. doi: 10.1021/la3048664

Gentili, D., Foschi, G., Valle, F., Cavallini, M., and Biscarini, F. (2012). Applications of dewetting in micro and nanotechnology. *Chem. Soc. Rev.* 41, 4430–4443. doi: 10.1039/c2cs35040h

Giorgi, R., Baglioni, M., and Baglioni, P. (2017). Nanofluids and chemical highly retentive hydrogels for controlled and selective removal of overpaintings and undesired graffiti from street art. *Anal. Bioanal. Chem.* 409, 3707–3712. doi: 10.1007/s00216-017-0357-z

Giorgi, R., Baglioni, M., Berti, D., and Baglioni, P. (2010). New methodologies for the conservation of cultural heritage: micellar solutions, microemulsions, and hydroxide nanoparticles. *Acc. Chem. Res.* 43, 695–704. doi: 10.1021/ar900193h

Holmberg, K. (2002). *Handbook of Applied Surface and Colloid Chemistry.* Hoboken, NJ: John Wiley and Sons.

Holmberg, K., Jönsson, B., Kronberg, B., and Lindman, B. (2002). *Surfactants and Polymers in Aqueous Solution.* Hoboken, NJ: John Wiley and Sons. doi: 10.1002/0470856424

Kavda, S., Richardson, E., and Golfomitsou, S. (2017). The use of solvent-gel systems for the cleaning of PMMA. *MRS Adv.* 2, 2179–2187. doi: 10.1557/adv.2017.249

Kline, S. R. (2006). Reduction and analysis of SANS and USANS data using IGOR Pro. *J. Appl. Crystallogr.* 39, 895–900. doi: 10.1107/S0021889806035059

Kotlarchyk, M., and Chen, S. H. (1983). Analysis of small angle neutron scattering spectra from polydisperse interacting colloids. *J. Chem. Phys.* 79, 2461–2469. doi: 10.1063/1.446055

Learner, T., and Institute, G. C. (2004). *Analysis of Modern Paints.* Los Angeles, CA: Getty Publications.

Liu, Y. C., Ku, C. Y., LoNostro, P., and Chen, S. H. (1995). Ion correlations in a micellar solution studied by small-angle neutron and x-ray scattering. *Phys. Rev. E* 51, 4598–4607. doi: 10.1103/PhysRevE.51.4598

Montis, C., Koynov, K., Best, A., Baglioni, M., Butt, H. J., Berti, D., et al. (2019). Surfactants mediate the dewetting of acrylic polymer films commonly applied to works of art. *ACS Appl. Mater. Interfaces* 11, 27288–27296. doi: 10.1021/acsami.9b04912

Murray, A., Berenfeld, C. C., de, Chang, S. Y. S., Jablonski, E., Klein, T., Riggs, M. C., et al. (2002). The condition and cleaning of acrylic emulsion paintings. *MRS Online Proc. Libr. Arch.* 712. doi: 10.1557/PROC-712-II1.4

Ormsby, B., and Learner, T. (2009). The effects of wet surface cleaning treatments on acrylic emulsion artists' paints – a review of recent scientific research. *Rev. Conserv.* 10, 29–41. doi: 10.1179/sic.2009.54.Supplement-1.29

Pintus, V., and Schreiner, M. (2011). Characterization and identification of acrylic binding media: influence of UV light on the ageing process. *Anal. Bioanal. Chem.* 399, 2961–2976. doi: 10.1007/s00216-010-4357-5

Raudino, M., Giamblanco, N., Montis, C., Berti, D., Marletta, G., and Baglioni, P. (2017). Probing the cleaning of polymeric coatings by nanostructured fluids: A QCM-D study. *Langmuir* 33, 5675–5684. doi: 10.1021/acs.langmuir.7b00968

Raudino, M., Selvolini, G., Montis, C., Baglioni, M., Bonini, M., Berti, D., et al. (2015). Polymer films removed from solid surfaces by nanostructured fluids: microscopic mechanism and implications for the conservation of cultural heritage. *ACS Appl. Mater. Interfaces* 7, 6244–6253. doi: 10.1021/acsami.5b00534

Sanmartín, P., Cappitelli, F., and Mitchell, R. (2014). Current methods of graffiti removal: a review. *Constr. Build. Mater.* 71, 363–374. doi: 10.1016/j.conbuildmat.2014.08.093

Sheu, E. Y., and Chen, S. H. (1988). Thermodynamic analysis of polydispersity in ionic micellar systems and its effect on small-angle neutron scattering data treatment. *J. Phys. Chem.* 92, 4466–4474. doi: 10.1021/j100326a044

Steward, P. A., Hearn, J., and Wilkinson, M. C. (2000). An overview of polymer latex film formation and properties. *Adv. Colloid Interface Sci.* 86, 195–267. doi: 10.1016/S0001-8686(99)00037-8

Stubenrauch, C. (2008). *Microemulsions: Background, New Concepts, Applications, Perspectives.* Hoboken, NJ: John Wiley and Sons.

Verschueren, K. (2001). *Handbook of Environmental Data on Organic Chemicals*. Hoboken, NJ: John Wiley and Sons.

Willneff, E. A., Schroeder, S. L., and Ormsby, B. A. (2014). Spectroscopic techniques and the conservation of artists' acrylic emulsion paints. *Herit. Sci.* 2:25. doi: 10.1186/s40494-014-0025-y

Winnik, M. A. (1997). Latex film formation. *Curr. Opin. Colloid Interface Sci.* 2, 192–199. doi: 10.1016/S1359-0294(97)80026-X

Xu, L., Sharma, A., and Joo, S. W. (2012). Dewetting of stable thin polymer films induced by a poor solvent: role of polar interactions. *Macromolecules* 45, 6628–6633. doi: 10.1021/ma301227m

**frontiers
in Chemistry**

Cellulose and Lignin Nano-Scale Consolidants for Waterlogged Archaeological Wood

Federica Antonelli [1]*, Giulia Galotta [2], Giancarlo Sidoti [3], Florian Zikeli [1], Rossella Nisi [4], Barbara Davidde Petriaggi [5] and Manuela Romagnoli [1]

[1] Department for Innovation in Biological, Agro-Food and Forestry Systems (DIBAF), Tuscia University, Viterbo, Italy, [2] Biology Laboratory, Istituto Superiore per la Conservazione e il Restauro (ISCR), Rome, Italy, [3] Testing Materials Laboratory, Istituto Superiore per la Conservazione e il Restauro (ISCR), Rome, Italy, [4] BioFaber srl, Mesagne, Italy, [5] Underwater Archaeological Operations Unit, Istituto Superiore per la Conservazione ed il Restauro (ISCR), Rome, Italy

Waterlogged archaeological wood comes from submerged archaeological sites (in lake, sea, river, or wetland) or from land waterlogged sites. Even if the wooden object seems to have maintained the original size and shape, the wood is more or less severely decayed because of chemical and biological factors which modify the normal ratio of cellulose and lignin in the cell wall. Drying procedures are necessary for the musealization but potentially cause severe shrinkages and collapses. The conservation practices focus not only on removing water from wood but also on substituting it with materials able to consolidate the degraded wood cell walls like polymers (e.g., PEG), sugars (e.g., lactitol), or resins (e.g., Kauramin). In the present work three different nano-scale consolidants were tested: lignin nanoparticles (LNPs) obtained form beech wood *via* a non-solvent method involving dialysis; bacterial nanocellulose (BC) obtained from cultures fed with agro-alimentary waste; cellulose nanocrystals (CNC) chemically extracted from native cellulose. Waterlogged archaeological wood samples of different species (oak, elm, stone pine, and silver fir) characterized by different levels of degradation were impregnated with the consolidants. The treatments efficiency was evaluated in terms of macroscopic observation of treated samples, anti-shrink efficiency (ASE) and equilibrium moisture content (EMC). The results obtained for the three consolidants showed substantial differences: LNPs and CNCs penetrated only about a millimeter inside the treated wood, while BC formed a compact layer on the surface of the cell walls throughout the thickness of the samples. In spite of successful BC penetration, physical evaluation of treatment efficiency showed that BC nanoparticles did not obtain a satisfying consolidation of the material. Based on the reported results more focused test protocols are optimized for future consolidation experiments.

INTRODUCTION

The European standard EN335 (2013) (Conservation of cultural heritage—Guidelines for management of waterlogged wood on terrestrial sites of archaeological significance) defines waterlogged archaeological wood as: "wood whose structure has been filled with water through the sustained inclusion in a water saturated environment." This wood comes from submerged archaeological sites (in lake, sea, river, or wetland) or from land waterlogged sites. Generally, waterlogged wooden artifacts preserve their original size and shape but often they undergo severe cell wall decay due to chemical and biological factors. The pH and the salinity of water as well as the chemical nature of sediments (Hedges, 1990; Unger et al., 2001; Pearson, 2014) together with the action of biological degraders (e.g., erosion and tunneling bacteria and soft rot fungi) (Blanchette et al., 1989) affect the wood causing a more or less severe mass loss and increased porosity and permeability which lead to a spongy and weakened material.

Drying waterlogged archaeological wooden artifacts is necessary for the musealization but it is always a high risk procedure because it could cause severe shrinkages and collapses. Thus, conservation practices focus not only on removing water from wood, but also on consolidating the degraded cell walls aiming for stabilized shape and size of the artifact as well as to enable it to withstand the conditions of the future preservation environment (Grattan and Clarke, 1987). An effective consolidant confers on wood a good stabilization by using the minimal amount of product while being stable to variations in relative humidity. However, these are not the only features required from an effective consolidant, conservation history highlighted no treatment exists which is able to preserve an artifact forever. Thus, all the materials used in restoration practices must be removable or, at least, leave the object retreatable. Several materials have been tested and used for the consolidation of waterlogged archaeological wood (for a review see Christensen et al., 2012). By now, the most used consolidants are polymers (e.g., polyethilene glicol, PEG), sugars (e.g., lactitol), or resins (e.g., Kauramin) (Unger et al., 2001; Christensen et al., 2012).

The use of nanomaterials in the conservation of Cultural Heritage expanded during the last few decades (Baglioni et al., 2015). Different kinds of nanoparticles were mainly used to clean and consolidate wall paintings. Tests with nanosols of silica and alkaline nanoparticles were conducted to consolidate wood artifacts and to deacidify waterlogged archaeological wood (Chelazzi et al., 2006; Mahltig et al., 2008). Even if Cipriani et al. (2010) tested cellulose derived consolidants and Christensen et al. (2012) report of consolidation attempts made with cellulose whiskers, no additional literature is available about the consolidation of waterlogged archaeological wood with nanomaterials obtained from renewable sources.

The present work is aimed to find bio-inspired consolidants that could substitute the chemicals currently in use. In particular, focusing on the concepts of bioeconomy and circular-economy, rarely applied until now to the filed of Cultural Heritage, the study tested three cellulose and lignin nano-scale consolidants: lignin nanoparticles (LNPs), bacterial nanocellulose (BC), and cellulose nanocrystals (CNCs).

LNPs can be synthesized from technical lignin obtained as a by-product of paper industry or second generation ethanol biorefineries and have been proposed for a wide range of applications as e.g., active components or fillers in polymer blends introducing lignin properties like anti-oxidant activity or UV protection on a nano-scale level (Beisl et al., 2017).

Nanocellulose can be obtained by processing plant cellulose or as a product of primary metabolic processes of certain bacterial strains (Kargarzadeh et al., 2017). Bacterial cellulose (BC), is produced by the fermentation of *Gluconoacetobacter* species, which can produce high aspect ratio (length to diameter) nanofibers, with three-dimensional porous networks, retaining the highest purity. Because of its hydrophilic nature (99% of the constituents is water), flexibility, non-toxicity, good biocompatibility, and wide availability BC has been extensively used in diverse fields from food and paper industry to biomedical applications (Kunjalukkal Padmanabhan et al., 2017).

CNCs, also known as nanocrystalline cellulose, nanowhiskers, nanorods, and rod-like cellulose crystals, are obtained by hydrolysis with highly concentrated acids (6–8 M) and high-power mechanical or ultrasonic treatments of the crystalline domains of cellulose nanofibrils. Their dimensions and the degree of crystallinity depend on the cellulose source and extraction conditions (Abdul Khalil et al., 2014; Kargarzadeh et al., 2017).

MATERIALS AND METHODS

Nanoparticles

Three different nanoparticles were tested as consolidants of waterlogged archaeological wood: lignin nanoparticles (LNPs), bacterial nanocellulose (BC), cellulose nanocrystals (CNCs).

LNPs were obtained from beech wood (*Fagus sylvatica* L.) from the Cimini Mountains in Lazio region, Italy (Piangoli Legno SNC, Soriano nel Cimino, VT). They were produced applying the "anti-solvent procedure" on acidolysis lignin using DMSO as lignin solvent, as reported in Zikeli et al. (2018). The obtained LNPs are hollow, sphere-shaped particles with diameters ranging between 40 and 120 nm.

BC was provided by Biofaber srl (Italy). It was obtained by fermentation of agro-alimentary waste, in accordance with Pal et al. (2017), in the form of hydrogel pellicles that were washed with distilled water and boiled in 0.5 M sodium hydroxide solution in order to purify the samples. Pellicles were dried at 60°C to get dried BC membranes and then were grinded with a rotary mill in order to obtain cellulose nanospheres.

The BC prepared for the test had never been studied before, so morphological characterization of BC spay-dried on a stub was performed on a Zeiss (Sigma VP; Carl Zeiss, Germany) FESEM.

CNCs were supplied by CelluForce (Montreal, Canada). CelluForce NCC® is a cellulose hydrogen sulfate sodium salt, provided as a spray dried powder, white in color. The CNCs are spindle shaped crystals, 2.3–4.5 nm in diameter and 44–108 nm in length (from CelluForce product specifications).

Wood Samples

Wood samples were obtained from two archaeological sites: Isola Sacra (Fiumicino, Italy) and the ancient port of Neapolis (Naples, Italy). The wood coming from Fiumicino belongs to the shipwreck named Isola Sacra 1 (sample P2550), an horeia-type vessel dated before the first half of the 3rd century AD and excavated in 2011 (Boetto et al., 2017). The wood from Naples pertains the shipwreck F (samples FTdis 4, Ftdis 9, and FTdis 48) (Di Donato et al., 2018), and a wooden pier (2514.28, 2514.30, and 2514.34) both dated to the roman age. The remains were recovered from the excavation area of Piazza Municipio in 2015 and 2018, respectively. After the recovery, the wood was stored in the biology laboratory of the Istituto Superiore per la Conservazione e il Restauro (IsCR). During all the storage period the fragments were left completely soaked to maintain the state of maximum water content.

From the wood samples 47 blocks were obtained with dimensions $2.5 \times 2.5 \times 1.5$ cm and $3.0 \times 1.5 \times 1.5$ cm, depending on the availability of the material. Ten blocks were used for each consolidant to be tested, the remaining were used as freeze- (7) and air-dried (10) not-consolidated controls.

Each sample was marked with an acronym indicating the consolidant (L, lignin nanoparticles; BC, bacterial cellulose; CNC, cellulose nanocrystals) or the drying method for controls (F, freeze-drying; A, air-drying), and the wood type (S, softwood; H, hardwood) followed by sequential numbers (**Table 1**).

Wood Characterization

Before the beginning of consolidation procedures the wood species were identified and the state of preservation of the material was characterized by micro-morphological and physical analyses according to the Italian standard and to the most used protocols (Jensen and Gregory, 2006; Schwarze, 2007; UNI11205, 2007; Capretti et al., 2008; Romagnoli et al., 2018).

The identification of wood species and micro-morphological examinations were carried out on thin sections (10–20 μm) cut in the three anatomical planes (cross, longitudinal-radial and longitudinal-tangential) by mean of transmission light microscopy (DMRB, Leitz) as prescribed by UNI11118 (2004). Samples were cut by hand with a razor blade or using a cryo-microtome (Cryostat CM 1900, Leica). To identify the wood species the observed anatomical features were compared to literature works (Jacquiot, 1955; Jacquiot et al., 1973; Schweingruber and Baas, 1990).

To highlight the presence of micro-organisms the sections were stained with an aqueous solution of 1% w/v methylene blue in 50% lactic acid. Microbial decay was evaluated using both bright-field and polarized light microscopy in order to identify decay patterns and highlight the loss of crystalline cellulose.

To assess the decay by means of physical tests wood blocks were weighted and their volume was defined by the water displacement method. Weight was measured again after the samples were dried in an oven at $103 \pm 2°C$ up to a constant weight. The physical parameters used for the characterization are reported in **Table 2**. Reference values for basic density of non-decayed wood were taken from the literature (Giordano, 1986; Capretti et al., 2008; Macchioni et al., 2012).

TABLE 1 | The utilized samples, type of wood, archaeological sample and consolidant, or drying method.

Sample name	Wood	Archaeological sample	Consolidant/ drying method
LS1	Softwood	P2550	Lignin nanoparticles
LS2		FTdis 4	
LS3		FTdis 48	
LH1–LH2–LH3	Hardwood	FTdis 9	
LH4–LH5		2514.28	
LH6		2514.30	
LH7		2514.34	
BCS1	Softwood	P2550	Bacterial cellulose
BCS2		FTdis 4	
BCS3		FTdis 48	
BCH1–BCH2–BCH3	Hardwood	FTdis 9	
BCH4–BCH5		2514.28	
BCH6		2514.30	
BCH7		2514.34	
CNCS1	Softwood	P2550	Cellulose nanocrystals
CNCS2		FTdis 4	
CNCS3		FTdis 48	
CNCH1–CNCH2–CNCH3	Hardwood	FTdis 9	
CNCH4–CNCH5		2514.28	
CNCH6		2514.30	
CNCH7		2514.34	
FS1	Softwood	P2550	Freeze-drying
FS2		FTdis 4	
FS3		FTdis 48	
FH1	Hardwood	FTdis 9	
FH2		2514.28	
FH3		2514.30	
FH4		2514.34	
AS1–AS2	Softwood	P2550	Air-drying
AS3		FTdis 4	
AS4		FTdis 48	
AH1–AH2	Hardwood	2514.28	
AH3–AH4		2514.30	
AH5–AH6		2514.34	

Methods Development of Impregnation and Wood Drying

Impregnation baths containing the nano-scale consolidants were prepared. LNPs' bath was obtained adding the nanoparticles to deionised water up to a concentration of 5 mg/ml. BC suspended in deionised water tended to precipitate, so to obtain a stable suspension several attempts were made. Following the suggestions of the Biofaber team, Tween 20, sucrose, polyethylene glycol 400 (PEG400), oil or a mix of them were added to the BC (concentration 5%), the suspensions were homogenized with the help of a magnetic shaker or a sonicator. The details of the performed tests are reported in **Table S1**. At the end of every test a more or less thick layer of BC had precipitated

TABLE 2 | Physical parameters used to asses the wood decay.

Physical parameter	Unit	Formula
Basic density (D_{bd})	$g \times cm^{-3}$	$D_{bd} = \frac{M_0}{V_f}$
Maximum water content (MWC)	%	$MWC = \frac{M_f - M_O}{M_O}$
Residual density (RD_b)	%	$RD_b = \frac{D_{bd}}{D_b}$

M_0, anhydrous mass; M_f, mass at maximum water content; V_f, volume at maximum water content; D_b, basic density of non-decayed wood.

at the bottom of the container, except for the suspension obtained with procedure reported as T2 in **Table S1** (0.5% Tween 20 + 1% Cinnamon oil + deionised water, sonication 50% amplitude—1 h, 5% BC, magnetic shaking 500/600 rpm—1 h), which in consequence was selected as the procedure to prepare the impregnation baths.

To obtain a liquid suspension of CNCs, 3% of powdered crystals were added to deionised water and shaken on a magnetic shaker for 1 h. By adding a greater amount of CNCs the suspension became a gel and thus not suitable for the consolidation treatment.

To perform the consolidation tests, the waterlogged archaeological wood blocks were completely soaked in the baths for 1 month at room temperature. After the treatment, the blocks were frozen (−20°C) and then freeze-dried following the procedure settled in the IsCR restoration laboratory *Excavated Organic Materials*. The lyophilizer (LIO 2000PNS) settings were: chamber temperature −30°C; condenser temperature −50°C; chamber vacuum 2 Pa. The wood temperature was monitored through the use of thermocouples positioned on the samples' surface. The pressure was raised up to room pressure and the blocks were removed from the lyophilizer when reaching a temperature of 18–20°C.

F control blocks were kept completely soaked in deionised water and were successively frozen and freeze-dried under the same condition as treated samples. A controls samples were air-dried at room temperature.

During the consolidation treatments different problems arose for the three tested consolidants. Soon after the beginning of consolidation procedure LNPs and BC precipitated on the bottom of the container. Therefore, to keep the nanoparticles suspended the impregnation baths were gently shaken on a magnetic stirrer for the rest of the test. Additionally, the wood blocks were periodically rotated in order to avoid nanoparticles deposition on their upper surface. In spite of all the precautions taken, at the end of the treatments a more or less thick layer of LNPs and BC was present on the wood (**Figures S1A,B**). Those nanoparticles were removed with a soft brush before freezing the blocks.

After 1 week of consolidation test, the CNCs impregnation bath turned into a gel (**Figure S1C**). A test carried out on a small aliquot of the gel showed that to regain a liquid bath the addition of the double volume water was necessary. This solution was not considered in order to avoid an excessive dilution of the consolidant. At the end of the treatment, the wood blocks were extracted from the gel and the residual CNCs on the wood surface were removed with a soft brush.

Evaluation of the Efficacy of the Treatments

A first evaluation of the efficacy of the treatments was obtained by macroscopic observation of the samples. Color, shape, presence of openings, and consistency were observed.

The penetration of the nanoparticles inside the wood tissues was evaluated by examining gold sputter-coated sections of treated blocks (LH5, BCH5, and CNCH5) and freeze-dried control (FH2) with a Scanning Electron Microscope (Zeiss EVO 60) in secondary electrons mode. For each sample three sections were observed: external cross section, internal cross section, and internal radial section. The internal sections were obtained splitting the block by hand, without the use of blades.

Anti-Shrink Efficiency

In order to evaluate the dimensional variations of treated wood, all the six sides of treated blocks, freeze- and air-dried controls were scanned on high definition scanner (HP scanjet G3010), together with a measuring ruler, before the consolidation treatment, and after the drying procedure (wood equilibrated at 20°C, 50% RH). Using an image processing software (ImageJ 1.52n) the cross section surface and the average height of each block were measured. The obtained values were used to calculate the blocks' volume (V_W, volume of waterlogged blocks; V_D, volume of treated blocks and controls after drying).

For each block, the percentage shrinkage, S, was calculated following the equation:

$$S(\%) = \frac{V_W - V_D}{V_W} * 100$$

The S values obtained for each treated sample were used to determine the anti-shrink efficiency (ASE) with respect to freeze-dried (ASE_F) and air-dried (ASE_A) controls following the equations:

$$ASE_F(\%) = \frac{S_F - S_T}{S_F} * 100 \text{ and}$$

$$ASE_A(\%) = \frac{S_A - S_T}{S_A} * 100$$

Where S_F and S_A are the shrinkages of freeze- and air-dried controls, respectively, and S_T is the shrinkage of treated blocks.

The ASE_C, expressed as the percentage of shrinkage that has been suppressed by freeze-drying treatment as compared to the shrinkage of air-dried controls, was calculated as follows:

$$ASE_C(\%) = \frac{S_A - S_F}{S_A} * 100$$

Equilibrium Moisture Content

To evaluate the effect of the different consolidation treatments with respect to moisture absorption the equilibrium moisture content (EMC) was determined. The test was performed on the treated wood blocks and freeze-dried controls not used for SEM observations. The obtained results were compared to sound wood EMC from literature (Giordano, 1981) and to values obtained for sound wood controls. The latter, four blocks of silver
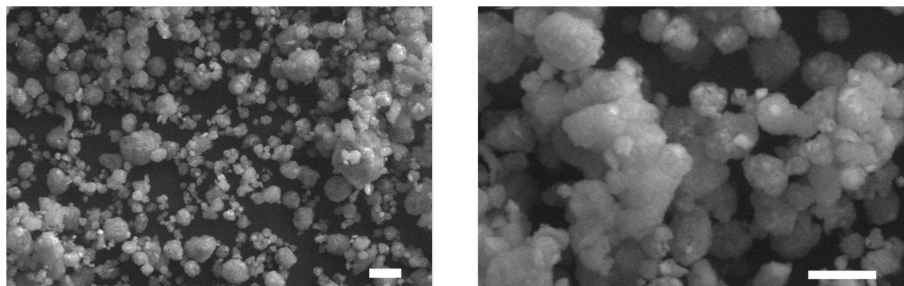
FIGURE 1 | SEM images of the spray dried bacterial cellulose. Scale bars 10 μm.
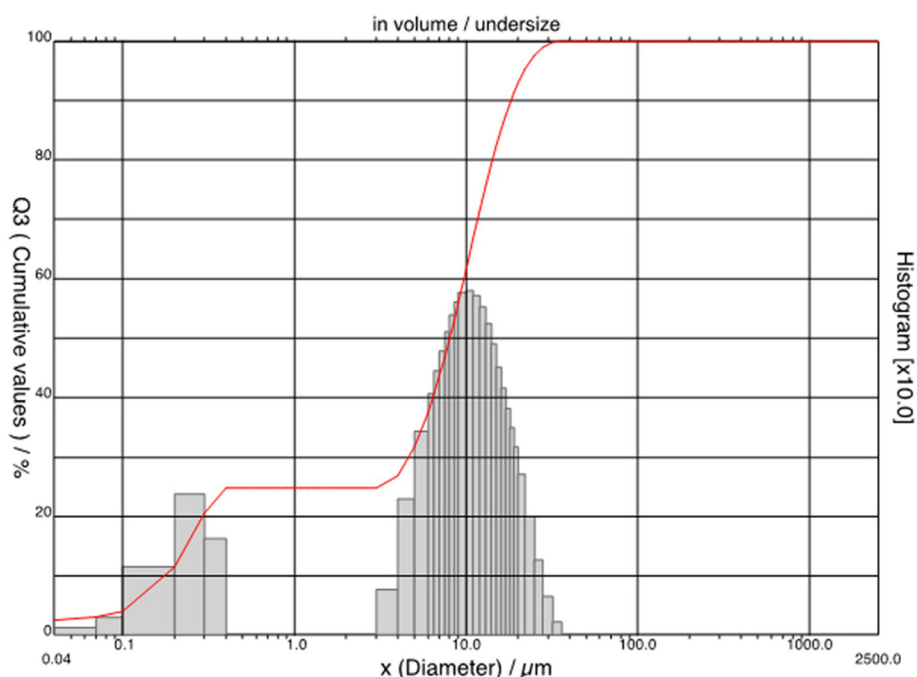
FIGURE 2 | Size distribution of the spray dried bacterial cellulose.

fir and six blocks of holm oak, $2.0 \times 2.0 \times 0.5$ cm in dimensions, were marked with a progressive number.

The samples were put in a climatic chamber at 20°C and the RH was varied according to the sequence 10, 35, 45, 55, 65, 85% reaching in each step the EMC (Giordano, 1981). The EMC for the RH value of 100% was obtained by putting the wood blocks in a closed container in presence of liquid water. At the end of the RH cycle, the samples were completely dried in a oven at 103 ± 2°C up to a constant weight.

RESULTS AND DISCUSSION

Bacterial Cellulose Nanoparticles

SEM observations of bacterial nanocellulose allowed for characterizing the consolidant. Most part of the observed nanoparticles was more or less spherical in shape (**Figure 1**), in some cases small, irregularly shaped particles were observed. The size distribution (**Figure 2**) showed that the nanoparticles could be divided into two dimensional classes with diameter ranges of 0.04–0.50 μm and 3–50 μm. Most part of the BC particles had a diameter of ca 10 μm.

Wood Characterization

Results regarding wood species identification and physical analyses are reported in **Table 3**. The softwood samples were referred to stone pine (*Pinus pinea* L.), silver fir (*Abies alba* Mill.) and cypress (*Cupressus sempervirens* L.). Regarding the hardwood samples, the sample FTdis 9 was identified as elm (*Ulmus* sp.) while the blocks obtained from the wooden pier belonged to the evergreen oak group and can be probably attributed to holm oak (*Quercus ilex* L).

Micro-morphological analyses of wood thin sections allowed for observing the microbial decay of the tissue which was

Archaeological sample	Wooden species	D_{bd} (g × cm^{-3})	MWC (%)	RD$_b$ (%)
P2550	*Pinus pinea*	0.31	254	61
FTdis 4	*Abies alba*	0.41	193	108
FTdis 9	*Ulmus* sp.	0.34	250	61
FTdis 48	*Cupressus* sp.	0.25	331	41
2514.28	*Quercus* cfr. *ilex*	0.15	616	20
2514.30	*Quercus* cfr. *ilex*	0.12	741	17
2514.34	*Quercus* cfr. *ilex*	0.14	648	19

mainly ascribed to erosion bacteria (**Figure S2A**), even though fungal hyphae and spores were observed in several sections (**Figure S2B**). The observations carried out in polarized light showed a severe loss of the birefringence typical of cellulose (**Figures S2C,D**), a sign that the crystalline structure of the polymer was almost completely lost due to microbial attack.

The physical parameters used to assess the decay showed different levels of degradation for the selected woods. The highest MWC values were recorded for the holm oak samples (616, 741, and 648% respectively). For the three poles the residual density ranged between 17 and 20%. According to the degradation classes established by De Jong (Grattan and Clarke, 1987) and by McConnachie et al. (2008) these samples can be considered as highly degraded.

The stone pine samples were the best preserved of the analyzed woods with MWC value of 254% and RD$_b$ of 61%. Cypress showed an intermediate level of degradation with an MWC of 331% and an RD$_b$ of 41%. According to De Jong these woods belong to the intermediate class of degradation.

Silver fir and elm samples deserve a special mention. Based on the MWC values (193 and 250%) these samples resulted as the best preserved of all analyzed wood. However, the fir RD$_b$ value (108%) and the fact that elm was much more degraded (spongy tissue, not resisting to the cut) with respect to wood with similar MWC indicated that the results could not be considered as reliable. The wood was characterized by the presence of several shipworm tunnels filled with sediments. During the cleaning operations carried out before the tests it was not possible to remove all the sediments from the samples, especially from the innermost part. It is known that the presence of sediments and/or mineral depositions inside archaeological waterlogged wood influences the RD$_b$ values (Schniewind, 1990), so the unreliable results obtained for the physical analyses must be attributed to this cause.

Evaluation of Efficacy of Consolidation Treatments

Macroscopic observation of treated samples and comparison between consolidated and un-consolidated wood allowed for a first evaluation of the effect of the respective consolidation treatments.

In contrast to air-dried controls, all treated samples and freeze-dried controls apparently maintained the original shape and no dimensional differences were perceivable by naked eye between differently consolidated blocks and freeze-dried controls (**Figure 3** and **Figures S3, S4**). In few cases, of both consolidated and freeze-dried blocks, small pieces of wood had detached during consolidation or drying procedure and small openings were present on the samples' surfaces.

Wood color and aspect were widely affected by consolidation treatments. LNPs treated samples resulted in dark brown color and a fine brown powder was present on the sample surface, even after freeze-drying. BC consolidated blocks were whitish or yellowish in color. When broken for SEM observation, it was evident that the color change had occurred throughout the block thickness. Finally, CNCs treated samples showed a color similar to the controls, but a thin, colorless film was present on almost all the surface of the blocks. That film was easily removable by touching the wood.

SEM observations of the treated wood samples allowed for observing how the nanoparticles had penetrated inside the wood tissues. **Figure 4** reports the images of external and internal cross sections and radial sections of all the observed blocks. The analysis of a control un-consolidated block showed that in the cross sections, both external and internal, cell lumens were empty and in several cases the secondary cell walls appeared mostly detached from the middle lamella (ML) with only thin filaments connecting the cell wall to the ML. In radial section the vessel and fiber walls appeared smooth and pits were well visible.

In the LNPs treated block a layer of nanoparticles was observed on the external cross section. Most of the cell lumens were covered with compact deposits of LNPs. In other cases, a coating of nanoparticles was well visible covering the whole cell lumen wall. In the internal cross section the cell lumens appeared empty and no nanoparticles were visible. Observing the radial section, it resulted that LNPs penetrated inside some vessels up to a depth of ca 1.2 mm and formed a more or less compact and irregular layer covering the cell walls for the first 400 μm. Only few sporadic particles penetrated deeper into the wood tissue and a part of wood vessels and fibers appeared completely empty.

On the external cross section of the BC treated block, only few sporadic deposits of nanoparticles were observed. Most of the cell lumens were filled with consolidant, the rest seemed empty and the secondary cell walls detached from the ML were well visible. Observing the internal cross section of the block, in most cases the degraded secondary cell walls appeared as "tubes" coming out of the section. In other cases, only the ML was present and the cell lumen was empty. In the radial section, a homogeneous and compact layer of BC was observed on the cell walls of both vessels and fibers throughout the thickness of the block, covering most part of the pits.

In the external cross section of the CNCs treated block, the cell lumens were empty and only in some cases a thin layer of CNCs was observed on the surface of the cell walls. Nanoparticles had penetrated up to a depth of ca 1.3 mm forming a compact and homogeneous coating that covered almost completely the pits, as visible in radial section. At greater depths, the CNCs layer was not visible anymore thus cell walls appeared smooth like observed for the control sample and all pits were well visible. The empty cell lumens and the absence of nanoparticles coating in the internal cross section confirmed the scarce consolidant penetration.
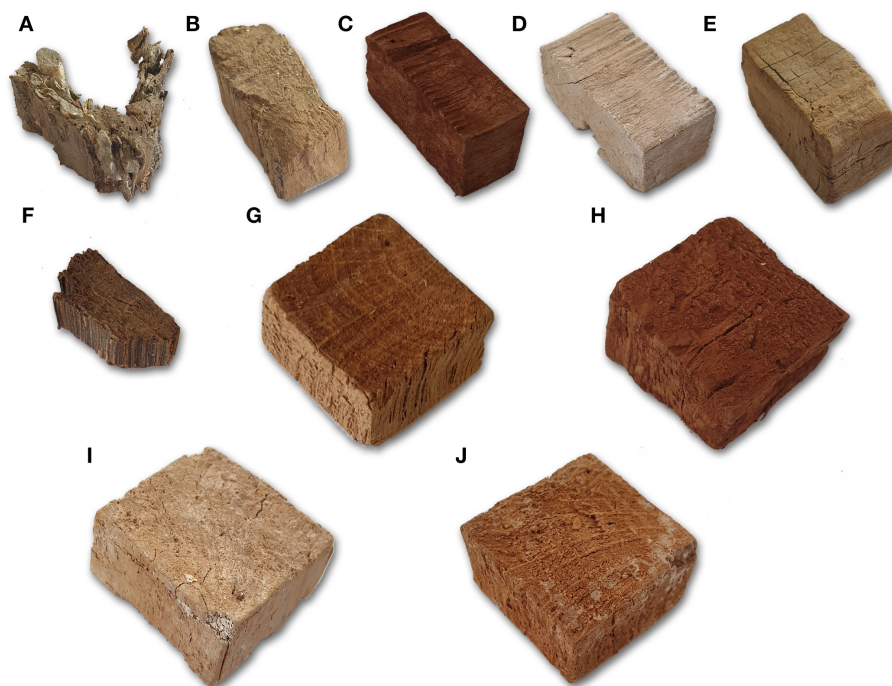
FIGURE 3 | Aspect of selected treated blocks and controls. **(A)** AS3—silver fir; **(B)** FS3—cypress; **(C)** LS1—stone pine; **(D)** BCS1—stone pine; **(E)** CNCS3—cypress; **(F)** AH3—elm; **(G)** FH4—holm oak; **(H)** LH4—holm oak; **(I)** BCH6—holm oak; **(J)** CNCH7—holm oak.

As shown, the results obtained with the three nano-scale consolidants were quite different. Shape and dimensions of the nanoparticles did not affect the treatment. In fact, CNCs showed almost the same penetration behavior as LNPs despite being much smaller and having a needle-like shape that initially suggested a greater ease of penetration inside the cells. In contrast, the BC nanoparticles penetrated evenly inside the material despite a more irregular shape and larger particle size.

The scarce LNPs penetration may be mainly linked to the nanoparticles hydrophobicity that lead to their aggregation and precipitation during the consolidation procedure and could present an obstacle for the penetration into the water-soaked samples. Further, substances present in the sediments inside the wood could have influenced the suspension's pH accelerating this phenomenon.
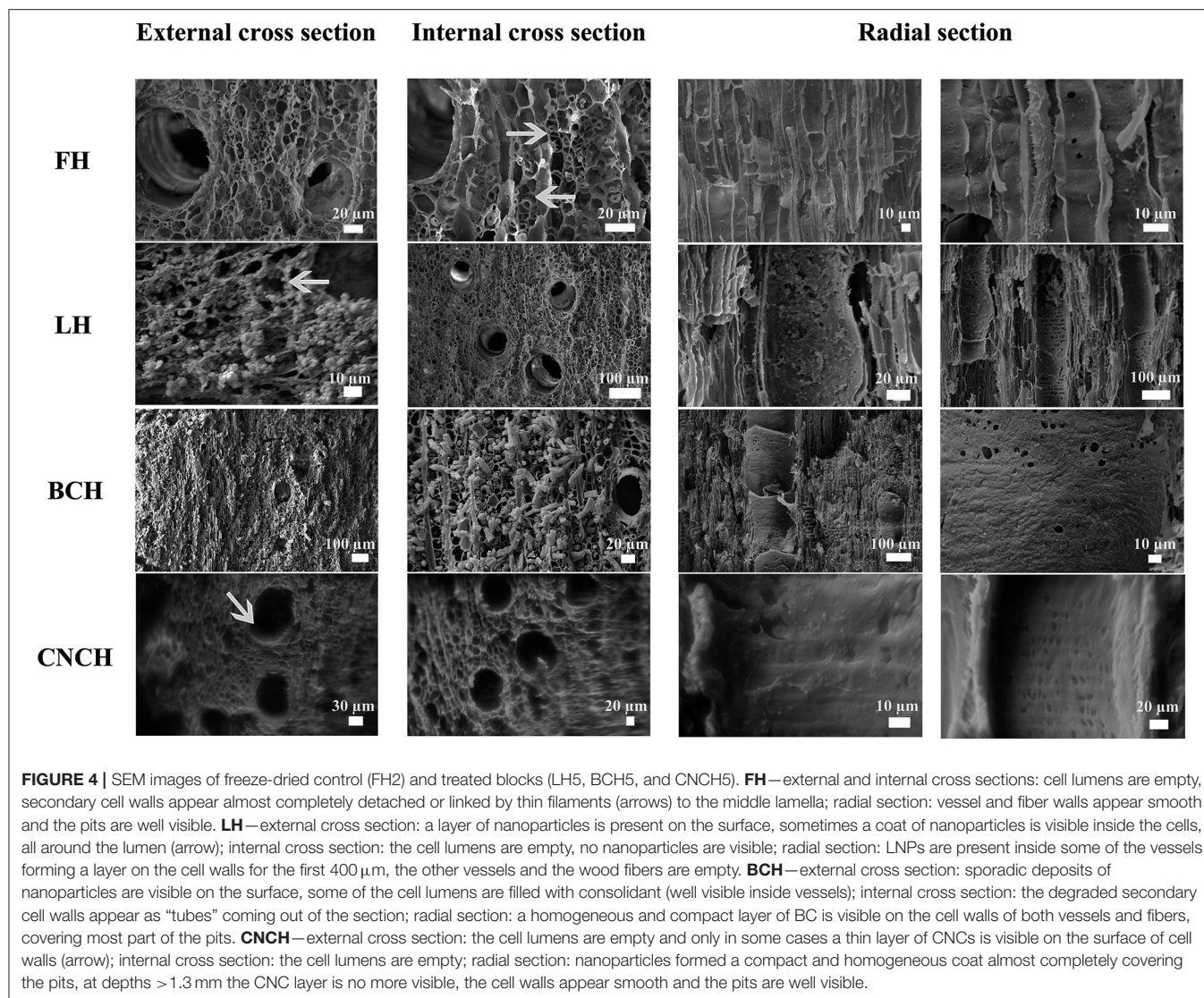
As mentioned above, the CNCs impregnation bath turned into a gel during the treatment, indicating that nanoparticles interacted with each other forming the gel matrix and thus preventing successful penetration inside the sample material. BC nanoparticles showed no interaction with each other and penetrated inside the wood not filling up the voids of the structure but creating a compact layer on cell walls. This observation suggested that the consolidant interacted with OH groups available from cellulose and/or degraded lignin in the cell walls. The presence of "tubes" coming out the internal cross section, not observed in the control block, suggested that in the block treated by BC the nanoparticles had impregnated the detached cell walls and thus prevented breaking of the cell walls

during splitting of the block. Nevertheless, the consolidation was not successful enough to allow the secondary walls to re-join the ML. Indeed, while in the control block in some cases subtle connections were observed between ML and secondary wall, in the BC treated wood these connections got lost. Probably, the BC present in the walls suffered from stress during freeze-drying that broke these links. The absence of this desired consolidant effect explains the fragile appearance of the treated wood, material loss and creation of openings in the blocks during treatment.

The nanocellulose shape affects how it interacts with the consolidated material. BC and CNCs penetrate inside the wood and precipitate on the cell walls' surface creating hydrogen bonds with the wall components. Christensen et al. (2012) report of an attempt of consolidation of waterlogged archaeological wood by using cellulose whiskers, rod-like nanoparticles 15 nm in diameter and 200–300 nm in length. The authors observed also in their case problems with flocculation and an altered wood aspect caused by the superficial adhesion of nanoparticles. However, a consolidation effect was observed, the whiskers acted as gap fillers interacting between each other and creating an open net-structure inside wood tissues.

Anti-Shrink Efficiency

The values of ASE_F, ASE_A, and ASE_C are shown in **Table 4**. The percentage of shrinkage suppressed by the consolidation and freeze-drying process with respect to air-dried controls, ASE_A, was higher than 50% for all samples with the only exception

FIGURE 4 | SEM images of freeze-dried control (FH2) and treated blocks (LH5, BCH5, and CNCH5). **FH**—external and internal cross sections: cell lumens are empty, secondary cell walls appear almost completely detached or linked by thin filaments (arrows) to the middle lamella; radial section: vessel and fiber walls appear smooth and the pits are well visible. **LH**—external cross section: a layer of nanoparticles is present on the surface, sometimes a coat of nanoparticles is visible inside the cells, all around the lumen (arrow); internal cross section: the cell lumens are empty, no nanoparticles are visible; radial section: LNPs are present inside some of the vessels forming a layer on the cell walls for the first $400\,\mu m$, the other vessels and the wood fibers are empty. **BCH**—external cross section: sporadic deposits of nanoparticles are visible on the surface, some of the cell lumens are filled with consolidant (well visible inside vessels); internal cross section: the degraded secondary cell walls appear as "tubes" coming out of the section; radial section: a homogeneous and compact layer of BC is visible on the cell walls of both vessels and fibers, covering most part of the pits. **CNCH**—external cross section: the cell lumens are empty and only in some cases a thin layer of CNCs is visible on the surface of cell walls (arrow); internal cross section: the cell lumens are empty; radial section: nanoparticles formed a compact and homogeneous coat almost completely covering the pits, at depths $>1.3\,mm$ the CNC layer is no more visible, the cell walls appear smooth and the pits are well visible.

of block CNCS1. More specifically, for all the consolidation treatments ASE_A obtained for hardwood ranged between 80 and 88%, while the values obtained for softwood showed a greater variability between the different consolidants as well as among the blocks treated with the same nanoparticles. In fact, for LNPs treated blocks the registered values ranged between 51 and 69%, for BC treated blocks between 55 and 94% and for CNCs treated samples between 37 and 66%.

ASE_F compares the volumetric shrinkages of consolidated/freeze-dried blocks to those of un-consolidated/freeze-dried controls representing the contribution of the consolidants to the shrinkage suppression. The results obtained for this parameter were generally lower than those calculated for ASE_A, and for six of the treated blocks negative values were obtained. The highest value was registered for the block BCS2 (75%), the other positive results ranged between a minimum of 2% and a maximum of 46%. The low and negative values obtained for LNPs and CNCs were obviously linked to the

fact that the consolidants had penetrated only into a thin layer inside the sample material and thus did not counteract sample shrinkage. The negative value of BCS3 and the low positive values obtained for the others BC treated samples may be linked to the fact that the bacterial cellulose was not able to recreate the bonds between middle lamella and cell wall upon successful sample penetration, as mentioned above.

Regarding the high ASE_A values calculated comparing treated blocks and air-dried controls the effect of freeze-drying must be considered. The values of ASE_C, representing the percentage of shrinkage suppressed by freeze-drying treatment compared to the shrinkage of air-dried controls, confirm the predominant anti-shrink efficiency of freeze-drying. In fact, for hardwood samples ASE_C values ranged between 78 and 80% and for softwood samples between 51 and 75%. It is known from literature (e.g., Pearson, 2014) that freeze-drying of waterlogged archaeological wood allows for avoiding collapses and reduces shrinkage conserving object shape and dimension. However, the

TABLE 4 | Anti-shrink efficiency of the consolidation treatments with respect to freeze-dried (ASE$_F$) and air-dried (ASE$_A$) controls and anti-shrink efficiency of freeze-drying procedure with respect to air-drying (ASE$_C$).

Sample	V$_W$ (mm^3)	V$_D$ (mm^3)	S (%)	ASE$_F$ (%)	ASE$_A$ (%)	ASE$_C$ (%)
LS1	5861.81	5449.78	7.02	17	60	–
LS2	5403.67	4196.31	22.34	−96	51	–
LS3	4121.53	3567.99	13.43	2	69	–
LH1	5608.21	5001.67	10.81	40	–*	–
LH2	6646.23	5704.47	14.17	21	–	–
LH3	5702.48	4981.53	12.64	30	–	–
LH4	11070.66	9921.53	10.38	43	88	–
LH5	9264.25	7679.67	17.10	7	80	–
LH6	9917.58	8714.65	12.13	28	86	–
LH7	10308.65	9062.89	12.08	36	86	–
BCS1	6320.24	5918.37	6.36	25	55	–
BCS2	5317.96	5164.92	2.88	75	94	–
BCS3	3314.78	2851.31	13.98	−2	68	–
BCH1	6625.52	5748.63	13.23	26	–	–
BCH2	6390.79	5620.76	12.05	33	–	–
BCH3	6342.45	5479.22	13.61	24	–	–
BCH4	9015.00	7552.07	16.23	12	81	–
BCH5	10739.92	9173.65	14.58	21	83	–
BCH6	9509.61	8041.09	15.44	9	82	–
BCH7	9736.55	8260.79	15.16	20	82	–
CNCS1	7580.56	6754.18	10.90	−28	37	–
CNCS2	6322.14	5337.42	15.58	−37	66	–
CNCS3	5700.13	4781.69	16.11	−18	63	–
CNCH1	5377.48	4854.08	9.73	46	–	–
CNCH2	5165.71	4516.12	12.57	30	–	–
CNCH3	6111.08	4970.19	18.67	−4	–	–
CNCH4	9557.40	8067.11	15.59	15	82	–
CNCH5	11624.52	10036.73	13.66	26	84	–
CNCH6	8864.71	7521.15	15.16	10	82	–
CNCH7	12059.45	10306.49	14.54	23	83	–
FS1	4482.83	4101.29	8.51	–	–	51
FS2	4402.86	3902.14	11.37	–	–	75
FS3	3178.20	2742.74	13.70	–	–	69
FH2	11569.56	9446.78	18.35	–	–	78
FH3	5413.94	4500.20	16.88	–	–	80
FH4	8646.58	7014.09	18.88	–	–	78

These ASE values are missing because the archaeological material was not enough to obtain an air-dried control.

use of lyophilization without a previous consolidation procedure leads to stress-caused cracking in the fragile material. Aspect and consistency of the nanoparticles treated blocks reflected the just mentioned problems, confirming that an effective consolidation was not achieved.

As shown in **Figure 5** no relations were found between MWC and ASE.

Equilibrium Moisture Content

Table 5 and **Figure 6** show the values and trends of the EMC of treated blocks compared to freeze-dried controls, sound wood controls (oak and fir) and sound wood values reported

TABLE 5 | Equilibrium moisture content (EMC) of treated samples, freeze-dried controls, sound wood controls, and sound wood from the literature at every RH stage.

Sample	EMC						
	10%	35%	45%	55%	65%	85%	100%
LS1	4.43	8.05	11.24	13.24	13.35	19.67	31.83
LS2	2.84	4.08	4.55	4.85	5.38	8.69	15.87
LS3	4.52	6.59	8.92	9.97	11.55	19.90	32.72
LH1	4.71	7.76	10.84	12.45	13.03	18.04	26.65
LH2	3.29	7.03	9.53	11.13	14.24	17.61	23.74
LH3	5.26	8.44	12.12	14.17	14.53	19.91	32.49
LH4	3.55	6.81	9.95	11.74	11.76	17.30	27.25
LH5	4.29	7.20	10.46	12.14	12.29	17.72	27.57
LH7	3.18	6.43	9.61	11.18	11.07	16.52	25.92
BCS1	4.30	7.53	10.56	12.31	13.06	18.84	31.83
BCS2	2.79	3.77	4.75	5.25	5.74	9.90	17.56
BCS3	4.21	6.14	8.44	9.68	11.35	18.53	33.60
BCH1	4.72	7.48	10.38	11.97	13.03	18.03	27.55
BCH2	4.66	6.91	9.66	11.25	12.15	16.67	28.66
BCH3	4.40	6.84	9.77	11.41	12.52	17.03	25.62
BCH4	4.18	6.39	9.11	10.51	11.53	17.42	40.32
BCH6	4.16	7.01	9.64	11.16	12.79	18.62	36.22
BCH7	4.27	6.75	9.55	10.93	12.26	17.98	35.81
CNCS1	4.36	8.14	11.56	13.46	13.30	19.40	27.04
CNCS2	2.83	3.50	4.26	4.28	4.72	7.10	13.24
CNCS3	4.13	6.25	8.59	9.68	11.26	18.74	32.85
CNCH1	2.69	4.61	6.49	7.60	8.34	10.93	15.99
CNCH2	2.95	4.53	6.40	7.42	8.65	11.28	15.34
CNCH3	4.83	8.08	11.27	12.91	13.15	18.61	28.81
CNCH4	3.35	6.47	9.57	11.36	11.27	16.64	24.69
CNCH6	3.30	6.25	9.46	10.99	10.68	16.09	28.19
CNCH7	3.17	6.50	9.65	11.20	10.83	16.42	26.52
FS1	4.67	8.32	11.59	13.39	13.16	19.02	27.05
FS2	2.76	3.77	4.00	4.25	4.54	7.21	12.72
FS3	4.68	6.60	8.95	10.06	11.55	20.22	33.53
FH1	3.31	6.29	9.67	12.12	14.09	17.05	22.87
FH3	4.08	6.65	9.83	11.08	10.85	15.96	22.93
FH4	3.29	6.45	9.67	11.31	10.77	16.36	26.34
Oak1	3.79	6.67	9.32	10.83	10.45	16.66	27.22
Oak2	4.31	6.55	9.20	10.71	10.17	16.26	23.87
Oak3	4.22	7.24	9.88	11.51	10.69	16.05	25.07
Oak4	4.60	7.23	9.85	11.48	10.26	14.37	24.08
Oak5	4.28	6.97	9.53	11.15	10.33	15.17	23.91
Oak6	3.94	6.75	9.29	10.94	10.23	15.58	24.43
Fir1	3.41	6.46	9.34	10.68	11.21	15.62	21.90
Fir2	3.56	6.58	9.39	10.68	11.09	15.75	21.92
Fir3	3.77	6.71	9.67	10.88	11.52	16.05	22.42
Fir4	3.78	6.66	9.57	10.79	11.52	15.91	22.14
Sound wood	3	7	9	10	12	18	30

in literature. The trends, obtained by averaging the values in **Table 5**, showed that the EMC of sound wood controls used during the experimentation were lower with respect to literature

FIGURE 5 | Graph of Anti-shrink efficiency (ASE) vs. MWC.
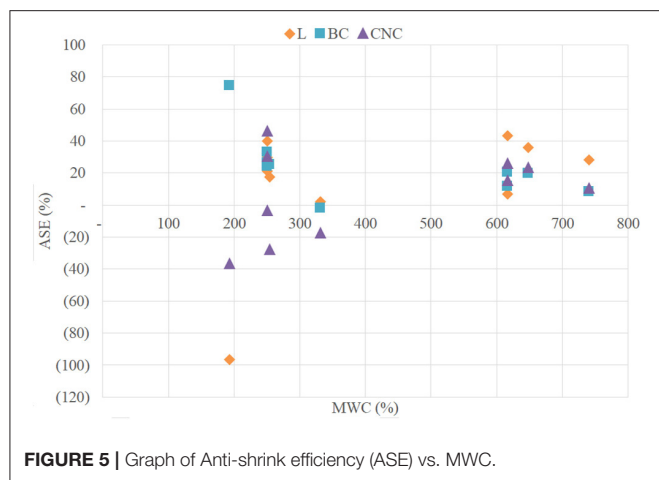
values. This can be linked to the natural variability of wood. The values obtained for freeze-dried wood were comparable to those of sound controls for all tested RH.
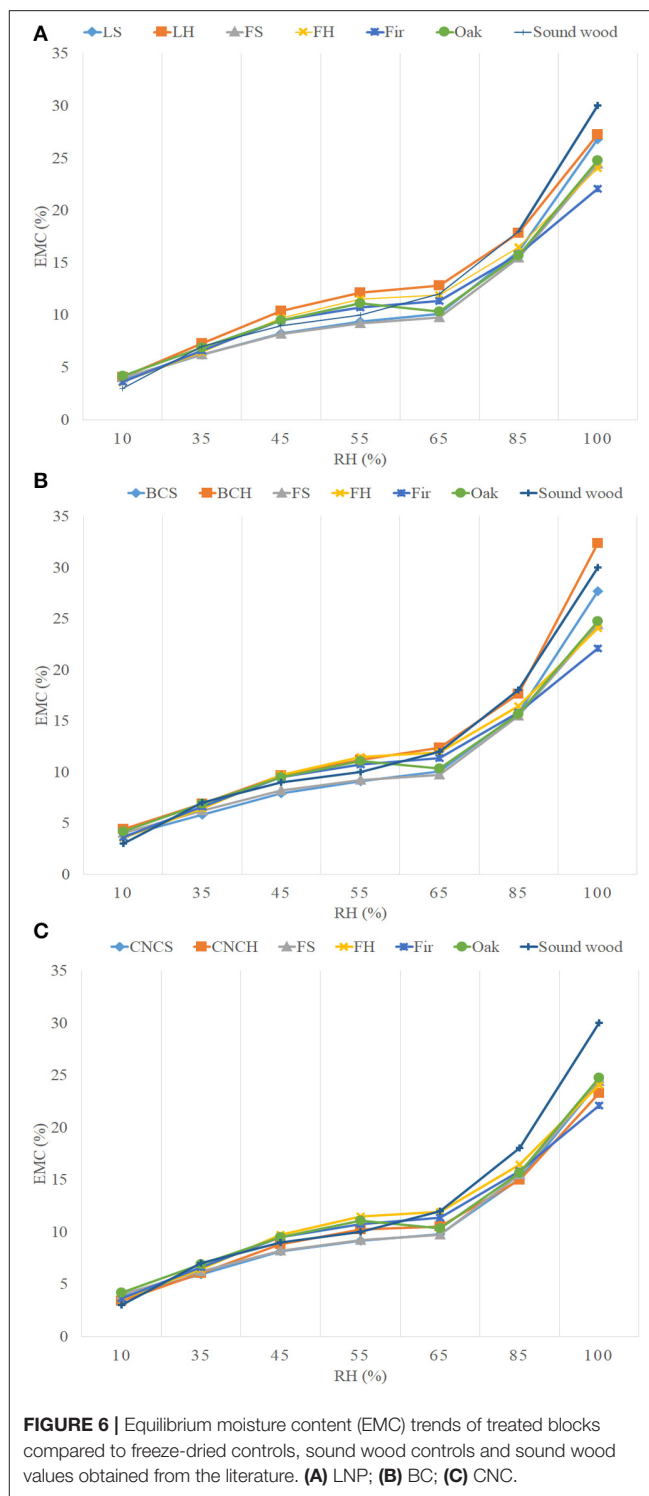
In general, the EMC values obtained for blocks belonging to the same archaeological source but treated with different consolidants varied slightly and not significantly. At 100% RH, the CNCs treated blocks had EMC values slightly lower than wood treated with the other two consolidants and comparable with freeze-dried controls. At the same RH, the LNPs and BC treated blocks showed an EMC in average higher with respect to lyophilized controls (2–3 and 3–8% respectively). However, the observed differences were too low to be considered significant. Based on the obtained results it could be concluded that the moisture equilibrium content of treated samples was not influenced by the hygroscopic features of nano-scale consolidants. Obvious deviations from data uniformity were observed for the blocks S2, both those treated with nanoparticles and the freeze-dried control, CNCH1 and CNCH2 whose EMC values were on average 2–15% lower with respect to the others. This discrepancy can be explained taking into account what already mentioned above with respect to fir and elm samples, the presence of sediments inside the wood must have influenced its relation with moisture.

It is interesting to note that in the RH range used for conservative purposes (35–85%), the average EMC values for all blocks never exceeded the 18% considered as the threshold for the risk of biological attacks.

CONCLUSION

The aim of the present work was to test three nano-scale consolidants based on cellulose and lignin. The obtained results did not allow for discriminating significant differences regarding their efficacy but they laid a profound base for more focused tests in future.

The problems in color changing observed for LNPs and BC could be solved by modifying the impregnation baths. For BC, a pigment compatible with the treated material could be added

FIGURE 6 | Equilibrium moisture content (EMC) trends of treated blocks compared to freeze-dried controls, sound wood controls and sound wood values obtained from the literature. **(A)** LNP; **(B)** BC; **(C)** CNC.

to the bath. For LNPs a careful selection of the wood source for lignin isolation could give LNPs of different color grades matching the color of the consolidation object (Zikeli et al., 2019).

Regarding the different penetration of the tested consolidants, it was not possible to identify relations neither with the state of preservation of wood nor with the shape and dimension of

the nanoparticles. Thus, the different behavior must be related to chemical interactions between the nanoparticles themselves and between them and the wood. LNPs and CNCs penetration problems could be solved by modifying the impregnation conditions in the first case to facilitate penetration, in the second to prevent the gel formation. For BC a satisfying penetration was observed but the consolidating effect was not substantial. A best result could be achieved by modifying the shape of the nanocellulose or combining filamentous with spherical nanoparticles in order to obtain web-like structures more suitable to fill the voids and to support the cell wall, exploiting the potential of nano-scale consolidants to enter wood ultrastructure.

DATA AVAILABILITY STATEMENT

All datasets generated for this study are included in the article/**Supplementary Material**.

AUTHOR CONTRIBUTIONS

FA, GG, and MR conceived and planned the experiments. FZ and RN produced and provided the nanoparticles used in the experimentation. GS, FZ, and RN contributed to define the settings of the tests. MR and BP helped supervise the project. FA and GG wrote the paper with inputs from all authors. All the authors contributed to the discussion.

FUNDING

SUPPLEMENTARY MATERIAL

The Supplementary Material for this article can be found online at: https://www.frontiersin.org/articles/10.3389/fchem.2020.00032/full#supplementary-material

REFERENCES

Abdul Khalil, H. P. S., Davoudpour, Y., Islam, M. N., Mustapha, A., Sudesh, K., Dungani, R., et al. (2014). Production and modification of nanofibrillated cellulose using various mechanical processes: a review. *Carbohydr. Polym.* 99, 649–665. doi: 10.1016/j.carbpol.2013.08.069

Baglioni, P., Carretti, E., and Chelazzi, D. (2015). Nanomaterials in art conservation. *Nat. Nanotechnol.* 10, 287–290. doi: 10.1038/nnano.2015.38

Beisl, S., Friedl, A., and Miltner, A. (2017). Lignin from micro- to nanosize: applications. *Int. J. Mol. Sci.* 18:2367. doi: 10.3390/ijms18112367

Blanchette, R. A., Nilsson, T., Daniel, G., and Abad, A. (1989). "Biological "Degradation of Wood," in *Archaeological Wood*," in *Properties, Chemistry, and Preservation*, eds R. M. Rowell and J. R. Barbour (Washington, DC: American Chemical Society), 141–174.

Boetto, G., Ghelli, A., and Germoni, P. (2017). "New Roman shipwrecks from Isola Sacra (Rome, Italy)," in *Ships and Maritime Landscapes: Proceedings of the Thirteenth International Symposium on Boat and Ship Archaeology, Amsterdam 2012*, eds J. Gawronski, A. van Holk, and J. Schokkenbroek (Eelde: Barkhuis), 260–266.

Capretti, C., Macchioni, N., Pizzo, B., Galotta, G., Giachi, G., and Giampaola, D. (2008). The characterization of waterlogged archaeological wood: the three Roman ships found in Naples (Italy). *Archaeometry* 50, 855–876. doi: 10.1111/j.1475-4754.2007.00376.x

Chelazzi, D., Giorgi, R., and Baglioni, P. (2006). Nanotechnology for vasa wood de-acidification. *Macromol. Symp.* 238, 30–36. doi: 10.1002/masy.200650605

Christensen, M., Kutzke, H., and Hansen, F. K. (2012). New materials used for the consolidation of archaeological wood-past attempts, present struggles, and future requirements. *J. Cult. Herit.* 13, S183–S190. doi: 10.1016/j.culher.2012.02.013

Cipriani, G., Salvini, A., Baglioni, P., and Bucciarelli, E. (2010). Cellulose as a renewable resource for the synthesis of wood consolidants. *J. Appl. Polym. Sci.* 118, 2939–2950. doi: 10.1002/app.32634

Di Donato, V., Ruello, M. R., Liuzza, V., Carsana, V., Giampaola, D., Di Vito, M. A., et al. (2018). Development and decline of the ancient harbor of Neapolis. *Geoarchaeology* 33, 542–557. doi: 10.1002/gea.21673

EN335 (2013). *Durability of Wood and Wood-Based Products – Use Classes: Definitions, Application to Solid Wood and Wood-Based Products*. Brussels: European Committee for Standardization

Giordano, G. (1981). *Tecnologia del Legno, Vol. 1*. Torino: UTET.

Giordano, G. (1986). *Tecnologia del Legno, Vol. 3*. Turin: UTET.

Grattan, D. W., and Clarke, R. W. (1987). "Conservation of waterlogged wood," in *Conservation of Marine Archaeological Objects*, ed C. Pearson (London: Butterworth), 164–206.

Hedges, J. I. (1990). "The chemistry of archaeological wood," in *Archaeological Wood. Properties, Chemistry and Preservation. Advances in Chemistry Series 225*, eds R. M. Rowell and R. J. Barbour (Washington, DC: American Chemical Society), 111–139.

Jacquiot, C. (1955). *Atlas D'anatomie des Bois des CONIFERES*. Paris: Centre Technique du Bois.

Jacquiot, C., Trenard, Y., and Dirol, D. (1973). *Atlas D'anatomie des Angiospermes (Essences Feuillues)*. Paris.

Jensen, P., and Gregory, D. J. (2006). Selected physical parameters to characterize the state of preservation of waterlogged archaeological wood: a practical guide for their determination. *J. Archaeol. Sci.* 33, 551–559. doi: 10.1016/j.jas.2005.09.007

Kargarzadeh, H., Ioelovich, M., Ahmad, I., Thomas, S., and Dufresne, A. (2017). "Methods for extraction of nanocellulose from various sources," in *Handbook of Nanocellulose and Cellulose Nanocomposites*, eds H. Kargarzadeh, I. Ahmad, S. Thomas, and A. Dufresne (Weinheim: Wiley-VCH), 1–49.

Kunjalukkal Padmanabhan, S., Esposito Corcione, C., Nisi, R., Maffezzoli, A., and Licciulli, A. (2017). PolyDiethyleneglycol–bisallyl carbonate matrix transparent nanocomposites reinforced with bacterial cellulose microfibrils. *Eur. Polym. J.* 93, 192–199. doi: 10.1016/j.eurpolymj.2017.05.037

Macchioni, N., Pizzo, B., Capretti, C., and Giachi, G. (2012). How an integrated diagnostic approach can help in a correct evaluation of the state of preservation of waterlogged archaeological wooden artefacts. *J. Archaeol. Sci.* 39, 3255–3263. doi: 10.1016/j.jas.2012.05.008

Mahltig, B., Swaboda, C., Roessler, A., and Böttcher, H. (2008). Functionalising wood by nanosol application. *J. Mater. Chem.* 18:3180. doi: 10.1039/b718903f

McConnachie, G., Eaton, R., and Jones, M. (2008). A re-evaluation of the use of maximum moisture content data for assessing the condition of waterlogged archaeological wood. *e-Preservation Sci.* 5, 29–35.

Pal, S., Nisi, R., Stoppa, M., and Licciulli, A. (2017). Silver-functionalized bacterial cellulose as antibacterial membrane for wound-healing applications. *ACS Omega* 2, 3632–3639. doi: 10.1021/acsomega.7b00442

Pearson, C. (Ed.). (2014). *Conservation of Marine Archaeological Objects*. London: Butterworths & co.

Romagnoli, M., Galotta, G., Antonelli, F., Sidoti, G., Humar, M., KrŽišnik, D., et al. (2018). Micro-morphological, physical and thermogravimetric analyses of waterlogged archaeological wood from the prehistoric village of Gran Carro (Lake Bolsena-Italy). *J. Cult. Herit.* 33, 30–38. doi: 10.1016/j.culher.2018.03.012

Schniewind, A. P. (1990). "Physical and mechanical properties of archaeological wood," in *Archaeological Wood. Properties, Chemistry and Preservation. Advances in Chemistry. Series 225*, eds R. M. Rowell and R. J. Barbour (Washington, DC: American Chemical Society), 87–109.

Schwarze, F. W. M. R. (2007). Wood decay under the microscope. *Fungal Biol. Rev.* 21, 133–170. doi: 10.1016/j.fbr.2007.09.001

Schweingruber, F., and Baas, P. (1990). *Anatomie Europaischer Holzer*. Bern: Verlag P. Haupt Available online at: http://agris.fao.org/agris-search/search.do?recordID=US201300684419 (accessed May 23, 2017).

Unger, A., Schniewind, A., and Unger, W. (2001). *Conservation of Wood Artifacts: a Handbook*. Berlin: Springer-Verlag Berlin Heidelberg.

UNI11118 (2004). *Cultural Heritage - Wooden Artefacts – Criteria for the Identification of the Wood Species*. Milan: Italian Technical Standard.

UNI11205 (2007). *Cultural Heritage - Archaeological and Archaeo-Botanic Wood - Guidelines to the Characterization*. Milan: Italian Technical Standard.

Zikeli, F., Vinciguerra, V., D'Annibale, A., Capitani, D., Romagnoli, M., and Scarascia Mugnozza, G. (2019). Preparation of lignin nanoparticles from wood waste for wood surface treatment. *Nanomaterials* 9:281. doi: 10.3390/nano9020281

Zikeli, F., Vinciguerra, V., Taddei, A. R., D'Annibale, A., Romagnoli, M., and Scarascia Mugnozza, G. (2018). Isolation and characterization of lignin from beech wood and chestnut sawdust for the preparation of lignin nanoparticles (LNPs) from wood industry side-streams. *Holzforschung* 72, 961–972. doi: 10.1515/hf-2017-0208

TEOS Modified With Nano-Calcium Oxalate and PDMS to Protect Concrete Based Cultural Heritage Buildings

Kali Kapetanaki[1], Eleftheria Vazgiouraki[1], Dimitris Stefanakis[1], Afroditi Fotiou[1], George C. Anyfantis[2], Ines García-Lodeiro[3], Maria T. Blanco-Varela[3], Ioannis Arabatzis[2] and Pagona N. Maravelaki[1]*

[1] Laboratory of Materials of Cultural Heritage and Modern Building, School of Architecture, Technical University of Crete, Chania, Greece, [2] NanoPhos S.A., Technological and Science Park of Lavrio, Lávrio, Greece, [3] Consejo Superior de Investigaciones Científicas - Instituto de Ciencias de la Construcción Eduardo Torroja (IETCC), Madrid, Spain

Cultural Heritage constructions of twentieth century consist largely of mortar and concrete substrates. These concrete structures have suffered different types of decay processes. One of the most widely used consolidants is the Tetraethoxysilane (TEOS), which forms the basis of most existing commercial strengthening agents to protect porous building materials against deterioration. A novel, non-toxic strengthening and protective agent for mortar and concrete substrates was synthesized in a one-pot sol-gel procedure, incorporating in TEOS, Polydimethyl siloxane (PDMS), and nanoparticles of synthesized calcium oxalate (CaOx). PDMS provided hydrophobicity and reduced surface tension that causes cracks on the surface of produced xerogel. The synthesized nanocomposite both in sol and xerogel form was assessed with a variety of analytical techniques (FTIR, XRF, SEM, Optical Microscopy, Dynamic Light Scattering, Thermogravimetric analysis). The excellent physical properties of the produced colloidal solution of the nanocomposite, such as low viscosity and density, allow a penetration up to 2 cm from the surface in the treated cement mortars. This involved improvement of the mechanical and physical properties, such as the dynamic modulus of elasticity and increased water repellency. The treated cement mortars exhibited well-preserved aesthetic surface parameters and significant maintenance of the treatment. Furthermore, no harmful byproducts were identified indicating the nanocomposite compatibility to the siliceous and carbonate nature of the treated cement mortars.

Keywords: PDMS-TEOS-nano-calcium oxalate nanocomposite, concrete conservation, hydrophobic consolidant, compatible, cultural heritage conservation

INTRODUCTION

Cultural heritage constructions of twentieth century consist largely of mortar and concrete substrates. Due to the time and weathering conditions, these structures undergo different types of decay processes (Schutter, 2012). One common methodology proposed for preserving concrete heritage is the use of structural and surface treatments. Among the different types of treatments we can highlight the use of impregnation treatments, such as the consolidant Tetraethoxysilane

(TEOS) that enables the filling of micro-cracks generated by the decay processes (Pigino et al., 2012; Barberena-Fernández et al., 2015, 2018; Pan et al., 2017).

Silicon compounds such as TEOS are widely used in the field of consolidation and protection of modern constructions and heritage monuments. TEOS penetrated in traditional stone-based substrate, forming a SiO_2 gel which acts as a new cement matrix. However, in the case of concrete-based substrate, the mechanism of interaction is different. In a first stage, the hydrolysis of TEOS takes place to produce $Si(OH)_4$ groups and ethanol. In a second stage, two competitive processes can take place; (i) $Si(OH)_4$ can polymerized forming a SiO_2 gel and (ii) $Si(OH)_4$ groups can interact with the Original Portland Cement (OPC) hydrated phases [such as $Ca(OH)_2$] to produce C-S-H gel, which is the main responsible of the binding properties of concrete (Moropoulou et al., 2004; Sandrolini et al., 2012).

TEOS based products fulfill many requirements, including the long-term stability and strength under adverse conditions. Some additional favorable features of them are correlated to the lack of toxicity, the easy way to apply and their high degree of penetration into the target area due to their initial low viscosity (Verganelaki et al., 2015). The exploitation of the aforementioned characteristics of TEOS-based consolidants to the restoration of building damages, combined with their simple and low cost synthesis route, establish them extremely promising for an extensive and massive production.

Despite all these special characteristics of the TEOS-based consolidants, in practice, they still suffer from some remarkable drawbacks. In particular, cracks are developed during the sol-gel drying process due to the exerted capillary pressure by the gel network. Furthermore, the inefficient chemical bonding of the silica to the non-silicate substrates may cause inefficient performance of the treatment. Another drawback is related to the limited hydrophobicity of these materials, thus the water ingress at the substrate is not avoided and the building decay can progress (Maravelaki-Kalaitzaki et al., 2006; Scherer and Wheeler, 2009). Last but not least, the unavoidable biological impact considerably contributes to the degradation of the consolidants and their further inefficient action onto the building (Ruffolo and La Russa, 2019).

In order to overcome the above limitations and to develop a more effective consolidating material, a variety of chemical species (metals, molecules, and nanoparticles) have been utilized (Scherer and Wheeler, 2009; Pinho et al., 2013). Advanced methods involve the utilization of modified silanes, as well as the addition of surfactants, salts, natural, and synthetic polymers (Son et al., 2009; Illescas and Mosquera, 2012). In several cases, the results are encouraging and the cracks are eliminated, due to the reduced capillary pressure and surface tension. Despite the progress that has been made concerning the cracks elimination, the limited effectiveness of TEOS on carbonate substrates still remains a significant issue to deal with.

During the past, a series of compounds were tested in order to improve the consolidation. Although calcium alkoxides or nanolimes have been suggested for this purpose, their limited stability toward atmospheric conditions, the tendency to agglomerate and the pure penetration depth in the substrates have prevented from wide range practical application (Baglioni et al., 2013; Rodriguez-Navarro et al., 2013).

Another challenging issue that has to be overcome is related to building decay caused by the water penetration into the substrate. In most of the cases, TEOS-based consolidants with alkyl siloxane water repellents commonly employed to prevent or reduce water ingress. The reduction of the surface energy of the consolidant has come to the foreground as a critical parameter which can regulate the water repellency (Illescas and Mosquera, 2012; Karapanagiotis et al., 2014). An ordinary methodology includes the utilization of a consolidant with a hydrophobic coating or the incorporation of hydrophobic agents into the consolidant materials. In particular, a mixture of modified TEOS, PDMS, and n-octylamine has been referred as a satisfactory solution for the problem of the water wetting (Mosquera et al., 2010).

Calcium oxalate (CaC_2O_4) is the main component of patina, which is found on well-preserved monumental surfaces and historical buildings. Patina layers originating from biological agents or transformation of previous protective treatments, offered a protective role on monuments and building stones (Ion et al., 2017). The contribution of calcium oxalate (CaOx) is important to the surface protection of monuments, by forming a thin compact non-porous shell. The film is highly resistant to acid attack, due to its pH independence which is a determinant factor during the carbonation process.

In a previous work, an inorganic nanocomposite based on silica and calcium oxalate was proposed. More specifically, amorphous CaOx was incorporated into the silica matrix. The addition of CaOx to the TEOS increased the pore volume during the gel formation producing a crack-free xerogel. At the same time compatibility and affinity between the nanocomposite and substrate was achieved, as CaOx enabled electrostatic interactions, offering chemical affinity between the silica and the carbonaceous substrates (Verganelaki et al., 2014).

In this study, an improved modified one-pot synthesis of this silica nanocomposite enriched with CaOx, in order to dispose chemical affinity with the concrete based-substrates eliminating the cracks, is described. The innovation of this preparation involves the synthesis of CaOx during the polymerization of TEOS, as well as the addition of a hydrophobic agent, PDMS (hydroxyl-terminated polydimethylsiloxane). PDMS is an organosilane, which provides hydrophobicity and water repellency. The chemically bonded chains of PDMS induce discontinuities in the resulting network, contributing to increased deformability and porosity. Finally, the enhancement of toughness and flexibility of the silica network, prevent the gel from cracking during drying.

This novel treatment is tested on different types of OPC based-substrates (sound, chemically, and physically aged mortars) in order to check its effectiveness. Treatment uptake and penetration depth, as well as the changes in the mechanical, hydric, and color properties of the substrate have been evaluated after treatment.

EXPERIMENTAL PART

Materials

Tetraethyl orthosilicate (Tetraethoxysilane, TEOS), the hydroxyl-terminated polythimethylsiloxane (PDMS: MEM 0347), oxalic acid dihydrate (Ox), and calcium hydroxide (CH) were purchased from NanoPhos (NanoPhos S.A. Technological and Science Park, Lavrio, Greece). Isopropanol (ISP, Aldrich) and deionized water were used as solvents. All chemicals were used as received, without further purification prior to use. Additionally, a high molecular weight with polystyrene blocks copolymer, the commercial dispersant (Disperbyk-190, BYK-Chemie, Wesel) was added during the sol production, thus contributing to the reduction of the surface tension and the elimination of the cracking of xerogel.

Synthesis Route

The synthesis of the consolidant product, named as FX-C is presented in **Figure 1**. CaOx was formed at the first solution (designated A_1), which contained CH, water and Ox. The solution A_1 underwent magnetic stirring for 5 min. In a second step, a part of TEOS and ISP were added to the solution A_1 (solution A_2) and remained under magnetic stirring and ultrasonic agitation for 5 and 10 min, respectively. This is the first part of TEOS hydrolysis which is enforced by the presence of the Ox, which acts as a catalyst (Verganelaki et al., 2015). Simultaneously, another solution designated as sol B was prepared mixing PDMS, TEOS, and ISP and stirring for 10 min. Solutions A_2 and B were mixed and left under stirring for 7 h. The quantities were optimized after several experiments aimed at producing a colloidal solution with low viscosity ($\sim$2–3 mPa·s) and a crack free xerogel. The final molar ratio of the precursors and solvents TEOS/ISP/H_2O/Ox/CH was equal to 1/10.4/8.01/0.06/0.007.

Hydrolysis and condensation of TEOS were monitored through FTIR. The derived final solution was cast into cylindrical transparent glass vessels of Ø35 × 38 mm dimensions. The vessels were appropriately covered in order to simulate the evaporation of solvent occurring into the pores of the cement substrate. The casting sols were exposed to laboratory conditions (RH = 60 ± 5%, T = 20 ± 2°C).

Test Methods

The produced nanocomposite was assessed with a variety of analytical techniques described in the following. A Brookfield DV-II + Pro spindle: S18 viscometer was used for the viscosity measurements of the sol vs. time with temperature control at 25°C. The percent volume and mass reduction of the xerogel was calculated from the volume and weight losses of the initial sol casted in the glass vessel. In order to get a first approximation concerning the surface tension of the solution, a pendant drop tensiometer was used according to EN Standard Procedure 15802:2009 (Berry et al., 2015). The FX-C xerogel was microscopically assessed with the aid of the digital microscope USB Dino-Lite AM4515T5 Edge. The microscope was equipped with a color CMOS sensor. The captured via the Dino Capture 2.0 software images had 1.3 megapixels resolution, and 500× zoom. The tests of Vickers hardness for the FX-C nanocomposite were performed with a microhardness tester Future-Tech FM-700, under loading of 300 g with dwell time 5 s. An optical tensiometer (Thetalite TL 101, KSV) was used for the contact angle measurements vs. time, determining the static contact angle (θs) of the FX-C itself.

A satisfactory insight into the evolution of the sol-gel process and the stability of the bonds between the newly formed chemical species was obtained via the Fourier transform infrared spectroscopy (FTIR) absorption spectra. The spectra were recorded with a PerkinElmer 1000 spectrometer, in the spectral range from 4,000 to 400 cm^{-1}.

The thermal behavior of the developed xerogel was carried out by thermogravimetric analysis (DTA-TG) in a Setaram LabSys
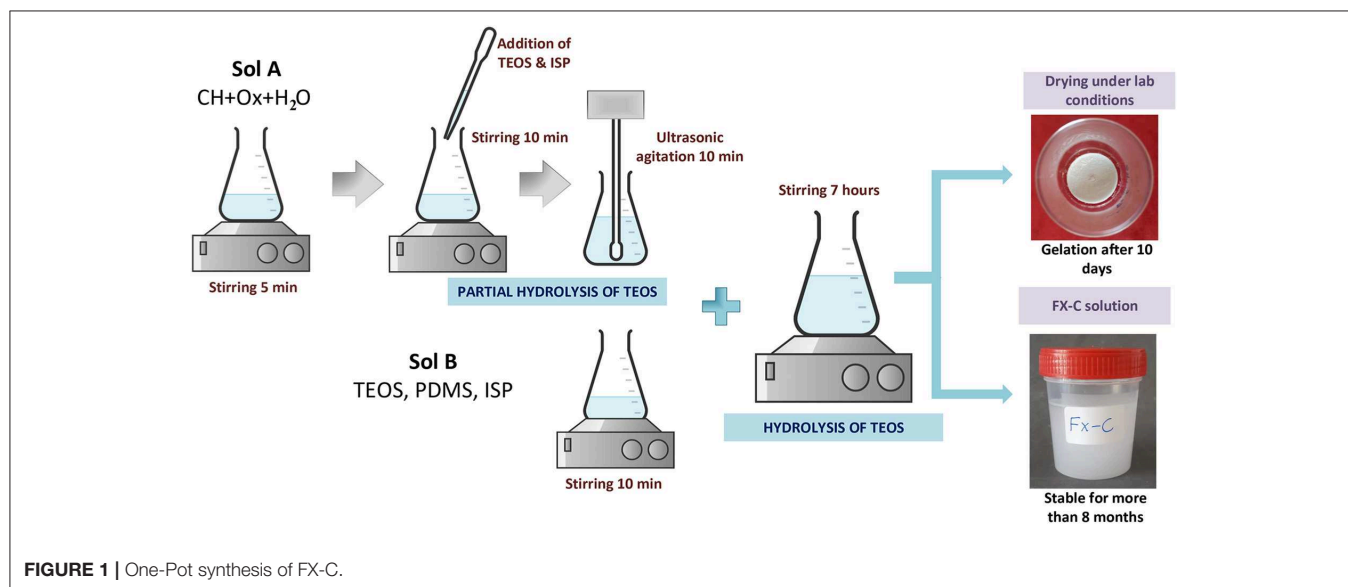

FIGURE 1 | One-Pot synthesis of FX-C.

TABLE 1 | Properties of the colloidal solution and xerogel FX-C.

Sample	Viscosity (mPa·s)	Volume reduction (%v/v)	Weight reduction (%w/w)	pH	Density (gr/cm^3)	Gelation time (days)*	Sol appearance	Xerogel state	Hardness
Solution	2.05	–		2.93	0.85	10	White, one phase	–	
Xerogel	–	71	49	–		–	White	Hard monolithic	199.3 Vickers

Evo 1,600°C. The sample under investigation was heated up to 1,000°C under nitrogen atmosphere with a heating rate of 10°C/min.

Scanning and transmission electron microscopy techniques (SEM and TEM, respectively) were used for the xerogel microstructure characterization. SEM micrographs were captured at the backscattered electrons mode using an energy-dispersive X-ray analysis system attached to a scanning electron microscope (Philips SEM 535 with EDAX equipment). Transmission electron microscopy (TEM) micrographs were recorded with a JEOL JEM 100C electron microscope operating at 200 kV, equipped with a Model 782 ES500W Erlangshen CCD camera.

Energy dispersive X-ray fluorescence (EDXRF) is a suitable technique for identifying the elemental composition of the compounds present at the xerogel. Measurements were directly performed on the xerogel sample ground to a powder. The EDXRF instrumentation included [109]Cd and [55]Fe radioactive sources, Si(Li) semiconductor detector (resolution 150 eV at 5.9 keV), TC-244 Spectroscopy Amplifier, PCA-II Nucleus Multichannel Card, AXIL (RN) computer program analysis.

A multimode AFM (Digital Instrumens Nanoscope IIIa) was used to study the AFM face images.

Total porosity and the average pore size diameter were determined by mercury intrusion porosimetry (MIP). Measurements were performed using Micrometrics Poresizer 9320. Aesthetic parameters (colorimetric analysis) were determined using a MINOLTA CM-2500d spectrophotometer.

Preparation of OPC Mortar Samples

OPC mortar specimens (with different sizes were prepared as specified in European standard EN 196-1 using CEM I 42.5R cement (**Table S1**), CEN-compliant sand at a cement/ratio of 1/3 and a water/cement ratio of 0.5 (sound mortars). Although no demolding product was applied, the inner surface of the mold was coated with a self-adhesive film. In order to simulate similar features than in an actual ordinary concrete, several sets of non-standard mortars were elaborated. Additionally, OPC non-standard mortars were prepared using a sand/cement ratio of 5/1 and water/cement ratio of 0.5.

The porosity of the non-standard mortars seemed to be closer to that of the deteriorated concrete surface, so they were selected to simulate the penetration way of the consolidant into the target substrate. To simulate the common types of decay processes in concrete, standard mortars were physically and chemically aged using different types of deterioration accelerated test. The aged samples were selected in order to simulate the more characteristic types of concrete decay. For this reason, the aging processes that were followed were (1) aging by chemical degradation caused by (a) carbonation and (b) chloride penetration and (2) aging through physical degradation caused by freeze-thaw cycles.

Aging through carbonation took place by exposing OPC mortar samples in CO_2 incubator chamber (2% CO_2, 25°C, R.H > 80%) for 8 months. Sound specimens were subjected to 4 cycles of chloride penetration. Each cycle included the samples immersion in saturated solution of NaCl for 48 h, followed by drying at 105°C for 24 h. After the end of the aforementioned 4 cycles, the samples were immersed in deionized water, where they remained for 2 weeks. Concerning the aging process through the freeze-thaw cycles, each cycle of this procedure included two stages-processes: temperature reduction from 4 ± 2°C to −18 ± 2°C during half an hour and maintenance at the final temperature for 2.5 h (freeze process) and vice versa (thaw process). During the freeze stage the samples remained under air conditions while they were immersed into the water during the thaw cycle (AST C666). Samples were subjected to 28 repetitive cycles.

Once the aging process finishes, OPC mortars were characterized (Total porosity and average pore size diameter, colorimetric analysis, FTIR) by different techniques mentioned in sections Test Methods and FX-C Application on Cement Mortars Samples.

FX-C Application on Cement Mortars Samples

Three cubic specimens (50 × 50 × 50 mm) from each aging set were brushed only on one side. Before the FX-C application, the sample surface was gently polished with an abrasive paper of fine grit size (P180 carborundum paper). Next, the specimens were rinsed with deionized water. Their dry took place in an oven at 60 ± 2°C for 3 days. They weighed up to obtain a constant mass and then they remained in a desiccator vessel until the consolidant application. The samples were sprayed with ISP at the beginning and in the middle of the application process to facilitate the sol entrance and migration inside the pores of the substrate. The brushing of the sample with the consolidant have taken place uniformly in two directions (vertically and horizontally) in order to avoid the formation of a thick nanocomposite layer onto it with the subsequent formation of cracks at the surface. After treatment, samples were exposed to lab conditions, at RH = 60 ± 5% and T = 20 ± 2°C.

Tests Methods for the Evaluation of the Treatment

The performance of the developed consolidant was assessed using the techniques described below, at sound, aged (chemical or physical degradation) and non-standard samples treated with FX-C. Aging process is used in order to simulate the decay process of cement and concrete surfaces.

Aesthetic, physico-chemical, mechanical properties, microstructure, and composition of the samples were checked through tests of colorimetry, optical microscopy, contact angle, FTIR analysis, water capillarity, peeling test, ultrasound pulse velocity, and SEM.

The treatment of samples aimed to enhance physical and mechanical properties without altering aesthetic parameters, as well as without over-strengthening the substrate. The color modifications were studied using a Konica Minolta, CM-2600d and Vis spectrophotometer adapted with a D65 illuminant at 8-degree viewing, in a wavelength range from 360 to 740 nm. The average values of the color parameters L^*, α^*, and b^*, were derived from five measurements of random areas of untreated and treated specimens and used for the calculation of the total color difference expressed as ΔE^* (Maravelaki et al., 2014; Lollino et al., 2015).

Optical microscopy was used to monitor the treated surface 1 day after the application, in order the crack formation to be checked. The images were captured with the Dino Lite microscope (for more details concerning the specifications of the system see nanocomposite section).

In order to evaluate the hydrophobicity of surfaces, water contact angle (WCA) measurements were carried out using the tensiometer, as it has already been described at the nanocomposite test methods section. Measurements were in accordance to EN Standard Procedure 15802:2009. On different points of each specimen, several water droplets ($\sim$5 μL) were deposited close to the surfaces using a needle. Afterwards, the images of the droplets were further processed revealing the average CA values. Additionally, water absorption by capillarity according to the EN 15801:2010 was performed to evaluate water repellency of treated samples (UNI 11432: 2011). The maximum water absorption per unit area (Q_i, expressed in mg·cm^{-1}) and the capillary water absorption coefficients (CA) in mg·cm^{-1}·s $^{1/2}$ were calculated before and after treatment, for all the substrates. The amount of water absorbed by the specimen per unit area Q_i (kg/m^2) at time t_i (s) is calculated by the following equation:

$$Q_i = \frac{m_i - m_0}{A}$$

where, m_i is mass of the specimen at time t_i, in kg; m_0 is the mass of the dry specimen, in kg and A is the area of the specimen in contact with water, in m^2. Additionally, water absorption coefficient by capillary (WCA) was estimated by the slope of linear section of the Q_i- $\sqrt{t_i}$ curve.

One of the most important parameters for evaluating the effectiveness of the consolidation is the determination of the penetration depth of the applied consolidant. The penetration depth of the FX-C into the treated samples was evaluated with FTIR analyses. Powders derived from the surface and at different depths from sections of the treated samples under investigation, were analyzed by FTIR analysis. The evaluation of the FX-C penetration depth was based on the identification of the characteristic peaks of the Si-O-Si stretching at the FTIR spectra corresponding to the nanocomposite. Furthermore, the colloidal FX-C solution was stained with thymol blue and the penetration depth was visually inspected after cutting the specimen and measuring the stained sol penetration depth at the perpendicular sections.

Mechanical assessment was held by measuring Ultrasound Pulse Velocity (UPV). The dynamic modulus of elasticity (E_{dyn}) according to EN 14579 (2004), was calculated through the equation:

$$E_{dyn} = d \times V^2$$

where, d is the density of the sample and V the measured velocity of ultrasound pulse (Miliani et al., 2007). The density of the samples derived from the ratio of weight to volume; the latter, was calculated from the dimensions of samples.

Finally, the treatment–substrate interface of the treated samples with FX-C was visualized by SEM microscopy. Transversal sections of treated materials, and their untreated counterpart, coated with a thin conducting layer of gold, were examined.

RESULTS AND DISCUSSION

Characterization of the Consolidant FX-C

The prepared nanocomposite exhibits a Newtonian behavior at the shear range evaluated, with the viscosity to be calculated 2 mPa·s, close to that of the commercial products. This value of viscosity indicates a sufficient and uniform penetration into the pores of inorganic materials, as the depth of penetration is related to the viscosity of the consolidants (Franzoni et al., 2014). Viscosity over time has been used as indicator of the consolidant stability. In this study, the viscosity remained unchanged under no evaporation conditions, according to the rheological observations.

The macroscopic evolution of the FX-C to gel, has been monitored by measuring the dry volume reduction. An amount of 71% was lost, which is comparable with similar xerogels referred in the literature (Facio et al., 2017). The derived xerogel has exhibited 70% weight loss (**Table 1**).

The macroscopic appearance of FX-C reveals a homogeneous monolithic xerogel, with a significant degree of cohesion and lack of crack. The surface tension of the FX-C sol was determined to be equal to 30 ± 2 mN/m.

The FTIR spectra of the FX-C are illustrated in **Figure 2**. They reveal the effective co-polymerization of PDMS with TEOS, as well as the successful synthesis and incorporation of CaOx in the silica network.

In **Figure 2**, the FTIR spectrum (A) of solution A1 shows that CaOx was formed after the reaction of CH and Ox. In
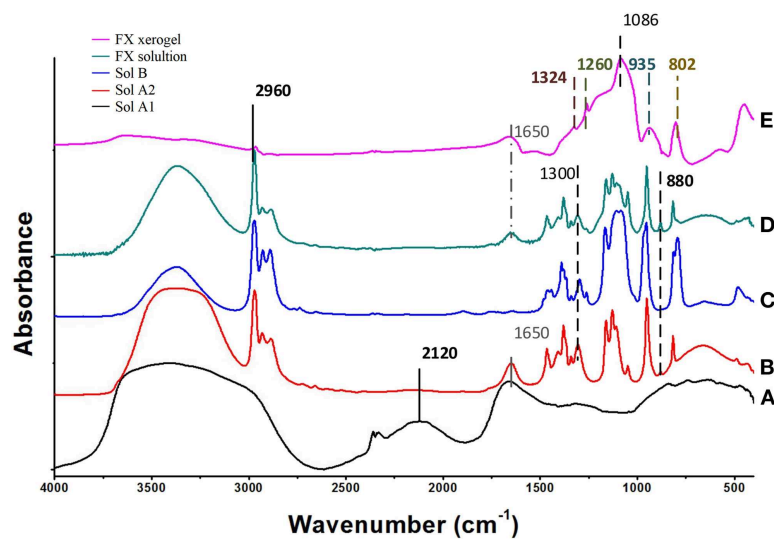
FIGURE 2 | FTIR spectra of the initial sols: (A) A1 (CH + H$_2$O + Ox), (B) A2 (ISP+TEOS) mixed with A1, (C) (TEOS+PDMS+ISP), (D) the derived FX-sol, and (E) the xerogel FX-C.
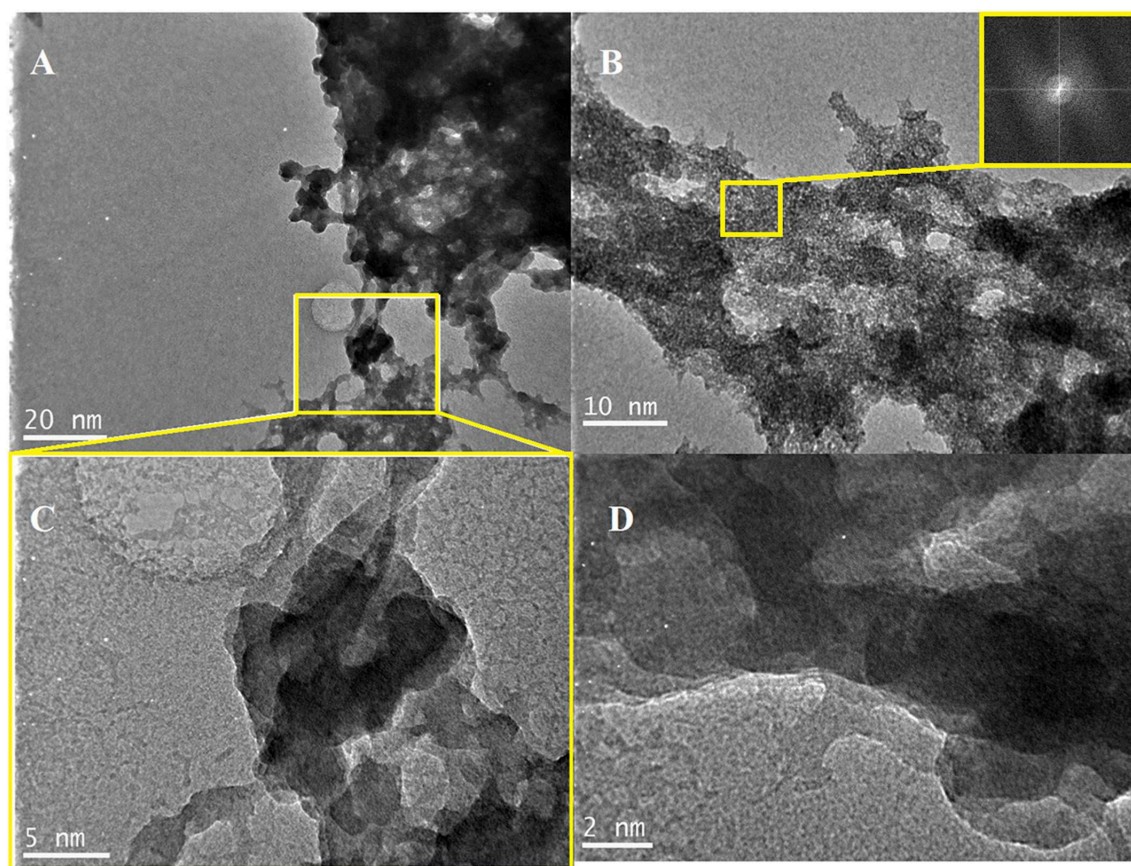

FIGURE 3 | TEM images of the produced consolidant: **(A,B,D)** images captured from random areas of the consolidant surface, **(C)** magnified image of the area selected at **(A)**.
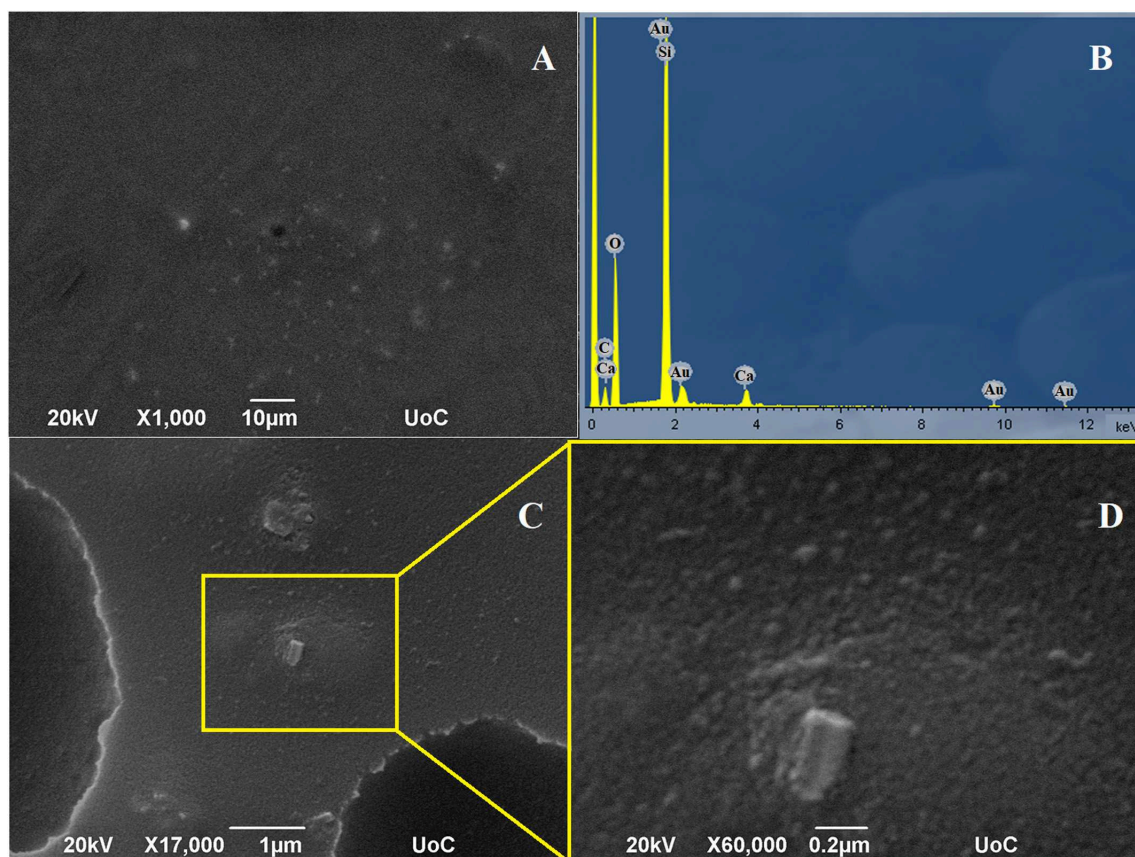
FIGURE 4 | SEM images of FX-C and EDS analysis: **(A,C)** images captured from random areas of the consolidant, **(D)** magnified image of the area selected at **(C)** and **(B)** EDS results.

particular, the bands identified at 1,324 and partially at 1,650 cm^{-1}, are associated with the O-C-O symmetric and anti-symmetric stretching of CaOx, respectively (Maravelaki et al., 2014; Lin et al., 2019). The band located at 1,650 cm^{-1} overlaps with the absorbed water bending vibration. The stretching bands of CaOx are shown both in spectra of FX solution (E) and xerogel (D). In addition, the absence of the characteristic and very sharp absorption band of portlandite [CH: $Ca(OH)_2$] at 3,640 cm^{-1} (spectrum A), indicates a consumption of CH, attributed to calcium isopropoxide transformation and reaction with Ox to yield CaOx (Verganelaki et al., 2015).

In the FTIR spectrum (B) of solution A2, a small band at 880 cm^{-1} is assigned to EtOH, which is produced from the hydrolysis of TEOS. After the mixing of A1 and A2 sols, FTIR bands of PDMS are observed at 2,960, 1,260, and 800 cm^{-1}. These bands correspond to antisymmetric stretching C-H bond in CH_3, the symmetric bending of the CH_3 groups in Si -(CH_3) and rocking -CH_3 of PDMS molecules, respectively (spectrum C) (Kapridaki and Maravelaki-Kalaitzaki, 2013). The same bands are shown in FTIR of FX xerogel and FX sol (E, D), indicating the existence of PDMS to the final product. In addition, two strong infrared bands are present at 1,086 and 802 cm^{-1}, which are assigned to the Si–O–Si antisymmetric and symmetric stretching vibrations, respectively. The FTIR spectrum of FX solution is
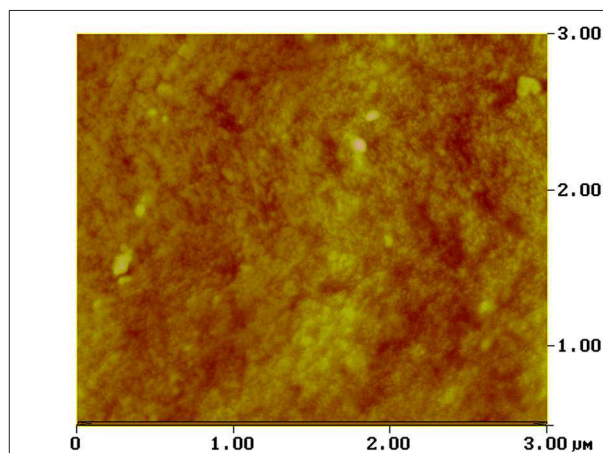

FIGURE 5 | AFM image of the FX-C xerogel.

more complicated, due to the overlapping of ISP, TEOS, and ethanol bands.

FTIR spectra indicate the acid catalysis of TEOS by Ox. Indeed, the role of Ox is dual; firstly to allow the catalysis of TEOS and secondly to react with CH and to produce CaOx. The

silica network is determined by the Si-O-Si formation at 1,086 and 802 cm^{-1}, attributed to the antisymmetric and symmetric stretching of Si-O-Si groups, respectively. Furthermore, the band at 935 cm^{-1} is assigned to overlapping of the newly-formed Si-O-Si bonds between Si-OH groups of hydrolyzed TEOS, the unpolymerized parts of the silica matrix and the silanol groups of PDMS.

The morphological profile of FX-C was inspected by transmission electron microscopy (**Figure 3**). TEM images exhibit FX-C nanocomposite to be present in an aggregated form, finding that can be explained by the polymeric chain modification due to the CaOx and PDMS incorporation from electrostatic interaction and hydrogen bonding. TEM images displayed two phases; the first covered a large area of the FX-C consisted of amorphous SiO$_2$, whereas the second one involved a semi-crystalline structure of the nanocomposite in the nanoscale. The semi-crystallinity of FX-C was confirmed by the characteristic pattern evidenced at the images captured with high magnification (**Figure 3B**). In addition, small dots are exhibited that are darker than the surrounding ones, as it is displayed in the images with the higher magnification. This appearance could be attributed to the nucleation seeds or crystal-like seeds. Another characteristic is the existence of dark and bright areas that could be attributed to different thickness produced by the PDMS and Ca^{2+} modification of the matrix.

Figure 4 shows the SEM micrographs of FX-C xerogel. A crack-free and roughed surface is displayed in the SEM images. The absence of cracking and micro-cracking is significant.

Different magnifications were received to inspect the surface morphology. The surface appeared to be considerably rough, as bumps and cavities were observed, due to TEOS and PDMS copolymerization process. The microstructure presented in **Figure 4C** which is presented with high magnification in **Figure 4D**, was identified as mainly silicon based, by EDS (**Figure 4B**). However, in other areas, as those indicated in the rectangular, Ca was also identified attributed to CaOx incorporated in the silica matrix. The elemental composition by EDS measurements (**Figure 4B**) confirmed the existence of calcium and silicon elements, related to CaOx and polymerized TEOS-PDMS, respectively. The appearance of the characteristic peaks of gold is due to the sputtering process, as this element was used to create a conductive layer. The results of SEM-EDS performed in the FX-C xerogel and presented in EDS Analysis section of the **Supplementary Material**, compared favorably with the derived EDXRF values for the Ca/Si ratio equal to 0.08.

It is well-known that the degree of the hydrophobicity of the materials increases with the surface roughness. AFM measurements were performed in order to provide the depth field and morphological analysis of FX-C surface (**Figure 5**). Pseudocolors were used to explain the surface, with more bright colors to correspond to the most elevated features of the image, while the darker represent the deepest ones. In particular, the patchy areas are exhibited with light yellow or brown color, depending on the dynamic range of the surface topography. The surface displays variation in the topography image, thus indicating remarkable roughness.

TABLE 2 | Correlation of the uptake and dry matter of the FX-C treated samples along with the porosity and average pore diameter of their untreated counterparts.

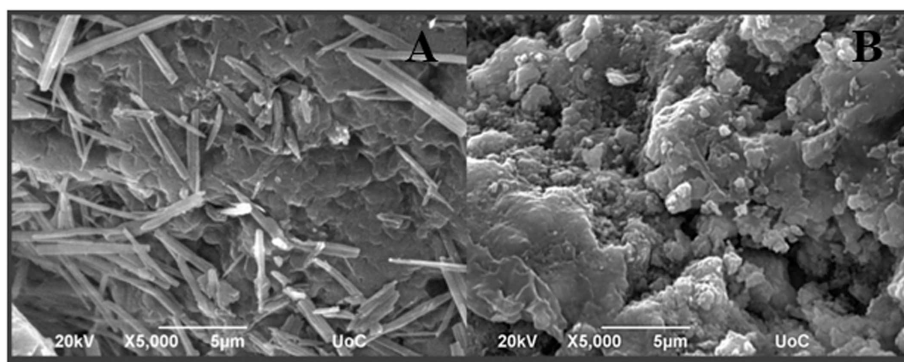| Treated samples	Uptake (g/cm^2) 10^{-3}	Dry matter (g/cm^2*) 10^{-3}	Porosity* (%)	Average Pore* diameter (μm)
Sound	6.00 ± 0.40	2.40 ± 0.16	11.98	0.031
Non-standard	12.50 ± 0.78	3.60 ± 0.06	13.21	0.038
Freeze-thaw	25.91 ± 1.85	12.44 ± 5.67	14.55	0.063
Carbonation	3.14 ± 1.26	1.26 ± 0.49	10.00	0.037
Chloride attack	13.25 ± 6.44	5.70 ± 2.77	11.89	0.034

*Untreated samples.

FIGURE 6 | SEM micrographs of **(A)** untreated freeze-thaw cement mortars and **(B)** freeze-thaw cement mortars treated with FX-C.

The reference plane divides the whole image area vertically, into two equal parts. The AFM image of FX-C shows a highly heterogeneous surface with patchy areas. The arithmetic mean of the roughness (Ra) and the square root (Rq) were estimated to 3.369 and 4.342 nm, respectively. These values of roughness are higher than the corresponding ones of traditional consolidants, showing a remarkable surface roughness, achieved by the described synthetic route (Petronella et al., 2018).

The Thermogravimetry/Differential Thermal Analysis (TG/DTA) curves of FX-C and synthesized CaOx nanoparticles (see **Figure S1**) show three endothermic peaks, which correspond to the thermal decomposition of CaOx.

Evaluation of the Consolidation Performance

The amount of the FX-C that was absorbed by the treated surfaces of sound and aged samples is presented in **Table 2**. Uptake varies according to the porosity of each investigated sample group. High amount of the consolidant was absorbed by the chloride attacked samples, non-standard and aged via freeze-thaw cycles, which is correlated with their higher total porosity and average pore size diameter. However, as we expected, the carbonated samples absorbed lower quantity than the sound mortars, due to their lower total porosity. Portlandite, as a consequence of the carbonation process, reacts with the CO_2 precipitating $CaCO_3$, which in turn filled the pores and makes the sol penetration in the substrate difficult.

The different dry matter of the treated substrates is in direct relationship with the values of the open porosity as presented in **Table 2**.

Textural Properties

Figure 6 illustrates the SEM micrographs of freeze-thaw cement samples (**Figure 6A**) and their treated with FX-C counterparts (**Figure 6B**). The untreated cement sample exhibits cement hydration crystals in needle-like or rod-like shape. The needle-like crystals resemble ettringite crystals formed in aged cement samples under sulfate attack. However, as it can be clearly seen, the treated sample is characterized by the absence of needle-like crystals and deposition of FX-C on the CSH phases, concentrated at the boundaries of grains without blocking the pores, thus contributing to the enhancement of the consolidation efficiency. The extended network of FX-C displays a remarkable coverage capability of cement rods. It seems that between the CSH of cement and the modified-TEOS with CaOx and PDMS a network was formed giving rise to a denser microstructure which binds the grains more firmly.
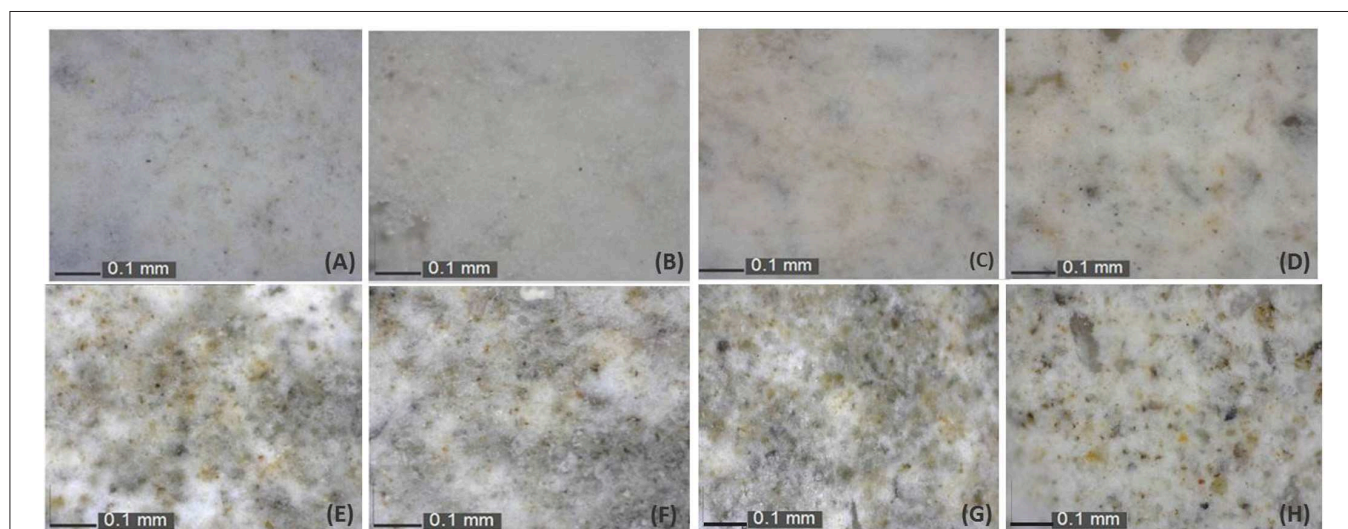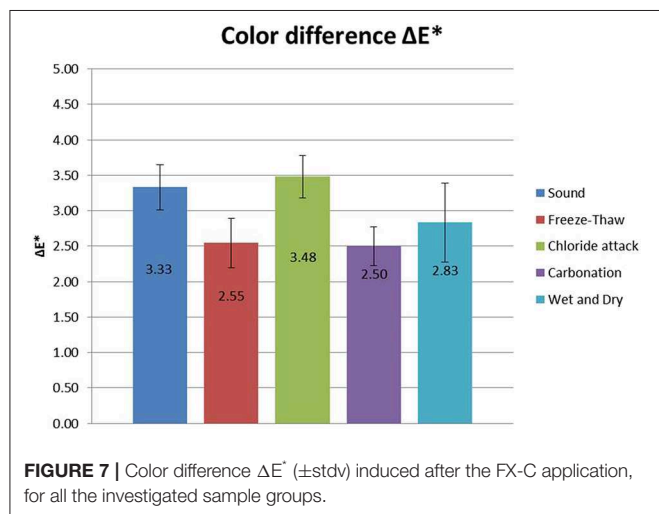

FIGURE 7 | Color difference ΔE^* ($\pm$stdv) induced after the FX-C application, for all the investigated sample groups.

FIGURE 8 | Optical microscope images captured before **(A,C,E,G)** and after **(B,D,F,H)** samples treatment with FX-C for: sound **(A,B)**, freeze-thaw **(C,D)**, carbonated **(E,F)**, and chloride-attacked **(G,H)** aged mortars.
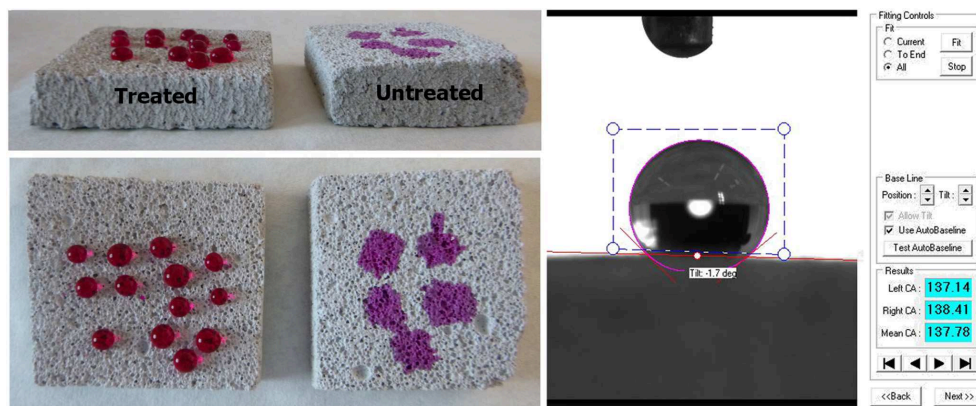
FIGURE 9 | WCA of a treated sound sample.

Aesthetic Parameters

The color changes induced after the FX-C application at the mortar surfaces were measured and are expressed as variations of ΔE^* (**Figure 7**). Taking into account that the general accepted threshold value for ΔE^* is equal to 5 (De Rosario et al., 2015; Ksinopoulou et al., 2016), the obtained values for the treated samples, are lower than the accepted limit.

The results of the application of the consolidant revealed that for the freeze-thaw and carbonated samples, the color change induced was insignificant. Although, sound and chloride attacked samples slightly surpassed this level, they still remained under the commonly accepted threshold for ΔE^* (equal to 5) (**Figure 7**).

The optical microscopy images of treated samples with FX-C are illustrated in **Figure 8**. The treated samples seem to be aesthetically similar to their untreated counterparts, having almost no alterations onto their surfaces. The magnified images reveal no cracking at the treated surfaces that is probably attributed to the PDMS low surface energy and the consequent prevention of TEOS cracking.

Water Repellency

Water Contact Angle (WCA) tests on sound cement samples presented in **Figure 9**, revealed that FX-C created a hydrophobic layer on the surface. WCA measurements were carried out in all of the sample groups treated with FX-C, and the corresponding bar diagram is presented in **Figure S5**. The WCA values of the treated samples ranged from 90 to 100 (°) exhibiting a considerable increase comparing to their untreated counterparts (**Figure S5**).

Water repellency also seems to be successfully improved, as assessed by the capillary absorption test. More specifically, the water absorption by capillary coefficient (WAC) illustrated in **Table 3** has significantly decreased especially in the aged samples, proving that FX-C penetrated into the pore system of the substrate, thus protecting against the action of water.

Mechanical Properties

The improvement of the mechanical behavior of the samples was studied in a non-destructive way by measuring the ultrasound

TABLE 3 | Water absorption by capillarity (WAC) coefficient of untreated and treated sound and aged samples measured in $kg/m^2 {*}s^{1/2}$.

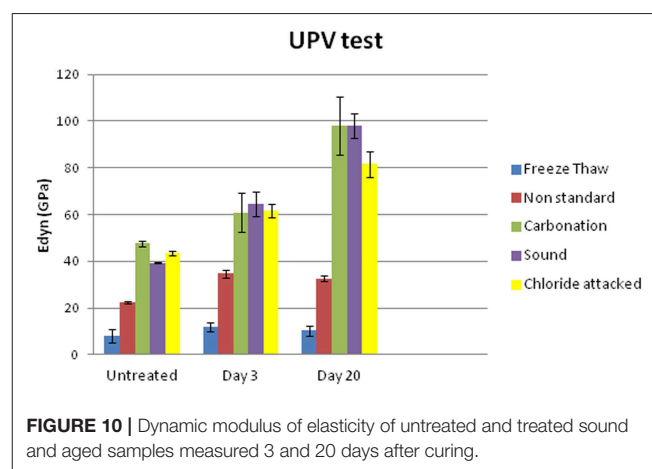| Set	Untreated (*10^{-3})	Treated (*10^{-3})	% Reduction of coefficient
Sound	18.6 ± 1.1	17.9 ± 0.6	3.76
Chloride attack	25.0 ± 5.0	15.2 ± 2.7	39.30
Freeze thaw	34.8 ± 2.3	30.0 ± 5.2	13.79
Carbonated	5.5 ± 1.0	4.4 ± 0.7	20.00

FIGURE 10 | Dynamic modulus of elasticity of untreated and treated sound and aged samples measured 3 and 20 days after curing.

pulse velocity (UPV), so that it could be inspected in a comparable procedure on site. Dynamic modulus of elasticity (E_{dyn}) has increased after the treatment for all sample sets of aging as illustrated in **Figure 10**, proving that FX-C achieved to re-aggregate the mortar microstructure.

Comparing the results of UPV test with the uptake of the product previously shown in **Table 2**, it is remarkable that freeze thaw aged samples, despite the high uptake of FX-C,
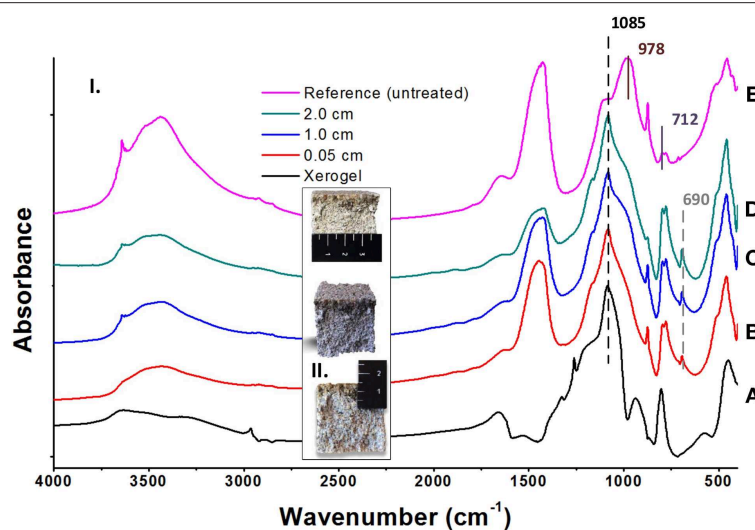
FIGURE 11 | Estimation of the FX-C penetration depth: (I) FTIR spectra of pure xerogel (A), cross-sections of treated depth from the surface (B: 0.05 cm, C: 1.0 cm, and D: 2.0 cm) and untreated (E) OPC mortar specimens; (II) Images of the cross-sections showing the penetration depth of the consolidant.

maintained the lowest values of E_{dyn} even after treatment. This could be explained by the high open porosity of samples indicated by the WAC coefficients shown in **Table 3**. Untreated samples from freeze thaw set exhibited the highest WAC coefficient, equal to 34.8 ± 2.3 kg/m^2∗s$^{1/2}$, which was reduced by 13.79% after treatment, thus maintaining a pore system that partially filled with consolidant, therefore, this was also reflected to the lowest E_{dyn} values comparing with the other samples.

Adhesion of the Treatment
Peeling test revealed almost insignificant removal of the FX-C for all the treated sample groups. This means that a good cohesion with the substrate was achieved, as no retained quantity was found onto the scotch tape after treatment. More specifically, concerning the treated, freeze-thaw and non-standard mortars an important reduction of the removal substrate was observed. The good adhesion of treatment to the mortar surface involved improvement of mechanical properties and water repellency.

Penetration Depth
In order to evaluate the penetration depth of the consolidant, FTIR spectra were collected before and after treatment of a non-standard sample. In particular, powders originating from the surface layer of the untreated sample and from different depths from the surface of a cross section of the same treated sample were examined (see **Figure 11**). These spectra were compared with the spectrum of the FX-C xerogel. The appearance of the xerogel characteristic peak at 1,085 cm^{-1} owed to the Si-O-Si formation, was considered indicative of the consolidant presence. Consequently, the penetration depth of the FX-C seems to be more than 2 cm, after the consolidation process (spectrum D of the **Figure 11**). This is a significant indication of the FX-C penetration depth and the successful treatment of the

mortars. Deconvolution process of the above spectra is included in **Supplementary Material** evidencing that the band at 1,085 cm^{-1} refers to the Si-O-Si of the xerogel and does not appear to the untreated sample.

CONCLUSIONS

A monolithic, non-toxic hydrophobic consolidant, namely FX-C, has been developed in an eco-friendly, one-pot procedure, incorporating to TEOS, PDMS, and nano calcium oxalate. CaOx displays a key role, due to its chemical affinity with the carbonate fragments which exist as aggregates in the concrete. Furthermore, FX-C, due to silica network and CaOx exhibited significant affinity to both siliceous and carbonate nature substrates, such as concrete and cement mortars. The derived product penetrated at least 2 cm into the cement mortar substrate affecting positively its mechanical properties, such as dynamic modulus of elasticity. Water repellency of the treated samples was particularly improved as indicated from WCA measurements and water absorption tests by capillarity. Absorption coefficients decreased 3–75% for sound and aged samples, respectively, and WCA was more than 90° at the treated samples. The treatment didn't alter the color of the surfaces and adhered well, as proved by the peeling test. Finally the absence of harmful byproducts after treatment established FX-C as a powerful consolidant for strengthening and protecting concrete structures.

DATA AVAILABILITY STATEMENT

All datasets generated for this study are included in the article/**Supplementary Material**.

AUTHOR CONTRIBUTIONS

KK, EV, and DS designed, performed the experiments, analyzed the experimental data, and collaborated in the writing of the paper. AF, GA, and IA carried out the experiments. IG-L and MB-V manufactured the OPC samples, carried out experiments, and reviewed the paper. PM conceived and designed the research, supervised the research activities, analyzed the experimental data, and wrote the paper.

FUNDING

ACKNOWLEDGMENTS

SUPPLEMENTARY MATERIAL

The Supplementary Material for this article can be found online at: https://www.frontiersin.org/articles/10.3389/fmats.2020.00016/full#supplementary-material

REFERENCES

Baglioni, P., Chelazzi, D., Giorgi, R., and Poggi, G. (2013). Colloid and materials science for the conservation of cultural heritage: cleaning, consolidation and deacidification. *Langmuir* 29, 5110–5122. doi: 10.1021/la304456n

Barberena-Fernández, A. M., Blanco-Varela, M. T., and Carmona-Quiroga, P. M. (2018). Use of nanosilica- or nanolime-additioned TEOS to consolidate cementitious materials in heritage structures: physical and mechanical properties of mortars. *Cement Concrete Composites* 95, 42–55. doi: 10.1016/j.cemconcomp.2018.09.011

Barberena-Fernández, A. M., Carmona-Quiroga, P. M., and Blanco-Varela, M. T. (2015). Interaction of TEOS with cementitious materials: chemical and physical effects. *Cement Concrete Composites* 55, 145–152. doi: 10.1016/j.cemconcomp.2014.09.010

Berry, J. D., Neeson, M. J., Dagastine, R. R., Chan, D. Y. C., and Tabor, R. F. (2015). Measurement of surface and interfacial tension using pendant drop tensiometry. *J. Colloid Interface Sci.* 454, 226–237. doi: 10.1016/j.jcis.2015.05.012

De Rosario, I., Elhaddad, F., Pan, A., Benavides, R., Rivas, T., and Mosquera, M. J. (2015). Effectiveness of a novel consolidant on granite: laboratory and *in situ* results. *Constr. Build. Mater.* 76, 140–149. doi: 10.1016/j.conbuildmat.2014.11.055

Facio, D. S., Carrascosa, L. A. M., and Mosquera, M. J. (2017). Producing lasting amphiphobic building surfaces with self-cleaning properties. *Nanotechnology* 28:265601. doi: 10.1088/1361-6528/aa73a3

Franzoni, E., Graziani, G., Sassoni, E., Bacilieri, G., Griffa, M., and Lura, P. (2014). Solvent-based ethyl silicate for stone consolidation: influence of the application technique on penetration depth, efficacy and pore occlusion. *Mater. Struct.* 48, 3503–3515. doi: 10.1617/s11527-014-0417-1

Illescas, J. F., and Mosquera, M. J. (2012). Producing surfactant-synthesized nanomaterials *in situ* on a building substrate, without volatile organic compounds. *ACS Appl. Mater. Interfaces* 4, 4259–4269. doi: 10.1021/am300964q

Ion, R. M., Teodorescu, S., Stirbescu, R. M., Bucurică, I. A., Dulamă, I. D., and Ion, M. L. (2017). Calcium oxalate on limestone surface of heritage buildings. *Key Eng. Mater.* 750, 129–134. doi: 10.4028/www.scientific.net/KEM.750.129

Kapridaki, C., and Maravelaki-Kalaitzaki, P. (2013). TiO2–SiO2–PDMS nano-composite hydrophobic coating with self-cleaning properties for marble protection. *Prog. Org. Coatings* 76, 400–410. doi: 10.1016/j.porgcoat.2012.10.006

Karapanagiotis, I., Pavlou, A., Manoudis, P. N., and Aifantis, K. E. (2014). Water repellent ORMOSIL films for the protection of stone and other materials. *Mater. Lett.* 131, 276–279. doi: 10.1016/j.matlet.2014.05.163

Ksinopoulou, E., Bakolas, A., and Moropoulou, A. (2016). Modifying Si-based consolidants through the addition of colloidal nano-particles. *Appl. Phys. A* 122:267. doi: 10.1007/s00339-016-9772-9

Lin, M.-H., Song, Y.-L., Lo, P.-A., Hsu, C.-Y., Lin, A. T. L., Huang, E. Y.-H., et al. (2019). Quantitative analysis of calcium oxalate hydrate urinary stones using FTIR and 950/912 cm^{-1} peak ratio. *Vibrational Spectrosc.* 102, 85–90. doi: 10.1016/j.vibspec.2019.03.006

Lollino, G., Giordan, D., Marunteanu, C., Christaras, B., Yoshinori, I., and Margottini, C. (2015). *Engineering Geology for Society and Territory – Volume 8.* Cham: Springer International Publishing.

Maravelaki, N., Verganelaki, A., Kilikoglou, V., and Karatasios, I. (2014). Synthesis and characterization of a calcium oxalate-silica nanocomposite for stone conservation. *Eng. Geol. Soc. Territory* 8, 525–529. doi: 10.1007/978-3-319-09408-3_93

Maravelaki-Kalaitzaki, P., Kallithrakas-Kontos, N., Korakaki, D., Agioutantis, Z., and Maurigiannakis, S. (2006). Evaluation of silicon-based strengthening agents on porous limestones. *Prog. Org. Coat.* 57, 140–148. doi: 10.1016/j.porgcoat.2006.08.007

Miliani, C., Velo-Simpson, M. L., and Scherer, G. W. (2007). Particle-modified consolidants: a study on the effect of particles on sol–gel properties and consolidation effectiveness. *J. Cult. Herit.* 8, 1–6. doi: 10.1016/j.culher.2006.10.002

Moropoulou, A., Cakmak, A., Labropoulos, K. C., Van Grieken, R., and Torfs, K. (2004). Accelerated microstructural evolution of a calcium-silicate-hydrate (C-S-H) phase in pozzolanic pastes using fine siliceous sources: comparison with historic pozzolanic mortars. *Cement Concrete Res.* 34, 1–6. doi: 10.1016/S0008-8846(03)00187-X

Mosquera, M. J., de los Santos, D. M., and Rivas, T. (2010). Surfactant-synthesized ormosils with application to stone restoration. *Langmuir* 26, 6737–6745. doi: 10.1021/la9040979

Pan, X., Shi, Z., Shi, C., Ling, T.-C., and Li, N. (2017). A review on surface treatment for concrete – part 2: performance. *Constr. Build. Mater.* 133, 81–90. doi: 10.1016/j.conbuildmat.2016.11.128

Petronella, F., Pagliarulo, A., Truppi, A., Lettieri, M., Masieri, M., Calia, A., et al. (2018). TiO2 nanocrystal based coatings for the protection of architectural stone: the effect of solvents in the spray-coating application for a self-cleaning surfaces. *Coatings* 8:356. doi: 10.3390/coatings8100356

Pigino, B., Leemann, A., Franzoni, E., and Lura, P. (2012). Ethyl silicate for surface treatment of concrete – part II: characteristics and performance. *Cement Concrete Composites* 34, 313–321. doi: 10.1016/j.cemconcomp.2011.11.021

Pinho, L., Elhaddad, F., Facio, D. S., and Mosquera, M. J. (2013). A novel TiO2–SiO2 nanocomposite converts a very friable stone into a self-cleaning building material. *Appl. Surface Sci.* 275, 389–396. doi: 10.1016/j.apsusc.2012.10.142

Rodriguez-Navarro, C., Suzuki, A., and Ruiz-Agudo, E. (2013). Alcohol dispersions of calcium hydroxide nanoparticles for stone conservation. *Langmuir*, 29, 11457–11470. doi: 10.1021/la4017728

Ruffolo, S. A., and La Russa, M. F. (2019). Nanostructured coatings for stone protection: an overview. *Front. Mater.* 6:147. doi: 10.3389/fmats.2019.00147

Sandrolini, F., Franzoni, E., and Pigino, B. (2012). Ethyl silicate for surface treatment of concrete – part I: pozzolanic effect of ethyl silicate. *Cement Concrete Composites* 34, 306–312. doi: 10.1016/j.cemconcomp.2011.12.003

Scherer, G. W., and Wheeler, G. S. (2009). Silicate consolidants for stone. *Key Eng. Mater.* 391, 1–25. doi: 10.4028/www.scientific.net/KEM.391.1

Schutter, G.D. (2012). *Damages to Concrete Structures*, Boca Raton, FL; London; New York, NY: CRC Press, Taylor & Francis Group.

Son, S., Won, J., Kim, J. J., Jang, Y. D., Kang, Y. S., and Kim, S. D. (2009). Organic-Inorganic hybrid compounds containing polyhedral oligomeric silsesquioxane for conservation of stone heritage. *ACS Appl. Mater. Interfaces* 1, 393–401. doi: 10.1021/am800105t

Verganelaki, A., Kapridaki, C., and Maravelaki-Kalaitzaki, P. (2015). Modified tetraethoxysilane with nanocalcium oxalate in one-pot synthesis for protection of building materials. *Ind. Eng. Chem. Res.* 54, 7195–7206. doi: 10.1021/acs.iecr.5b00247

Verganelaki, A., Kilikoglou, V., Karatasios, I., and Maravelaki-Kalaitzaki, P. (2014). A biomimetic approach to strengthen and protect construction materials with a novel calcium-oxalate–silica nanocomposite. *Constr. Build. Mater.* 62, 8–17. doi: 10.1016/j.conbuildmat.2014.01.079

Effects of the Ionizing Radiation Disinfection Treatment on Historical Leather

Monia Vadrucci[1]*, Giovanni De Bellis[2,3], Claudia Mazzuca[4], Fulvio Mercuri[5], Fabio Borgognoni[1], Emily Schifano[6], Daniela Uccelletti[3,6] and Cristina Cicero[2,3]

[1] Particle Accelerator for Medical Application Laboratory, Italian National Agency for New Technologies, Energy and Sustainable Economic Development (ENEA), Rome, Italy, [2] Department of Astronautical, Electrical and Energy Engineering (DIAEE), Sapienza University of Rome, Rome, Italy, [3] Research Center for Nanotechnology Applied to Engineering (CNIS), Rome, Italy, [4] Department of Chemical Sciences and Technologies, Tor Vergata University of Rome, Rome, Italy, [5] Department of Industrial Engineering, Tor Vergata University of Rome, Rome, Italy, [6] Department of Biology and Biotechnology "C. Darwin," Sapienza University of Rome, Rome, Italy

Microorganisms often cause significant damage on historical objects. The archive or library materials as well as textile or leather artifacts suffer serious attacks that need appropriate care treatments. Several biocide processes have been implemented but often their application does not preserve the material of the good. The objective of this work is the disinfection through ionizing radiation of leather wallpaper from the museum building Palazzo Chigi in Ariccia (Rome, Italy). The controlled sterilization treatments were carried out using X-ray beams to eliminate the microorganisms present on the leather and maintaining unchanged the properties of the constituent material. Some fragments of decorated leather wallpaper, dating back to the 1700s, were irradiated with X-rays up to 5,000 Gy. The amount of microorganisms was evaluated by microbiological analysis before and after X-ray irradiation treatments to identify the dose that inhibits the bacterial load. It will be shown how the results obtained by the application of different chemical-physical techniques (Scanning Electron Microscopy, Fourier Transform Infrared spectroscopy and Light Transmission Analysis) have helped in the evaluation of the impact of the X-rays on leather chemical and physical integrity.

Keywords: leather, bio-deterioration, antimicrobial, X-ray, SEM, FTIR-ATR, LTA, cultural heritage

INTRODUCTION

The *Palazzo Chigi* of Ariccia (Rome) is an ancient residence of princes having the rooms enriched and decorated with precious seventeenth-century leather products: worked and printed leather with decorative motifs used in the form of panels for furnishing. The wallpapers in impressed leather are commonly called "cordovani," from the manufacturing arts imported to Cordoba, Spain, from the east. These wallpapers still cover the walls of many rooms of the building and are a unique case in this genre (Petrucci, 2014). The whole covered rooms of the *Palazzo Chigi* and the numerous fragmented and incomplete wallpapers preserved in their archives could constitute a real "leather museum" (with pieces that can also be traced back to different types of use: table covers, for "dresser beds," chair covers, valances, hat covers, etc.).

The realization of leather wallpapers dates back to ancient times and had a slow decline during the eighteenth century (replaced by fabrics and then printed papers): at the end of the century it seems that laboratories were active only in Barcelona, Mechelen, Venice, and Amsterdam (Contadini, 1989).

As most of the collagen-based artifacts, leather is frequently involved in bio-deterioration caused by microorganisms (Strzelczyk et al., 1989). The non-adequate environmental conditions of artifacts conservation constitute a crucial factor in the promotion and development of the bio-deterioration favored, in particular, by altered values of temperature and/or relative humidity (Strzelczyk et al., 1987, 1997; Montanari et al., 2012). The bio-deteriorating agents can cause structural and chromatic alterations inducing hydrolysis of the collagen fibers, modifying the leather's inorganic components, producing pigments, and organic acids causing chromatic alteration or discolouration of the support (Pinzari et al., 2012; Piñar et al., 2015a,b; Cicero et al., 2018; Mercuri et al., 2018). In some cases, they induce the crack and the partial detachments of the surface layers (Migliore et al., 2017, 2019).

High energy irradiation is a powerful tool for disinfection: archived and retained artifacts can be attacked and destroyed by microorganisms but they can be successfully treated in irradiation facilities, conventionally made with Co-60 gamma-ray sources (Adamo et al., 1998, 2001; Magaudda, 2004; da Silva et al., 2006; D'Almeida et al., 2009; Nunes et al., 2012; Sendrea et al., 2015, 2017).

Recently, the possibility to employ the X-rays to inhibit the microbial growth on bio-deteriorated parchment artifacts has been presented (Vadrucci et al., 2019a). The encouraging results obtained on this kind of collagenous material are due to the possibility to operate with a minimal intervention, the non-contact method and to reach the inside of 3-dimension items, by the high penetration power of the beams. All that suggests the possibility that X-ray irradiation treatment could be employed as a sterilization method more efficacious in terms of germicidal power, lowering of exposition time, better preservation of the substrate and less interference of the environment (powder, humiditiy) also in the case of the historical leather coming from the *Palazzo Chigi* of Ariccia.

Within the ADAMO project (developed thanks to the Excellence's Center of the Technological District for Culture (DTC) of Regione Lazio), it has been possible to perform biodeteriogens removal campaigns by the use of X-ray irradiation as efficacious, non-toxic and non-invasive system to inhibit bio-degradation and, at the same time, to make the characterization of the chromatic richness (Fantoni et al., 2019; Iorio et al., 2019; Vadrucci et al., 2019b).

The developed analytical methodology will be presented and discussed. The use of the nuclear technique for the bacterial growth inhibition on historical artcraft employing low dose levels, the use of microbiology procedures to control biodeteriogens and the use of surface and bulk physical analysis for material monitoring and characterization will be described in order to test the applicability of the irradiation treatment on these historical leathers.

Fragments of leather wall coverings were subjected to X-ray irradiation that inhibits bacterial growth at doses lower than 1 kGy which did not affect the characteristics of the substrate, as shown by the physical analysis carried out for material monitoring.

MATERIALS AND METHODS

Artifacts Description

The leather wallpapers in the *Palazzo Chigi* have been designed to furnish the home. They have been made with "green and gold," "red and gold," "red, green," and "gold and silver" decorations, showing patterns from the Renaissance tradition in the Venetian manner, or embossed in the Dutch manner.

Many fragments of the leather panels are widespread on the antiquarian market and others are preserved in the warehouse halls where restoration laboratories were set up. Some of the pieces not worked by the restorers were made available for this work. They were all placed together in shelves not exposed to the sun but certainly not in optimal storage conditions.

The dimensions of the fragments that were the object of our research were a few tens of cm^2.

Isolation and Characterization of Bacterial Strains

Bacteria from the leather samples were collected using sterile cotton swabs and then placed in sterile tube containing 2 mL of Nutrient Broth (NB) and finally incubated in laboratory at 30°C for 24 h. The collected samples were then plated on NB agar plates and, after further incubation at 30°C for 24 h, morphologically different colonies were purified.

DNA was extracted and amplified according to Bergkessel and Guthrie (2013). A region of about 1,400 bp from the 16S rRNA gene was amplified using the primers F8 (5′-AGAGTTTGATCCTGGCTCAG-3′) and R1492 (5′-GGTTACCTTGTTACGACTT-3′). The PCR reaction was performed utilizing the Taq DNA polymerase from Accuzyme DNA Polymerase (Bioline). BMR Genomics (Padova, Italy) sequenced the amplified region and the obtained sequences were analyzed with BLAST database. Bacterial strains isolated from the leather wallpapers and used in this study were the Gram-positive *Bacillus cereus* (Accession number: MN173590) and the Gram-negative *Massilia timonae* (Accession number: MN173589). They were grown in 2 mL of NB at 30°C overnight.

Antibiotic susceptibility tests were performed according to Schifano et al. (2019). One hundred microliters of overnight cultures of *B. cereus* or *M. timonae* were spread onto NB agar plates, in which the antibiotic discs were placed. The plates were then incubated for 24 h at 30°C. The zones of inhibition were measured from the center of the disc and recorded.

The biofilm formation was evaluated according to Zanni et al. (2017) with some differences: each well was filled with 200 μL of NB broth and *B. cereus* or *M. timonae* (1×10^7 cells/mL) in triplicate. Wells without bacteria were utilized as controls. Next, plates were incubated at 30°C for 24 h and Crystal Violet assay was performed. Absorbance at 600 nm was then measured by using a multiplate reader (Promega, GloMax multi+detection system). The experiment was repeated three times in triplicates.

Preparation of bio-deteriorated leather samples for irradiation treatments is performed cutting 1×1 cm^2 pieces from the original leather fragment, than UV sterilized in both sides and stored in 3.5 cm Petri dishes at room-temperature until the load of bacteria for the irradiation tests (**Figure 1A**).

Irradiation Treatment

The irradiation care treatments were performed using the new REX source capable of emitting MeV energy X-ray beams (Vadrucci et al., 2019c). The REX setup consists of a linear electron accelerator, an irradiation chamber and a removable X-rays/electrons conversion system (**Figures 1B,C**).

The accelerator conditions used for the irradiation treatment were: 3 μs pulse length, 20 Hz repetition rate, and 120 mA output peak current. The X-rays dose and the dose rate measurements were performed by a parallel plate ionization chamber (mod. PPC05 from IBA). The samples were irradiated with different doses as indicated.

Antimicrobial Tests

Microbiological analysis were used to compare the total microbial count of bacteria cells before (untreated control samples, Ctr) and after (treated samples, Tr) the irradiation treatment; each dose was tested on three leathers fragment replicates. Liquid cultures of bacterial cells were spotted on specimens at the concentration of 7×10^3 cells/mL. After the irradiation, the microbes were collected by dipping the leather samples in 2 mL of PBS 1X, shaked for 2 min and spread an aliquot on the NB solid media. Plating was performed in triplicate and the microbial colonies on the plates were counted after 24 h at 25 $\pm$ 2°C. The differences in the colonization rate (in percentage) between untreated control samples and treated samples were statistically investigated by one-way ANOVA analysis with the Bonferroni post-test (GraphPad Prism 4.0 software, $^*p < 0.05$, $^{**}p < 0.01$, and $^{***}p < 0.001$).

Physical Analysis for Material Monitoring

Scanning Electron Microscopy Analysis

Scanning Electron Microscopy (SEM) was employed in order to evaluate morphological changes in the collagen fibers networking.

The microscopic analysis has been performed using a Zeiss Auriga Field Emission SEM (FE-SEM). In order to prevent charging, before each imaging session samples were sputter coated with a 30 nm Cr layer. The images were acquired at an accelerating voltage of 3 keV, using 1 kX and 5 kX magnifications. In order to evaluate the effects of the irradiation treatment on leather, SEM investigations have been performed on both pristine and irradiated specimens (untreated, 750, 1,000, and 5,000 Gy).

Fourier Transform Infrared Spectroscopy Attenuated Total Reflectance

The Fourier Transformed Infrared spectroscopy in the Attenuated Total Reflectance mode (FTIR-ATR) was used as surface technique to monitor the variations in secondary structures of the collagen protein in order to determine the variations induced by the deterioration processes eventually occurring in the sample after being irradiated (Badea et al., 2012).

FTIR absorption spectra were acquired on a Thermo-Scientific (mod. Is50) instrument (Thermo Scientific Inc., Madison WI) in Attenuated Total Reflectance (ATR) mode using
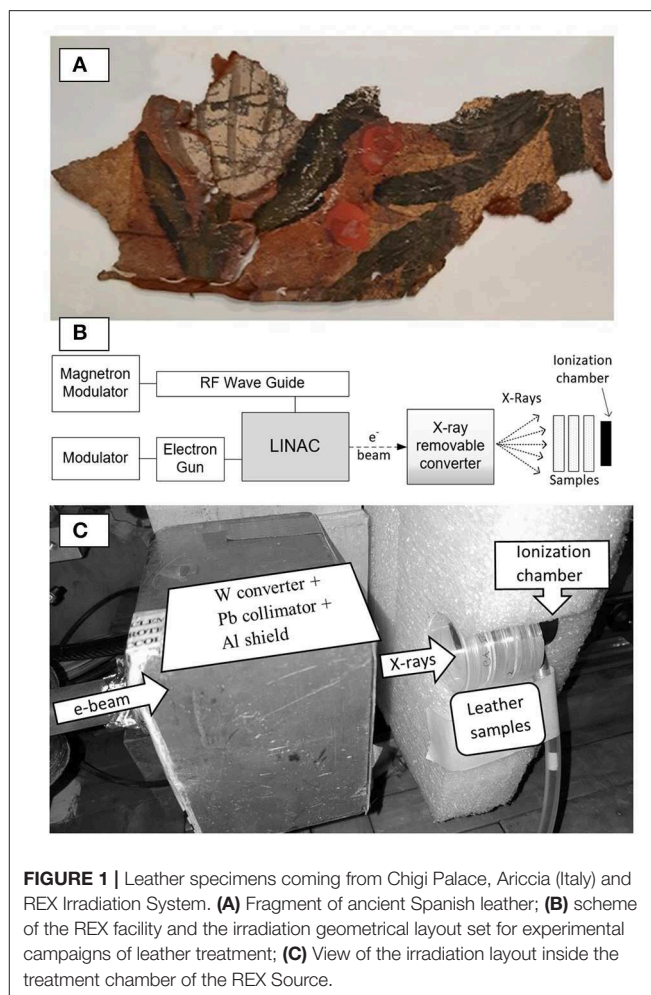
FIGURE 1 | Leather specimens coming from Chigi Palace, Ariccia (Italy) and REX Irradiation System. **(A)** Fragment of ancient Spanish leather; **(B)** scheme of the REX facility and the irradiation geometrical layout set for experimental campaigns of leather treatment; **(C)** View of the irradiation layout inside the treatment chamber of the REX Source.

a one reflection diamond cell, on which the sample was located during the measurement. Spectra were recorded from 4,000 to 750 cm^{-1}, mediating over 32 scans with a resolution of 2 cm^{-1}.

Light Transmission Analysis

The irradiated samples have been investigated also by the Light Transmission Analysis (LTA) (Cicero et al., 2019), as additional bulk analysis of the damage induced by the irradiations on the leather substrate, in order to determine the denaturation temperature, a parameter related to the deterioration degree of the collagenous material (Vadrucci et al., 2019a).

LTA was employed to analyze the hydrothermal denaturation process of the collagen fibers before and after irradiation procedure. The employed experimental configuration allows to characterize the phenomenon both in a qualitative and in a quantitative way enabling the imaging evaluation of the variations induced in the sample during the hydrothermal denaturation and, simultaneously, the recording of the variations of the optical properties of the investigated sample (Mercuri et al., 2016).

RESULTS

In the following, the results obtained on the evaluation of the sterilization technique by X-ray irradiation as an alternative to the use of chemical biocides on historical leather artifacts are presented. The identification and characterization of the bacterial species together with their ability to form biofilms are reported. The data collected on the leather substrates subjected to increasing X-ray doses of the sterilization treatment are shown through the analysis carried out with the techniques presented in the previous paragraph.

Identification and Characterization of Bacterial Strains From Leather Samples

Different bacterial colonies were isolated from leather wallpaper of *Palazzo Chigi* in Ariccia and identified at the molecular level by the amplification of 16S rDNA. Among them, the comparison of the obtained sequences with those held in BLAST database allowed to identify the Gram-positive *Bacillus cereus,* and the Gram-negative *Massilia timonae*, which are involved in bio-deterioration, as reported in many works (Herrera and Videla, 2004; Jroundi et al., 2017). Antibiotic susceptibility test was performed using a panel of 20 antibiotics, including inhibitors of cell wall synthesis, protein synthesis, nucleic acid synthesis, and the results are reported in **Table 1**. The bacterial strains resulted resistant to different types of molecules, with *M. timonae* more resistant than *B. cereus*.

Evaluation of Biofilm Formation

The biodegradation of cultural heritage is mainly caused by the ability of microorganisms to form biofilms (Rivera et al., 2018). Indeed, bacteria can aggregate and adhere to a surface, forming a group of cells producing an extracellular matrix composed of DNA, proteins and polysaccharides. In these biofilms, microorganisms resist to adverse abiotic conditions (Dakal and Cameotra, 2012) and their metabolic activity, such as production of organic and inorganic acids, contributes to decay of different substrates (Scheerer et al., 2009; Sterflinger and Piñar, 2013). The biofilm on plastic surface was quantified after 24 h by Crystal Violet method. The biofilm formation capacity of *B. cereus* is about 80% lower than *M. timonae* (**Figure 2A**).

Since *M. timonae* resulted to be a higher biofilm producer, its capacity of forming biofilm was also evaluated on Spanish leather samples, through SEM analysis. In **Figures 2B,C**, it is possible to observe, as an example, the leather specimen covered by *M. timonae* biofilm. In particular, FE-SEM analysis allowed the observation of *M. timonae* biofilm matrix and, at higher magnification, single cells adhered on the substrate (**Figures 2B,C**, respectively).

Microbiological Tests After Irradiation

After irradiation of leather samples, the percentage of survival microorganisms collected from treated specimens were compared to untreated control sample. When leathers spread with *B. cereus* were irradiated, a bacterial growth reduction

TABLE 1 | Antibiotic susceptibility of *B. cereus* and *M. timonae*.

	B. cereus	*M. timonae*
Vancomycin	1.1 cm	1 cm
Clindamycin	1.5 cm	R
Cefalotin	R	R
Tobramycin	0.7 cm	0.7 cm
Ampicillin	R	R
Cefotaxime	R	R
Chloramphenicol	1.7 cm	0.9 cm
Tetracycline	1.2 cm	1.0 cm
Erythromycin	1.4 cm	0.7 cm
Amikacin	0.8 cm	0.7 cm
Oxacillin	R	R
Fosfomycin	1.2 cm	0.4 cm
Rifampicin	1.0 cm	1.0 cm
Gentamicin	0.6 cm	0.6 cm
Penicillin	0.5 cm	R
Aztreonam	R	R
Carbenicillin	R	R
Mezlocillin	1.2 cm	R
Streptomycin	1.0 cm	0.8 cm
Cefuroxime	R	R

Bacterial strains resulting resistant to antibiotic were referred as R.

of 8, 66, and 84% was observed with 250, 500, and 750 Gy, respectively, as compared to control. The antibacterial activity was highlighted when samples were covered with the Gram-negative *M. timonae* culture and then treated. As the irradiation dose increased, a reduction of the number of cell recovery was obtained: the bacterial growth decreased of 56 and 89% when 250 and 500 Gy treatments were performed. Moreover, the total absence of growth was observed with 750 Gy treatment (**Figures 2D,E**).

SEM Characterization of the Morphological Changes in the Fibers Networking

SEM was employed in order to evaluate morphological changes in the fibers networking. The investigation was performed on all the irradiated samples with the aim of correlating the preservation conditions of the hierarchical structure to the irradiation dose employed in the treatment.

SEM micrographs of the non-irradiated sample (**Figure 3A** and magnification **Figure 3B**) show an intact fibers networking of the collagen, regardless of the long history of the specimen. Long and ordered bundles of fibers can be recognized within the pristine sample revealing, after all, a good preservation condition of the artifact. Comparing the obtained images of the untreated sample with the ones recorded on the leather sample irradiated at 750 Gy (**Figures 3C,D**) and 1,000 Gy (**Figures 3E,F**) dose levels, it is possible to notice that the ordered surface morphology is maintained also in the irradiated samples. Only slight differences can be observed in the sample treated with a dose of 1,000 Gy where some fibers start to shows a disordered structure due
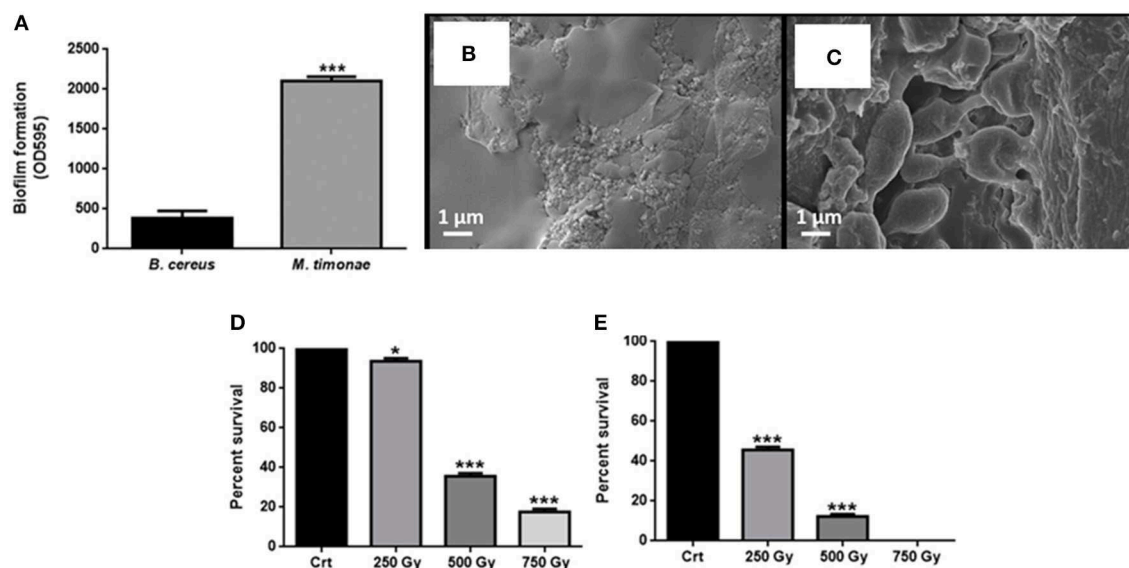
FIGURE 2 | Evaluation of biofilm formation and cell viability after irradiation. **(A)** Biofilm formation capacity of *B. cereus* and *M. timonae* after 24 h of incubation at 30°C. For statistical analysis one-way ANOVA method coupled with the Bonferroni post-test was used (***$p < 0.001$). **(B)** FE-SEM micrograph of *M. timonae* biofilm after 24 h at 30°C, biofilm matrix, **(C)** particular of *M. timonae* cells. **(D,E)** Indicate respectively *B. cereus* and *M. timonae* cells recovered after irradiation. Crt represent the recovery from unexposed samples, set to 100%. To evaluate statistical significance a one-way ANOVA analysis with the Bonferroni post-test was used (*$p < 0.5$. and ***$p < 0.001$ with respect to Crt).

to the effects of a partial unwinding, revealing the onset of a gelatinization process.

Differently, the sample irradiated at the maximum dose of 5,000 Gy shows a completely different surface morphology with respect to the non-irradiated one. The image recorded at low magnification (**Figure 3G**) shows the total lack of the bundled organization of the fibers networking and the presence of areas of gelatinization with the typical melt-like appearance (Badea et al., 2008). At higher magnification (**Figure 3H**), the effect of the irradiation dose is clearly visible in the aspect of the remaining bundles where the ordered fibrillary structure is dramatically lost, the bundle dimension is heavily reduced and the remaining fibers appear frayed and fragmented.

FTIR-ATR Characterization of the Protein Induced Deterioration

FTIR-ATR is one of the most powerful, non-destructive techniques to monitor the changes in secondary structure (due to for example, denaturation) of proteins. The peptide groups are described in IR spectroscopy with nine characteristic bands named amide A, B, and I–VII in order of decreasing frequency (Haris and Chapman, 1995). Among them Amide I and amide II are the two major bands of the protein infrared spectrum; the amide I band falling in 1,680–1,610 cm^{-1} region, is mainly associated with the C=O stretching vibration related to the protein backbone and thus is sensitive to protein conformations and in turn, to water bound to the macromolecule. The amide II results essentially from the N–H bending vibration and from the C–N stretching vibration, and is in the 1,540–1,500 cm^{-1} region, depending

on the conformation adopted by the peptide (Jackson and Mantsch, 1995; Tatulian, 2019). Due to the high sensitivity to conformation, an analysis on the relative intensities and shifts of these two bands furnishes information on the protein denaturation.

Data reported in the **Table 2**, indicates that the intensity of the Amide I band ($I_{Amide\ I}$) decreases significantly after the irradiation treatment with respect to amide II band. This is ascribable to hydrolysis of the collagen present in the leather (Plavan et al., 2010; Vyskočilová et al., 2019). The slight difference between the position of the Amide I and Amide II main peaks, indicates that gelatinization does not occur even after high level treatment. Moreover, a slight increase of the band at about 1,720 cm^{-1}, related to side chain oxided groups, is observed on increasing dose treatment (**Figure 4A**).

LTA Characterization of the Deterioration Degree of Irradiated Leather

As mentioned in the previous paragraphs, the LTA allows to characterize the artificially induced hydrothermal denaturation of collagen-based materials and to determine the so-called denaturation temperature, the temperature at which, heating a fully hydrated specimen, the collagen fibers accomplish their thermal unfolding. When heated under condition of full hydration the collagen fibers lose their hierarchical well-structured arrangement turning into an amorphous one with a gel-like appearance. In a partially deteriorated collagen based material the maximum rate of the denaturation activity is reached at lower temperatures with respect to non-deteriorated and well-structured samples because these partially degraded
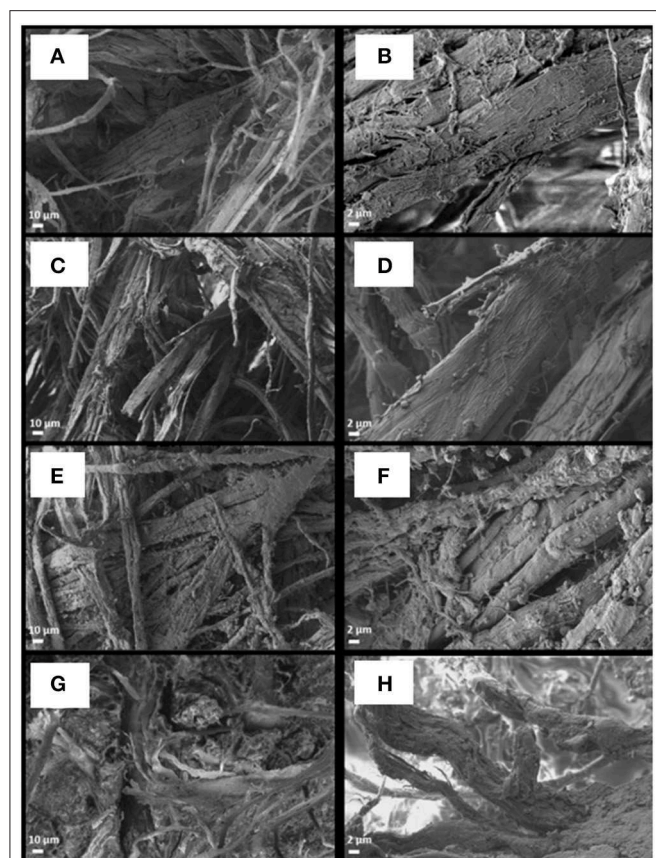
FIGURE 3 | Surface evaluation of the leather damage. SEM micrographs of the non-irradiated sample [(A) and its magnification (B)], of the leather irradiated with a dose of 750 Gy (C,D), with a dose of 1,000 Gy (E,F) and with the maximum dose of 5,000 Gy (G,H). Non-significant differences can be observed in the surface morphology of the sample irradiated with doses up to 1,000 Gy with respect to the non-irradiated one. A huge variation is instead visible in the fibers preservation condition of the sample irradiated with 5,000 Gy, where the surface shows wide areas of gelatinized materials [particularly visible in (G)] and the fibers bundles appear reduced in their dimension, frayed and fragmented (H).

TABLE 2 | Intensity ratio of Amide-I and Amide-II bands ($I_{Amide-I}/I_{Amide-II}$).

Treatment Dose (Gy)	$I_{Amide-I}/I_{Amide-II}$	$\Delta \bar{v}$ (cm−1)	$I_{Amide-I}/I_{1,720\ cm^{-1}}$
0	1.12 ± 0.05	85	0.12 ± 0.01
1,000	1.65 ± 0.07	83	0.13 ± 0.01
5,000	1.88 ± 0.06	81	0.14 ± 0.01

Differences in the position of the Amide I and Amide II main peaks ($\Delta \bar{v}$).

irradiated ones can be considered as indication of a possible effects of the irradiation dose.

In **Figure 4B** the curves of the variation rate of the LTA signal as a function of the sample temperature for all the analyzed leather samples are reported. The curves describe the rate at which the hydrothermal denaturation takes place. Unlike curves describing the denaturation process of parchment, in the case of leather only one well-defined symmetric peak can be recognized. This is mainly due to the presence, in this kind of collagen based artifact, of a unique stabilized collagen population with a general more uniform and higher hydrothermal stability (Cucos et al., 2014) recognizable by higher values of Td with respect to the ones recorded for parchment (Vadrucci et al., 2019a). As it is shown in the graph, only a slight difference can be observed between the temperature of the sample irradiated with a dose of 1,000 Gy (ΔTd = 0.3°C) and the non-irradiated one. Typical intrinsic inhomogeneity of the sample microstructure has to be considered and such a small variation cannot be ascribed to the effect of the irradiation dose with absolute confidence. Differently, the large Td variation observed between the sample irradiated with a dose of 5,000 Gy and the reference one (ΔTd = 2.9°C) reveals a substantial deteriorating effect of the irradiation dose on the collagen structural stability.
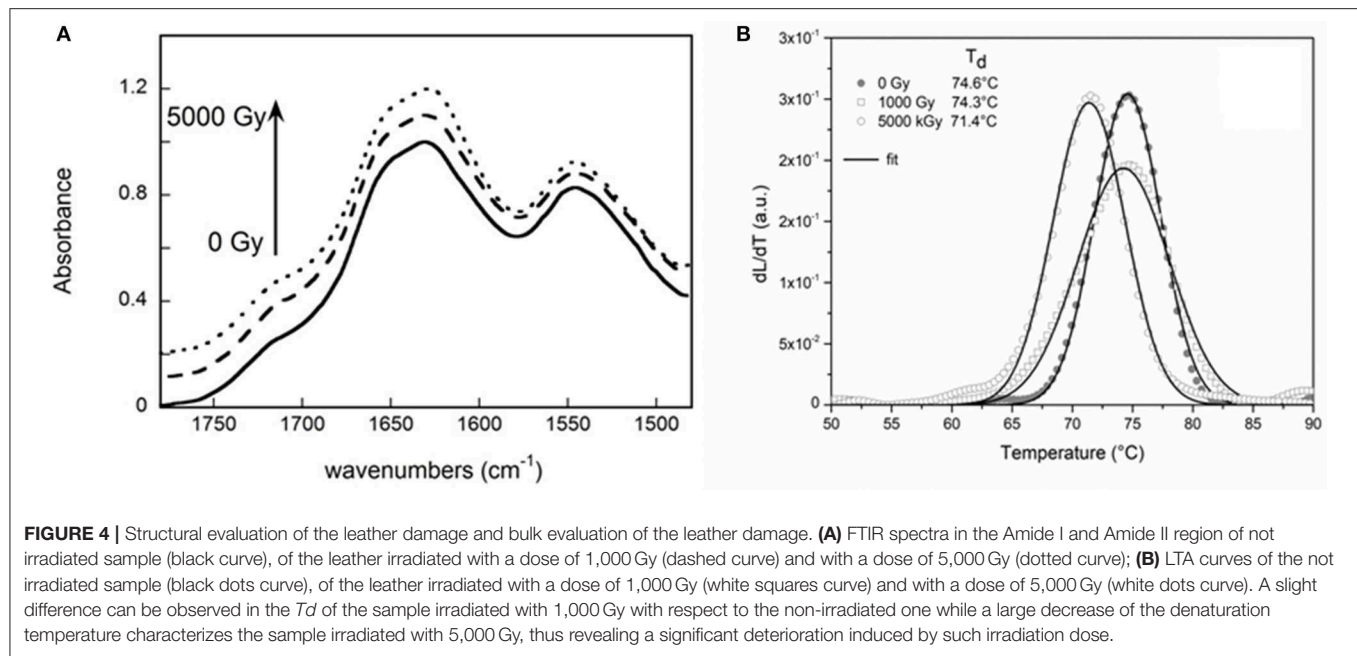
Therefore, these preliminary results show that, with respect to parchment the leather manifests to better tolerate irradiation doses till 1,000 Gy that do not seem to induce significant variations of the thermal stability.

DISCUSSION AND CONCLUSIONS

Bio-deterioration is one of the main problems encountered in the conservation of cultural heritage, in all types of historic and modern relics (Sterflinger et al., 2018). There are several methods to control this phenomenon such as physical, mechanical and biochemical.

However, commercial biocides show often their effect only for a limited time, since they can be utilized as a nutrient source by autochthonous microorganisms that develop resistance (Kakakhel et al., 2019).

In this work, an alternative method to chemical biocides has been evaluated in the case of ancient leathers. In order to get insight on the efficacy of the treatment, two different bacterial isolated from the leather samples were used to contaminate the surface. *B. cereus* and *M. timonae* were isolated for this analysis because of their ability to form biofilm on the surface, a bacterial aggregation resistant to many biocides and able to

collagen molecules require lower energy with respect to the intact collagen, while undergoing the gelatinization process. With respect to other collagen based materials such as parchment, leather accomplishes its hydrothermal denaturation at higher temperature values. This capability is mainly due to its peculiar manufacturing process: the tanning step gives the collagen fibers a higher and more uniform stabilization with respect to those obtained by the parchment manufacturing process, making them more resistant to the effect of deterioration agents (Cucos et al., 2014).

The analysis has been performed maintaining the samples immersed in water while heating them in the temperature range 25–100°C. The denaturation temperature recorded for the non-irradiated sample can be considered as the reference for the original preservation state of the leather samples while the variation from this starting value in the recorded Td for the

FIGURE 4 | Structural evaluation of the leather damage and bulk evaluation of the leather damage. **(A)** FTIR spectra in the Amide I and Amide II region of not irradiated sample (black curve), of the leather irradiated with a dose of 1,000 Gy (dashed curve) and with a dose of 5,000 Gy (dotted curve); **(B)** LTA curves of the not irradiated sample (black dots curve), of the leather irradiated with a dose of 1,000 Gy (white squares curve) and with a dose of 5,000 Gy (white dots curve). A slight difference can be observed in the *Td* of the sample irradiated with 1,000 Gy with respect to the non-irradiated one while a large decrease of the denaturation temperature characterizes the sample irradiated with 5,000 Gy, thus revealing a significant deterioration induced by such irradiation dose.

deteriorate manufactures (Stewart, 2002; Rivera et al., 2018). This was confirmed also in this case by the antibiotic susceptibility test, revealing several resistances for both strains. The bacterial cells were spotted on the specimens and irradiated by X-ray. A linear accelerator for the production of X-rays allows numerous advantages compared to the traditional gamma-ray radioactive sources traditionally employed in the treatment of collagen based artifacts (Nunes et al., 2012; Sendrea et al., 2015, 2017). In fact, radioactive sources such as the Co-60 require massive shielding, compliance with stringent regulations for use and management, obtaining authorization for use, costly procedures for controlled disposal of the source at end of life. As mentioned in the previous paragraphs, this facility was already employed on the COBRA project (COBRA, 2017) for the preservation treatment of cultural assets, with the case studies of processes biodegradation removal from fabric, wood and parchment writing supports (Borgognoni et al., 2017).

Concerning the evaluation of the effects of the irradiation dose on the structural stability of the collagen molecule it is possible to say that, although its locally-destructive nature, SEM analysis remains a reference technique in order to collect images of the surface morphology and preservation condition of collagenous materials. It allows the evaluation of the eventual disruption of the surface fibers networking and the appearance of areas of gelatinization of the collagen fibers (Della Gatta et al., 2005; Badea et al., 2008, 2012). This preliminary surface analysis puts in evidence that the variation in the fibers morphology and dimension can be slightly appreciated starting from the dose of 1,000 Gy highlighting this dose as the threshold one to be not exceeded in order to not induce further deterioration factors in the treated substrate.

The preliminary test of the potential damage induced by the irradiations on differently irradiated leather substrates performed

by the LTA gives us the possibility to obtain an indication of the average damage induced over the entire leather sample by different irradiation doses. The slight variation in the denaturation temperature obtained for the sample treated with the dose of 1,000 Gy confirms the surface information obtained by the SEM investigation and still indicates this dose as the threshold one.

Further and decisive information has been obtained by the employment of the FTIR-ATR analysis on the deterioration processes induced by the different irradiation doses with respect to the ones obtained by the previous analysis. This technique provides further and specific information on the characteristic deterioration processes induced in the treated substrate by the different irradiation doses. Specifically, it confirms the results obtained by the previous presented techniques regarding the gelatinization processes occurring noticeably only at high doses of irradiation. Furthermore, it gives important information also on the hydrolysis of the collagen molecule already occurring at the lowest investigated dose of irradiation (1,000 Gy).

In conclusion our data point out the irradiation method to be exploited as alternative to biocides for historical leathers since it doesn't lead to unacceptable changes in their functional or decorative properties.

Further researches are still in progress in order to discriminate damages eventually induced in collagen within ancient and modern leather manufactured with different tanning processes.

DATA AVAILABILITY STATEMENT

All datasets generated for this study are included in the article/supplementary material.

AUTHOR CONTRIBUTIONS

FUNDING

ACKNOWLEDGMENTS

REFERENCES

Adamo, M., Brizzi, M., Magaudda, G., Martinelli, G., Plossi-Zappalà, M., Rocchetti, F., et al. (2001). Gamma radiation treatment of paper in different environmental conditions: chemical, physical and microbiological analysis. *Restaurator* 22:107. doi: 10.1515/REST.2001.107

Adamo, M., Giovannotti, M., Magaudda, G., Plossi Zappalà, M., Rocchetti, F., and Rossi, G. (1998). Effect of gamma rays on pure cellulose paper as a model for the study of a treatment of "biological recovery" of biodeteriorated books. *Restaurator* 19, 41–59. doi: 10.1515/rest.1998. 19.1.41

Badea, E., Della Gatta, G., and Usacheva, T. (2012). Effects of temperature and relative humidity on fibrillar collagen within parchment: a micro Differential Scanning Calorimetry (micro DSC) study. *Polym. Degrad. Stabil.* 97, 346–353. doi: 10.1016/j.polymdegradstab.2011.12.013

Badea, E., Miu, L., Budrugeac, P., Giurginca, M., Mašić, A., Badea, N., et al. (2008). Study of deterioration of historical parchments by various thermal analysis techniques complemented by SEM, FTIR, UV-Vis-NIR and unilateral NMR investigations. *J. Thermal Anal. Calor.* 91, 17–27. doi: 10.1007/s10973-007-8513-x

Bergkessel, M., and Guthrie, C. (2013). Colony PCR. *Methods Enzymol.* 529, 299–309. doi: 10.1016/b978-0-12-418687-3.00025-2

Borgognoni, F., Vadrucci, M., Bazzano, G., Ferrari, P., Massa, S., Moretti, R., et al. (2017). X-ray sterilization of insects and microorganisms for cultural heritage applications. *Nuclear Instr. Methods Phys. Res. Sect. B* 406, 309–313. doi: 10.1016/j.nimb.2017.03.033

Cicero, C., Mercuri, F., Paoloni, S., Orazi, N., Zammit, U., Glorieux, C., et al. (2019). Integrated adiabatic scanning calorimetry, light transmission and imaging analysis of collagen deterioration in parchment. *Thermochim. Acta* 676, 263–270. doi: 10.1016/j.tca.2019.05.007

Cicero, C., Pinzari, F., and Mercuri, F. (2018). 18th century knowledge on microbial attacks on parchment: analytical and historical evidence. *Int. Biodeter. Biodegrad.* 134, 76–82. doi: 10.1016/j.ibiod.2018. 08.007

COBRA (2017). *Project (lr13/2008 project n. 1031), 2015-2018 Methods, Technologies and Advanced Tools for the Conservation of Cultural Heritage, Based on the Application of Radiation and Enabling Technologies.* Available online at: http://cobra.enea.it/english (accessed July 21, 2015).

Contadini, A. (1989). ""Cuoridoro": tecnica e decorazione di cuoi dorati veneziani e italiani con influssi islamici," In: *Arte veneziana e arte islamica: atti del Primo simposio internazionale sull'arte veneziana e l'arte islamica,* ed E. J. Grube (Venice: Edizioni l'Altra Riva), 231–251.

Cucos, A., Budrugeac, P., and Miu, L. (2014). DMA and DSC studies of accelerated aged parchment and vegetable-tanned leather samples. *Thermochim. Acta* 583, 86–93. doi: 10.1016/j.tca.2014.03.022

da Silva, M., Moraes, A. M. L., Nishikawa, M. M., Gatti, M. J. A., Vallim de Alencar, M. A., Brandão, L. E., et al. (2006). Inactivation of fungi from deteriorated paper materials by radiation. *Int. Biodet. Biodegrad.* 57, 163–167. doi: 10.1016/j.ibiod.2006.02.003

Dakal, T. C., and Cameotra, S. S. (2012). Microbially induced deterioration of architectural heritages: routes and mechanisms involved. *Environ. Sci. Europe* 24:36. doi: 10.1186/2190-4715-24-36

D'Almeida, M. L. O., Barbosa, P.,d,.S. M., Boaratti, M. F. G., and Borrely, S.I. (2009). Radiation effects on the integrity of paper. *Radiat. Phys. Chem.* 78, 489–492. doi: 10.1016/j.radphyschem.2009.03.032

Della Gatta, G., Badea, E., Ceccarelli, R., Usacheva, T. Maši, A., and Coluccia, S. (2005). Assessment of damage in old parchments by DSC and SEM. *J. Therm. Anal. Calorim.* 82, 637–649. doi: 10.1007/s10973-005-0944-7

Fantoni, R., Lazic, V., Vadrucci, M., Sorrentino, B., Chiari, M., Mazzinghi, A., et al. (2019). "Complementary characterization of ancient Roman frescoes by PIXE and LIBS techniques," in *EMSLIBS-2019* (Brno).

Haris, P. I., and Chapman, D. (1995). The conformational analysis of peptides using fourier transform IR spectroscopy. *Biopolymers* 37, 251–263. doi: 10.1002/bip.360370404

Herrera, L., and Videla, H. (2004). The importance of atmospheric effects on biodeterioration of cultural heritage constructional materials. *Int. Biodet. Biodegrad.* 54, 125–134. doi: 10.1016/j.ibiod.2004.06.002

Iorio, M., Graziani, V., Lins, S., Ridolfi, S., Branchini, P., Fabbri, A., et al. (2019). Exploring manufacturing process and degradation products of gilt and painted leather. *J. Appl. Sci.* 9:3016. doi: 10.3390/app9153016

Jackson, M., and Mantsch, H. H. (1995). The use and misuse of FTIR spectroscopy in the determination of protein structure. *Crit. Rev. Biochem. Mol. Biol.* 30, 95–120. doi: 10.3109/10409239509085140

Jroundi, F., Schiro, M., Ruiz-Agudo, E., Elert, K., Martín-Sánchez, I., González-Muñoz, M. T., et al. (2017). Protection and consolidation of stone heritage by self-inoculation with indigenous carbonatogenic bacterial communities. *Nat. Commun.* 8:279. doi: 10.1038/s41467-017-00372-3

Kakakhel, M. A., Wu, F., Gu, J.-D., Feng, H., Shah, K., and Wang, W. (2019). Controlling biodeterioration of cultural heritage objects with biocides: a review. *Int. Biodet. Biodegrad.* 143:104721. doi: 10.1016/j.ibiod.2019.104721

Magaudda, G. (2004). The recovery of biodeteriorated books and archive documents through gamma radiation: some considerations on the results achieved. *J. Cult. Heritage* 5, 113–118. doi: 10.1016/j.culher.2003.07.003

Mercuri, F., Buonora, P., Cicero, C., Helas, P., Manzari, F., Marinelli, M., et al. (2018). Metastructure of illuminations by infrared thermography. *J. Cult. Heritage* 31, 53–62. doi: 10.1016/j.culher.2017.10.008

Mercuri, F., Zammit, U., Paoloni, S., Cicero, C., and Orazi, N. (2016). *Apparato e Metodo per l'analisi della Denaturazione di Collagene Strutturato in Materiali Membranacei.* Patent pending - 102016000079558.

Migliore, L., Perini, N., Mercuri, F., Orlanducci, S., Rubechini, A., and Thaller, M. C. (2019). Three ancient documents solve the jigsaw of the parchment purple spot deterioration and validate the microbial succession model. *Sci. Rep.* 9, 1623–1623. doi: 10.1038/s41598-018-37561-y.

Migliore, L., Thaller, M. C., Vendittozzi, G., Mejia, A. Y., Mercuri, F., Orlanducci, S., et al. (2017). Purple spot damage dynamics investigated by an integrated approach on a 1244 A.D. parchment roll from the Secret Vatican Archive. *Sci. Rep.* 7:9521. doi: 10.1038/s41598-017-05398-7

Montanari, M., Melloni, V., Pinzari, F., and Innocenti, G. (2012). Fungal biodeterioration of historical library materials stored in Compactus movable shelves. *Int. Biodet. Biodegrad.* 75, 83–88. doi: 10.1016/j.ibiod.2012.03.011.

Nunes, I., Mesquita, N., Cabo Verde, S., João Trigo, M., Ferreira, A., Manuela Carolino, M., et al. (2012). Gamma radiation effects on physical properties of parchment documents: assessment of Dmax. *Rad. Phys. Chem.* 81, 1943–1946. doi: 10.1016/j.radphyschem.2012.07.016

Petrucci, F. (2014). "Vita e arte negli arredi dei palazzi barocchi tra tradizione e modernità," in *Edizioni Musei Vaticani: Città del Vaticano*, eds P. Dentro Il, R. A. Volpi, and C. Vatican, 249–282.

Piñar, G., Sterflinger, K., Ettenauer, J., Quandt, A., and Pinzari, F. (2015b). A combined approach to assess the microbial contamination of the archimedes palimpsest. *Microb. Ecol.* 69, 118–134. doi: 10.1007/s00248-014-0481-7

Piñar, G., Sterflinger, K., and Pinzari, F. (2015a). Unmasking the measles-like parchment discoloration: molecular and microanalytical approach. *Environ. Microbiol.* 17, 427–443. doi: 10.1111/1462-2920.12471

Pinzari, F., Cialei, V., and Piñar, G. (2012). "A case study of ancient parchment bio-deterioration using variable pressure and high vacuum scanning electron microscopy," in *Historical Technology, Materials and Conservation: SEM and Microanalysis,* eds N. Meeks, C. Cartwright, A. Meek, A. Mongiatti (London: Archetype Publications), 93–99.

Plavan, V., Giurginca, M., Budrugeac, P., Vilsan, M., and Miu, L. (2010). Evaluation of the physico-chemical characteristics of leather samples of some historical objects from kiev. *Rev. Chim.* 61, 627–631.

Rivera, L. E. C., Ramos, A. P., Sánchez, J. I. C., and Serrano, M. E. D. (2018). "Origin and Control Strategies of Biofilms in the Cultural Heritage," in *Antimicrobials, Antibiotic Resistance, Antibiofilm Strategies and Activity Methods*, ed S. Kirmusaoğlu (IntechOpen). doi: 10.5772/intechopen.79617

Scheerer, S., Ortega-Morales, O., and Gaylarde, C. (2009). Microbial deterioration of stone monuments–an updated overview. *Adv. Appl. Microbiol.* 66, 97–139. doi: 10.1016/s0065-2164(08)00805-8.

Schifano, E., Zinno, P., Guantario, B., Roselli, M., Marcoccia, S., Devirgiliis, C., et al. (2019). The foodborne strain *Lactobacillus fermentum* MBC2 triggers pept-1-dependent pro-longevity effects in *Caenorhabditis elegans*. *Microorganisms* 7:45. doi: 10.3390/microorganisms7020045

Sendrea, C., Badea, E., Stănculescu, I., Lucreţia, M., and Horia, I. (2015). Dose-dependent effects of gamma irradiation on collagen in vegetable tanned leather by mobile NMR spectroscopy. *Leather Footw. J.* 15:139. doi: 10.24264/lfj.15.3.1

Sendrea, C., Carsote, C., Radu, M., Badea, E., and Miu, L. (2017). The effect of gamma irradiation on shrinkage activity of collagen in vegetable tanned leather. *Revista Chim.* 68, 1535–1538.

Sterflinger, K., Little, B., Pinar, G., Pinzari, F., de los Rios, A., and Gu, J.-D. (2018). Future directions and challenges in biodeterioration research on historic materials and cultural properties. *Int. Biodet. Biodegrad.* 129, 10–12. doi: 10.1016/j.ibiod.2017.12.007

Sterflinger, K., and Piñar, G. (2013). Microbial deterioration of cultural heritage and works of art — tilting at windmills? *Appl. Microbiol. Biotechnol.* 97, 9637–9646. doi: 10.1007/s00253-013-5283-1

Stewart, P. S. (2002). Mechanisms of antibiotic resistance in bacterial biofilms. *Int. J. Med. Microbiol.* 292, 107–113. doi: 10.1078/1438-4221-00196

Strzelczyk, A. B., Bannach, L., and Kurowska, A. (1997). Biodeterioration of archeological leather. *Int. Biodet. Biodegrad.* 39, 301–309. doi: 10.1016/S0964-8305(97)00026-7

Strzelczyk, A. B., Kuroczkin, J., and Krumbein, W. E. (1987). Studies on the microbial degradation of ancient leather bookbindings: part I. *Int. Biodet.* 23, 3–27. doi: 10.1016/0265-3036(87)90039-X

Strzelczyk, A. B., Kuroczkin, J., and Krumbein, W. E. (1989). Studies on the microbial degradation of ancient leather bookbindings. part 2. Int. Biodet. 25, 39–47. doi: 10.1016/0265-3036(89)90027-4

Tatulian, S. A. (2019). "FTIR analysis of proteins and protein–membrane interactions," in *Lipid-Protein Interactions: Methods and Protocols*, ed J.H. Kleinschmidt (New York, NY: Springer New York), 281–325. doi: 10.1007/978-1-4939-9512-7_13

Vadrucci, M., Borgognoni, F., Cicero, C., Perini, N., Migliore, L., Mercuri, F., et al. (2019a). Parchment processing and analysis: ionizing radiation treatment by the REX source and multidisciplinary approach characterization. *Appl. Rad. Isotopes* 149, 159–164. doi: 10.1016/j.apradiso.2019.04.021

Vadrucci, M., Chiari, M., Giuntini, L., Picardi, L., Ronsivalle, C., and Sorrentino, B. (2019b). "PIXE spectroscopy for the ADAMO project," in *3th European Conference on Accelerators in Applied Research and Technology, ECAART13* (Split, CR: Ruder Boškovic Institute).

Vadrucci, M., Ferrari, P., Borgognoni, F., and Campani, L. (2019c). The REX irradiation facility and its applications. *Nuclear Inst. Methods Phys. Res. Sect. A* 930, 126–131. doi: 10.1016/j.nima.2019.02.066

Vyskočilová, G., Ebersbach, M., Kopecká, R., Prokeš, L., and Príhoda, J. (2019). Model study of the leather degradation by oxidation and hydrolysis. *Heritage Sci.* 7:26. doi: 10.1186/s40494-019-0269-7

Zanni, E., Bruni, E., Chandraiahgari, C. R., De Bellis, G., Santangelo, M. G., Leone, M., et al. (2017). Evaluation of the antibacterial power and biocompatibility of zinc oxide nanorods decorated graphene nanoplatelets: new perspectives for antibiodeteriorative approaches. *J. Nanobiotechnol.* 15:57. doi: 10.1186/s12951-017-0291-4

Check for updates

Metals and Environment: Chemical Outputs From the Interaction Between Gilded Copper-Based Objects and Burial Soil

Valerio Graziani[1], Morena Iorio[1], Monica Albini[2], Cristina Riccucci[2], Gabriella Di Carlo[2], Paolo Branchini[1] and Luca Tortora[1,3]*

[1] Surface Analysis Laboratory, INFN Roma Tre, Rome, Italy, [2] Institute of Nanostructured Materials, National Research Council, Research Area Montelibretti, Rome, Italy, [3] Department of Sciences, Roma Tre University, Rome, Italy

Three-dimensional chemical mapping was adopted to investigate an ancient fire-gilded buckle found in Rome. Time-of-flight secondary ion mass spectrometry (ToF-SIMS) and scanning electron microscopy with energy dispersive spectroscopy (SEM-EDS) were used to detect and locate degradation products aiming to identify the alteration processes. Inorganic and organic compounds present in the outermost part of such a class of cultural heritage objects can be considered the result of long-term interaction with the burial environment. ToF-SIMS depth profiling experiments can provide chemical information at the molecular level and high resolved spatial information (about 1 μm laterally, and 1 nm in depth). In this work, the attention was focused on the identification and localization of the ionic and molecular species involved in the degradation process. Results showed the presence of copper oxides, chlorides, and sulfides as common corrosion products but also the presence of species related to copper and bronze corrosion process, such as atacamite and its polymorphs. 3D maps for all the relevant molecular species allowed to visualize at the same time the eruption of copper chlorides throughout the micro/nanochannels present on the gold surface, the recrystallization of compounds of minor elements from the substrate, a pathway followed by silico-aluminates from the surface toward the internal corrosion layers, but mostly the evidence of biological activity of Sulfur Reducing Bacteria (SRB) living in anaerobic conditions.

Keywords: gilding, corrosion, copper, bronze disease, gold, soil, ToF-SIMS

INTRODUCTION

Mercury-gilding is one of the most complex techniques used in the past millennia to apply a thin layer of gold or silver onto the surface of a metal substrate. It was used by arts men and craftsmen for the decoration of jewels, statues, artworks, weapons, armors, ornaments, coins, and other everyday objects; sometimes in a fraudulent manner (Ingo et al., 2013). Two different methods for mercury gilding were available in the past (Lins and Oddy, 1975; Oddy, 1981, 1990; Anheuser, 1996, 1997, 2000).

The first one approaches the use of mercury as a "glue" able to attach a gold leaf to the substrate by forming an amalgam at the interface (namely, cold mercury gilding).

The second method is based on a solid-state reaction involving the use of an Au-Hg amalgam with doughy consistency, which can be applied to create a preliminary coarse coating of the object. This paste is produced by simple grinding gold dust with mercury and it requires a clean and oxide-free metal substrate. After that, a thermal treatment for a few minutes (heating in air at about 250–350°C, below the mercury boiling point at 357°C) is needed to volatilize the large part of the mercury and leave a gold film, whose thickness ranges from a few tenths of micron to about one micron (Ingo et al., 2013). A variable amount of residual mercury can be found in the gold layer due to an incomplete release (Anheuser, 1996, 1997, 2000). Finally, a mechanical finishing using bone or agate burnishers was always required to create a smooth, shiny, gold-like surface (Lins and Oddy, 1975; Oddy, 1981, 1990; Ingo et al., 2013).

However, the second manufacturing process intrinsically contains even the causes of the typical corrosion mechanisms. The aforementioned process produces a well-bonded but irregular and porous layer of gold. Furthermore, a thermal treatment at too high temperature or a too fast approach to the mercury boiling point can increase the extent of the irregularity due to the formation of gas bubbles. Defects in the multilayer architecture are represented by micro/nanochannels induced by the mercury evaporation, micro-discontinuities or breakages of the golden layer leaving uncovered the non-noble metal substrate. For these reasons, a mechanical finishing is mandatory to obtain a regular, smooth, and gold-like surface.

The typology of degradation phenomena and corrosion products depends on the surrounding environment in which they lived, in some cases for about two millennia (Scott, 1990, 1991; Robbiola et al., 1988; Ingo et al., 2002, 2019; Abdelhamid et al., 2010). The samples here studied underwent underwater burial for a long time of about four centuries thus representing a chance to study degradation phenomena of this type of artifact occurring in this specific condition. Understanding the chemical processes involved in the deterioration of gilded objects in a such extreme environment as well as the chemical and structural modifications due to a long-term interaction with organic/biological materials could pave the way for new strategies for the conservation-restoration of these pieces of cultural heritage.

The sample studied in this work is part of a couple of fire-gilded metallic buckles found during the dredging of Tiber river (Rome, Italy) and dated back to 16th–17th century AD. They were the subject of previous works of the authors aiming to give elemental information about the structure of the artifacts, the corrosion products, and the degradation phenomena that occurred during the burial (Ingo et al., 2016, 2018). In the present work, we focused the attention on giving a more detailed information about the chemical species involved in such phenomena. In particular, organic and inorganic compounds were detected providing, at the same time, three-dimensional chemical maps of the degradation products. Such chemical and structural information were acquired by using ToF-SIMS technique in dual beam mode. The 3D distribution of the molecular ion species was used to correlate degradation products with changes in the sample multilayer structure. In the last

decade, only a few works considered corrosion mechanisms and products in ancient gilded artifacts similar to those here reported (Ingo et al., 2013; Chiavari et al., 2015; Masi et al., 2016), among which an even shorter number of studies employed SIMS technique (Lechtman, 1984; De Ryck et al., 2003) providing also results about depth profiling (Yin et al., 2008; Ingo et al., 2018). On the other hand, the majority of the literature regards corrosion in non-gilded artifacts, studies in manufacturing techniques or studies on gilding of different, non-metallic artworks (Schreiner and Grasserbauer, 1985; Hackea et al., 2004; Adriaens, 2005; Dowsett et al., 2005; Van Ham et al., 2005; Bonaduce et al., 2007; Balta et al., 2009; Sandu et al., 2011; Tortora et al., 2014; Biocca et al., 2016; Di Tullio et al., 2016; Iorio et al., 2019). To the best of our knowledge, this is the first work that correlates structural information and three-dimensional distribution of organic and inorganic chemical species coming from corrosion process of an ancient gilded artifact.
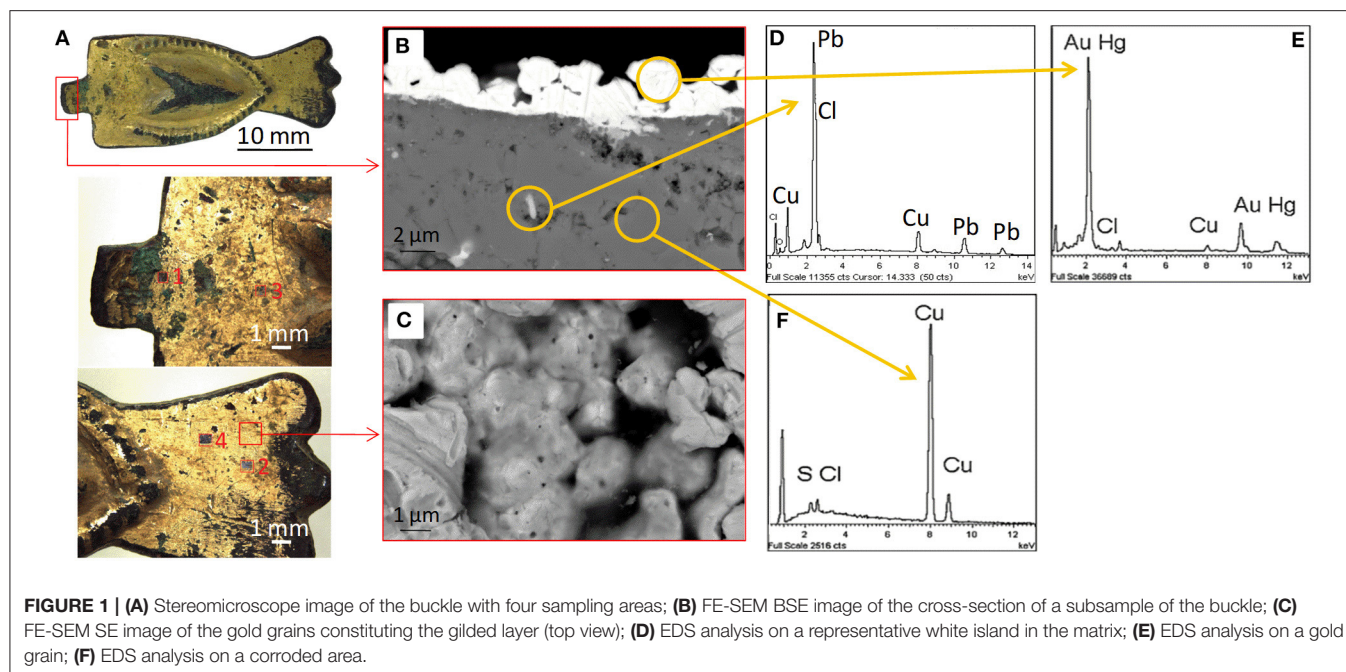
MATERIALS AND METHODS

Samples

The sample surface was cleaned up by using first distilled water and then ethanol to remove adventitious carbon contamination and to assure dehydration (Ingo et al., 2016, 2018). The buckle was subsampled by taking a small representative fragment both of the layered corrosion products (patina) and the underlying metal substrate. To preserve the structure of the patina, the subsampled fragments were embedded in a suitable resin for 24 h and carefully micro-sectioned by using a diamond saw. The section was polished with different SiC papers gradually increasing until 1,200 grit. The last polishing procedure was performed by using diamond pastes up to 0.25 μm.

Part of the analyses was carried out on the surface of the entire objects while the remaining techniques employed the embedded subsample.

Time of Flight—Secondary Ion Mass Spectrometry (ToF-SIMS)

ToF-SIMS technique was used to study chemical features and their distribution on the sample surface and in depth (3D chemical mapping). Measurements were performed by using a ToF-SIMS 5-300 (ION-TOF Munster, Gmbh, Germany) secondary ion mass spectrometer, equipped with bismuth liquid metal ion gun (LMIG) and cesium ion sputter gun. The sample was first analyzed in bunched mode using Bi^+ at 30 keV as a primary beam with dose density below the static limit ($<10^{12}$ ions/cm^2) to distinguish deteriorated areas from the unaltered. A low energy electron flood gun (20 eV) was utilized to investigate the non-conductive blackish degraded areas. ToF-SIMS depth profiles were acquired in dual beam mode, using Bi^+ at 30 keV and 15.6 ns pulse width as primary ions and Cs^+ gun at 2 keV as erosion beam, operating in interlaced mode. Cesium ion dose density was estimated as ~10^{18} ion/cm^2. The analysis area (100 × 100 μm^2) was set at the center of the sputter region (300 × 300 μm^2). Special attention was paid to choose the analysis area on a flat portion of the sample surface. All the images were collected

FIGURE 1 | **(A)** Stereomicroscope image of the buckle with four sampling areas; **(B)** FE-SEM BSE image of the cross-section of a subsample of the buckle; **(C)** FE-SEM SE image of the gold grains constituting the gilded layer (top view); **(D)** EDS analysis on a representative white island in the matrix; **(E)** EDS analysis on a gold grain; **(F)** EDS analysis on a corroded area.

at a pixel density of 128×128 pixels, with a lateral resolution of $2\,\mu m$ approximately. Secondary ions were extracted at 2 keV voltage and traveled through the ToF analyzer for a time of 100 μs per cycle allowing to obtain an m/z range from 1 to 800. Mass spectra were acquired in both positive and negative ion mode. All the ToF-SIMS images shown were normalized to the total ion image and processed with an averaging filter to remove topographical effects, and salt-and-pepper noise. All the data presented in this case study are shown in negative polarity, even for elements that are usually easier to detect in positive polarity. A stylus profilometer P7 (KLA-Tencor, San Jose, CA) was used to measure the depth of the ToF-SIMS craters.

Scanning Electron Microscopy With Energy Dispersive Spectroscopy (SEM-EDS)

LaB_6 filament equipped SEM (Stereoscan 360, Cambridge, UK) and highly brilliant Field Emission SEM (LEO Gemini 1530, Zeiss, Germany) with high spatial resolution were employed to study morphological and chemical features, coupled with INCA 250 and INCA 450 energy-dispersive X-ray spectrometers (EDS, by Oxford Instruments Analytical, UK), respectively. Secondary electron (SE) and backscattered electron (BSE) images were collected with acceleration voltages up to 20 kV, both on the surface and the cross-section of the samples. Before the analysis, the surface of the sample was coated with a thin layer of carbon or chromium to avoid charging effects. The former was deposited by using an Emitech sputter coater K550 unit, a K250 carbon coating attachment and a carbon cord at a pressure of 1×10^{-2} mbar to obtain an $\sim$3.0 nm thick film. The latter was deposited by using a Bal-Tech SCD 500 equipped with turbo pumping for ultra-clean preparations at a pressure of 5×10^{-3} mbar in order to obtain an $\sim$0.5 nm thick film.

RESULTS AND DISCUSSION

Figure 1A shows the buckle studied in this work. The gold layer still covers a large part of the sample surface even if several damaged areas are present in correspondence to the borders and decorative reliefs. The presence of greenish corrosion compounds originating from the copper substrate can be easily appreciated with the optical microscope. In the same figure, the four analyzed areas are highlighted as well. It is evident that the surface of the sample is poorly planar and homogeneous. FE-SEM BSE cross-section image (**Figure 1B**) gives representative details of the internal structure of the object. The EDS analysis in **Figure 1E** confirms the presence of mercury and thus the manufacturing processes afore introduced. In this cross-section, the gold layer is continuous and tight to the substrate. It is about $2–3\,\mu m$ thin with irregular thickness. Gold grains are well distinguishable with visible traces due to the finishing process. Some of the grains are quite isolated, with a few points in contact with the adjacent ones. Under the gold layer, the grains of the altered substrate are distinguishable, thus evidencing the crystalline nature of this layer. The presence of spaces and interstices homogeneously dispersed along the whole thickness indicates that this layer could be the product of a reaction or recrystallization starting from an even inner copper substrate (image not shown). The EDS analysis in **Figure 1F** shows the presence of sulfur and chlorine in addition to that expected of copper, confirming the penetration of active corrosive agents from the external environment which could play a role in such reaction-recrystallization process. White islands in the substrate copper-based matrix (not shown) are composed of lead (Ingo et al., 2018), analogously to those present also in the altered layer (**Figure 1D**). This was usually added to reduce the melting temperature of copper or bronze, resulting in easier-to-cast
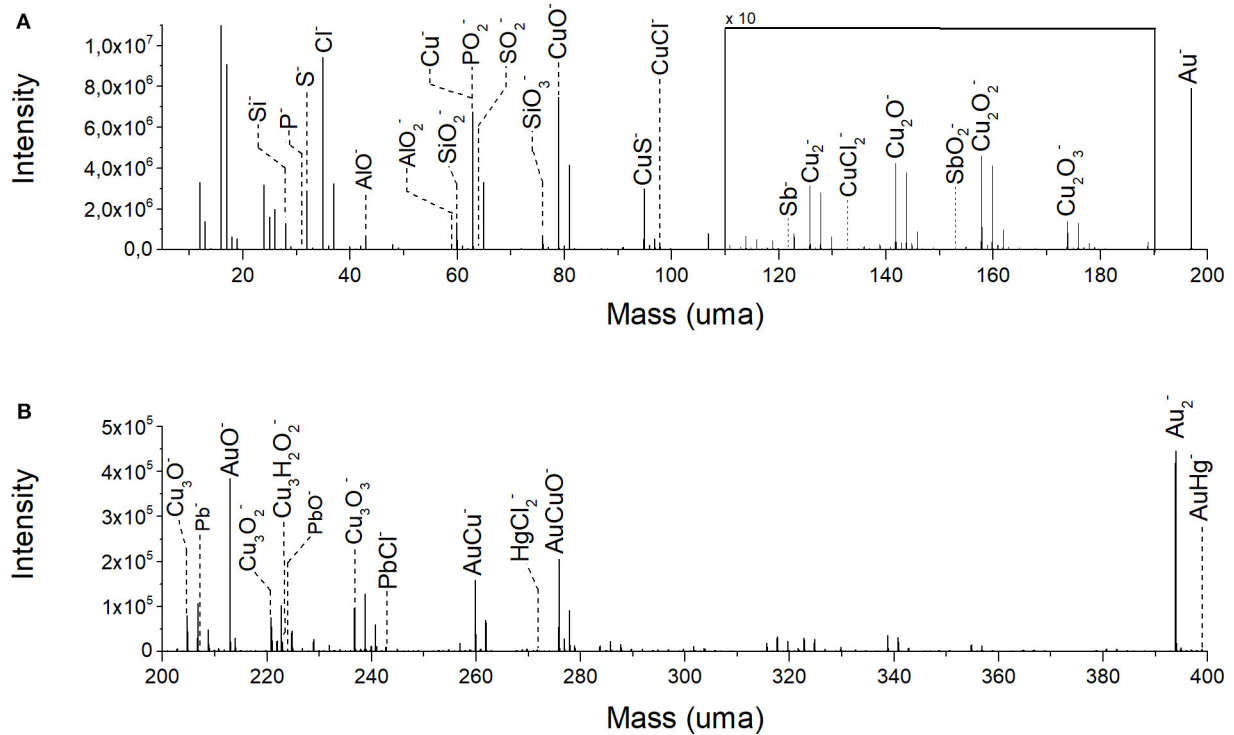
FIGURE 2 | ToF-SIMS negative ion spectrum of the analyzed volume: **(A)** mass fragmentation range from m/z 5 to 150; **(B)** mass fragmentation range from m/z 150 to 400.
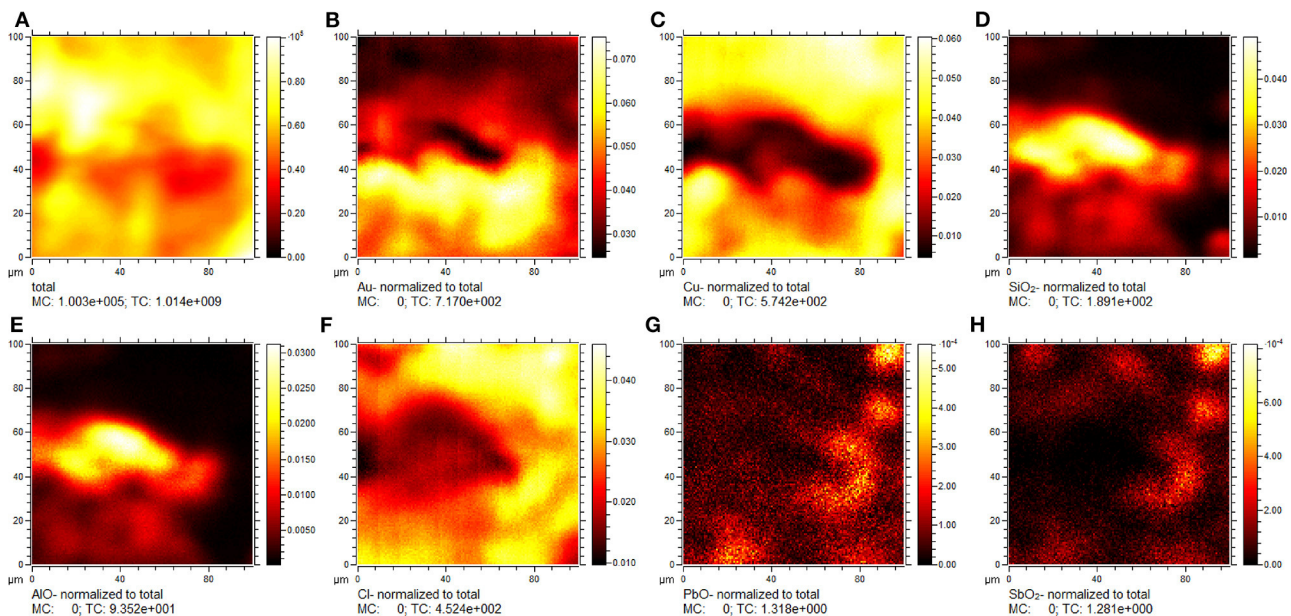

FIGURE 3 | ToF-SIMS negative ion chemical maps showing the distribution of selected species on the analyzed sample surface: **(A)** total ion intensity; **(B)** Au⁻; **(C)** Cu⁻; **(D)** SiO_2^-; **(E)** AlO⁻; **(F)** Cl⁻; **(G)** PbO⁻; **(H)** SbO_2^-. Signal ion intensity in figures **(B–H)** is normalized to the total ion intensity.

alloys. In this case, this could have been used in the fabrication of the copper substrate. The surface of the object at higher magnifications shows the aggregation of gold grains and the interstices among them (**Figure 1C**). Grain dimensions are quite homogeneous and range around 2 μm. Interstices have lower diameters. The very small pores on the grains (~20 nm) are

the channels created during the evaporation of the mercury. In the lower-left corner of the image, some of the traces left by the ancient polishing procedures are clearly visible (about 1 μm wide). **Figures 1B,C** confirm the high irregularity of the sample surface, as stated before.

A representative ToF-SIMS mass spectrum in negative ion mode of the gilded object is reported in **Figure 2**. The mass spectrum was obtained collecting all the ion signals during the depth profiling experiment. As expected, the most intense ion signals are Au^- (m/z 196.96), Cu^- (m/z 63.54), Cu_2^- (m/z 127.08), and $AuCu^-$ (m/z 259.89) and their related oxygen-containing species CuO^- (m/z 78.93), Cu_2O^- (m/z 141.85), $Cu_2O_2^-$ (m/z 157.85), $Cu_2O_3^-$ (m/z 173.85), Cu_3O^- (m/z 204.79), $Cu_3O_2^-$ (m/z 220.79), $Cu_3O_3^-$ (m/z 236.78), and $AuCuO^-$ (m/z 275.89). Secondary ions with a lower signal intensity are $CuCl^-$ (m/z 97.90), Sb^- (m/z 121.76), $CuCl_2^-$ (m/z 132.86), SbO_2^- (m/z 152.89), $Cu_3H_2O_2^-$ (m/z 224.79), $HgCl_2^-$ (m/z 270.92), and $AuHg^-$ (m/z 398.93). As reported in the previous works (Ingo et al., 2016, 2018), the copper oxide ions are originated from the outermost layer of the substrate underlying the gold layer. In this case, it is worth to note the presence of the signal of $Cu_3H_2O_2^-$ ion. The copresence of $Cu_3H_2O_2^-$ and $CuCl_2^-$ ions suggests the formation of atacamite $[CuCl_2 \cdot 3Cu(OH)_2]$ as a degradation product of the copper substrate. Details about the manufacturing process were revealed by the presence of mercury (in the adduct $AuHg^-$) and lead. In fact, the amount of mercury can be explained as a residual of the use of Hg-Au amalgam for the realization of the gold plate. For what concerns the presence of lead [Pb^- (m/z 207.20), PbO^- (m/z 223.97), and $PbCl^-$ (m/z 242.94)], it could be migrated from the copper substrate toward the gold surface due to alteration processes during the long-term burial. Lead and mercury can give rise to additional compounds constituting part of the corrosion patina, as suggested by the following detected ions: PbO^-, $PbCl^-$, and $HgCl_2^-$. Antimony can be imputed to a lead impurity in the Cu-Pb alloy. In the low-mass range (**Figure 2A**), further ion signals are originated from S^- (m/z 32.06), CuS^- (m/z 94.90), Cl^- (m/z 34.96), Si^- (m/z 27.97), AlO^- (m/z 42.97), AlO_2^- (m/z 58.97), SiO_2^- (m/z 59.96), SiO_3^- (m/z 75.96), P^- (m/z 30.97), PO_2^- (m/z 62.96), and SO_2^- (m/z 63.96). In general, the noble metal layer of ancient metallic artifacts, subjected to corrosion phenomena, has often an irregular surface characterized by fractures, cracks, and nano-channels induced by the fabrication procedure (Ingo et al., 2018). These surface defects represent preferential access points for aggressive soil species, organic contaminants and biological material dissolved in water that come in contact with the less noble underlying copper substrate. The intense signal from S^-, SO_2^-, P^-, and PO_2^- ions could be mainly due to environmental contamination. In particular, the significant presence of such sulfur- and phosphorus- based compounds can be related to the biological activity of Sulfur Reducing Bacteria (SRB) living in anaerobic conditions, namely those present in the burial condition at the ground of the Tiber river (Pope et al., 1968; Podany and Considine, 1994; Bastidas et al., 2008). The interaction between environmental aggressive chemical species and the metal composite object produces galvanic areas with consequent complex corrosion phenomena. Examples of these

phenomena are the surfacing of degradation products having a molar volume increased compared to the starting material (Abdelhamid et al., 2010; Bastidas et al., 2010; Ingo et al., 2013) or the formation of crystalline nodules and multilayered patinas (Scott, 1985). Moreover, elements present inside the metallic matrix can move toward the surface and rearrange in new spatial configurations, originating also new compounds and structures. Finally, external compounds and minerals can deposit on the object defected surface from the surrounding environment and penetrate its structure. In this case, this is suggested by the presence of the AlO^- and SiO_2^- ion signals which could be interpreted as contamination from clay.

2D chemical maps of some constituents from a representative area of the sample are reported in **Figure 3**. As mentioned above, the surface of the sample is highly inhomogeneous with spaces and interstices due to the presence of aggregates of gold grains. In this case, the Au^- and Cu^- distribution (**Figures 3A,B**) highlights the presence of a channel with a length of 80 μm and a width of 20 μm, approximately. This channel seems to be occupied by Si- and Al-based compounds (**Figures 3C,D**) supporting the hypothesis of contamination from clay. The degradation of the copper substrate is confirmed by the co-localization of the Cl^- ion signal with the Cu^- ion (**Figure 3E**). Furthermore, the presence of Pb^- and Sb^- ion signals can be indicative of a specific production process.

In depth profiling experiments, changes in signal intensity of elements and compounds can be measured in function of depth, as shown in **Figure 4**. In secondary ion mass spectrometry, different physico-chemical and geometrical factors contribute to the signal intensity of each ion peak. In this case, it is not possible to exactly correlate sputter time and sputter depth considering that the observed secondary ion signal intensity can be affected by several aspects, such as the complex architecture of the sample, the extremely irregular sample surface, and the inhomogeneous chemical distribution of elements and compounds. Therefore, in the depth profiles reported below the ion signal intensity was represented as a function of the sputter time. However, the depth of the ToF-SIMS craters was measured in order to estimate the volume of material removed in the sputtering process. Depth profiles were reported in two separate graphs in order to better observe changes in signal intensity **Figures 4A,B**. As expected, the signal intensity of the Au^- in **Figure 4A** shows an initial fast growth. After that, the ion signal slightly decreases without reaching zero counts. The $AuHg^-$ profile confirms the accumulation of mercury in the outermost part of the gold layer. The depth profiles of Cu^- as well as those of the related oxygen, chlorine, and sulfur adducts (CuO^-, Cu_2O^-, $CuCl^-$, CuS^-) show a common behavior with a fast growth at the beginning and in the interval 750 ÷ 1,470 s, then a slow increase till the end of the analysis. The very similar trend of depth profiles of Cu^- and $CuCl^-$ makes evident the close relationship between these species. On the other hand, the profile for $CuCl_2^-$ strongly differs from the previous ones, showing a decreasing trend till ~750 s and a slow-growing trend after ~3,000 s. The $Cu_3H_2O_2^-$ signal is more intense near the surface and then slowly decreases with the depth of the sample. In **Figure 4B**, the Cl^- profile shows a fast growth at the beginning till ~150 s; then it slightly decreases till
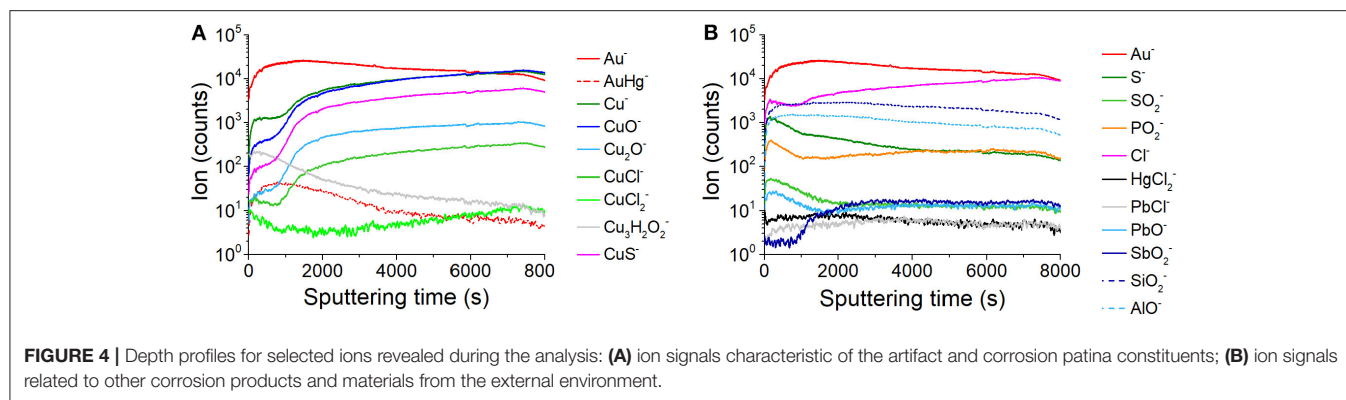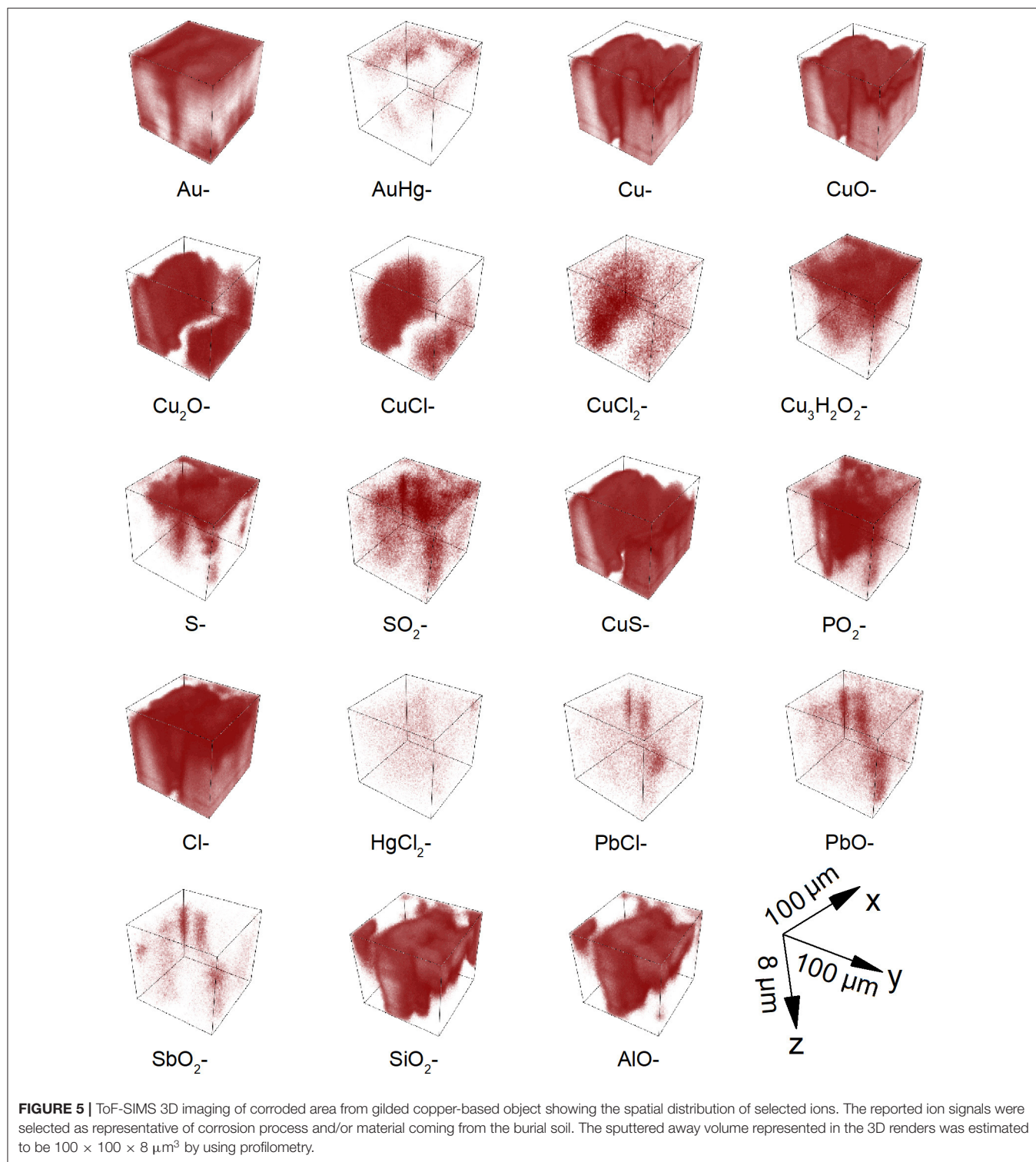
FIGURE 4 | Depth profiles for selected ions revealed during the analysis: **(A)** ion signals characteristic of the artifact and corrosion patina constituents; **(B)** ion signals related to other corrosion products and materials from the external environment.

TABLE 1 | Correspondence among observed secondary ions, structural information, and source attribution in the object/environment system.

Observed secondary ions	Structural information	Source attribution
Au^-, $AuHg^-$	Metallic Au	Gold Layer
PbO^-	Pb oxides	Alloying element with copper (white islands in the substrate copper-based matrix)
SbO_2^-	Sb oxides	Lead impurity in the Cu-Pb alloy
Cu^-, CuO^-, Cu_2O^-	Cu_2O (cuprite)	Corrosion patina (red corrosion)
Cu^-, $CuCl^-$	CuCl (nantokite)	Corrosion patina (green Corrosion)
Cu^-, $CuCl^-$, $CuCl_2^-$, $Cu_3H_2O_2^-$	$CuCl_2 \cdot 3Cu(OH)_2$ (atacamite)	Corrosion patina (green Corrosion)
Cl^-, S^-, SO_2^-, PO_2^-	Cl, H_2S, SO_4^{2-}, PO_4^{3-}	Environmental contamination and/or Biological Activity of Sulfur Reducing Bacteria(SRB)
CuS^-	CuS	Corrosion patina
$HgCl_2^-$, $PbCl^-$	$HgCl_2$, $PbCl_2$	Corrosion patina
SiO_2^- and AlO^-	Aluminosilicates	Contamination from soil (clay)

~950 s and finally shows a new growing trend till the end of the acquisition. The $HgCl_2^-$ and $PbCl^-$ profiles are about constant during the entire acquisition. Profiles for S^-, SO_2^-, PO_2^-, PbO^- ions show a very similar trend, with a rapid increase in the first ~150 s and a final decreasing trend. The profile of SbO_2^- shows a growth after ~860 s, then a constant trend till the end of the acquisition. The profiles of SiO_2^- and AlO^- are strongly coherent throughout the duration of the analysis, showing the same maximum curvature point at ~170 s, a common maximum at ~450 s and a common trend of decrease. To summarize and correlate the most relevant ions revealed by ToF-SIMS with the structural information, and source attribution in the object/environment system, the **Table 1** is given.

The 3D spatial distribution of signal intensity can be useful to recognize structures in a complex material and it is shown for some relevant chemical species in **Figure 5**. Comparing the distribution of Au^- and $AuHg^-$, an empty space can be appreciated in the middle of the analyzed volume; this constitutes a sort of channel connecting the burial environment with the substrate. Considering that the sputtered away volume

represented in the 3D renders was estimated to be 100 × 100 × 8 μm^3 by using profilometry, the gold signals are widely distributed, but mostly in the first 3–4 microns of the sample. The Au^- ion distribution puts in evidence the sample surface morphology and in particular the channel in the middle. Furthermore, observing the 3D map of the adduct $AuHg^-$, it is interesting to note that the ion signal distribution reveals that the mercury is more concentrated on the surface of the sample as well as the surface of the channel. Copper, copper oxides (CuO^-, Cu_2O^-), Cl^-, copper chlorides ($CuCl^-$, $CuCl_2^-$) ions are prevalently located under the gold layer. Chloride ions could migrate and spread throughout the mass of copper, being both the micro- and nanochannels induced by amalgam evaporation and the central channel preferential ways of penetration of the corrosion agents. The presence of copper chlorides (in particular nantokite, CuCl) is well in accordance with the evidence of newly formed compounds having erupted throughout the gold surface causing its spalling, break up, and partial detachment caused by the difference of molar relative volume between these minerals and copper. Furthermore, cuprite plays also a crucial role in the corrosion phenomena of copper-based alloys as discussed by Lucey (1972) and has been considered to act as an electrolytic membrane allowing the transport of anions, such as Cl^- or O-containing radicals inward, and cuprous ions outward. This is in accordance with the experimental evidence obtained by ToF-SIMS, as well: (1) the distribution of the signals from Cl^- is not only ubiquitous and clearly overlapping to that of Cu^- in the entire analyzed volume but also is continuously growing; (2) depth profiles of CuO^-, Cl^- and $CuCl^-$ share very similar growth rates while Cu_2O^- shows a slightly lower rate. $Cu_3H_2O_2^-$ 3D map shows that this chemical specie is concentrated on the top surface with some signals originating from the central part of the volume, filling the channel defined by the other species. The coexistence of signals of $Cu_3H_2O_2^-$ and $CuCl^-$ could prove the specific presence of atacamite (or its polymorphs) among all the possible chlorides. This points out also that the central channel is not only an available passage for external corrosion agents but allows accumulating both alteration products emerging from the inside of the object and materials from the external environment. 3D renders for S^-, SO_2^-, and CuS^- ions show that sulfur-containing compounds are present in the entire analyzed volume, being sulfides formed (or preserved) mainly under the surface

FIGURE 5 | ToF-SIMS 3D imaging of corroded area from gilded copper-based object showing the spatial distribution of selected ions. The reported ion signals were selected as representative of corrosion process and/or material coming from the burial soil. The sputtered away volume represented in the 3D renders was estimated to be $100 \times 100 \times 8 \ \mu m^3$ by using profilometry.

and the sulfates on its top and in correspondence of the central channel. Considering the sample cleaning procedure, the typical high solubility of sulfates for the copper ion (316 g/L at 20°C) and finally the low amount found in the first layers, the signals of SO_2^- are very likely related to a late recrystallization of an amount

of sulfates which were originally formed among the corrosion layers during the burial. On the contrary, the high density of CuS^- ion signals indicates the presence of its significant amount under the gold layer, as part of the internal corrosion layer together with copper oxides and chlorides thus revealing the

presence of environmental sulfides species likely due to sulfate reducing bacteria (SRBs). Signals from $HgCl_2^-$ originate from diffuse points, especially in the middle of the analyzed volume. The distribution of $HgCl_2^-$ can be explained considering that mercuric chloride shows high solubility in water (74 g/L at 20°C) and could move from the original positions, filling, in particular, the cracks of the gold layer. 3D renders for PbO^-, $PbCl^-$, and SbO_2^- ions show thickenings of points originating signals at common positions, whose longest dimensions range between $1 \div 4\,\mu m$. These values are comparable with those found in the FE-SEM BSE images for lead islands (such as in **Figure 1B** or in Ingo et al., 2018), thus confirming this interpretation of their nature. It is worth notice also that the few diffuse points from PbO^- and $PbCl^-$ are mainly in correspondence of the central channel, as preferred accumulation site of the degradation products. 3D renders for PO_2^-, SiO_2^-, and AlO^- show the presence of a thickening elongated on the z direction, ideally in correspondence of the limit surface of the central channel. The presence of PO_2^- ions is very likely to be related to organic or biological compounds which penetrated through the sample surface defects. Differently from chlorine, these ions did not diffuse in the substrate to react and form compounds. As seen in **Figures 3C,D**, the 3D spatial coherence of SiO_2^- and AlO^- ion source points in the same conic sub-volume supports the hypothesis that clay (silico-aluminates) penetrated through an accessible crack in the gilding layer (the central channel) toward the inside of the object during its burial in the soil.

CONCLUSIONS

ToF-SIMS was employed to fully explore the external part of an ancient gilded copper buckle, which has been subjected to a long-term burial in the soil causing the degradation. ToF-SIMS enabled to obtain accurate, stratigraphic, spatially referred information about the elemental, ionic, and molecular composition of constituent materials and degradation products of the object. In particular, it emerged that:

- Surface defects in addition to micro and nanochannels present on the gold surface represent the access door for organic, inorganic, and biological material.
- The presence of chlorine, phosphorus and oxygen leads to the formation of several corrosion products, such as cuprite, nantokite, atacamite.
- 3D chemical maps clearly show the new altered composite layered structure formed during the long-term burial in the soil

where the nantokite is located below the atacamite. In the same maps it is possible to observe the eruption of atacamite from the copper substrate.
- Chlorine and oxygen also interact with impurities and minor constituent materials leading to the formation of degradation products, such as $HgCl_2$, $PbCl_2$, Pb oxides and Sb oxides.
- The interaction with the environment is proved by the presence of aluminosilicates within the surface defects but also by the presence of molecular species, such as SO_2^- and PO_2^- that indicate a possible microbial induced corrosion (MIC). This latter aspect will be deeply investigated in future work.

Depth profiles and 3D renders were provided for all the species detected as graphical tools to investigate the internal structure of the sample, without sampling and cross-sectioning. Such information can be useful to generate models for the corrosion of this class of artifacts.

DATA AVAILABILITY STATEMENT

The datasets generated for this study are available on request to the corresponding author.

AUTHOR CONTRIBUTIONS

VG and MI drafted the work and conducted ToF-SIMS experiments and analysis. MA, CR, and GD carried sample treatment and sectioning, and conducted SEM-EDS analyses. GD and PB revised and commented on the manuscript. LT designed the research, conceptualized, and reviewed the paper.

FUNDING

ACKNOWLEDGMENTS

REFERENCES

Abdelhamid, M., Angelini, E., Grassini, S., Ingo, G. M., and El Harith, M. (2010). Depth profiling of coated metallic artefacts adopting laser-induced breakdown spectrometry. *Spectrochim. Acta B* 65, 695–701. doi: 10.1016/j.sab.2010.03.017

Adriaens, A. (2005). Non-destructive analysis and testing of museum objects: an overview of 5 years of research. *Spectrochim. Acta Part B* 60, 1503–1516. doi: 10.1016/j.sab.2005.10.006

Anheuser, K. (1996). Cold and hot mercury gilding of metalwork in antiquity. *Bull. Met. Mus.* 26, 48–52.

Anheuser, K. (1997). The practice and characterization of historic fire gilding techniques. *JOM* 49, 58–62. doi: 10.1007/s11837-997-0015-6

Anheuser, K. (2000). Amalgam tinning of chinese bronze antiquities. *Archaeometry* 42, 189–200. doi: 10.1111/j.1475-4754.2000.tb00875.x

Balta, I. Z., Pederzoli, S., Iacob, E., and Bersani, M. (2009). Dynamic secondary ion mass spectrometry and X-ray photoelectron spectroscopy on artistic

bronze and copper artificial patinas. *Appl. Surf. Sci.* 255, 6378–6385. doi: 10.1016/j.apsusc.2009.02.020

Bastidas, D. M., Cano, E., González, A. G., Fajardo, S., Lleras-Pérez, R., Campo-Montero, E., et al. (2008). An XPS study of tarnishing of a gold mask from a pre-Columbian culture. *Corros. Sci.* 50, 1785–1788. doi: 10.1016/j.corsci.2008.04.009

Bastidas, D. M., Criado, M., Fajardo, S., La Iglesia, V. M., Cano, E., and Bastidas, J. M. (2010). Copper deterioration: causes, diagnosis and risk minimisation. International Materials. *Reviews* 55, 99–127. doi: 10.1179/095066009X12506721665257

Biocca, P., Santopadre, P., Sidoti, G., Sotgiu, G., de Notaristefani, F., and Tortora, L. (2016). ToF-SIMS study of gilding technique in the fresco Vela della Castità by Giotto's school. *Surf. Interface Anal.* 48, 404–408. doi: 10.1002/sia.5956

Bonaduce, I., Boon, J. J., Colombini, M. P., and Lanterna, G. (2007). "Chemical imaging techniques for the characterization of materials and techniques in the art of gilding: a case study from a mural painting by F. Lippi," in *Proceedings of Conservation Science*, eds J. H. Townsend, L. Toniolo, and F. Cappitelli (London: Archetype Books), 121–130.

Chiavari, C., Bernardi, E., Balbo, A., Monticelli, C., Raffo, S., Bignozzi, M. C., et al. (2015). Atmospheric corrosion of fire-gilded bronze: corrosion and corrosion protection during accelerated ageing tests. *Corros. Sci.* 100, 435–447. doi: 10.1016/j.corsci.2015.08.013

De Ryck, I., Adriaens, A., Pantos, E., and Adams, F. (2003). A comparison of microbeam techniques for the analysis of corroded ancient bronze objects. *Analyst* 128, 1104–1109. doi: 10.1039/b303588c

Di Tullio, V., Capitani, D., Atrei, A., Benetti, F., Perra, G., Presciutti, F., et al. (2016). Advanced NMR methodologies and micro-analytical techniques to investigate the stratigraphy and materials of 14th century Sienese wooden paintings. *Microchem. J.* 125, 208–218. doi: 10.1016/j.microc.2015.11.036

Dowsett, M. G., Adriaens, A., Soares, M., Wouters, H., Palitsin, V. V. N., Gibbons, R., et al. (2005). The use of ultra-low-energy dynamic SIMS in the study of the tarnishing of silver. *Nuclear Instrum. Methods Phys. Res. B* 239, 51–64. doi: 10.1016/j.nimb.2005.06.179

Hackea, A. M., Carra, C. M., and Brown, A. (2004). "Characterisation of metal threads in Renaissance tapestries," in *Proceedings of Metal 2004*, eds J. Ashton and D. Hallam (Canberra, ACT: National Museum of Australia), 415–426.

Ingo, G. M., Angelini, E., Bultrini, G., De Caro, T., Pandolfi, L., and Mezzi, A. (2002). Contribution of surface analytical techniques for the microchemical study of archaeological artefacts. *Surf. Interface Analysis* 34, 328–336. doi: 10.1002/sia.1311

Ingo, G. M., Guida, G., Angelini, E., Di Carlo, G., Mezzi, A., and Padeletti, G. (2013). Ancient mercury-based plating methods: combined use of surface analytical techniques for the study of manufacturing process and degradation phenomena. *Acc. Chem. Res.* 46, 2365–2375. doi: 10.1021/ar300232e

Ingo, G. M., Riccucci, C., Guida, G., Albini, M., Giuliani, C., and Di Carlo, G. (2019). Rebuilding of the burial environment from the chemical biography of archeological copper-based artifacts. *ACS Omega* 4, 11103–11111. doi: 10.1021/acsomega.9b00569

Ingo, G. M., Riccucci, C., Lavorgna, M., Salzano de Luna, M., Pascucci, M., and Di Carlo, G. (2016). Surface investigation of naturally corroded gilded copper-based objects. *Appl. Surf. Sci.* 387, 244–251. doi: 10.1016/j.apsusc.2016.06.082

Ingo, G. M., Riccucci, C., Pascucci, M., Messina, E., Giuliani, C., Biocca, P., et al. (2018). Combined use of FE-SEM+EDS, ToF-SIMS, XPS, XRD and OM for the study of ancient gilded artefacts. *Appl. Surf. Sci.* 446, 168–176. doi: 10.1016/j.apsusc.2018.01.278

Iorio, M., Graziani, V., Lins, S., Ridolfi, S., Branchini, P., Fabbri, A., et al. (2019). Exploring manufacturing process and degradation products of gilt and painted leather. *Appl. Sci.* 9:3016. doi: 10.3390/app9153016

Lechtman, H. (1984). Pre-Columbian surface metallurgy. *Sci. Am.* 250, 38–45. doi: 10.1038/scientificamerican0684-56

Lins, P. A., and Oddy, W. A. (1975). The origins of mercury gilding. *J. Archaeol. Sci.* 2, 365–373. doi: 10.1016/0305-4403(75)90007-2

Lucey, V. F. (1972). Developments leading to the present understanding of the mechanisms of pitting corrosion of copper. *Br. Corros. J.* 7, 36–41. doi: 10.1179/000705972798323332

Masi, G., Chiavari, C., Avila, J., Esvan, J., Raffo, S., Bignozzi, M. C., et al. (2016). Corrosion investigation of fire gilded bronze involving high surface resolution spectroscopic imaging. *Appl. Surf. Sci.* 366, 317–327. doi: 10.1016/j.apsusc.2016.01.101

Oddy, W. A. (1981). Gilding through the Ages. *Gold Bull.* 14, 75–79. doi: 10.1007/BF03214601

Oddy, W. A. (1990). Gilding: an outline of the technological history of the plating of gold on to silver or copper in the old world. *Endeavour* 15, 29–33. doi: 10.1016/0160-9327(91)90085-P

Podany, J., and Considine, B. B. (1994). *Symposium organised by the Paul Getty Museum Proc.* Malibou, USA: Paul Getty Museum.

Pope, D., Gibbens, H. R., and Moss, R. L. (1968). The tarnishing of silver at naturally occurring H2S and SO2 levels. *Corros. Sci.* 8, 883–887. doi: 10.1016/S0010-938X(68)80141-6

Robbiola, L., Blengino, J. M., and Fiaud, C. (1988). Morphology and mechanisms of formation of natural patinas on archaeological Cu-Sn alloys. *Corros. Sci.* 40, 2083–2111. doi: 10.1016/S0010-938X(98)00096-1

Sandu, I. C. A., de Sá, M. H., and Pereira, M. C. (2011). Ancient 'gilded' art objects from European cultural heritage: a review on different scales of characterization. *Surf. Interface Anal.* 43, 1134–1151. doi: 10.1002/sia.3740

Schreiner, M., and Grasserbauer, M. (1985). Microanalysis of art objects: objectives, methods and results. *Fresenius J. Anal. Chem.* 322:181. doi: 10.1007/BF00517657

Scott, D. A. (1985). Periodic corrosion phenomena in bronze antiquities. *Stud. Conserv.* 30, 49–57. doi: 10.1179/sic.1985.30.2.49

Scott, D. A. (1990). Bronze disease: a review of some chemical problems and the role of relative humidity. *J. Am. Inst. Conserv.* 29, 193–206. doi: 10.2307/3179583

Scott, D. A. (1991). *Metallography and Microstructure of Ancient and Historic Metals*. Marina del Rey, LA: Getty Conservation Institute in association with Archetype Books.

Tortora, L., de Notaristefani, F., and Ioele, M. (2014). ToF-SIMS investigation of gilt and painted leather: identification of indigo, oil binder and gold varnish. *Surf. Interface Anal.* 46, 807–811. doi: 10.1002/sia.5450

Van Ham, R., Van Vaeck, L., Adams, F., and Adriaens, A. (2005). Feasibility of analyzing molecular pigments in paint layers using TOF S–SIMS. *Anal. Bioanal. Chem.* 383, 991–997. doi: 10.1007/s00216-005-0088-4

Yin, Y. S., Chen, B. J., and Ling, Y. C. (2008). ToF-SIMS study of official seals from Han Dynasty. *Appl. Surf. Sci.* 255, 1534–1537. doi: 10.1016/j.apsusc.2008.05.160

Nanopore Sequencing and Bioinformatics for Rapidly Identifying Cultural Heritage Spoilage Microorganisms

Alessandro Grottoli[1,2], Marzia Beccaccioli[1,2], Emma Zoppis[3], Rosita Silvana Fratini[2], Emily Schifano[3], Maria Laura Santarelli[4], Daniela Uccelletti[3] and Massimo Reverberi[1,2]*

[1] SARA EnviMob s.r.l., Rome, Italy, [2] Department of Environmental Biology, Sapienza University of Rome, Rome, Italy, [3] Department of Biology and Biotechnology Charles Darwin, Sapienza University of Rome, Rome, Italy, [4] Department of Chemical Engineering Materials Environment, Sapienza University of Rome, Rome, Italy

Microbiological methodologies allow understanding the causes that lead to the development of a certain microbial community colonizing an artistic surface, to characterize its composition and describe its role in the deterioration of the constituent materials. Metagenomics allows identifying microbial communities directly in their natural environments, bypassing the need for isolation and cultivation of individual species, thus providing a more comprehensive picture of the biodiversity present on a surface compared with standard cultivation methods. Furthermore, molecular analyses require small amounts of material, favoring the preservation of the artistic surface during sampling. Here, we verified the suitability of a protocol consisting in DNA extraction with micro-invasive sampling, using adhesive tape, PCR amplification with universal primers [bacteria (16S), fungi (ITS), and Viridiplantae (18S)], and amplicon sequencing by Oxford Nanopore Technologies (ONT) in the hypogeum of *Basilica di San Nicola in Carcere* Church (Rome, Italy). Sequence data were analyzed with a bioinformatic pipeline customized for pinpointing cultural heritage spoiling organisms, named "AmpLIcon SequencIng Analysis" (ALISIA). These data were integrated with traditional microbiology techniques that allowed the isolation of cultivable bacteria; three species were also characterized through their capability of biofilm formation and antibiotic resistance. Further, Fourier-transform infrared spectroscopy (FTIR) spectroscopy was performed to characterize the main products present on the masonry surface providing indications on the type of decay present. This novel biological workflow represents a powerful opportunity to investigate the microbial colonization of artistic surfaces aimed at implementing preservation strategies of cultural heritage from bio-spoilage.

Keywords: nanopore, bioinformatic, microbial community, artistic surfaces, non invasive approach

INTRODUCTION

Cultural heritage (CH), such as statues, books, paintings, and frescoes, may be frequently exposed to the effects of physical and chemical deterioration. Moreover, microorganisms may interact among them and with the surface, establishing a real ecosystem with trophic chains and microbiological successions (Caneva and Salvadori, 1989). Biological interaction with the CH

may be an important cause of biodeterioration (Sterflinger and Piñar, 2013). Microorganisms, in fact, carry out micro- and macrosurface decoesidation processes causing physical damage and activate chemical degradation processes due to the emission of primary and secondary metabolism products and assimilation processes that can occur with or without the production of extracellular enzymes (Pinna and Salvadori, 2005). The aesthetic damages are among the most obvious and often compromise the readability of the work. They are due to the precipitation of mineral phases or to the presence of biofilms, which may have different thickness, microstructure, and color. The color depends on the type of biocenosis, the stage of development and the growth phase of the microorganisms involved, and the eventual endo-pigments produced (Warscheid and Braams, 2000). Adopting microbiological methodologies in order to understand the causes that lead to the development of a certain microbial community, identifying its composition, and describing its role in the deterioration of the constituent materials are the first important and necessary steps for understanding the effects of microorganisms on CH. The identification of certain microorganisms on the surface of an artistic object does not link them directly as responsible for deterioration. In fact, some microorganisms might derive from secondary colonization, and therefore, their activity is addressed to organic substances released in the environment by death and lysis of pioneer species (Radaelli et al., 2004). Thus, the reconstruction of the succession of populations on the surface is the only way to understand the role of each identified species in the deterioration process (Caneva et al., 2008). Furthermore, a microbiological point of view allows identifying and developing strategies to manage the growth of biodeteriogens and to study fitting prevention strategies through a better knowledge of the growth-limiting nutrients and the dynamics of biological aerosol diffusion for the conservation and protection of monuments and artworks (González and Saiz-Jiménez, 2005; Caneva et al., 2008).

Microbial diversity can be explored mainly through two distinct approaches: isolation and direct cultivation or indirect molecular analysis. Microorganisms' isolation and cultivation is the traditional method for exploring the microbial diversity, however, it is estimated that only 0.1 up to 3.0% of the environmental bacteria and up to 70% of fungi (with huge variability depending upon the genera) are cultivable using standard cultivation methods (Amann et al., 1995; Hanson et al., 2016).

On the other hand, molecular approaches are not linked to this limit and thus allow obtaining a more comprehensive picture and a realistic view of the biodiversity present on the surface. Furthermore, by repeating molecular analysis at different moments in time, it is also possible to retrieve important information regarding the history of successive colonization. Another advantage of the use of cultural-independent molecular methods is the significant reduction in the quantity of material that these methods require for sampling. This is an important aspect to consider when working on artistic objects in order to preserve their integrity. Metagenomics is the application of modern genomics techniques to the study of communities of microbial organisms directly in their natural environments,

bypassing the need for isolation and lab cultivation of individual species (Hugenholtz, 2002; Rappé and Giovannoni, 2003). Within the molecular techniques, next generation sequencing (NGS) metagenomics-based methods represent a minimally invasive and powerful opportunity to investigate the microbial communities, composition, and functional diversity that may be present on artistic surfaces or in different environments from soil to human gut (Gutarowska et al., 2015). Nonetheless, molecular analysis investigation methods should preferably be supported by cultural-dependent methods, which allow the study of the physiology and metabolism of the isolated microorganisms and understanding of their potential role in biodeterioration (Qi-Wang et al., 2011; Otlewska et al., 2014).

This work aims at identifying by molecular methods, namely ONT sequencing, the microbiological composition of the hypogeum of one of the most characteristic Roman monuments for architectural and historical formation: the *Basilica di San Nicola in Carcere* Church, in Rome. The structure incorporates three temples and a medieval tower transformed into a bell tower. The Church shares the basement and part of the structures with three Roman temples below; its location near the Tiber River has made it vulnerable since its first construction in 1128 AD. Indeed, the high level of humidity present in the masonries made necessary the periodic reconstruction of its frescoes, which in the last version date back to the XIX century.

Micro-invasive sampling of the hypogeum involving the use of adhesive tape was performed; due to the low recovery of materials, we inserted a PCR amplification step of the total DNA extracted, using universal primers for three kingdoms, 16S for bacteria, ITS for fungi and 18S for Viridiplantae. We then used a metagenomics approach for sequencing the amplicons through ONT and analyzing the output data with a customized bioinformatic pipeline. Parallel, from the same area of sampling, microbial and chemical characterizations were performed. Specifically, cultivable bacteria were evaluated, and three isolates were analyzed in terms of antibiotic resistance and biofilm formation ability, in order to highlight the importance of a combined approach to investigate biodegradation phenomena.

MATERIALS AND METHODS

Sampling for the Molecular Analysis and Bacteria Isolation

In this study, two different approaches were used in order to investigate the presence of microorganisms on CH surfaces: isolation of microorganisms for the nanopore sequencing analysis and isolation of cultivable bacteria for Fourier-transform infrared spectroscopy (FTIR) analysis. For the sequencing analysis, biological material was collected using a non-invasive or micro-invasive sampling technique for CH and using adhesive tape (Urzí and De Leo, 2001). This non-invasive sampling technique allows collecting enough biological material, without affecting the integrity of the CH. The adhesive tape sampling method was used for collecting samples in *Basilica di San Nicola in Carcere* Church in Rome for metagenomics analysis along the hypogeum wall of the church. Samples collected (*n* = 6) were

pooled in two samples (Samples 1 and 2) and stored in 50 ml sterile tubes at −20°C until the DNA extraction procedures. In the cases of isolation of cultivable bacteria and FTIR analysis, cotton swabs were utilized for sampling very near the area where adhesive tape sampling was performed. Cotton swabs were pressed firmly over the surface of the wall and then placed in sterile tubes containing 2 ml of Nutrient Broth (NB). Successively, samples were incubated in the laboratory at 30°C for 24 h and plated on NB agar plates. Plates, further incubated at 30°C for 24 h, allowed the isolation and purification of morphologically different colonies. Bacterial isolates were then identified at the molecular level by the amplification of 16S rDNA.

DNA Extraction and rDNA Amplification

Genomic DNA extraction was performed using the C-TAB III extraction method as described in Scala et al. (2017), with some modifications. Adhesive tape used for collecting the samples was grounded in liquid nitrogen in the presence of polyvinylpolypyrrolidone. The first step of extraction was performed in a 50 ml tube in presence of 1.5 ml of C-TAB I, 1.5 ml of SOL2A, and 15 µl of Proteinase K (20 mg/ml) and incubated at 55°C at 250 rpm overnight. After this first step, the extraction was performed as protocol. Total DNA extract was resolved by electrophoresis in agarose gel (1%).

Spectrophotometric quantification was performed using a ThermoScientific NanoDrop spectrophotometer, and DNA purity was assessed through the evaluation of 260/280 and 260/230 absorbance ratios. PCR amplification was performed on about 50 ng of DNA of each sample using rDNA kingdom-specific primers; 27 For (5′-GAGATTTGATCCTGGCTCAG-3′) and 1495 Rev (5′-CTACGGCTACCTTGTTACGA-3′) primers were used for the bacteria rDNA 16S region (Lane, 1991); ITS1 (5′-TCCGTAGGTGAACCTGCGG-3′) and ITS4 (5′-TCCTCCGCTTATTGATATGC-3′) primers were used for the fungi rDNA 18S region (Glass and Donaldson, 1995); and EUK-A (5′-ACCCTGGTTGATCCTGCCA-3′) and EUK-B (5′-TGATCCTTCTGCAGGTTCACCTAC-3′) primers were used for the Viridiplantae rDNA 18S region (Medlin et al., 1988). Amplification was performed by using Taq polymerase (Bioline), and the PCR products were verified through gel electrophoresis in agarose gel (1%).

Amplicon Sequencing

Amplicon sequencing was performed on PCR products deriving from the rDNA amplification belonging to bacteria, fungi, and Viridiplantae present in the total DNA extracted from adhesive tape. PCR products were sequenced through Oxford Nanopore Technologies (ONT) by a MinION sequencer. A total amount of 200 ng using a ratio of 1:1:1 for 16S, ITS, and 18S PCR product was used for sequencing. Rapid barcoding of PCRs was carried out following the protocol released by ONT (SQK-RBK004).

A customized bioinformatic pipeline called "AmpLIcon SequencIng Analysis" (ALISIA) was used in order to pinpoint CH spoiling organisms. ALISIA uses BLASTn version 2.8.1+ (Camacho et al., 2009) following a few steps: (i) Each read is analyzed and associated to a single taxon. (ii) Final output is divided into the three analyzed kingdoms: bacteria, Viridiplantae,

and fungi. (iii) Reads are filtered by matching length in order to remove eventual sequencing artifacts following these criteria: 700–1,500 bp for bacteria reads, 250–2,000 bp for Viridiplantae reads, and 500–1,200 bp for fungi reads (Medlin et al., 1988; Lane, 1991; Glass and Donaldson, 1995); moreover, the reads were selected by e-value $\leq 1 \cdot 10^{-6}$, length of alignment $\geq 80\%$, and percentage of identical matches $\geq 85\%$ because of the high error rate of the ONT MinION sequencer (Tyler et al., 2018). (iv) Lastly, a virtual gel, representing the density of the sequenced reads, was drawn in R version 3.6.1 (R Core Team, 2018) and using the package ggplot2 version 3.2.0 (Gómez-Rubio, 2017) in order to emulate a DNA electrophoretic run for comparison.

Isolation and Characterization of Bacterial Strains

Different bacteria were isolated from the hypogeum wall in *Basilica di San Nicola in Carcere* Church, in Rome. Molecular characterization of the isolated bacteria was performed by DNA extraction according to Bergkessel and Guthrie (2013) and the amplification of a region of approximately 1,400 bp from the 16S rRNA gene using the primers F8 (5′-AGAGTTTGATCCTGGCTCAG-3′) and R1492 (5′-GGTTACCTTGTTACGACTT-3′). The PCR reaction was performed utilizing Taq DNA polymerase from Accuzyme DNA Polymerase (Bioline). BMR Genomics (Padova, Italy) sequenced the amplified region, and the obtained sequences were analyzed with the BLAST database. The bacterial species used in this work were *Paenibacillus pabuli* IP3 (accession number: MN493858), *Kocuria rhizophila* IP5 (accession number: MN493859), *Bacillus licheniformis* IP7 (accession number: MN493860), and *Stenotrophomonas maltophilia* IP9 (accession number: MN493861).

Bacterial strains isolated from hypogeum surfaces were grown in NB at 30°C.

Antibiotic Susceptibility Tests

Antibiotic susceptibility tests were performed according to Schifano et al. (2019). Overnight cultures of the different bacterial cultures (100 µl) were spread onto NB agar plates. Then, antibiotic disks were placed on plates, which were incubated for 24 h at 30°C. The zones of inhibition were measured from the center of the disk and recorded.

Biofilm Formation Assay

The biofilm formation assay on the plastic surface was performed as described in Zanni et al. (2017) with some differences. Briefly, each well was filled with 200 µl of NB broth and a concentration of each bacterial stain of $1 \cdot 10^7$ cell/ml, in triplicate. Wells without bacteria were utilized as controls. Next, plates were incubated at 30°C for 24 h, and Crystal Violet assay was performed. The experiment was repeated three times with three replicates for each treatment. For biofilm formation on glass, $1 \cdot 10^7$ cells/ml of each bacterial strain were separately inoculated in 3 ml of NB, put in a 35 mm Petri plate with a sterile cover slide, and then incubated at 30°C. After 24 h, cultures were gently removed, washed twice with sterile water, and stained using SYTO9

staining (Kit 7012, Invitrogen, Mount Waverley, Australia) for 15 min at room temperature in the dark. Stained cells were observed under a Zeiss Axiovert 25 fluorescence microscope.

Chemical Characterization by FTIR Analysis

The chemical analysis of the efflorescence present on the hypogeum of the church was performed by infrared spectroscopy with a Fourier-transform infrared spectrometer (FTIR, Vertex 70, Bruker Optik GmbH, Ettlingen, Germany) equipped with a single-reflection Diamond ATR cell, a standard MIR source (HeNe), and a room temperature DTGS detector. The ATR-FTIR spectra were recorded with 256 scans in the mid-infrared range ($400–4,000$ cm^{-1}) at a resolution of 4 cm^{-1}.

RESULTS

ALISIA

PCR amplifications were performed on the two sampling pools (Samples 1 and 2) derived from the hypogeum of *Basilica di San Nicola in Carcere* Church (see section "Materials and Methods") in order to investigate the presence of organisms belonging to bacteria, fungi, and Viridiplantae using, respectively, specific rDNA 16S, ITS, and 18S region primers (see section "Materials and Methods"). Electrophoresis agarose gel verified the presence and the length of amplification products for all three regions investigated. Both genomic DNA from Sample 1 and Sample 2 provided amplicons with each kingdom-specific primer: (i) ITS (fungi), one for Sample 1 at ~600 bp and two separate bands at ~600 and ~900 bp in Sample 2; (ii) 18S (Viridiplantae), both samples resulted as positive to a single band ~1,800 bp; and (iii) 16S (bacteria), single band in both samples at ~1,500 bp (**Figure 1A**). However, in every PCR run, a light smear could be identified near the bands of the expected size; this possibly indicated the presence of the DNA of several microorganisms. ONT MinION sequencing was assessed to rapidly classify the PCR amplicon products: the run produced ~6 Mb of data (~100 k reads) and ~11 Mb of data (~190 k reads) respectively for Samples 1, 2. A customized bioinformatic pipeline called ALISIA was used in order to pinpoint CH spoiling organisms. The sequenced reads were analyzed following four basic steps described in section "Materials and Methods." In the first two steps, 94,353 reads for Sample 1 and 155,506 reads for Sample 2 were assigned to a taxon (~80% of the total reads). In the third step, 21,597 reads corresponded to the bacteria kingdom, 47,729 to fungi, and 5,571 to Viridiplantae for Sample 1, while in Sample 2, 34,803 reads corresponded to bacteria, 36,176 to fungi, and 1,055 to Viridiplantae (**Figure 2**), however, 19,456 reads for Sample 1 and 83,472 reads for Sample 2 corresponded to the Metazoa and Protista kingdoms, or virus or matched with unknown organisms. Interesting, 69,056 reads belonged to the Metazoa kingdom in Sample 2. In fact, the EUK-A and EUK-B primers could have amplified portions of rDNAs belonging to this kingdom (Hugerth et al., 2014). Further analysis will bring to light the convolution of the found species (**Table 1**). In the last ALISIA steps, a virtual gel was drawn using the density of

the reads assigned to a specific kingdom in order to emulate, and in this case compare, a real PCR electrophoretic gel. The virtual gel shows a similar pattern of read length distribution compared to the real agarose PCR gel for both fungi and bacteria lanes, however, in the virtual gel Viridiplantae lanes, the reads were distributed along the Sample 1 lane, while a very low number of reads of Sample 2 were found (respectively 2,026 and 304 reads), showing a different pattern compared to the real agarose PCR gel (**Figure 1B**). Within these reads, ~94 and ~150 k were associated to a single taxon. In bacteria, "uncultured bacteria" was the most abundant association found in the NCBI database for both Samples 1 and 2 (~1,000 reads, 28.68% of total bacterial reads for Sample 1; ~2,000 reads, 32.06% of total bacterial reads for Sample 2), however, in both samples, *Nesterenkonia* was the most abundant genus found (1,666 reads and 812 reads corresponding to 40.80 and 11.30% respectively for Samples 1 and 2) (**Table 1**). Although also in fungi, in both samples, ~4,000 reads (respectively 4 and 3% of the total reads for the analyzed samples corresponding to respectively 49.13 and 65.29% of the total fungal species found in the samples) were assigned to an uncultured fungus, in Sample 1, the most abundant fungal taxon found was *Capnobotryella* spp. (695 reads, 7.82% of total fungal reads), a genus already found on monument surfaces (Sert et al., 2007); while in Sample 2, the most abundant fungal taxon found was *Parastagonospora forlicesenica* (1,589 reads, 22.66% of total fungal reads) (**Table 1**). The most abundant plant species found were *Parietaria judaica* and *Platanus occidentalis* respectively in Samples 1 and 2 (374 reads and 51 reads corresponding to 18.26 and 15.84% of the total Viridiplantae reads found). However, the second most abundant taxon in Sample 2 was "embryophyte environmental sample" (27 reads, 8.39% of the total Viridiplantae found in the sample) (**Table 1**).

Identification and Characterization of Culturable Bacterial Strains

Since the most abundant reads found were ascribed to non-cultivable microorganisms, we decided to proceed with standard isolation techniques, taking the case of the culturable bacteria as an example. The amplification of 16S rDNA of bacteria isolated from the hypogeum revealed the presence of different *genera*: *Arthrobacter, Bacillus, Kocuria, Paenibacillus, Pseudomonas, Staphylococcus, Stenotrophomonas*, and *Streptomyces*. Among them, four different isolates, *P. pabuli* IP3, *K. rhizophila* IP5, *B. licheniformis* IP7, and *S. maltophilia*, IP9 were further characterized. An antibiotic susceptibility test was performed using 19 antibiotics involved in inhibition of cell wall synthesis, protein synthesis, and nucleic acid synthesis. As reported in **Table 2**, all bacterial strains resulted as resistant to aztreonam. Moreover, *S. maltophilia* IP9 showed a higher resistance than the other bacterial strains. It was resistant to 12 antibiotics, among which were penicillin, erythromycin, and ampicillin. On the contrary, *B. licheniformis* IP7 showed a low antibiotic resistance, since inhibition zones were visible only in the case of tetracycline, fosfomycin, and aztreonam. Since the biodeterioration process is mainly caused by microorganisms' capacity to aggregate and produce an extracellular matrix able to protect them from adverse conditions, biofilm formation of bacterial isolates was

FIGURE 1 | Kingdom rDNA-specific PCR amplicon agarose gel and virtual gel: **(A)** Electrophoretic gel (agarose 1%) shows three separate and different PCR runs for both samples analyzed: ITS1-4 for fungi, 18S EUK-a/b for Viridiplantae, and 16S for bacteria. Bioline HyperLadder[TM] 1 kb was used. **(B)** Virtual gel showing the distribution of the reads per kingdom. Samples in the both images are ordered as follows: Sample 1 and Sample 2.

evaluated on both plastic and glass surfaces. *K. rhizophila* IP5, *B. licheniformis* IP7, and *S. maltophilia* IP9 showed a high ability of biofilm production on both the two surfaces, while

P. pabuli IP3 resulted as being unable to aggregate on plastic and glass (**Figure 3**).

FTIR-ATR Characterization of the Efflorescence on the Hypogeum Wall

The formation of efflorescences is due to different phenomena, such as stone weathering. Because of changes in temperature or humidity, salts can precipitate on surfaces, causing a destructive effect (Wilimzig, 1996). Salts deposited are composed of a variety of different chemical compounds, including carbonates, chlorides, nitrates, and sulfates. Salt efflorescences can be observed in environments with high levels of humidity, where they are generated by the action of nitrifying bacteria that convert the organic compounds into nitrate salts (Castrillón Rivera et al., 2019). Thus, studying these efflorescences could provide a means for identifying at least the type of microorganisms that are spoiling that specific CH. The IR spectra of the sample showed the presence of typical vibration bands of calcium sulfate hydrate, known also as gypsum ($CaSO_4 \times 2H_2O$), centered at 1,109, 669, and 596 cm^{-1}, as well as the stretching and deformation vibrations of the O–H bond of water at 3,525, 3,492, and 3,401 cm^{-1} and at 1,692 and 1,627 cm^{-1}, respectively. At 1,424 cm^{-1} is recognized the presence of calcium carbonate; instead, the absorption at 1,343 cm^{-1} is due to the presence of sodium and/or potassium nitrates. A band of silicates was present at 1,032 and 1,006 cm^{-1}. Gypsum is due to the presence of sulfates in the masonries of the monument for capillarity rise of water from the soil. A strong exchange of cations between the $CaCO_3$ (calcite) of the mortars with the sulfates diluted in the
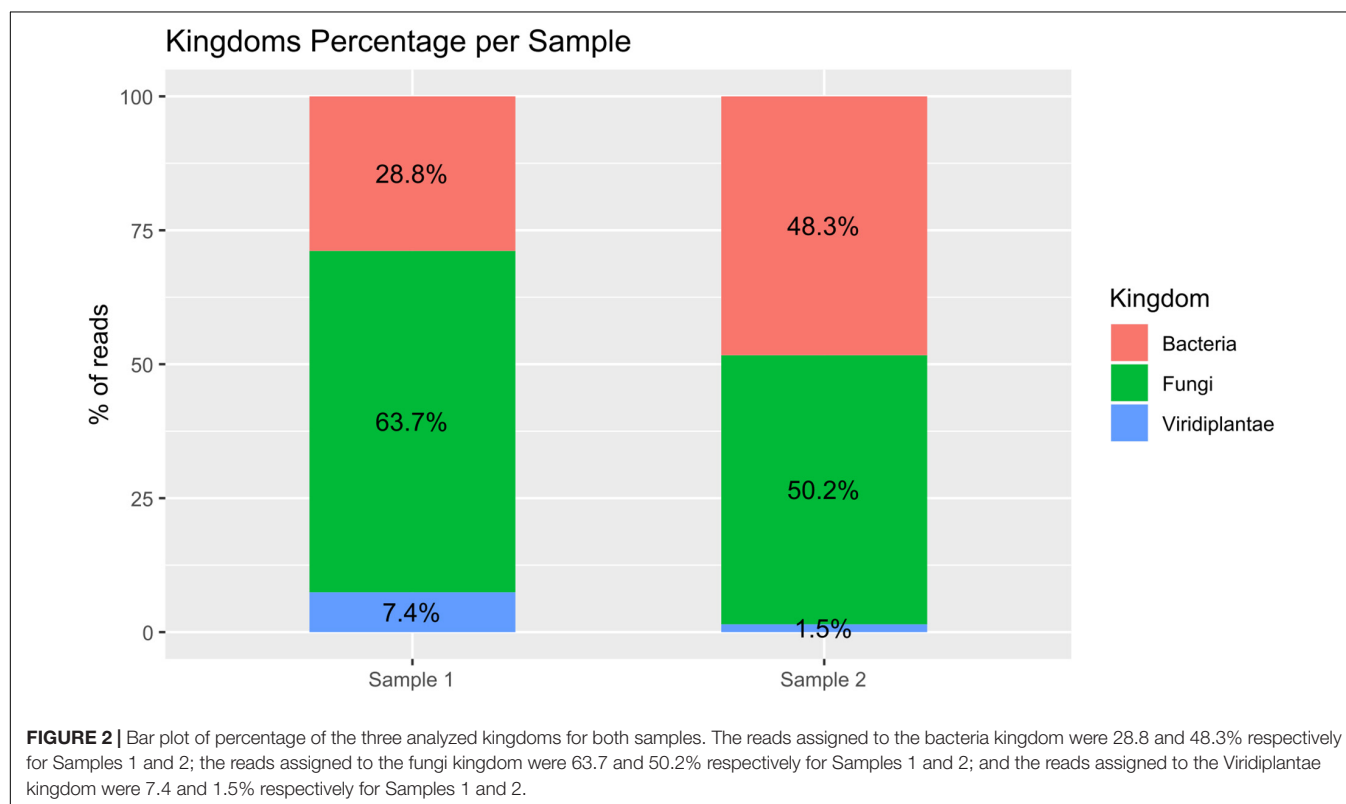

FIGURE 2 | Bar plot of percentage of the three analyzed kingdoms for both samples. The reads assigned to the bacteria kingdom were 28.8 and 48.3% respectively for Samples 1 and 2; the reads assigned to the fungi kingdom were 63.7 and 50.2% respectively for Samples 1 and 2; and the reads assigned to the Viridiplantae kingdom were 7.4 and 1.5% respectively for Samples 1 and 2.

TABLE 1 | The table shows percentage and raw number of reads of the three analyzed kingdoms for Samples 1 and 2.

Sample 1			Sample 2		
Percent	**Reads**	**Species**	**Percent**	**Reads**	**Species**
Bacteria					
28.68%	1,171	Uncultured bacterium	32.06%	2,302	Uncultured bacterium
22.95%	937	*Nesterenkonia* sp.	7.10%	510	*Nocardiopsis nanhaiensis*
11.46%	468	*Nesterenkonia xinjiangensis*	6.96%	500	*Nesterenkonia* sp.
2.25%	92	*Pseudonocardia* sp.	5.35%	384	*Aliihoeflea aestuarii*
1.89%	77	*Nesterenkonia suensis*	4.40%	316	*Luteimonas huabeiensis* HB2
1.86%	76	*Amycolatopsis albispora*	3.34%	240	*Pseudonocardia* sp.
1.86%	76	*Kibdelosporangium kanagawaense*	2.24%	161	Uncultured Actinomycetales bacterium
1.84%	75	*Prauserella* sp.	1.99%	143	*Lysobacter* sp.
1.67%	68	*Nesterenkonia aethiopica*	1.96%	141	*Pseudomonas putida*
1.30%	53	*Actinophytocola burenkhanensis*	1.89%	136	*Pseudonocardia autotrophica*
Fungi					
49.13%	4,365	Uncultured fungus	65.29%	4,578	Uncultured fungus
7.82%	695	*Capnobotryella* sp.	22.66%	1,589	*Parastagonospora forlicesenica*
6.47%	575	*Devriesia* sp.	3.76%	264	Uncultured *Devriesia*
3.93%	349	*Passalora* sp.	1.47%	103	*Passalora* sp.
3.26%	290	*Capnodiales* sp.	1.25%	88	*Devriesia* sp.
3.23%	287	Uncultured *Ascomycota*	0.66%	46	*Capnobotryella* sp.
2.47%	219	Uncultured sp.	0.66%	46	*Neodevriesia lagerstroemiae*
2.35%	209	*Teratosphaeriaceae* sp.	0.58%	41	*Teratosphaeriaceae* sp.
0.99%	88	*Graphiola phoenicis*	0.56%	39	Uncultured sp.
0.99%	88	*N. lagerstroemiae*	0.29%	20	*Phlebiopsis gigantea*
Viridiplantae					
18.26%	374	*Parietaria judaica*	15.84%	51	*Platanus occidentalis*
5.37%	110	*Trichilia emetica*	8.39%	27	Embryophyte environmental sample
3.96%	81	*P. occidentalis*	6.83%	22	*Platanus* x *hispanica*
2.78%	57	*Cupressus gigantea*	4.66%	15	*Juniperus recurva*
2.73%	56	*Panicum hallii*	4.35%	14	*C. gigantea*
2.64%	54	*Urtica angustifolia*	4.35%	14	*Platanus orientalis*
2.59%	53	*Citrus clementina*	3.73%	12	*P. judaica*
2.29%	47	*Selaginella moellendorffii*	3.11%	10	*Cupressus sempervirens*
2.05%	42	*Spondias tuberosa*	3.11%	10	*Pinus densiflora*
1.95%	40	*Urtica mairei*	2.80%	9	*Pinus taeda*

The percentages indicate the number of reads of a single taxon over the total number of its kingdom reads.

water creates the condition to crystallize gypsum. The presence of silicates is aswell justified by crystallization processes with compounds deriving for capillarity rise of water from the soil.

DISCUSSION

Dealing with CH, the primary concern is that of the preservation of the artistic surface. In this context, sampling must be performed adopting the least invasive method possible and collecting the smallest amount of material required for analysis. The micro-invasive sampling through adhesive tape only causes minimal damage to the superficial layer of the artistic object. However, further investigations could be performed to assess if the micro-invasive character of the method may be maintained also in the case of highly fragile artistic surfaces.

Since this sampling method only allows sampling of the surface of the artistic object, the microbiological components that might have colonized the porous cavities are excluded. It was observed that this sampling method allows the extraction of quantities of DNA enough to carry out genomic analysis without the need of previous amplification. Even so, the overall quantity and quality of the extracted DNA was unsuitable for NGS metagenomics shotgun analysis. To skip this bug, PCR amplification of rDNA kingdom-specific regions allows us to exponentially amplify DNA in order to be suitable for NGS analysis. The use of the ONT MiniION sequencer allows quickly sequencing samples directly in your laboratory for a rapid and real-time analysis. More classic sequencing technologies require a greater amount of time waiting for sequencing data. The high number of reads related to the amplicons belonging to the different organisms sampled by micro-tape in the hypogeum of

TABLE 2 | Antibiotic susceptibility of the four different bacterial strains.

Antibiotic	*Paenibacillus pabuli* IP3	*Kocuria rhizophila* IP5	*Bacillus licheniformis* IP7	*Stenotrophomonas maltophilia* IP9
Vancomycin	− (1.3 cm)	− (0.8 cm)	− (1 cm)	− (0.5 cm)
Clindamycin	+	+	− (0.6 cm)	+
Cefalotin	+	+	− (1 cm)	+
Tobramycin	− (0.7 cm)	− (0.5 cm)	− (0.7 cm)	− (0.5 cm)
Ampicillin	− (0.8 cm)	− (0.9 cm)	− (1.2 cm)	+
Cefotaxime	+	+	− (0.7 cm)	+
Chloramphenicol	− (0.6 cm)	− (1 cm)	− (1 cm)	− (1 cm)
Tetracycline	− (1.7 cm)	− (0.8 cm)	+	− (0.5 cm)
Erythromycin	− (1.5 cm)	+	− (0.5 cm)	+
Amikacin	− (1.1 cm)	− (0.6 cm)	− (0.9 cm)	− (0.5 cm)
Oxacillin	+	+	− (0.5 cm)	+
Fosfomycin	+	− (1.1 cm)	+	+
Rifampicin	− (1.2 cm)	− (1.2 cm)	− (1.5 cm)	+
Gentamicin	− (0.7 cm)	− (0.7 cm)	− (0.7 cm)	− (0.4 cm)
Penicillin	− (1 cm)	+	− (1 cm)	+
Aztreonam	+	+	+	+
Carbenicillin	− (0.4 cm)	+	− (0.7 cm)	+

Basilica di San Nicola in Carcere Church have been decrypted by tailoring a bioinformatic tool for this specific need: ALISIA. ALISIA is a practical bioinformatic tool that allows you to analyze quickly raw amplicon sequencing data from different sequencing technologies, such as Illumina or ONT. The use of ALISIA in CH metagenomics studies provides a clear and immediate view of the microbiome present on the analyzed CH. ALISIA revealed many species present in the microbiome collected by the adhesive tape sampling method in the three kingdoms. Despite the large number of species found, in both the fungi and bacteria kingdoms, the most abundant reads were assigned, by BLAST analysis, to uncultured microorganisms. This can be attributed to the impossibilities and difficulties in isolating microorganisms by traditional cultural methodologies (Amann et al., 1995; Hanson et al., 2016). Thus, it resulted as problematic to have confirmation of the reliability of these taxonomic results.

Interestingly, ALISIA highlighted the presence of different species of genus *Nesterenkonia* (**Table 1**). This genus, belonging to the *Micrococcaceae* family, includes mesophilic moderate haloalkaliphilic species (Stackebrandt et al., 1995). Even if this genus was not found on the bacteria isolation, *Kocuria*, a closely related genus (Stackebrandt et al., 1995), was isolated and characterized by molecular analysis. Although there is a mismatch between swab isolation bacteria species found and ALISIA analysis, further investigations will be carried out in order to improve ALISIA's result accuracy in detecting the microbiome present on a CH surface. In fact, it is difficult to compare the high specificity that metagenomic analysis can reach to isolation and cultivation of individual species. A functional metagenomics analysis can be performed in order to find the degradation molecular mechanisms involved in the analyzed CH, completely skipping the identification step, acting directly on the molecular process. Moreover, despite this being bacteria-centric

work, a wide number of fungal species, likely involved in CH deterioration, were found. Nevertheless, a plus in the accuracy of ONT and ALISIA could be suggested by results in 18S amplicon sequencing: most of the plant species found are tree plants very common in Rome, such as *Platanus*, *Pinus*, or *Cupressus*, or herbaceous plants typical of cracks in rock faces: *P. judaica*. Very likely, the DNA of these plants belongs to pollen deposited on sampled wall surfaces. Metagenomic amplicon sequencing by ONT MinION is revealed to be a fast tool to investigate the taxa present on the surface of CH.

To investigate deeply on the bacterial composition of the masonry of the hypogeum, cultivable bacteria were isolated. While many of them were reported to be involved in the formation of salt efflorescences such as the *genera* of *Bacillus, Kocuria, Paenibacillus,* and *Arthrobacter* (Laiz et al., 2000), *Pseudomonas* spp. resulted as being involved in calcite production (Rivera et al., 2018). Among the isolates, three strains were chosen as representatives to be further characterized, as they belong to the Gram-positive *P. pabuli, K. rhizophila,* and *B. licheniformis* and one to the Gram-negative *S. maltophilia* species. All of them are involved in biodeterioration, as reported in many works (Tarsitani et al., 2014; Saiz-Jimenez, 2017). *P. pabuli*, besides the microbial corrosion of glass, is also involved in biodeterioration of historic limestone buildings (Marvasi et al., 2009; Skipper and Skipper, 2016); *B. licheniformis*, instead, is a facultative anaerobe, and it has been identified on deteriorated paintings (Capodicasa et al., 2010). Moreover, *Bacillus, Kocuria,* and *Paenibacillus* spp. can grow in presence of nitrate without oxygen on organic substrates and are reported to be involved in salt efflorescence (Laiz et al., 2000). Indeed, nitrifying bacteria oxidize ammonia to nitrite and nitrate ions, which lead to nitric acid formation. This process causes stone dissolution and formation of soluble nitrate salts, appearing as efflorescence; this phenomenon is also triggered by humidity
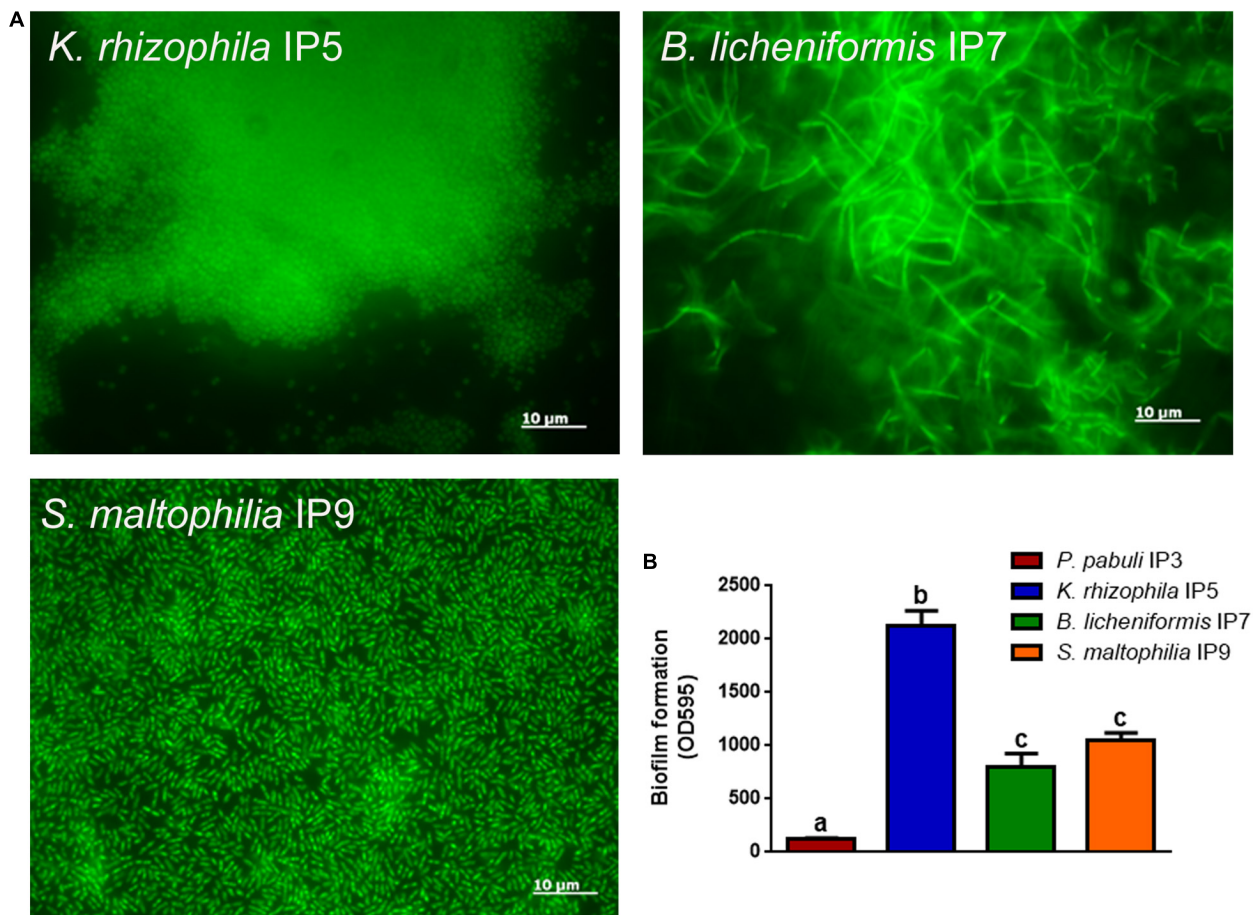
FIGURE 3 | Biofilm formation on glass or plastic surfaces. **(A)** Fluorescence microscope images of the different bacterial strains forming biofilm on glass. **(B)** Biofilm formation ability of the bacteria on plastic. To evaluate statistical significance, a one-way ANOVA analysis with the Bonferroni post-test was used (different letters indicate $p < 0.05$).

(Kumar and Kumar, 1999). *Basilica di San Nicola in Carcere* Church, located near the Tiber River, is rich in humidity, favoring the growth of microorganisms. Humidity can react with the matrix of stones, inducing degradation, and especially may cause dissolution of carbonates, solubilization of other elements, and subsequently, erosion of the materials. Microorganisms, together with these abiotic factors, use stone materials as a substrate, contributing to the increase of deterioration and the aesthetic damage (Sterflinger and Piñar, 2013; Dubey and Jain, 2014). Indeed, it is known that the biodeterioration process can be due to the production of inorganic acids like nitrous and nitric acid and salts like nitrite and nitrate by nitrifying bacteria (Mansch and Bock, 1998). Therefore, the results of FTIR analysis, which highlighted the presence of nitrate residues and gypsum on salt efflorescences, strongly correlate with metabolism of *Bacillus, Kocuria*, and *Paenibacillus* species isolated from the hypogeum wall (Laiz et al., 2000; Castrillón Rivera et al., 2019) (**Figure 4**). In agreement, at high humidity, soluble calcium carbonate is transformed into calcium sulfate, namely gypsum, causing visible salt efflorescence (Atlas et al., 1988).

Moreover, among the isolated bacteria, *K. rhizophila* IP5, *B. licheniformis* IP7, and *S. maltophilia* IP9 were able to form biofilm. This bacterial aggregation is the main cause of biodeterioration, since microorganisms can resist adverse abiotic conditions and many biocides and are also able to deteriorate manufactures (Stewart, 2002; Dakal and Cameotra, 2012; Rivera et al., 2018). This was confirmed by the antibiotic susceptibility test that revealed several resistances for the different strains; indeed, it has been reported that some resistance mechanisms are common to both biocides and antibiotics (Scientific Committee on Emerging and Newly Identified Health Risks [SCENIHR], 2009). In recent years, to solve problems linked to resistance to biocides, new technologies have been developed to combat biodeterioration and to restore stone buildings, using bacterial metabolism. Microbially induced carbonate precipitation was studied as a promising technology for the bioremediation of such structures, thanks to the eco–friendly, self-healing, and highly durable nature of these remedies. Furthermore, nitrate-reducing aerobic and facultative anaerobic bacteria could be chosen for their ability to remove nitrate crusts and efflorescences from stone materials (Dhami et al., 2014; Romano et al., 2019).
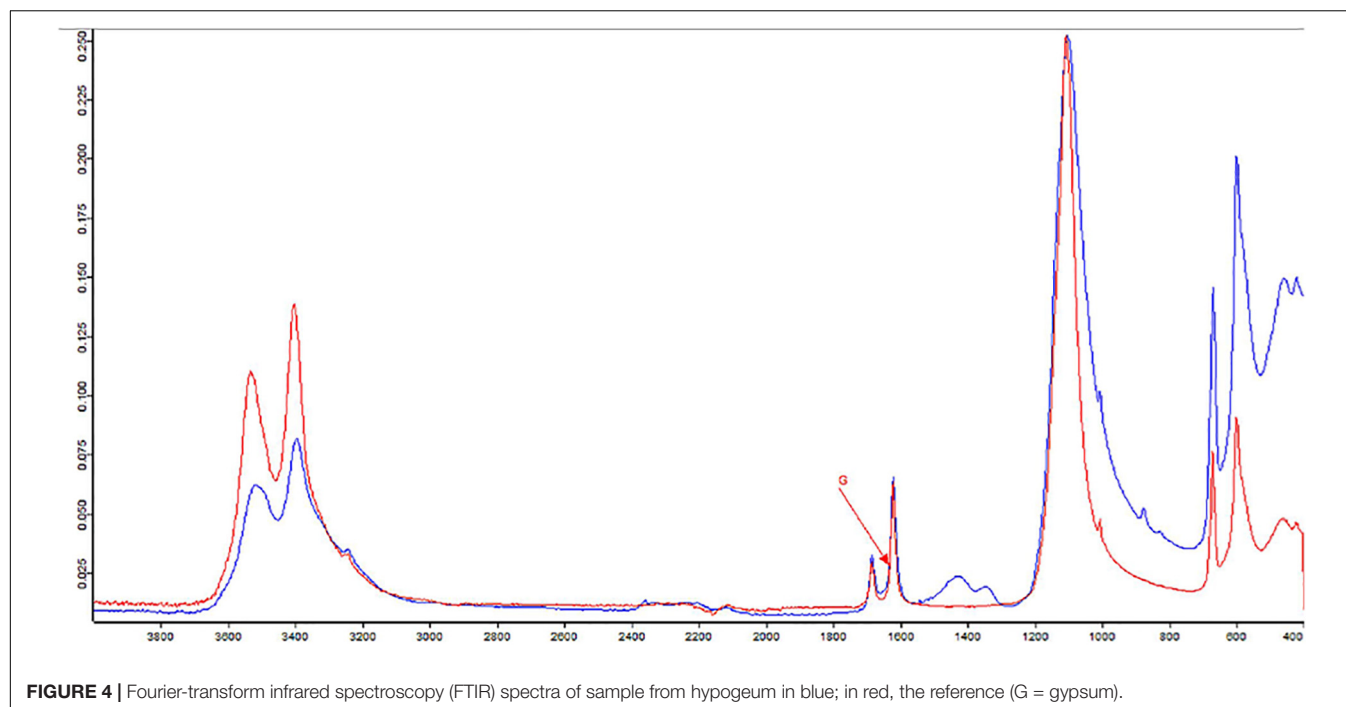
FIGURE 4 | Fourier-transform infrared spectroscopy (FTIR) spectra of sample from hypogeum in blue; in red, the reference (G = gypsum).

The combination of the metagenomic approach with the traditional microbiology integrated with the powerful diagnostic technique of FTIR spectroscopy might reveal new complex structures of microbial communities that will help to establish preservation and restoration strategies.

CONCLUSION

Preservation of CH is very difficult, and multidisciplinary approaches are highly demanded. Abiotic- and biotic-derived damages in CH mix continuously make the individuation of the cause impossible or extremely difficult, as well as its removal. For instance, efflorescence from a fresco could pave the way for microbial colonization that, in turn, could activate other chemical reactions transforming the materials. Thus, combined strategies for monitoring damages on CH and finding their cause are needed. This study proposes and tries validating a workflow consisting in novel molecular approaches and standard microbiological and chemical analysis. Notably, we here define an intervention protocol for sampling, sequencing, and analysis of the taxonomical composition of the microbiome on the surface of the hypogeum of the *Basilica di San Nicola in Carcere* Church. The overlap between the two approaches is feeble but present; probably, the huge number of uncultivable microorganisms bias the output and make the comparison with standard isolation procedures difficult. Nevertheless, the new bioinformatic tool here presented, ALISIA, could represent a fast and reliable means for understanding the complex composition of the biotic components of CH such as frescos, paintings, and statues, allowing, where needed, a tailored intervention for restoring the manufactures.

DATA AVAILABILITY STATEMENT

The datasets generated and analyzed for this study can be found in the repositories DDBJ/ENA/GenBank as BioProject PRJNA578894 and BioSample SAMN13086612.

AUTHOR CONTRIBUTIONS

AG designed ALISIA, performed the sequencing, performed the bioinformatic analysis, and edited the manuscript. MB performed the molecular analysis, performed the metadata analysis, and edited the manuscript. EZ performed the molecular analysis and drafted and edited the manuscript. RF performed the molecular analysis. ES performed the microbiological experiments. MS performed the FTIR analysis. DU conceived the study, edited the manuscript, and provided funding. MR conceived the study, drafted and edited the manuscript, and provided funding.

REFERENCES

Amann, R. I., Ludwig, W., and Schleifer, K. H. (1995). Phylogenetic identification and in situ detection of individual microbial cells without cultivation. *Microbiol. Rev.* 59, 143–169. doi: 10.1128/mmbr.59.1.143-169.1995

Atlas, R. M., Chowdhury, A. N., and Gauri, K. L. (1988). Microbial calcification of gypsum – rock and sulfated marble. *Stud. Conserv.* 33, 149–153. doi: 10.1179/sic.1988.33.3.149

Bergkessel, M., and Guthrie, C. (2013). Colony PCR. *Biolab* 529, 299–309. doi: 10.1016/B978-0-12-418687-3.00025-2

Camacho, C., Coulouris, G., Avagyan, V., Ma, N., Papadopoulos, J., Bealer, K., et al. (2009). BLAST+: architecture and applications. *BMC Bioinform.* 10:421. doi: 10.1186/1471-2105-10-421

Caneva, G., Nugari, M. P., and Salvadori, O. (2008). "Control of biodeterioration and bioremediation techniques," in *Plant Biology for Cultural Heritage: Biodeterioration and Conservation*, eds M. P. Nugari, and O. Salvadori (Los Angeles: Getty Conservation Institute).

Caneva, G., and Salvadori, O. (1989). "Sistematica e sinsistematica delle comunità vegetali nella pianificazione di interventi di restauro TT - Systematics and synsystematics of plant communities in the planning of conservation treatment," in *Il Cantiere Della Conoscenza: il Cantiere del RESTAuro: Atti Del Convegno Di Studi*, Bressanone.

Capodicasa, S., Fedi, S., Porcelli, A. M., and Zannoni, D. (2010). The microbial community dwelling on a biodeteriorated 16th century painting. *Int. Biodeterior. Biodegrad.* 64, 727–733. doi: 10.1016/j.ibiod.2010.08.006

Castrillón Rivera, L., Palma Ramos, A. I., Castañeda Sánchez, J., and Elisa Drago Serrano, M. (2019). "Origin and control strategies of biofilms in the cultural heritage," in *Antimicrobials, Antibiotic Resistance, Antibiofilm Strategies and Activity Methods*, ed. S. Kırmusaoğlu (London: IntechOpen), doi: 10.5772/intechopen.79617

Dakal, T. C., and Cameotra, S. S. (2012). Microbially induced deterioration of architectural heritages: routes and mechanisms involved. *Environ. Sci. Eur.* 24:36. doi: 10.1186/2190-4715-24-36

Dhami, N. K., Reddy, M. S., and Mukherjee, A. (2014). Application of calcifying bacteria for remediation of stones and cultural heritages. *Front. Microbiol.* 5:304. doi: 10.3389/fmicb.2014.00304

Dubey, S., and Jain, S. K. (2014). Effect of humidity on fungal deteriogens of ancient monuments. *Int. Res. J. Biol. Sci.* 3, 84–86.

Glass, N. L., and Donaldson, G. C. (1995). Development of primer sets designed for use with the PCR to amplify conserved genes from filamentous ascomycetes. *Appl. Environ. Microbiol.* 61, 1323–1330. doi: 10.1128/aem.61.4.1323-1330.1995

Gómez-Rubio, V. (2017). ggplot2 - elegant graphics for data analysis. *J. Stat. Softw.* 77, 1–3. doi: 10.18637/jss.v077.b02

González, J. M., and Saiz-Jiménez, C. (2005). Application of molecular nucleic acid-based techniques for the study of microbial communities in monuments and artworks. *Int. Microbiol.* 8, 189–194.

Gutarowska, B., Celikkol-Aydin, S., Bonifay, V., Otlewska, A., Aydin, E., Oldham, A. L., et al. (2015). Metabolomic and high-throughput sequencing analysis-modern approach for the assessment of biodeterioration of materials from historic buildings. *Front. Microbiol.* 6:979. doi: 10.3389/fmicb.2015.00979

Hanson, B., Zhou, Y., Bautista, E. J., Urch, B., Speck, M., Silverman, F., et al. (2016). Characterization of the bacterial and fungal microbiome in indoor dust and outdoor air samples: a pilot study. *Environ. Sci. Process. Impacts* 18, 713–724. doi: 10.1039/C5EM00639B

Hugenholtz, P. (2002). Exploring prokaryotic diversity in the genomic era. *Genom. Biol.* 3:REVIEWS0003.

Hugerth, L. W., Muller, E. E. L., Hu, Y. O. O., Lebrun, L. A. M., Roume, H., Lundin, D., et al. (2014). Systematic design of 18S rRNA gene primers for determining eukaryotic diversity in microbial consortia. *PLoS One* 9:e95567. doi: 10.1371/journal.pone.0095567

Kumar, R., and Kumar, A. V. (1999). *Biodeterioration of Stone in Tropical Environments: An Overview*. Los Angeles, CA: Getty Publications.

Laiz, L., Recio, D., Hermosin, B., and Saiz-Jimenez, C. (2000). "Microbial communities in salt efflorescences," in *Of Microbes and Art*, eds O. Ciferri, P. Tiano, and G. Mastromei (Boston, MA: Springer), 77–88. doi: 10.1007/978-1-4615-4239-1-6

Lane, D. J. (1991). "6S/23S rRNA sequencing," in *Nucleic Acid Techniques in Bacterial Systematic*, eds E. Stackebrandt, and M. Goodfellow (New York: John Wiley and Sons), 115–175.

Mansch, R., and Bock, E. (1998). Biodeterioration of natural stone with special reference to nitrifying bacteria. *Biodegradation* 9, 47–64. doi: 10.1023/A:1008381525192

Marvasi, M., Vedovato, E., Balsamo, C., Macherelli, A., Dei, L., Mastromei, G., et al. (2009). Bacterial community analysis on the mediaeval stained glass window "Natività" in the florence cathedral. *J. Cult. Herit.* 10, 124–133. doi: 10.1016/j.culher.2008.08.010

Medlin, L., Elwood, H. J., Stickel, S., and Sogin, M. L. (1988). The characterization of enzymatically amplified eukaryotic 16S-like rRNA-coding regions. *Gene* 71, 491–499. doi: 10.1016/0378-1119(88)90066-2

Otlewska, A., Adamiak, J., and Gutarowska, B. (2014). Application of molecular techniques for the assessment of microorganism diversity on cultural heritage objects. *Acta Biochim. Pol.* 61, 217–225.

Pinna, D., and Salvadori, O. (2005). "Meccanismi generali dei processi di biodeterioramento," in *La Biologia Vegetale Per i Beni Culturali, Biodeterioramento e Conservazione*, eds G. Caneva, M. P. Nugari, and O. Salvadori (Firenze: Nardini Editore), 15–34.

Qi-Wang, Ma, G. Y., He, L. Y., and Sheng, X. F. (2011). Characterization of bacterial community inhabiting the surfaces of weathered bricks of Nanjing Ming city walls. *Sci. Total Environ.* 409, 756–762. doi: 10.1016/j.scitotenv.2010.11.001

R Core Team (2018). *R: A Language and Environment for Statistical Computing*. Vienna: R Core Team.

Radaelli, A., Paganini, M., Basavecchia, V., Elli, V., Neri, M., Zanotto, C., et al. (2004). Identification, molecular biotyping and ultrastructural studies of bacterial communities isolated from two damaged frescoes of St Damian's Monastery in Assisi. *Lett. Appl. Microbiol.* 38, 447–453. doi: 10.1111/j.1472-765X.2004.01514.x

Rappé, M. S., and Giovannoni, S. J. (2003). The uncultured microbial majority. *Annu. Rev. Microbiol.* 57, 369–394. doi: 10.1146/annurev.micro.57.030502.090759

Rivera, L. E. C., Ramos, A. P., Sánchez, J. I. C., and Serrano, M. E. D. (2018). "Origin and control strategies of biofilms in the cultural heritage," in *Antimicrobials, Antibiotic Resistance, Antibiofilm Strategies and Activity Methods*, ed. S. Kırmusaoğlu (London: IntechOpen), doi: 10.5772/intechopen.79617

Romano, I., Abbate, M., Poli, A., and D'Orazio, L. (2019). Bio-cleaning of nitrate salt efflorescence on stone samples using extremophilic bacteria. *Sci. Rep.* 9:1668. doi: 10.1038/s41598-018-38187-x

Saiz-Jimenez, C. (2017). *Molecular Biology and Cultural Heritage*. Milton Park: Taylor & Francis Company, doi: 10.1201/9780203746578

Scala, V., Grottoli, A., Cigliano, R. A., Anzar, I., Beccaccioli, M., Fanelli, C., et al. (2017). Careful with that axe, gene, genome perturbation after a PEG-mediated protoplast transformation in *Fusarium verticillioides*. *Toxins* 9:E183. doi: 10.3390/toxins9060183

Schifano, E., Zinno, P., Guantario, B., Roselli, M., Marcoccia, S., Devirgiliis, C., et al. (2019). The Foodborne strain *Lactobacillus fermentum* MBC2 triggers pept-1-dependent pro-longevity effects in *Caenorhabditis elegans*. *Microorganisms* 7:45. doi: 10.3390/microorganisms7020045

Scientific Committee on Emerging and Newly Identified Health Risks [SCENIHR] (2009). Assessment of the antibiotic resistance effects of biocides. *Eur. Comm.* 6, 25–64.

Sert, H., Sümbül, H., and Sterflinger, K. (2007). A new species of *Capnobotryella* from monument surfaces. *Mycol. Res.* 111, 1235–1241. doi: 10.1016/j.mycres.2007.06.011

Skipper, P., and Skipper, L. (2016). "A survey of bacterial colonisation of historic limestone buildings: lincoln cathedral and St. Peter at Gowts, United Kingdom," in *Rehab 2014 – Proceedings of the International Conference on Preservation, Maintenance and Rehabilitation of Historic Buildings and Structures* (Hoboken, NJ: Green Lines Institut).

Stackebrandt, E., Koch, C., Gvozdiak, O., and Schumann, P. (1995). Taxonomic dissection of the genus *Micrococcus: Kocuria* gen. nov., *Nesterenkonia* gen. nov., *Kytococcus* gen. nov., *Dermacoccus* gen. nov., and micrococcus cohn 1872 gen. emend. *Int. J. Syst. Bacteriol.* 45, 682–692. doi: 10.1099/00207713-45-4-682

Sterflinger, K., and Piñar, G. (2013). Microbial deterioration of cultural heritage and works of art — tilting at windmills? *Appl. Microbiol. Biotechnol.* 97, 9637–9646. doi: 10.1007/s00253-013-5283-1

Stewart, P. S. (2002). Mechanisms of antibiotic resistance in bacterial biofilms. *Int. J. Med. Microbiol.* 292, 107–113. doi: 10.1078/1438-4221-00196

Tarsitani, G., Moroni, C., Cappitelli, F., Pasquariello, G., and Maggi, O. (2014). Microbiological analysis of surfaces of leonardo da vinci's atlantic codex: biodeterioration risk. *Int. J. Microbiol.* 2014:214364. doi: 10.1155/2014/214364

Tyler, A. D., Mataseje, L., Urfano, C. J., Schmidt, L., Antonation, K. S., Mulvey, M. R., et al. (2018). Evaluation of oxford nanopore's minion sequencing device for microbial whole genome sequencing applications. *Sci. Rep.* 8:10931. doi: 10.1038/s41598-018-29334-5

Urzí, C., and De Leo, F. (2001). Sampling with adhesive tape strips: an easy and rapid method to monitor microbial colonization on monument surfaces. *J. Microbiol. Methods* 44, 1–11. doi: 10.1016/S0167-7012(00)00227-X

Warscheid, T., and Braams, J. (2000). Biodeterioration of stone: a review. *Int. Biodeterior. Biodegrad.* 46, 343–368. doi: 10.1016/s0964-8305(00)00109-8

Wilimzig, M. (1996). "Deterioration and conservation of stone," in *Proceedings of the 8th International Congress on Deterioration and Conservation of Stone* (Dixon, CA), 579–584.

Zanni, E., Schifano, E., Motta, S., Sciubba, F., Palleschi, C., Mauri, P., et al. (2017). Combination of metabolomic and proteomic analysis revealed different features among *Lactobacillus delbrueckii* subspecies bulgaricus and lactis strains while in vivo testing in the model organism *Caenorhabditis elegans* highlighted probiotic properties. *Front. Microbiol.* 8:1206. doi: 10.3389/fmicb.2017.01206

Conflict of Interest: AG, MB, and MR are associates of the academic startup of Sapienza, SARA EnviMob s.r.l.

The remaining authors declare that the research was conducted in the absence of any commercial or financial relationships that could be construed as a potential conflict of interest.

Differential X-Ray Attenuation in MA-XRF Analysis for a Non-invasive Determination of Gilding Thickness

Sergio Augusto Barcellos Lins [1,2]*, Stefano Ridolfi [3], Giovanni Ettore Gigante [1], Roberto Cesareo [4], Monica Albini [5], Cristina Riccucci [5], Gabriella di Carlo [5], Andrea Fabbri [2], Paolo Branchini [2] and Luca Tortora [2,6]

[1] Department of Basic and Applied Sciences for Engineering, Sapienza University of Rome, Rome, Italy, [2] Surface Analysis Laboratory, Istituto Nazionale di Fisica Nucleare Sezione di Roma Tre, Rome, Italy, [3] Ars Mensurae srl, Rome, Italy, [4] Istituto di Matematica e Fisica, Università degli Studi di Sassari, Sassari, Italy, [5] Institute for the Study of Nanostructured Materials, National Research Council, Rome, Italy, [6] Department of Sciences, Roma Tre University, Rome, Italy

When investigating gilded artifacts or works of art, the determination of the gilding thickness plays a significant role in establishing restoration protocols or conservation strategies. Unfortunately, this is done by cross-sectioning the object, a destructive approach not always feasible. A non-destructive alternative, based on the differential attenuation of fluorescence radiation from the sample, has been developed in the past years, but due to the intrinsic random nature of X-rays, the study of single or few spots of an objects surface may yield biased information. Furthermore, considering the effects of both porosity and sample inhomogeneities is a practice commonly overlooked, which may introduce systematic errors. In order to overcome these matters, here we propose the extrapolation of the differential-attenuation method from single-spot X-ray fluorescence (XRF) measurements to macro-XRF (MA-XRF) scanning. In this work, an innovative algorithm was developed for evaluating the large amount of data coming from MA-XRF datasets and evaluate the thickness of a given overlapping layer over an area. This approach was adopted to study a gilded copper-based buckle from the sixteenth to seventeenth century found in Rome. The gilded object under investigation was also studied by other analytical techniques including scanning electron microscopy coupled with energy dispersive spectroscopy (SEM-EDS). Previous results obtained from SEM-EDS were used to confront the data obtained with the proposed methodology and validate it. MA-XRF elemental distribution maps were fundamental in identifying and choosing sampling areas to calculate the thickness of the gilding layer, avoiding lead islands present in the sample that could negatively influence the results. Albeit the large relative standard deviation, the mean thickness values fell within those found in literature and those obtained from previous studies with SEM-EDS. Surface fissure has been found to deeply affect the results obtained, an aspect that is often disregarded.

Keywords: gilding, MA-XRF, differential attenuation, Cu-based artifacts, thickness estimation

INTRODUCTION

The practice of gilding dates back from antiquity and is still performed until today by means of different techniques, as electrochemical deposition instead of the toxic mercury fire-gilding (Anheuser, 1997). With the course of time, a wide array of gilding methods has been developed and those most widespread in antiquity were the application of a gold foil (or leaf) to a prepared substrate, mercury gilding, or depletion (Lechtman et al., 1982; Ingo et al., 2013; Pessanha et al., 2019b). The method chosen also depends on the type of substrate used, which varies from leather, plaster and wood to metals (Cesareo, 2003; Eveno et al., 2014; Tortora et al., 2014; Biocca et al., 2016; Shabunya-Klyachkovskaya et al., 2017; Iorio et al., 2019). In the case of fire-gilding, a mixture made of mercury and gold (amalgam) is applied to a clean metallic substrate and fired in temperatures around $300°C$ to volatilize the mercury. The surface is then finished with the use of burnishers and the resulted thickness can range from $1\,\mu m$ to about $10\,\mu m$ or more (Anheuser, 1997; Ingo et al., 2013).

Due to the variety of gilding methods used in the past and their intrinsic variations (amalgam composition and thickness), the investigation of archaeological gilded objects has raised interest in the community, aiming to investigate the methodology and materials used and the conservation state of these objects (Abdelhamid et al., 2010; Ingo et al., 2016, 2018; Graziani et al., 2020). The most straightforward way of studying a gilded objects' characteristics and gilding method is by analyzing a cross-section of the object. This approach yields direct information of the thickness of the gold layer and the binding mechanism between gold layer and substrate. Scanning electron microscopy coupled with energy dispersive spectroscopy (SEM-EDS) goes even further, giving a direct information on the chemical composition of the substrate and the gilding layer (Ingo et al., 2016). Nevertheless, the study of cross-sections requires sampling and is a destructive method, being rarely feasible when it comes to valuable artifacts (Nørgaard, 2017).

The focus on non-destructive techniques has always been a priority in cultural heritage science, and X-rays fluorescence (XRF) is commonly used as a standard approach (Guerra, 2000; Bottaini et al., 2017). This technique can provide information on the chemical composition of a sample surface and even the thickness of an existing overlapping layer—giving the conditions are optimal (van Espen, and Lemberge, 2000; Giurlani et al., 2019). Nonetheless, archaeological artifacts are known to be extremely inhomogeneous and the analysis of only few spots of the sample's surface may lead to misleading conclusions (Cesareo et al., 2010; Brunetti et al., 2016). Extrapolating the one-dimensionality of XRF technique to another dimension, i.e., scanning [or capturing in full field (Romano et al., 2014)] a surface instead of analyzing few spots, is a practice that is now becoming widespread in cultural heritage science and is generally known as macro-XRF scanning (MA-XRF) (Dik et al., 2008). This approach increases significantly the understanding of the sample, by generating bi-dimensional maps of elemental distribution and providing a large XRF dataset to work with.

Measuring the thickness of a given surface layer placed to protect an artifact or, as in the case of gilding, to turn it more attractive, can be performed by a method that uses the differential attenuation of fluorescence radiation coming from the internal matrix (substrate) (Cesareo et al., 2015). This method is based on the concatenated effect of two distinct processes: (a) the production of fluorescence photons in the internal matrix and (b) the differential attenuation in the surface layer. The latter can become quite complex when dealing with amalgam gilded objects, since the chemical composition of the surface layer is not constant throughout the sample and micro-fissures can be present in amounts sufficient to introduce significant errors. Moreover, the metallic substrate of archaeological artifacts can present considerable inhomogeneities in their composition, caused by either smelting, molding, or working. Inhomogeneities in the sample hinders a precise estimation of the matrix un-attenuated signal and therefore must be avoided. Furthermore, the presence of protective layers, such as mica or paraloids, must be cautiously accounted. The existence of an "extra" layer on top of the gilding layer further attenuates the photons coming from the substrate and therefore introduce systematic errors. If the protective layer is known, as in the case of paraloids, the further attenuation introduced can be calculated and Equation (5) can be adjusted accordingly (Nardes et al., 2019). Past interventions or cleaning routines applied to the objects surface can be assessed by the complete absence of soil impurities in the elemental distribution maps generated with the MA-XRF data. Therefore, a proper interpretation of these maps and the assessment of the presence or not of additional layers are crucial for selecting suitable regions where to apply the differential attenuation method.

In this context, the current research proposes the use of MA-XRF scan datasets to investigate the gilding technique employed in a Sixteenth to Seventeenth century AD buckle found during the dredging of Tiber river (Rome, Italy), by applying the differential attenuation method and calculating the gilding thickness in a totally non-invasive manner. The use of MA-XRF elemental distribution maps is crucial to select suitable regions from the sample surface where to calculate the thickness. Moreover, an algorithm capable of analyzing thousands of *spectra* and simulating the chemical composition of the overlapping layer, considering the presence of fissures or pores, was developed to account for the variations present in this layer. This allows a more precise calculation of the superficial layer attenuation coefficients. The method dismisses any need for cross-sectioning, sampling or even sample preparation, being completely non-destructive. Nonetheless, the buckle investigated has been previously studied by SEM-EDS (Ingo et al., 2018), where a sectioning of a small part in the rightmost portion of the object was made. Results from SEM-EDS analysis have been used to validate the proposed methodology.

MATERIALS AND METHODS

A gilded Cu-based buckle dating from the Sixteenth to Seventeenth century found during the dredging of the Tiber river

in Rome was analyzed by scanning electron microscopy (SEM) coupled with energy dispersive spectroscopy (EDS) and by macro X-ray fluorescence (MA-XRF) scanning. The object was cleaned with distilled water followed by ethanol rinsing. No conservation treatment was performed. SEM images were used to confront the data obtained from the differential attenuation calculations and assess the reliability and quality of the data.

To obtain the most representative data, the thickness calculations were performed in specific regions of the sample in a way to avoid great geometrical variations and matrix composition inhomogeneities. The intensity ratio of Cu-K_α and Cu-K_β characteristic lines for an infinitely thick matrix were experimentally measured in the central portion of the sample (where no gold cover is visible), being the mean value obtained with 6 different spots.

The Differential Attenuation Method

Considering one of the two monochromatic radiations used in the differential attenuation method (for example the K_α line of one of the elements present in the internal matrix) and a generic tube-sample-detector geometry (**Figure 1**), the following equation is valid for the photons detected in the spectral window a (I_a):

$$I_a = I_0 \; AK \cdot \varepsilon \, (E_a) \cdot e^{-(\mu_L(E_0) \cos \Psi_1 + \mu_L(E_a) \cos \Psi_2)d}$$
$$\int_0^t e^{-[\mu_s(E_0)] \cos \Psi_1 + \mu_s(E_a)] \cos \Psi_2 \,]x} \cdot dx \tag{1}$$

By integrating the equation above one obtains:

$$I_a = I_0 \; AK \cdot \varepsilon \, (E_a) \cdot \frac{1 - e^{-[\mu_s(E_0) \cos \Psi_1 + \mu_s(E_a) \cos \Psi_2]t}}{\mu_s \, (E_0) \cos \Psi_1 + \mu_s \, (E_a) \cos \Psi_2}$$
$$\cdot e^{-(\mu_L(E_0) \cos \Psi_1 + \mu_L(E_a) \cos \Psi_2)]d} \tag{2}$$

where I_0 is the exciting photons beam intensity at energy E_0, A is the overall term taking into account all the factors that determine the production of photons detected in the spectral window a, K is the geometrical factor, $\varepsilon(E_a)$ is the detector efficiency, $\mu_L(E_0)$ and $\mu_L(E_a)$ are the superficial layer attenuation coefficients at impinging and outgoing photon energies, respectively, d represents its thickness, $\mu_s(E_0)$ and $\mu_s(E_a)$ are the attenuation coefficients of the internal matrix, Ψ_1 and Ψ_2 are the incident beam and output angles with the sample surface, respectively and t is the internal matrix thickness.

The ratio between two monochromatic radiations can then be written, assuming that the detector efficiency and geometrical factors are the same for both lines, as:

$$\left(\frac{I_a}{I_b}\right) = \left(\frac{I_a}{I_b}\right)_{thin} \cdot \frac{\mu_s \, (E_0) \cos \Psi_1 + \mu_s \, (E_b) \cos \Psi_2}{\mu_s \, (E_0) \cos \Psi_1 + \mu_s \, (E_a) \cos \Psi_2}$$
$$\cdot \chi \cdot e^{[-\mu_L(E_a) + [\mu_L(E_b)] \cos \Psi_2 d} \tag{3}$$

where $\chi = \frac{1 - e^{-[\mu_s(E_0)\cos(\Psi_1) + \mu_s(E_a)\cos(\Psi_2)]t}}{1 - e^{-[\mu_s(E_0)\cos(\Psi_1) + \mu_s(E_b)\cos(\Psi_2)]t}}$

The first term (referred to as thin) is the ratio when the self-attenuation in the internal matrix is completely negligible,

the second and third terms consider the contribution of this effect and the fourth term considers the differential attenuation undergone in the surface layer. Only the fourth term depends on the surface layer, while the remaining terms depend only on the internal matrix. When the exponential contributions in the third term (χ) are negligible (having t large enough that the term can be approximated to 1), the sample can be assumed infinitely thick.

When the two lines are relative to a single element, as in the case of the lines K_α and K_β of copper, their ratio is fixed and well-known (Cesareo et al., 2009).

Neglecting the differential attenuation in the superficial layer and considering an infinitely thick approximation, the matrix ratio can be given by the following equation:

$$\left(\frac{I_a}{I_b}\right)_{thick} = \left(\frac{I_a}{I_b}\right)_{thin} \cdot \frac{\mu_s \, (E_0) \cos \Psi_1 + \mu_s \, (E_b) \cos \Psi_2}{\mu_s \, (E_0) \cos \Psi_1 + \mu_s \, (E_a) \cos \Psi_2} \tag{4}$$
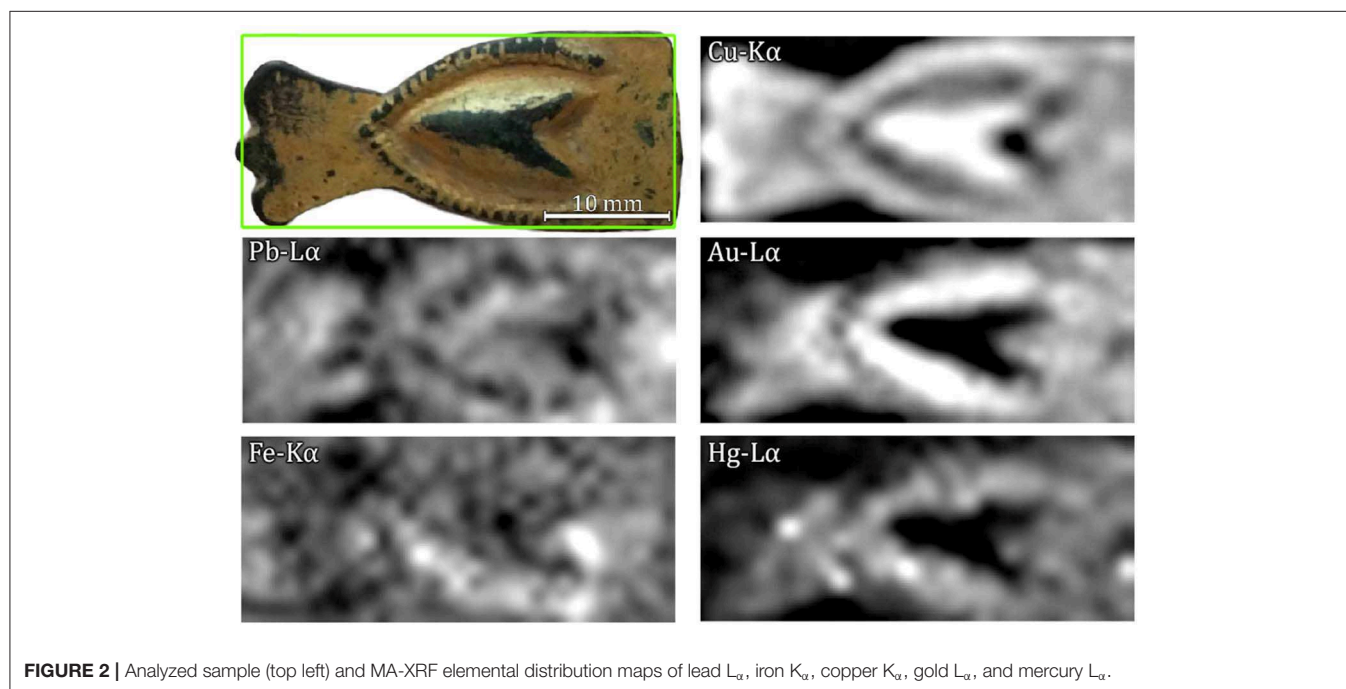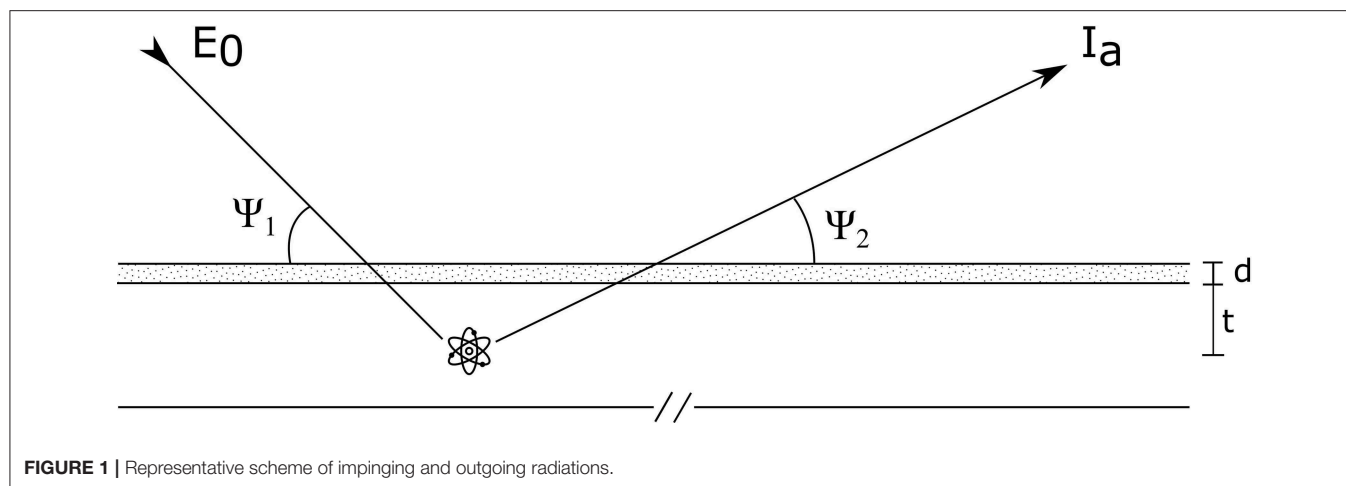
The values for infinitely thin samples can be calculated from the fundamental parameters (Cesareo et al., 2010), and therefore—if the sample composition is known—one can calculate the intensity ratio for a thick sample. This value can also be experimentally determined by directly measuring the sample exposed substrate or by creating a calibration model via Monte Carlo simulations (Pessanha et al., 2019a) when the former is not feasible.

Therefore, assuming the attenuation coefficient of the overlapping layer is known (its composition is known or experimentally determined using the acquired XRF data) and that the matrix can be considered infinitely thick, the superficial layer thickness is finally given by Equation (5) below (Cesareo et al., 2016; Nardes et al., 2019):

$$d = \frac{sin \Psi_2}{-\mu_L\left(E_{K_\alpha}\right) + \mu_L\left(E_{K_\beta}\right)} \ln \left[\frac{\left(\frac{I_{K_\alpha}}{I_{K_\beta}}\right)}{\left(\frac{I_{K_\alpha}}{I_{K_\beta}}\right)_{thick}} \right] \tag{5}$$

MA-XRF Scanning

The system used to record and process the XRF data was a *custom-made* portable scanner, made by the *Istituto Nazionale di Fisica Nucleare (INFN)—Roma Tre Division*, and a private company *Ars Mensurae*. This system has been employed in previous studies (Iorio et al., 2019) and comprises a movable stage—where the sample is positioned—and an exchangeable head composed of a collimated Moxtek® Ta-target X-ray tube and an AMPTEK® 123SDD detector. The spot size is of roughly 1 mm^2 and the total scanned area was of 34×15 mm^2, enough to cover the entirety of the sample. The tube operated at 37 KV and 17 μA. The dwell-time per pixel was of 7 s, resulting in roughly 60 min of acquisition time. The system was calibrated using an SRM 1115 NIST Standard reference material with the following composition expressed as mass fraction, in %: Copper 87.96, Zinc 11.73, Lead 0.013, Iron 0.13, Tin 0.10, Nickel 0.074, and Phosphorus 0.05.

FIGURE 1 | Representative scheme of impinging and outgoing radiations.

FIGURE 2 | Analyzed sample (top left) and MA-XRF elemental distribution maps of lead L_α, iron K_α, copper K_α, gold L_α, and mercury L_α.

SEM-EDS

Backscattered images and Field-emission (FE) SEM images were acquired with a SEM Stereoscan 360 system from Cambridge, UK, equipped with a LaB_6 filament and a LEO Gemini 1530 microscope from Zeiss, Germany. The former coupled to an INCA 250 and the latter to an INCA 450 energy-dispersive X-ray spectrometers (EDS) both by Oxford Instruments Analytical, UK. The images were collected with acceleration voltages up to 20 kV.

Prior to the analysis, the sample cross-section was coated with either C or Cr. This procedure is required to avoid charging effects. Carbon was deposited with an Emitech sputter coater model K550, a K250 carbon coating attachment and a carbon cord. The carbon film deposited was ∼3 nm thick. As for the chromium film, the deposition procedure

was performed with a Bal-Tech SCD 500 at a 5×10^{-3} mbar pressure to ensure a constant thickness of about 0.5 nm.

RESULTS AND DISCUSSION

Figure 2 reports the elemental maps distribution acquired by the MA-XRF scanning system. The elemental distribution maps show mercury correlated to gold. The simultaneous and correlated presence of both elements are an indicative that mercury and gold are mixed in the uppermost, gilded layer. Although MA-XRF information cannot be used to distinguish fire-gilding from cold-gilding, it certainly can strongly suggest the use of a mercury-gilding technique. This was also confirmed by previous SEM analysis performed by Ingo et al. (2018),
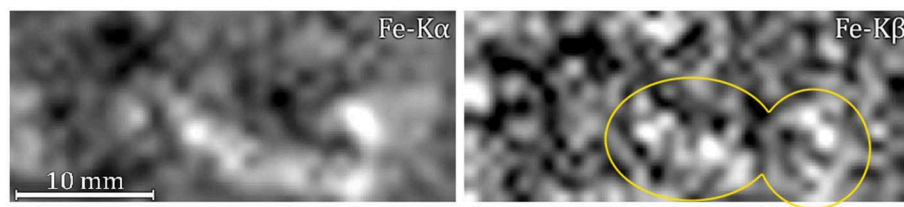
FIGURE 3 | Elemental distribution maps of iron K_α **(left)** and iron K_β **(right)**.

which demonstrated that this gilded object was produced by fire-gilding technique.

The elemental maps also show a rather inhomogeneous distribution of certain elements, with a higher concentration of lead in the rightmost part of the sample and of iron in the lower part.

The explanation for the latter may be three-fold: (a) the tube-sample-detector geometry—being the detector on the left-hand side of the tube—causing an overestimation of iron peaks or an increase in Cu-escape peaks (Trojek, 2011), (b) the preferential deposition of iron impurities during the burial period in the lower-concave region, or (c) a deposition of iron in both concave regions during the burial period combined with the geometrical factor. Due to the central relief in the sample, the combined effect described in (c) results in an increase in the signal from the lower concave region and a lower signal from the upper concave region. The elemental distribution map of iron is better represented in **Figure 3**, where a comparison between iron-K_α and iron-K_β maps is shown. It can be observed that the signal contribution is due mostly to the K_α-line (maximum net area of 242 counts against 55 from K_β), meaning that iron is not present as an alloying element but as an impurity deposited in the concave parts of the sample probably during the burial period. Furthermore, the characteristic low signal of alloy impurities detected by XRF would be suppressed by the gold layer deposited on the surface. Moreover, concentrations of secondary metals, such as iron and aluminum, appear frequently in corroded bronzes that have been buried for prolonged periods of time (Nørgaard, 2017).

For what concerns the lead presence, a lead segregation can occur if its content within the copper alloy exceeds 10 wt.% (Quaranta et al., 2014). On the other end, casting conditions, can play a significant role in the lead segregation/precipitation. In fact, lead and copper have significantly different melting temperatures and if the cooling rate is fast enough, the phase-diagram is disturbed and lead precipitates into a different phase (Callister, 2007). Moreover, both lead-L_α and -L_β elemental distribution maps are identical and with reasonable maximum net areas of 227 and 124, respectively, being indicative that the lead signal comes indeed from underneath the gilding layer.

Since inhomogeneities and contaminations were detected in the sample, some areas of interest (AoIs) shown in **Figure 4** were selected to well-define the areas where to apply the differential attenuation method. This was done in order to avoid the presence of lead islands and areas with higher iron signal for
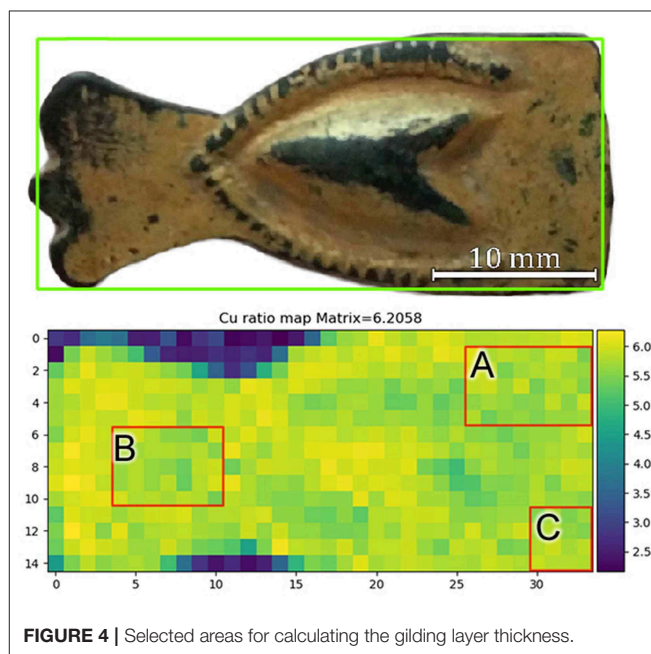
FIGURE 4 | Selected areas for calculating the gilding layer thickness.

TABLE 1 | Variations in the linear attenuation coefficients with varying quantities of mercury and gold.

Hg (%)	μ_L(Cu-K_a) (cm^{-1})	μ_L(Cu-K_β) (cm^{-1})	$-\mu_L$(Cu-K_a) + μ_L(Cu-K_β) (cm^{-1})
2	3,930	3,038	−892
4	3,909	3,021	−887
6	3,888	3,005	−882
8	3,867	2,989	−877
10	3,846	2,972	−873
12	3,824	2,956	−868
14	3,803	2,940	−863
16	3,782	2,923	−858
18	3,761	2,907	−853
20	3,739	2,890	−848
22	3,718	2,874	−844

the calculation of the gilding layer thickness. The dataset is then restricted to 91 pixels out of the 310 pixels where gold was detected (**Figure 4**).

Amalgam-gilded artifacts can undergo corrosion (Ingo et al., 2016, 2018), as opposed to what is normally expected from golden

FIGURE 5 | SEM-EDS images from sample's cross section reporting different gilding thicknesses ranging from 3 μm **(A)** to 1.6 μm **(B)**. A general overview of the gilding layer on top of a corrosion substrate presenting a high porosity and variable thickness **(C)**.
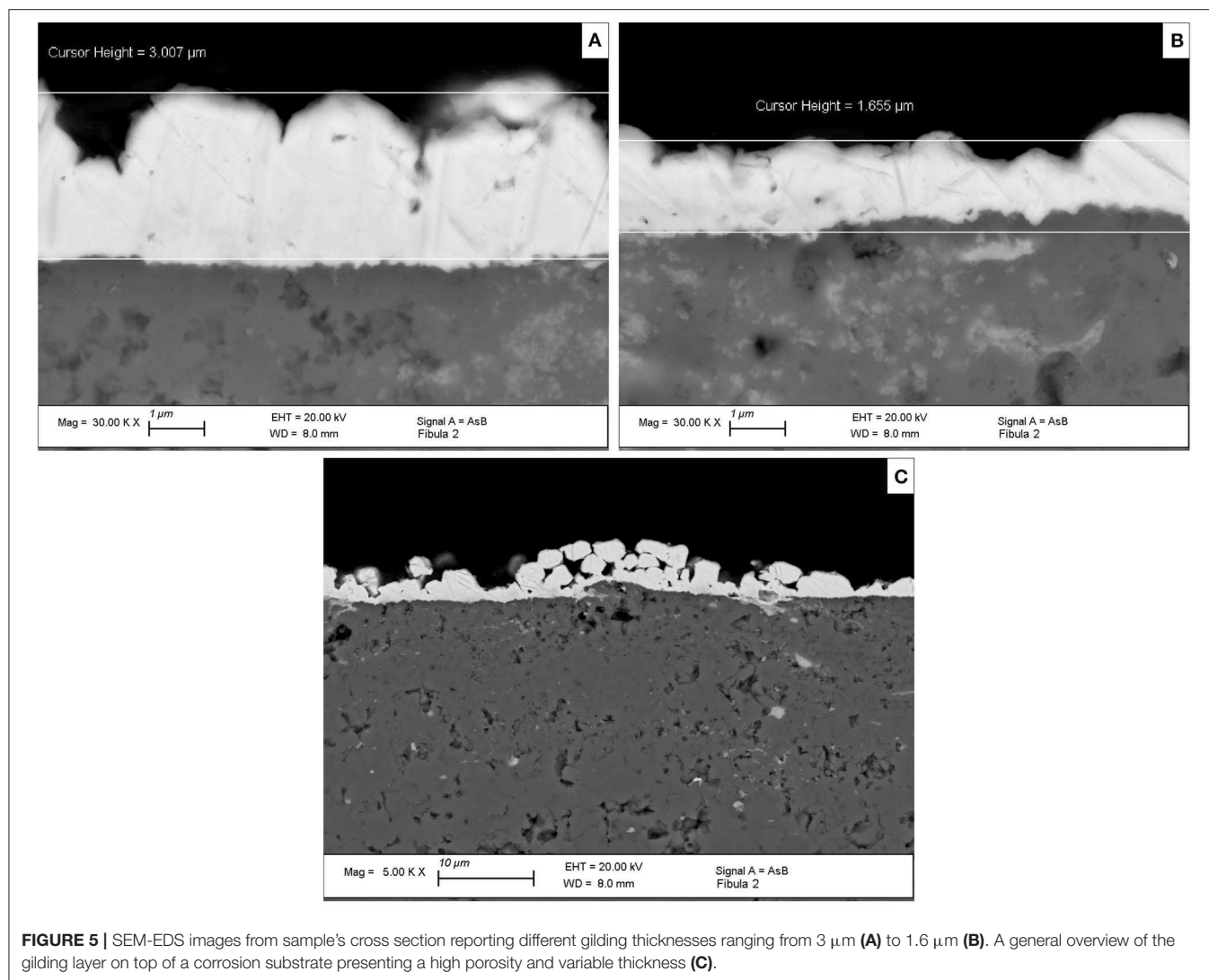
objects. Micro-pores and fissures that remain in the finished gilded surface still allow the interaction between copper and corroding species from the environment (Ingo et al., 2018). The intermediate corrosion product layer created by this process and between the gold surface and the bulk metal can vary in thickness (Robbiola et al., 1998). In Equation (5) for the thickness calculation, the thick sample ratio $[(I_{K\alpha}/I_{K\beta})_{thick}]$ is used acting as a calibration factor and it was determined by measuring six spots in the central portion of the artifact, where no gold was observed (**Figure 2**). This thick ratio supposedly represents the substrate directly in contact with the overlapping gilded layer, and the average measured value obtained was 6.206.

The amount of residual mercury present in the finished gilded layer can vary from 25 wt.% (near the ζ-phase α′-phase border in the Au-Hg phase-diagram) to 0.05 wt.% under a 600°C heating. However, a finished layer will usually retain about 8–25% of mercury (Anheuser, 1997). This amount varies according to the temperature used in the firing step, the initial mercury concentration (about 80–90 wt.%) and the thickness of the layer

applied prior firing (Anheuser, 1997; Ingo et al., 2013). Gold and mercury have very close atomic numbers (92 and 93, respectively) but have a slight discrepancy in density (19.28 and 13.53 g/cm^3, respectively). Variations in the mercury content present in the alloy (±10%) induce changes in the attenuation coefficients difference (2–3%) that are much less than the observed statistical uncertainty. Therefore, to estimate the attenuation coefficient for the K-lines of copper [μL variables in Equation (5)] of the gold layer, a chemical composition of 88 wt.% Au and 12 wt.% Hg was simulated and attributed to the layer (**Table 1**).

As previously stated, fire-gilded objects are usually characterized by the presence of several micro-pores and fissures. In **Figure 5**, SEM-EDS analysis of the sample cross-sections is reported. A highly fissured bright layer on top of a darker region (corrosion product layer) can be observed in **Figure 5C**. The presence of fissures drastically reduces the density of the superimposing gold layer (Ager et al., 2017; Giurlani et al., 2019) and if not taken into account may lead to misleading conclusions in regard of thickness calculation. As the

method used in the study proposes a non-invasive approach, the fissure percentage estimated to account for the fissure influence was calculated through a simple image analysis of top-view (backscattered) SEM images, comparing the difference between the bright (gold) and dark (copper) pixels.

The estimated fissure value was fed into the algorithm to correct the attenuation coefficients and density of the gold layer, simulating the gold *stratum* as a homogeneous mixture of air and gold-mercury alloy. **Figure 6** shows an exponential increase in both standard deviations and mean values obtained when fissure percentage increases. The joint effect of substrate composition thickness variation (corrosion) and varying fissure volumes greatly contribute to a high standard deviation. In this way, as the mean thickness values may fall within a similar region, the direct influence of fissures over the mean calculated thickness cannot be directly measured. Nevertheless, a large standard deviation is not unreasonable. The gilding layer presents an inhomogeneous thickness distribution as demonstrated by the SEM-EDS images (1.6 and 3 μm) (**Figures 5A,B**).

The minimum detectable thickness can be calculated by the following relation:

$$\Delta d = \frac{\sqrt{1 + \left(\frac{I_{K_\alpha}}{I_{K_\beta}} \right)}}{\sqrt{I_{K_\alpha}}} \frac{\sin \Psi_2}{-\mu_L \left(E_{K_\alpha} \right) + \mu_L \left(E_{K_\beta} \right)} \quad (6)$$

The copper Kα/Kβ ratio statistical error is 2.5%, having a corresponding minimum detectable thickness of 0.26 (Equation 6), which is almost constant. The observed standard deviation in the AoI (0.43 μm) can be interpreted, being statistical, as the square root of the quadratic sum of the statistical contribution and the remaining sample variation. The latter being 0.32 μm for the AoI, whereas the statistical uncertainty is 0.25, slightly less. The measured error (surface roughness, solid angle, etc.) is part of the sample contribution (σ^2_{sample}). This is true because the measuring error comes mostly from the sample through geometrical factors. When calculating the same parameters for the entire region where gold is found (310 pixels), a larger observed standard deviation is found (0.42 μm), demonstrating that the selected AoI is in fact more homogeneous in respect to the whole sample.The histogram of the calculated thickness distribution for the AoI (91 pixels) is shown in **Figure 7** and, for the selected fissure percentage (12%), the gilded layer thickness mean value obtained was of 1.24 ± 0.43 μm. There is no significant variation between the individual thickness means of the three sampled areas (1.26 ± 0.43, 1.20 ± 0.42, and 1.25 ± 0.39). In addition, it is observed that the histogram shows a normal distribution that supports the statement that the measured mean value looks unbiased.

In **Figure 8** the 3D plot of thickness distributions for the entirety of the gold layer is shown. When performing the calculations over the entire range where gold is detected (310 pixels), the results present systematic errors, where mean thickness values of up to 6.24 μm were observed. The high values are obtained exclusively in the regions where iron or lead are
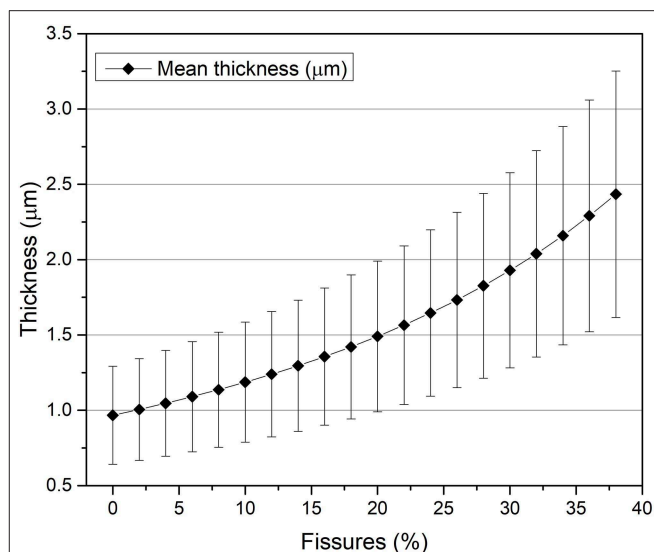
FIGURE 6 | Mean thickness variation with increasing fissure volume.
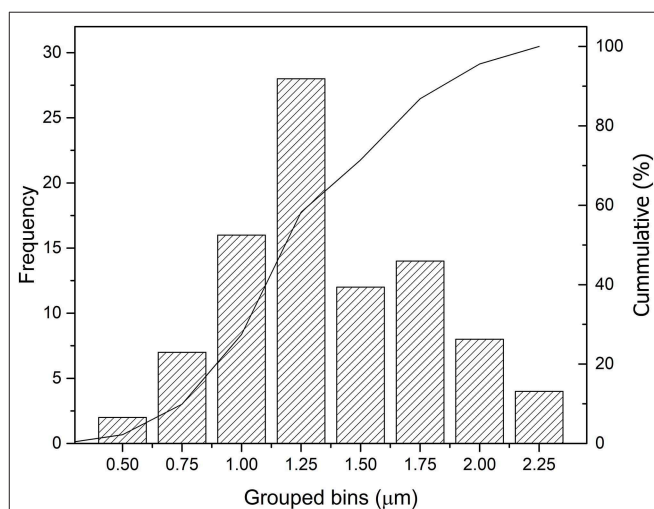
FIGURE 7 | Grouped bins histogram of mean thickness values obtained with all 91 sampled pixels from the limited region of interest.

present in higher quantities, demonstrating the strong influence caused by great sample inhomogeneity.

CONCLUSIONS

In the overall framework of recent research developments in MA-XRF analysis, which started in the last decade (Dik et al., 2008), an attempt was made to evaluate the capacity of measuring thin metallic layers deposited on a sample surface. For the first time, a new algorithm applied to MA-XRF datasets was developed to automatically extract net peak areas and, at the same time, to non-invasively determine the average thickness of an area of a given superimposing layer. The innovative algorithm

FIGURE 8 | 3D plot of mean thickness values obtained for the entire sample region.
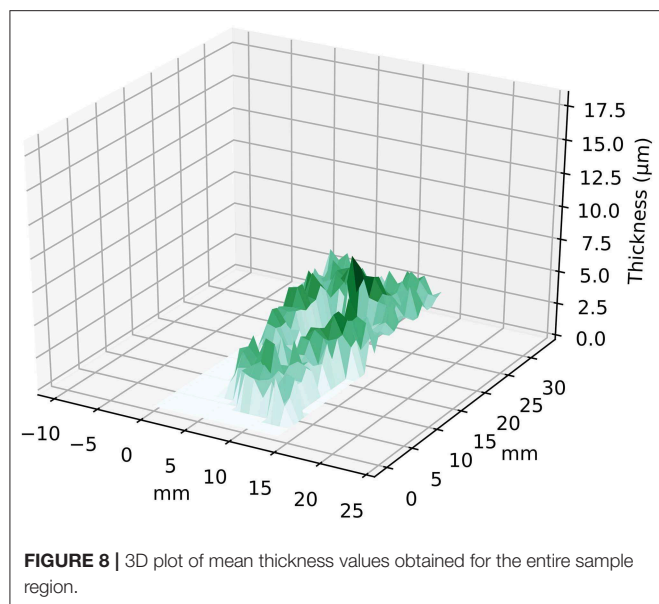
was able to account different layer chemical compositions and fissure volumes, recalculating the linear attenuation coefficient according to the user input.

The results obtained with the proposed methodology were confronted with SEM-EDS cross-section analysis to assess its reliability. The non-invasive approach suggested a mean thickness value of $1.24 \pm 0.43\,\mu m$, with a maximum of $2.20\,\mu m$ for the amalgam-gilded layer, whereas the latter pointed to values of 1.65 and $3.00\,\mu m$ in two different analyzed regions.

Some parameters needed to be considered and cautiously studied to achieve the most accurate results possible. Small variations in the gold and mercury concentration within the binary (Au/Hg) gilding layer were found to not significantly affect the mean thickness results. This is shown by the fact that the changes in the value measured in different areas of interest do not vary between them. Nonetheless, considering the influence of fissures percentage in the superficial gilding layer demonstrated to be of fundamental importance as it influences exponentially the final results. Last, the substrate in direct contact with the studied gilding layer had to be considered homogeneous throughout the sample. Because of that, areas with observable inhomogeneities or considerably different from the exposed central relief had to be unconsidered by the algorithm to not bias the final results.

The larger dataset naturally provided by MA-XRF scans yielded greater statistics than traditional spot measurements and in a faster fashion, thus making it possible to obtain a more accurate mean value as shown by the histogram distribution. Moreover, MA-XRF scans and the elemental distribution maps provided crucial information for selecting suitable regions where to perform the thickness calculations.

Finally, the indirect determination of a mean thickness value for an ancient amalgam-gilding *stratum* in a total non-invasive manner that is satisfactorily close to results obtained through other destructive methods was demonstrated to be possible.

DATA AVAILABILITY STATEMENT

The datasets generated for this study are available on request to the corresponding author.

AUTHOR CONTRIBUTIONS

SB drafted the work and performed the MA-XRF scanning experiments together with SR. SB, GG, and RC performed the scripting and MA-XRF data evaluation. GC, MA, and CR provided the sample for analysis, performed the sample treatment, sectioning, and SEM-EDS analysis. AF and PB developed a custom electronic readout for the MA-XRF scanner. LT conceptualized and reviewed the paper.

FUNDING

ACKNOWLEDGMENTS

REFERENCES

Abdelhamid, M., Grassini, S., Angelini, E., Ingo, G. M., and Harith, M. A. (2010). Depth profiling of coated metallic artifacts adopting laser-induced breakdown spectrometry. *Spectrochi.m Acta. B.* 65, 695–701. doi: 10.1016/j.sab.2010.03.017

Ager, F. J., Ferretti, M., Grilli, M. L., Juanes, D., Ortega-Feliu, I., Respaldiza, M. A., et al. (2017). Reconsidering the accuracy of X-ray fluorescence and ion beam based methods when used to measure the thickness of ancient gildings. *Spectrochim. Acta. B.* 135, 42–47. doi: 10.1016/j.sab.2017.06.017

Anheuser, K. (1997). The pratice and characterization of historic fire gilding techniques. *JOM* 49, 58–62. doi: 10.1007/s11837-997-0015-6

Biocca, P., Santopadre, P., Sidoti, G., Sotgiu, G., de Notaristefani, F., and Tortora, L. (2016). ToF-SIMS study of gilding technique in the fresco Vela della Castità by Giotto's school. *Surf. Interface Anal.* 48, 404–408. doi: 10.1002/sia.5956

Bottaini, C., Brunetti, A., Bordalo, R., Valera, A., and Schiavon, N. (2017). Non-destructive characterization of archeological Cu-based artifacts from the early metallurgy of southern Portugal. *Archaeol. Anthropol. Sci.* 10, 1903–1912. doi: 10.1007/s12520-017-0501-x

Brunetti, A., Fabian, J., la Torre, C., and Schiavon, N. (2016). A combined XRF/Monte Carlo simulation study of multilayered peruvian metal artifacts from the tomb of the priestess of chornancap. *Appl. Phys. A-Mater.* 22, 1–8. doi: 10.1007/s00339-016-0096-6

Callister, W. D. J. (2007). *Materials Science and Engineering An Introduction*, 7th ed. New York, NY: John Wiley & Sons, Inc.

Cesareo, R. (2003). Non-destructive EDXRF-analysis of the golden haloes of Giotto's frescos in the chapel of the scrovegni in Padua. *Nucl. Instrum. Methods Phys. Res. B.* 211, 133–137. doi: 10.1016/S0168-583X(03)01165-0

Cesareo, R., Buccolieri, G., Castellano, A., Lopes, R. T., de Assis, J. T., Ridolfi, S., et al. (2015). The structure of two-layered objects reconstructed using EDXRF-analysis and internal X-ray ratios. *X-Ray Spectrum.* 44, 233–238. doi: 10.1002/xrs.2611

Cesareo, R., Bustamante, A., Fabian, J., Calza, C., dos Anjos, M., Lopes, R. T., et al. (2010). Energy-dispersive X-ray fluorescence analysis of a pre-Columbian funerary gold mask from the museum of Sicán, Peru. *X-Ray Spectrum.* 39, 122–126. doi: 10.1002/xrs.1192

Cesareo, R., Franco Jordan, R., Fernandez, A., Bustamante, A., Fabian, J., del Pilar Zambrano, S., et al. (2016). Analysis of the spectacular gold and silver from the Moche tomb "Señora de Cao." *X-Ray Spectrum.* 45, 138–154. doi: 10.1002/xrs.2680

Cesareo, R., Rizzutto, M. A., Brunetti, A., and Rao, D. V. (2009). Metal location and thickness in a multilayered sheet by measuring Kα/Kβ, Lα/Lβ and Lα/Lγ X-ray ratios. *Nucl. Instrum. Methods Phys. Res. B.* 267, 2890–2896. doi: 10.1016/j.nimb.2009.06.119

Dik, J., Janssens, K., van der Snickt, G., van der Loeff, L., Rickers, K., and Cotte, M. (2008). Visualization of a lost painting by vincent van gogh using synchrotron radiation based X-ray fluorescence elemental mapping. *Anal Chem.* 80, 6436–6442. doi: 10.1021/ac800965g

Eveno, M., Ravaud, E., Calligaro, T., Pichon, L., and Laval, E. (2014). The louvre crucifix by giotto – unveiling the original decoration by 2D-XRF, X-ray radiography, emissiography and SEM-EDX analysis. *Herit. Sci.* 2, 1–9. doi: 10.1186/s40494-014-0017-y

Giurlani, W., Berretti, E., Innocenti, M., and Lavacchi, A. (2019). Coating thickness determination using x-ray fluorescence spectroscopy: monte carlo simulations as an alternative to the use of standards. *Coatings* 9:79. doi: 10.3390/coatings9020079

Graziani, V., Iorio, M., Albini, M., Riccucci, C., di Carlo, G., Branchini, P. and Tortora, L., (2020). Metals and environment: chemical outputs from the interaction between gilded copper-based objects and burial soil. *Front. Mater.* 7, 1–32. doi: 10.3389/fmats.2020.00032

Guerra, M. F. (2000). "The study of the characterisation and provenance of coins and other metalwork using XRF, PIXE and activation analysis," in *Radiation in Art and Archeometry*, eds D. C. Cragh, and D. A. Bradley (Amsterdam: Elsevier), 378–416. doi: 10.1016/B978-044450487-6/50063-8

Ingo, G. M., Guida, G., Angelini, E., di Carlo, G., Mezzi, A., and Padeletti, G. (2013). Ancient mercury-based plating methods: combined use of surface analytical techniques for the study of manufacturing process and degradation phenomena. *Acc. Chem. Res.* 46, 2365–2375. doi: 10.1021/ar300232e

Ingo, G. M., Riccucci, C., Lavorgna, M., Salzano de Luna, M., Pascucci, M., and di Carlo, G. (2016). Surface investigation of naturally corroded gilded copper-based objects. *Appl. Surf. Sci.* 387, 244–251. doi: 10.1016/j.apsusc.2016.06.082

Ingo, G. M., Riccucci, C., Pascucci, M., Messina, E., Giuliani, C., Biocca, P., et al. (2018). Combined use of FE-SEM+EDS, ToF-SIMS, XPS, XRD and OM for the study of ancient gilded artifacts. *Appl. Surf. Sci.* 446, 168–176. doi: 10.1016/j.apsusc.2018.01.278

Iorio, M., Graziani, V., Lins, S., Ridolfi, S., Branchini, P., Fabbri, A., et al. (2019). Exploring manufacturing process and degradation products of gilt and painted leather. *Appl. Sci.* 9:3016. doi: 10.3390/app9153016

Lechtman, H., Erlij, A., and Barry, E. J., Jr. (1982). New perspectives on moche metallurgy: techniques of gilding copper at loma negra, northern peru. *Soc. Am. Archaeol.* 47, 3–30. doi: 10.2307/280051

Nardes, R. C., Silva, M. S., Rezier, A. N. S., Sanches, F. A. C. R. A., Filho, H. S. G., and Santos, R. S. (2019). Study on Brazilian 18th century imperial carriage using x-ray nondestructive techniques. *Radiat. Phys. Chem.* 154, 74–78. doi: 10.1016/j.radphyschem.2018.04.005

Nørgaard, H. W. (2017). Portable XRF on prehistoric bronze artifacts: limitations and use for the detection of bronze age metal workshops. *Open Archaeol.* 3, 101–122. doi: 10.1515/opar-2017-0006

Pessanha, S., Manso, M., Antunes, V., Carvalho, M. L., and Sampaio, J. M. (2019a). Monte Carlo simulation of portable XRF setup: non-invasive determination of gold leaf thickness in indo-Portuguese panel paintings. *Spectrochim. Acta. B.* 156, 1–6. doi: 10.1016/j.sab.2019.04.006

Pessanha, S., Queralt, I., Carvalho, M. L., and Sampaio, J. M. (2019b). Determination of gold leaf thickness using X-ray fluorescence spectrometry: accuracy comparison using analytical methodology and Monte Carlo simulations. *Appl. Radiat. Isot.* 152, 6–10. doi: 10.1016/j.apradiso.2019.06.014

Quaranta, M., Catelli, E., Prati, S., Sciutto, G., and Mazzeo, R. (2014). Chinese archaeological artifacts: microstructure and corrosion behaviour of high-leaded bronzes. *J. Cult. Herit.* 15, 283–291. doi: 10.1016/j.culher.2013.07.007

Robbiola, L., Blengino, J. M., and Fiaud, C. (1998). Morphology and mechanisms of formation of natural patinas on archaeological Cu-Sn alloys. *Corrosi. Sci.* 40, 2083–2111. doi: 10.1016/S0010-938X(98)00096-1

Romano, F. P., Caliri, C., Cosentino, L., Gammino, S., Giuntini, L., Mascali, D., et al. (2014). Macro and micro full field X-ray fluorescence with an X-ray pinhole camera presenting high energy and high spatial resolution. *Anal. Chem.* 86, 10892–10899. doi: 10.1021/ac503263h

Shabunya-Klyachkovskaya, E. V., Kulakovich, O. S., Mitskevich, A. G., Moiseev, Y. F., Kiris, V., Matsukovich A. S., et al. (2017). A multi-analytical study of the belarusian icon "Virgin Eleusa" (XVII cent.). *J. Cult. Herit.* 28, 158–163. doi: 10.1016/j.culher.2017.02.016

Tortora, L., de Notaristefani, F., and Ioele, M. (2014). ToF-SIMS investigation of gilt and painted leather: Identification of indigo, oil binder and gold varnish. *Surf. Interface Anal.* 46, 807–811. doi: 10.1002/sia.5450

Trojek, T. (2011). Reduction of surface effects and relief reconstruction in X-ray fluorescence microanalysis of metallic objects. *J. Anal. At. Spectrom.* 26, 1253–1257. doi: 10.1039/c0ja00187b

van Espen, P., and Lemberge, P. (2000). ED-XRF Spectrum evaluation and quantitative analysis using multivariate and nonlinear techniques. *Advances in X-Ray Analysis* 43, 560–569. Available online at: https://www.scopus.com/record/display.uri?eid=2-s2.0-0347227295&origin=inward&txGid=5d6916ffd27f7c79d81b380ac22c6e95

Model Protective Films on Cu-Zn Alloys Simulating the Inner Surfaces of Historical Brass Wind Instruments by EIS and XPS

Marzia Fantauzzi [1,2], Bernhard Elsener [1,2,3], Federica Cocco [1,2], Cristiana Passiu [4] and Antonella Rossi [1,2*]

[1] *Dipartimento di Scienze Chimiche e Geologiche, Università degli Studi di Cagliari, Cagliari, Italy,* [2] *INSTM, University of Cagliari Research Unit (UdR), Cagliari, Italy,* [3] *Institute for Building Materials, ETH Zurich, ETH Hönggerberg, Zurich, Switzerland,* [4] *Laboratory for Surface Science and Technology, Department of Materials, ETH Zurich, Zurich, Switzerland*

The present work focuses on the characterization of brass surfaces after contact with artificial saliva solution at pH 7.4 and phosphate buffer solution at pH 7 simulating two extreme conditions that might occur when playing ancient brass wind instruments in the context of historically informed performance practice. The composition and the morphology of the film formed following the contact with the solutions for 1, 3, and 16 h were investigated by *ex situ* X-ray photoelectron spectroscopy (XPS) and scanning electron microscopy (SEM) to shed a light on the surface changes upon time. *In situ* electrochemical impedance spectroscopy (EIS) was used to study the mechanism of corrosion and protection of the alloys. The results could be interpreted using a reliable equivalent electrical circuit; they provided evidence that the alloys behave differently when in contact to the various solutions. In saliva solution the formation on the brass surface of a thick surface film was observed, composed of crystallites of about 200 nm size mainly composed of CuSCN and $Zn_3(PO_4)_2$. This layer hinders the alloy dissolution. The contact of the alloys with the buffer solution originated a much thinner layer composed of Cu_2O, ZnO, and a small amount of $Zn_3(PO_4)_2$. This film is rapidly formed and does not evolve upon time in a protective film.

Keywords: brass alloys, nanostructured surface film, neutral solutions, electrochemical impedance spectroscopy (EIS), X-ray photoelectron spectroscopy (XPS) and scanning electron microscopy (SEM)

INTRODUCTION

This work is part of a larger project whose overall goal was the development of an electrochemical sensor to understand the mechanism of corrosion and to monitor its evolution over time on brass musical instruments of the nineteenth and twentieth century[1]. The brass wind instruments collection under investigation is well-conserved in the Burri Museum in Bern (Switzerland) and it

---

[1]Web site of the project "Brass instruments of the nineteenth and early twentieth centuries between long-term conservation and use in historically informed performance practice" Available online at: http://p3.snf.ch/Project-146330.

contains more than 1,200 artifacts. Some of them are going to be used in concerts in the context of the "historically informed performance practice" (HIP) (Butt, 2002), which is a dominant trend in contemporary musical practice that intends to play restored original period instruments in concerts. To verify the efficiency of preventive conservation measures and to obtain information on the corrosion state and rate inside the instruments, non-destructive electrochemical techniques were chosen. The goal was achieved using a miniaturized electrochemical cell that could be used outside but especially inside the tuning slides of the artifacts (Elsener et al., 2016b). Firstly, the work (Elsener et al., 2016b) has involved the development of the electrochemical sensor and subsequently its calibration; afterward the sensor has been applied on reference materials and then used on the historical brass musical instruments (Elsener et al., 2016a). Unfortunately, the surface state inside the tuning slides is unknown and it is difficult to find a technique able to characterize for instance the inside surface of the trumpets.

In our previous work (Cocco et al., 2016a) the electrochemical behavior of a series of brasses (Zn content from 18 to 38 wt. %) was investigated after contact with two neutral solutions: artificial saliva solution and diluted pH = 7 phosphate buffer solution at the open circuit potential (OCP). The first one was chosen as an aggressive medium. The composition of natural saliva may differ considerably and can be affected by the type and intensity of stimulation, diet, age, time of day, diseases, and pharmacological agents. Hence, an exact replica of human saliva is hardly possible. Different formulations have been developed for different purposes. Here the Tani-Zucchi artificial saliva has been chosen because its composition is very close to the actual conditions existent in a cavity media when considering the inorganic components (Tani and Zucchi, 1967). The pH 7-phosphate solution was chosen as a mild exposure condition. The results showed that the corrosion resistance increases with increasing exposure time. Moreover, brasses with high zinc content showed higher dissolution rates for both solutions. As far as the samples in contact with saliva solution the corrosion rate decreased from 60 to 0.5 μm/year after 16 h of exposure, while in the less aggressive phosphate buffer solution it decreased only by a factor of two, from 3 to 5 μm/year (1 h) to 1.5–2.5 μm/year (16 h). This difference could be ascribed to the different surface films: a thicker and more protective film composed of CuSCN and zinc phosphate was formed upon contact with the artificial saliva solution whereas a nanometer thick film was formed in the pH 7-phosphate solution made mainly of copper and zinc oxides.

This work is focused on obtaining a deeper insight into the corrosion and protection mechanism of brass alloys (Zn content 18–37%) when in contact to neutral solutions. It exploits the electrochemical impedance spectroscopy (EIS), a powerful tool in corrosion science for following the electrochemical behavior of metals exposed to different electrolytes. Moreover, the EIS is a non-destructive technique since the application of a small AC signal during the measurement does not alter the electrochemical properties (Barsoukov and Macdonald, 2018). An insight on the composition of surface films was gained by XPS/XAES surface analysis to contribute to explain their

stability, the dissolution mechanism and the corrosion behavior. The occurrence of corrosion phenomena due to the exposure to the different electrolytes and the morphology of the different oxide films were also examined by optical- and scanning electron microcopies (SEM).

MATERIALS AND METHODS

Materials and Surface Preparation

Experiments were carried out on five different brass alloys with a zinc content ranging from 18 to 38 wt. % Zn. The composition of the alloys, determined by XRF, is reported in Cocco et al. (2016a). The alloys CuZn18, CuZn28, CuZn35Pb1, and CuZn38Pb2 were produced according a procedure that allows obtaining compositions and metallurgical structures as close as possible to alloys used in the nineteenth century (Von Steiger et al., 2013). CuZn37 was a standard alloy purchased from Goodfellow Cambridge Ltd., UK. Thin sheets, about 0.5 mm thick, of the brass alloys were mechanically polished using a sequence of abrasive SiC papers down to 4,000 mesh (Struers, Ballerup—DK) using ethanol as cooling lubricant during grinding. The samples were mirror-like polished with a DP Dur cloth (Struers) using diamond pastes up to 1 μm, rinsed with ethanol and dried using an argon stream.

Electrochemical Impedance Spectroscopy

The EIS measurements were performed on the mechanically polished samples immersed in artificial saliva (Tani and Zucchi, 1967) and in phosphate buffer solutions (1:10) at pH 7.4. The EIS analyses were conducted using a potentiostat/galvanostat VersaSTAT3 (Ametek, Inc., Princeton Applied Research, USA) connected to a three-electrode electrochemical cell. A saturated calomel electrode (0.241 V vs. NHE at 25°C, SCE) was chosen as reference electrode and all the measured potentials are referred to its value. A platinum mesh was used as counter electrode. The EIS measurements were carried out over a frequency range from 10 kHz to 0.01 Hz with 7 points per decade using AC amplitude of 5 mV. The EIS spectra were acquired after 1, 3, and 16 h exposure to both solutions. All measurements were carried out at ambient temperature (25 $\pm$ 2°C) with the solutions open to air.

X-Ray Photoelectron Spectroscopy (XPS)

Surface analyses were performed using a Theta Probe spectrometer (Thermo Fisher Scientific, East Grinstead, UK). The residual pressure in the main chamber during the acquisition was lower than 10^{-7} Pa. The XPS spectra were collected using a 400 μm monochromatic beam (AlKα source 1486.6 eV) operated at 4.7 mA and 15 kV (70 W). The analyzed area is estimated to be 0.5 mm^2 (Passiu et al., 2017). The average emission angle is 53° while the angle between the source and the analyser axis is 67.38°. Survey and high-resolution (HR) spectra were acquired in fixed analyzer transmission mode (FAT) setting the pass energy equal to 200 and to 100 eV, respectively, selecting the standard lens mode. The full-width at half-maximum (FWHM) of the Ag3d$_{5/2}$ peak acquired in the same conditions used for the HR spectra was 0.84 eV. The linearity of the binding energy (BE) scale was performed according to ISO 15472:2010

with an accuracy of $\pm0.1\,eV$. The BE values were referenced to the aliphatic carbon at $285.0\,eV$. Data were acquired under computer control (Avantage v. 3.45). Three different areas were analyzed on each sample. BE values and atomic percentages are reported in this work as mean values on three points with their corresponding standard deviations. The curve fitting procedure was performed using CasaXPS software (v2.3.16, Casa Software Ltd., Wilmslow, Cheshire, UK); the background was subtracted according to the Shirley-Sherwood background subtraction routine (Shirley, 1972) and then Gaussian and Lorentzian product functions were used for curve fitting. The quantitative analysis of brasses was performed on the basis of the integrated intensity using the first-principle approach (Briggs and Grant, 2003) under the assumption that the sample was homogeneous. The peak areas of each element were corrected for the respective sensitivity factor calculated taking into account Scofield's photoionization cross-sections (Scofield, 1976), the asymmetry factors (Reilman et al., 1976), the analyser transmission function $T(E_i)$ of the instrument (Fantauzzi et al., 2012), and the inelastic mean free paths (IMFP). The IMFP was calculated using the equation proposed by Tanuma et al. (2003). The accuracy of the calculated atomic concentrations is estimated to be $\pm10\%$. The sampling depth is estimated to be about 4 nm. In the following the authors will refer to thick film and thin films meaning films that are thicker and thinner than the sampling depth, respectively.

Quantitative analysis of the brass surfaces exposed to the phosphate buffer solution was also performed according to the three-layer model (Rossi and Elsener, 1992; Cocco et al., 2016b) and the thickness and composition of the surface layer together with the composition of the metal phase beneath the film could be calculated from a single XPS/XAES measurement. Since in the samples exposed to saliva solution the signals due to metallic copper and zinc were not detectable, the three-layer model was not appropriate and was not applied.

Scanning Electron Microscopy (SEM)

Scanning Electron Microscopy (SEM) was used to observe the surface of the brass alloys before and after the EIS measurements. The instrument used in this work was a Zeiss Ultra-55 (Carl Zeiss, Feldbach, Switzerland) equipped with InLens, SE2 (Everhart-Thornley Secondary Electron) e EsB (energy selective backscattered) detectors but only the InLens and SE2 were used in this work. The applied beam potential was 5 kV.

RESULTS

SEM Investigations

The surface morphology of brass samples was investigated by SEM analysis before and after the contact with the test solutions to monitor the surface modifications over the exposure time. **Figure 1** shows the SEM images acquired on two different brasses: Cu37Zn and Cu38Zn2Pb before and after 16 h of exposure to the buffer and the artificial saliva solutions. The surface prior to contact showed thin scratches due to the mechanical polishing and no particles were found on it. Some white spots were observed, probably due to a residue of the

diamond paste (diamond particles with an average size of $0.25\,\mu m$) used in the last step of the polishing procedure. After the contact with the buffer solution several black spots were visible at the surface of the alloy and they might be due to localized corrosion or dezincification areas. The surface of the alloy after the exposure to the saliva solution was homogeneously covered by particles of about $0.2\,\mu m$ in size; in contrast to the buffer solution no scratches were detectable on the surface of the metal.

Electrochemical Impedance Spectroscopy (EIS)

The electrochemical behavior of brass in contact with the test solutions was investigated by EIS at the open circuit potential (OCP), the values can be seen in **Tables 1, 2**. The change of the OCP with time was in agreement with a previous paper (Cocco et al., 2016a). The impedance spectra of all brass alloys after 1 and 16 h immersion in the phosphate buffer solution are shown in **Figure 2**. Whereas, there is no significant difference among the brass alloys, a clear evolution of the spectra with time can be seen (**Figure 2**), indicating an increase of the impedance at low frequencies and the more pronounced appearance of two maxima in the phase angle after 16 h (**Figure 2B**). The Nyquist plots (**Figures S.3, S.4**) showed only one depressed semicircle. The extrapolation to the x-axis at the low frequency end of the EIS data indicates the polarization resistance Rp.

The impedance spectra of all brass alloys after 1 and 16 h immersion in the artificial saliva solution are shown in **Figure 3**. In this solution the alloys with lower Zn content clearly show lower impedance values both after 1 and 16 h immersion. The impedance at low frequency is increasing with time and in the phase angle the time constants are more broadly distributed after 16 h of immersion (**Figure 3B**). Also in saliva solution the Nyquist plots (**Figures S.3, S.4**) showed only one depressed semicircle. The polarization resistance Rp (extrapolation at the low frequency end) in artificial saliva solutions is much higher than in the phosphate buffer solution.

The Bode plots (**Figures 2, 3**) show two more or less pronounced maxima in the phase angle, indicating two time constants. The EIS data were thus fitted using the equivalent circuit shown in **Figure 4**, consisting of a solution or ohmic resistance Rs, in series with two time constants, R1/CPE1 and R2/CPE2. The first one, R1/CPE1, was associated to the resistive and capacitive effects of the surface film formed after contact with the solution: R1 can be interpreted as the film resistance, R_{film} (blocking ionic or electronic transport) and the CPE1 as the surface film capacitance, CPE_{film}. In the second time constant, R2 could be related to the charge transfer resistance R_{ct} and the related CPE2 describe the capacitance of the double layer, CPE_{dl}. The results are summarized in **Table 1** (buffer solution) and in **Table 2** (artificial saliva solution). As the parameters given are the result of a non-linear curve fitting process, the accuracy of the fit or better the errors in the individual parameters are important. It has been found that the error is usually in the range of a few to 10%.
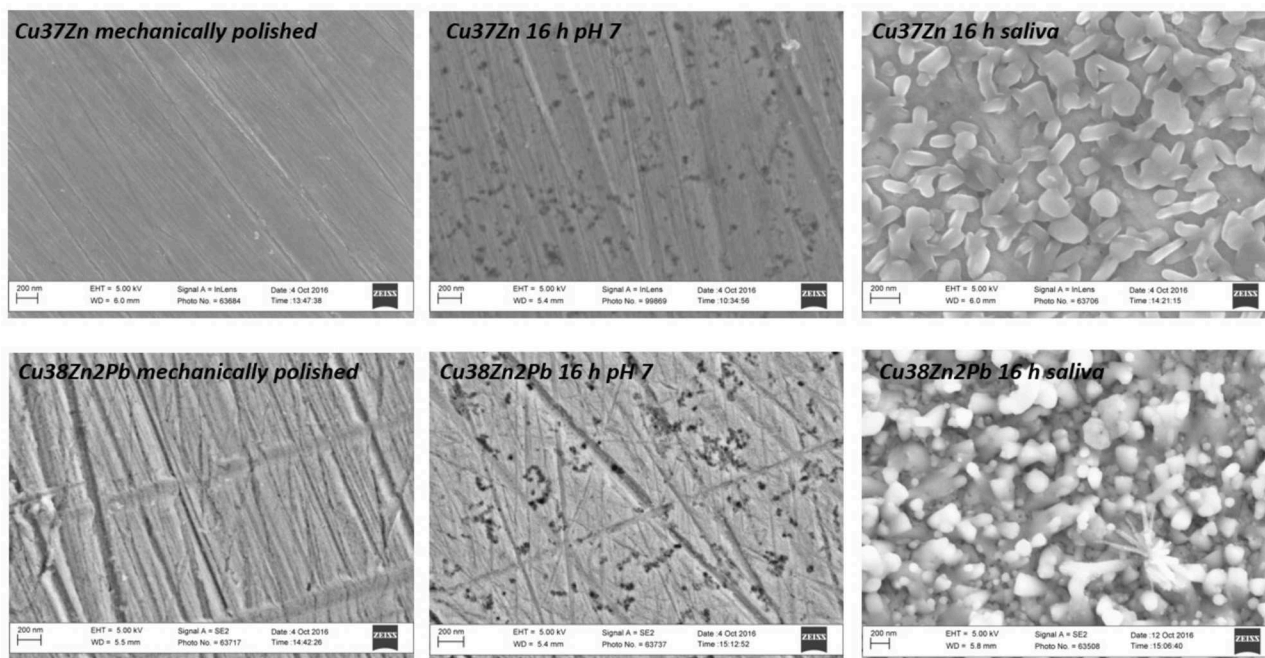
FIGURE 1 | SEM images acquired on the Cu37Zn and Cu38Zn2Pb alloys following the mechanical polishing procedure, after 16 h of exposure to the phosphate buffer and to the artificial saliva solutions.

TABLE 1 | Calculated fitting parameters for brass alloys after 1, 3, and 16 h of immersion in phosphate buffer solution; the standard deviation in percentage of the value is obtained from three replica measurements and is reported in parentheses.

	Time (h)	OCP (mV)	R_s (Ω)	$CPE1_{film}$ (μFcm^{-2})	n_{film}	R_{film} ($k\Omega cm^2$)	$CPE2_{dl}$ (μFcm^{-2})	$n2$	R_{ct} ($k\Omega cm^2$)
Cu18Zn	1	−59	614 (8)	18 (30)	0.87 (7)	2 (16)	88 (5)	0.7 (3)	37 (9)
	3	−44	653 (8)	10 (20)	0.93 (7)	5 (23)	59 (6)	0.7 (12)	87 (20)
	16	−48	569 (1)	8 (15)	0.94 (3)	4 (21)	36 (3)	0.7 (2)	95 (5)
Cu28Zn	1	−69	603 (6)	22 (16)	0.83 (2)	4 (21)	71 (19)	0.7 (2)	31 (20)
	3	−49	683 (3)	10 (17)	0.92 (3)	5 (20)	47 (12)	0.7 (1)	12 (14)
	16	−63	514 (1)	11 (15)	0.89 (2)	2 (25)	54 (2)	0.6 (2)	70 (5)
Cu37Zn	1	−83	652 (6)	21 (33)	0.88 (5)	2 (27)	90 (14)	0.6 (3)	32 (12)
	3	−82	565 (10)	18 (18)	0.86 (7)	3 (30)	69 (16)	0.6 (5)	40 (27)
	16	−76	608 (1)	12 (20)	0.96 (3)	1 (14)	86 (2)	0.7 (2)	17 (3)
Cu35Zn1Pb	1	−79	618 (1)	31 (25)	0.84 (7)	3 (30)	91 (17)	0.6 (12)	26 (25)
	3	−66	661 (4)	18 (30)	0.83 (11)	3 (22)	53 (3)	0.7 (5)	56 (30)
	16	−61	651 (5)	14 (20)	0.91 (11)	3 (18)	53 (6)	0.7 (5)	78 (20)
Cu38Zn2Pb	1	−86	623 (10)	53 (6)	0.80 (3)	6 (16)	90 (6)	0.6 (12)	23 (20)
	3	−68	656 (6)	17 (25)	0.91 (8)	4 (23)	58 (13)	0.6 (5)	49 (32)
	16	−75	629 (1)	11 (9)	0.91 (1)	3 (15)	47 (1)	0.6 (2)	91 (4)

The results for all brass alloys immersed in *buffer solution pH 7* (**Table 1**) show that the film resistance R_{film} is very low. It is in the same order for all the brass alloys studied, thus does not depend on the zinc content, and remains nearly constant with the immersion time. This suggests the presence of a thin and non-protective surface film; indeed, the SEM analyses of the surface (**Figure 1**) do not show a surface film. The charge transfer resistance, R_{ct}, instead, in the case of the buffer solution

is much higher than the film resistance, R_{film}. R_{ct} is similar for the different brass alloys and increasing with time for all alloys. This would indicate that the corrosion reaction in the system brass alloys/buffer solution is charge transfer controlled.

The results obtained by the EIS analysis carried out in *artificial saliva solution,* listed in **Table 2** show that the film resistance R_{film} is much higher than the charge transfer resistance R_{ct}. The film resistance increases with increasing zinc content in the brass

TABLE 2 | Calculated fitting parameters for brass alloys after 1, 3, and 16 h of immersion in artificial saliva solution.

	Time (h)	OCP (mV)	R (Ω)	CPE1$_{film}$ (μFcm^{-2})	n$_{film}$	R$_{film}$ (kΩcm^2)	CPE2$_{dl}$ (μFcm^{-2})	n$_{dl}$	R$_{ct}$ (kΩcm^2)
Cu18Zn	1	−348 (1)	170 (11)	–	–	–	109 (2)	0.81 (1)	2 (1)
	3	−330 (2)	139 (14)	24 (12)	0.51 (1)	22 (37)	22 (9)	0.82 (2)	3 (7)
	16	−159 (20)	139 (16)	93 (26)	0.67 (20)	17 (20)	23 (4)	0.83 (6)	7 (30)
Cu28Zn	1	−347 (1)	164 (7)	–	–	–	103 (1)	0.82 (1)	2 (2)
	3	−314 (3)	160 (1)	23 (11)	0.51 (3)	36 (20)	24 (20)	0.83 (2)	3 (13)
	16	−230 (3)	160 (2)	11 (38)	0.55 (5)	371 (5)	2 (40)	0.86 (7)	1 (37)
Cu37Zn	1	−338 (3)	150 (1)	–	–	–	122 (14)	0.77 (1)	5 (4)
	3	−279 (4)	176 (8)	15 (17)	0.51 (3)	72 (12)	25 (24)	0.80 (2)	3 (22)
	16	−320 (7)	159 (2)	21 (5)	0.43 (5)	77 (13)	5 (5)	0.80 (1)	2 (6)
Cu35Zn1Pb	1	−344 (1)	158 (4)	–	–	–	81 (19)	0.81 (2)	4 (16)
	3	−277 (12)	164 (4)	2 (12)	0.52 (3)	77 (30)	34 (15)	0.77 (3)	3 (19)
	16	−187 (19)	198 (2)	12 (30)	0.50 (3)	427 (18)	2 (33)	0.85 (5)	2 (24)
Cu38Zn2Pb	1	−341 (1)	154 (6)	–	–	–	115 (2)	0.78 (1)	4 (2)
	3	−304 (2)	208 (36)	10 (32)	0.51 (3)	44 (18)	34 (22)	0.77 (2)	4 (23)
	16	−167 (3)	128 (1)	8 (1)	0.49 (1)	743 (1)	1 (4)	0.86 (3)	1 (10)

The standard deviation in percentage of the value is obtained from three replica measurements and is reported in parentheses.

FIGURE 2 | Bode plots of all the brass alloys in contact with the phosphate buffer pH 7 for 1 h **(A)** and for 16 h **(B)**.
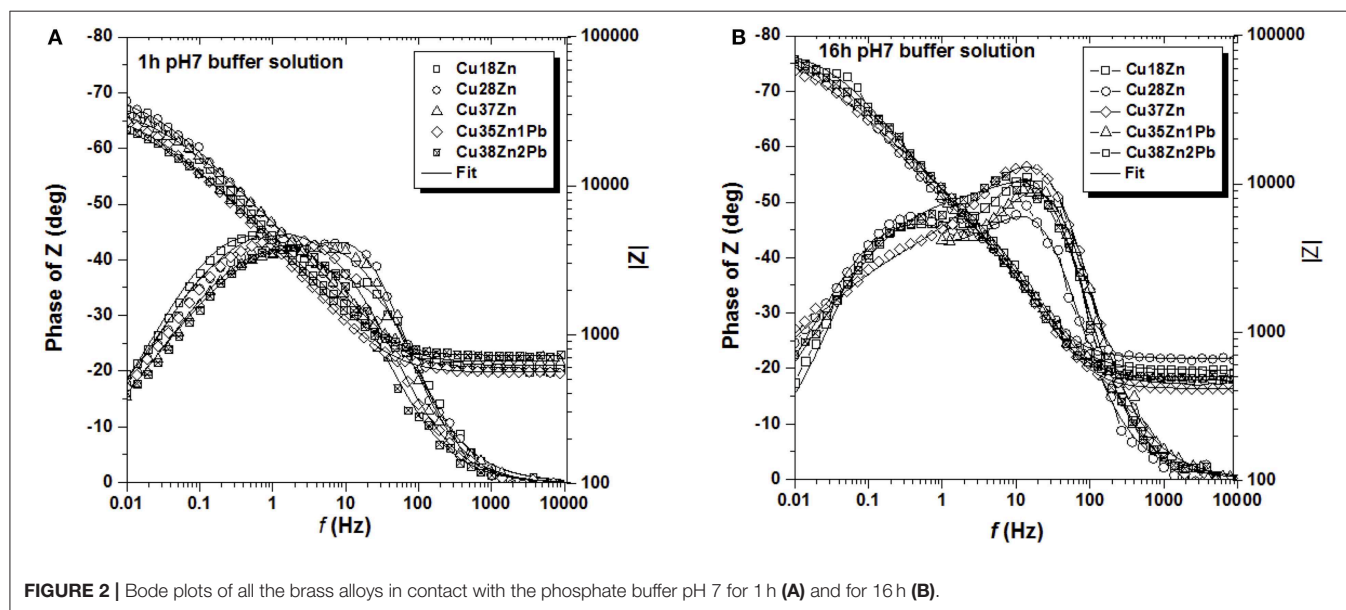
alloys studied. This suggests the presence of an increasingly thick and protective surface film that is forming on the brass surface as is documented by the SEM analysis (**Figure 1**). The charge transfer resistance, R$_{ct}$, instead, in the case of the artificial saliva solution is much lower than the film resistance, R$_{film}$. R$_{ct}$ is slightly increasing with the zinc content of the different brass alloys and remains nearly constant with the immersion time. This would indicate, that the corrosion reaction in the system brass alloys/artificial saliva solution is controlled by the film resistance.

XPS Results

The surface chemical state and composition of the brass samples after the exposure to the two neutral solutions was investigated by XPS/XAES surface analysis. Here, results of the Cu37Zn alloy are presented in detail. The survey spectra of Cu37Zn after

contact with the pH 7 buffer solution and with the artificial saliva solution are shown in the supporting information together with the XPS/XAES spectra of the other alloys (**Figures S.5–S.16**). The surface composition of the alloys after mechanical polishing has been published in a previous work (Cocco et al., 2016b). Curve fitting of the spectra was performed using parameters obtained in reference materials as described elsewhere (Cocco et al., 2016b). In particular the differences in KEs and area ratios of the different components ascribed to the different chemical states in XAES signals were constrained and equal to those determined on the reference materials (Cocco et al., 2016b).

Buffer Solution

Survey spectra of the brass samples following the contact with phosphate buffer solution allow one to identify the presence of
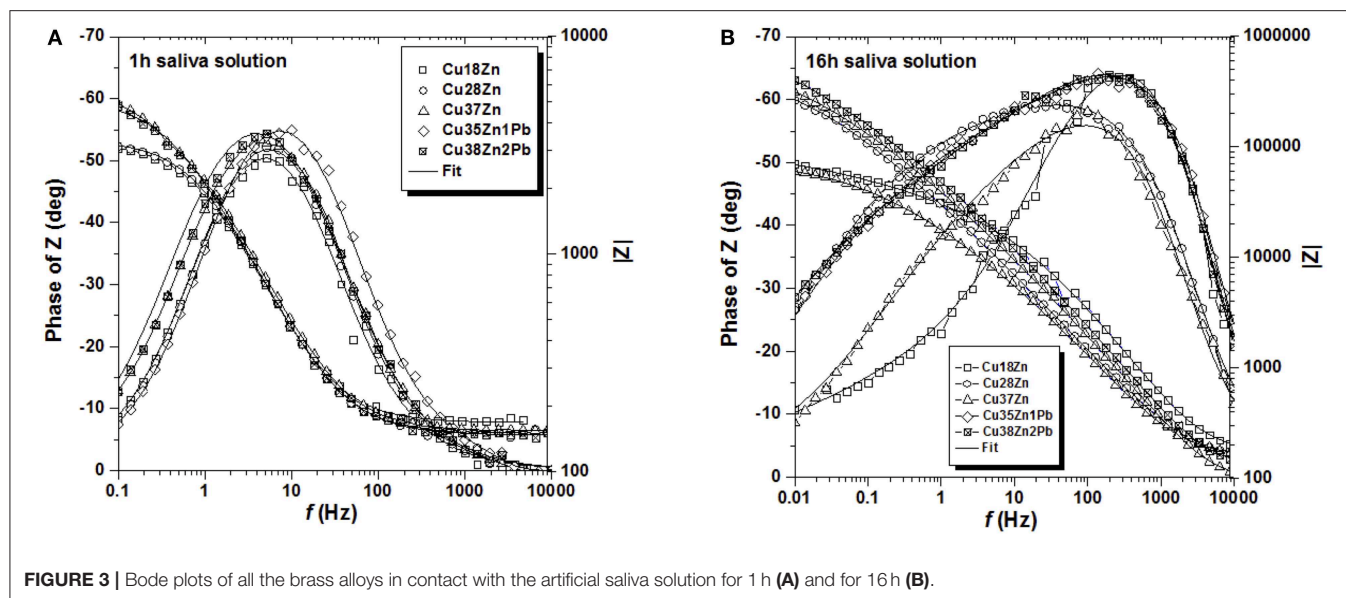
FIGURE 3 | Bode plots of all the brass alloys in contact with the artificial saliva solution for 1 h **(A)** and for 16 h **(B)**.
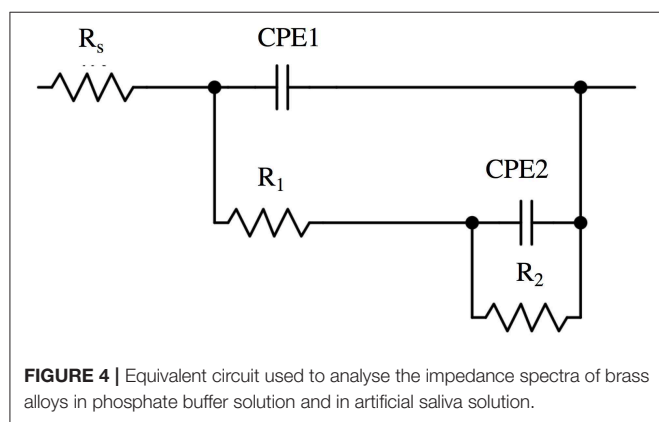

FIGURE 4 | Equivalent circuit used to analyse the impedance spectra of brass alloys in phosphate buffer solution and in artificial saliva solution.

copper, zinc and lead (in samples Cu35Zn1Pb and Cu38Zn2Pb), together with oxygen, phosphorus and, in some samples, small amounts of sodium. Carbon is also present due to the presence of the organic contamination layer, which is always detected on the surface of samples exposed to solutions and to the atmosphere. The survey spectra of Cu37Zn brass are provided in **Figure S.5**.

The high-resolution spectra of the signals of Cu2p, CuLMM, Zn2p, ZnLMM, and P2p of the brass alloys were acquired after 1, 3, and 16 h of immersion in the phosphate buffer solution. Examples of the photoelectron spectra of Cu, Zn, and P for the CuZn37 alloy in contact the solution for 1 and 16 h are shown in **Figure 5**. The binding energy (BE) of the photoelectron lines, the kinetic energy (KE) of the Auger lines and the quantitative composition are given in **Table 3**.

The detailed Cu $2p_{3/2}$ signals for all exposure times to the pH 7.4 solution showed two main signals for both short and long contact times: one signal located at BE 932.6 eV related to the presence of Cu (0) and Cu$_2$O (Cocco et al., 2016b) and the other signal at about BE 934.9 eV due to the presence of Cu (II) together

with the typical satellite structure at the high BE side (944.1 eV Sat 1, 941.5 eV Sat 2) probably due to Cu(OH)$_2$ (Biesinger, 2017).

In order to ascertain the presence of Cu (0) following the contact with the buffer solution, the curve fitting approach proposed in Cocco et al. (2016b) for Cu $L_3M_{45}M_{45}$ peaks was applied and the components of the multiplet associated to the metal and to the oxidized copper (^1G) were found at about KE 918.8 and 916.8 eV, respectively. This suggests the simultaneous presence of Cu (0), Cu (I) and Cu (II). The relative amount of the three different copper species, calculated following (Cocco et al., 2016b), is reported in **Table 3**. Cu $L_3M_{45}M_{45}$ spectra are shown in the supporting information (**Figures S.6–S.16**).

The Zn $2p_{3/2}$ photoelectron signal showed a single peak at a BE of about 1022.1 eV. (**Figure 5**) As in the case of Cu $L_3M_{45}M_{45}$ also the Zn $L_3M_{45}M_{45}$ Auger signal exhibited both the metallic and the oxidized Zn (II) components; their KEs are 991.3 and 987.5 eV, respectively. The former component is assigned to Zn (0) and the latter might be assigned to zinc oxide and hydrogen phosphate according to the literature (Onyiriuka, 1993; Cocco et al., 2016b). The P $2p_{3/2}$ signal was found at a BE of about 132.8–133.0 eV: an in depth discussion on P chemical state is provided in the following section (Onyiriuka, 1993).

The binding energies of the photoelectron peaks as well as the kinetic energies of the XAES signals are the same for all the alloys studied as shown in **Table 3**. This indicates that irrespective of the zinc content of the alloy the same chemical compounds are present on the surface after exposure to the phosphate buffer solution.

The amount of oxidized zinc and copper species increases upon contact time. The application of a three layer model to XPS areas of carbon, oxygen, metallic copper and zinc and oxidized copper and zinc allows us to estimate the thickness of the organic contamination layer (l_c), of the surface layer containing Cu (I), Cu (II), and Zn (II) species as oxides, hydroxides and hydrogen phosphates (t), and the composition
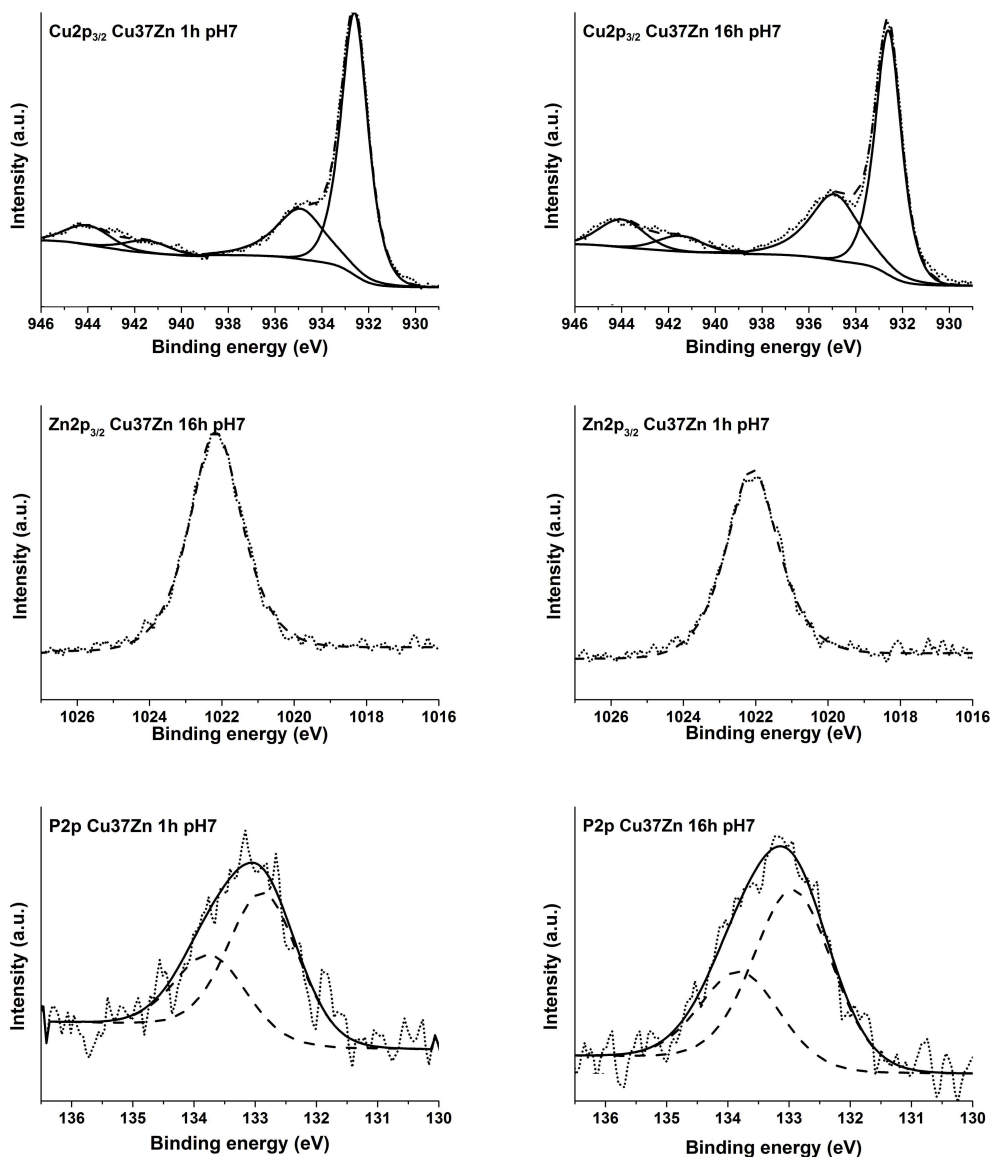
FIGURE 5 | High-resolution spectra of Cu 2p$_{3/2}$, Zn 2p$_{3/2}$, and P 2p for the alloy Cu37Zn after 1, and 16 h of contact with the phosphate buffer solution.

of the surface layer and of the interface bulk/surface layer. The surface layer is richer in copper, mainly as Cu_2O and $Cu(OH)_2$, than in zinc, as oxide and/or hydrogen phosphate. On the contrary, the bulk/surface layer interface is enriched in zinc in comparison with the composition of the interface in the mechanically polished Cu37Zn. In this case the interface was found to be close to the nominal composition (63% copper, 37% zinc) (Cocco et al., 2016b). Zn content of the interface increases upon immersion time.

Artificial Saliva Solution

The high-resolution spectra of the signals Cu 2p, Cu L$_3$M$_{4,5}$M$_{4,5}$, Zn 2p, Zn L$_3$M$_{4,5}$M$_{4,5}$, P 2p, S 2p, and N 1s of the brass alloys were acquired after 1, 3, and 16 h of immersion in the saliva solution.

As an example the spectra of the CuZn37 alloy are shown in **Figure 6**. The binding energy (BE) of the photoelectron peaks and the kinetic energy (KE) of the XAES signals together with the atomic concentration calculated excluding the carbon intensity are provided in **Table 4**. The results related to the other alloys are comparable with those obtained for the here-presented sample and are shown in **Tables S.1–S.3**.

The Cu 2p$_{3/2}$ signal showed a single peak at 932.6 eV for both short and long contact times and for all the analyzed samples. The Cu L$_3$M$_{45}$M$_{45}$ Auger signals were composed of five peaks associated to different final states of oxidized copper (Cocco et al., 2016b), here only the envelope of the XAES signal is shown. No metallic component has been detected in the CuLMM Auger spectra even after only 1 h of exposure; hence the thickness of

TABLE 3 | Average binding energy (BE) of the most intense photoelectron peaks, kinetic energy of Auger peaks and quantitative composition (at %) of the main elements detected on Cu37Zn after exposure to the phosphate buffer solution.

CuZn37	1 h pH7		3 h pH7		16 h pH7	
	BE (eV)	at %	BE (eV)	at %	BE (eV)	at %
Cu $2p_{3/2}$ Cu (0)	932.5 (0.1)	5 (2)	932.6 (0.1)	1.7 (0.8)	932.6 (0.1)	0.9 (0.4)
Cu $2p_{3/2}$ Cu (I)	932.5 (0.1)	7 (2)	932.6 (0.1)	12 (3)	932.6 (0.1)	12 (1)
Cu $2p_{3/2}$ Cu (II)	934.9 (0.1)	5 (2)	934.9 (0.1)	5 (2)	934.9 (0.1)	6 (2)
Sat 1	944.1 (0.1)		944.0 (0.1)		944.0 (0.1)	
Sat 2	941.8 (0.3)		941.5 (0.1)		941.5 (0.1)	
O 1s	530.7 (0.1)	59 (7)	530.6 (0.1)	64 (6)	530.7 (0.1)	64 (7)
	531.7 (0.1)		531.6 (0.1)		531.7 (0.1)	
	533.2 (0.2)		532.5 (0.2)		533.1 (0.2)	
P 2p $_{3/2}$	133.0 (0.2)	12 (3)	132.8 (0.2)	10 (2)	133.0 (0.1)	9 (3)
Zn $2p_{3/2}$ Zn (0)	1022.1 (0.1)	3 (1)	1022.1 (0.1)	1.7 (0.2)	1022.2 (0.1)	1.4 (0.3)
Zn $2p_{3/2}$ Zn (II)	1022.1 (0.1)	9 (2)	1022.1 (0.1)	5 (1)	1022.2 (0.1)	3.2 (0.6)
	KE (eV)		**KE (eV)**		**KE (eV)**	
Cu $L_3M_{4,5}M_{4,5}$ met	918.8 (0.2)		918.8 (0.1)		918.9 (0.2)	
Cu $L_3M_{4,5}M_{4,5}$ Ox	916.8 (0.1)		916.9 (0.1)		916.9 (0.2)	
Zn $L_3M_{4,5}M_{4,5}$ met	992.3 (0.1)		992.4 (0.1)		992.3 (0.1)	
Zn $L_3M_{4,5}M_{4,5}$ Ox	987.4 (0.2)		987.7 (0.2)		987.5 (0.1)	

Thickness of the layers and composition of surface layer and of the interface bulk/surface layer

	1h pH 7	3h pH 7	16h pH 7
l_c	1.7 (0.3) nm	1.9 (0.2) nm	2.1 (0.1) nm
t	0.9 (0.1) nm	1.05 (0.03) nm	0.7 (0.1) nm
Surface layer	Cu ox = 64 (22)%	Cu ox = 75 (10)%	Cu ox = 82 (2)%
	Zn ox = 36 (22)%	Zn ox = 25 (10)%	Zn ox 18 (2)%
Surface/bulk interface	Cu met = 47 (4)%	Cu met = 47 (9)%	Cu met = 30 (7)%
	Zn met = 53 (4)%	Zn met = 53 (9)%	Zn met = 70 (7)%

The thicknesses of the contamination layer (lc) and of the surface layer (t), together with the composition of the surface layer and of the bulk/surface layer interface, estimated by the three-layer model (Rossi and Elsener, 1992; Cocco et al., 2016b) are provided. Standard deviations are given in parentheses.

the film formed was greater than the sampling depth of the XPS technique. The kinetic energy of the main component of the Cu LMM signals was found at about 915.7 eV for all the alloys. The Cu $L_3M_{45}M_{45}$ Auger peak overlaps with the Zn $L_2M_{45}M_{45}$ (black line in **Figure 6**) on the high KE side of the main peak. After 16 h of immersion this superposition is the highest, this could be explained as a result of the increasing zinc content in the film formed on the surface of the alloy.

The KE values of the main Cu $L_3M_{45}M_{45}$ peak could be assigned to the presence of copper thiocyanate, CuSCN according to Cocco et al. (2016b). Moreover, this assignment was also confirmed by the presence of N 1s and S 2p and by their BE values. The N 1s spectra showed two components: (1) the most intense peak at about 398.5 eV might be due to nitrogen in SCN^- (Pattanasattayavong et al., 2013; Aldakov et al., 2014)[2]; (2) the

---

[2]https://srdata.nist.gov/xps/ (access October 11, 2016).

---

less intense component at about 399.9 eV is probably due to residual urea from saliva formulation[2]. The S $2p_{3/2}$ signal was found at 163.3 eV and its BE does not change upon exposure time. The position of the signal might be ascribed to a sulfur atom in ^-S–CN[2].

The Zn $2p_{3/2}$ spectra (**Figure 6**) showed a single peak at about 1022.8 eV for each exposure time and for all the alloys. The related Zn $L_3M_{45}M_{45}$ Auger signals exhibited a complex shape with five components as a result of different final states; the main peak was located at KE 986.3 eV. This could be assigned to the presence of oxidized zinc in the form of zinc orthophosphate according to literature (Crobu et al., 2012; Cocco et al., 2016b). The P 2p showed a well-separated spin-orbit doublet; the energy separation between $2p_{3/2}$ and $2p_{1/2}$ is 1.2 eV. The P $2p_{3/2}$ signal was found at 133.8 eV and it was likely assigned to the presence of phosphate group according to Cocco et al. (2016a).

Unlike the case of the buffer solution where the metallic components are still detectable after 16 h of exposure, no signals from Cu (0) and Zn (0) were revealed (**Figure 6**), indicating that in saliva solution a thicker film was formed on the brass surface.

DISCUSSION

In a previous work (Cocco et al., 2016a), based on open circuit potential, DC polarization resistance measurements, and preliminary XPS/XAES surface analysis data, it was hypothesized that the dissolution of the brass alloys exposed to phosphate buffer solution and to artificial saliva solution was controlled by the different surface films formed. Using electrochemical impedance spectroscopy (EIS) and a full set of XPS/XAES surface analysis data, a more detailed insight into the reaction mechanism of the brass alloys with zinc content ranging from 18 to 38% exposed to the two different solutions can be provided and the rate controlling step can be established. This information is important for brass wind instruments where corrosion occurs due to the high internal humidity formed after playing.

Curve Fitting and Interpretation of the Impedance Spectra

Electrochemical impedance spectroscopy (EIS) is a powerful tool to study the reaction mechanism of corrosion processes as the technique allows differentiating between various partial processes and reaction steps. Today the use of software packages that allow simulating different processes and adapting the calculations to the experimental spectra facilitates greatly their interpretation. However, two points should be considered: first, every element in an equivalent circuit has to have a physical meaning, and second, the errors associated to the individual elements resulting from the curve fitting procedure should be visible.

The EIS spectra in this work (**Figures S.1, S.2**) showed one broad or two resolved maxima in the phase angle, indicating two time constants related to two different reactions at the surface of the brass alloys exposed to the solutions. The corresponding equivalent circuit (**Figure 4**) has, in addition to the ohmic resistance R_Ω, two time constants: R1/CPE1 and R2/CPE2. The constant phase element (CPE) was used instead of a
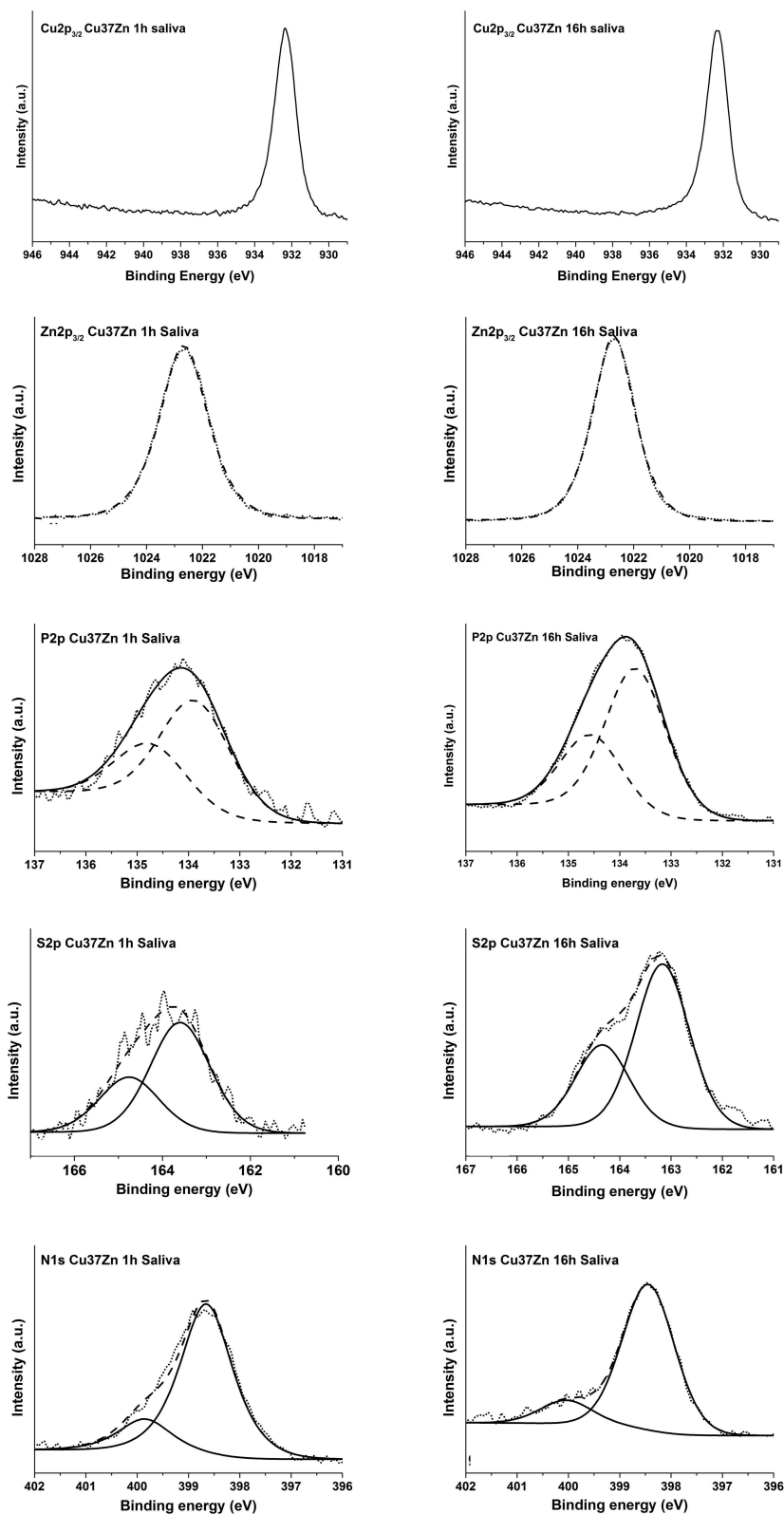
FIGURE 6 | High resolution spectra of Cu 2p$_{3/2}$, Zn 2p$_{3/2}$, P 2p, S 2p, and N 1s of the Cu37Zn sample after 1, 3, and 16 h of contact with the saliva solution.

TABLE 4 | Average binding energy (BE) of the most intense photoelectron peaks, kinetic energy of the Auger peaks and quantitative composition (at %) of the main elements detected on Cu37Zn after contact with the saliva solution.

CuZn37	1 h		3 h		16 h	
	BE (eV)	**at %**	**BE (eV)**	**at %**	**BE (eV)**	**at %**
Cu 2p	932.6 (0.1)	13 (1)	932.5 (0.1)	13 (4)	932.5 (0.1)	6 (1)
N 1s	398.6 (0.1)	10 (2)	398.5 (0.1)	25 (16)	398.5 (0.1)	5 (1)
N 1s	399.9 (0.2)		400.0 (0.1)		400.1 (0.1)	
O 1s	531.1 (0.2)	40 (4)	532.1 (0.2)	29 (3)	532.4 (0.1)	50 (1)
O 1s	532.3 (0.2)		532.5 (0.2)		533.6 (0.1)	
O 1s	533.3 (0.2)		533.0 (0.1)		531.7 (0.1)	
P 2p$_{3/2}$	134.2 (0.2)	7(1)	134.3 (0.2)	6 (1)	133.8 (0.1)	13 (2)
S 2p SCN	163.3 (0.2)	11 (1)	163.3 (0.1)	15 (7)	163.2 (0.1)	6 (1)
Zn 2p	1022.9 (0.2)	18 (1)	1022.8 (0.1)	12 (1)	1022.7 (0.1)	20 (3)
	KE (eV)		**KE (eV)**		**KE (eV)**	
Cu L$_3$M$_{4,5}$M$_{4,5}$	915.7 (0.1)		915.5 (0.1)		915.5 (0.1)	
Zn L$_3$M$_{4,5}$M$_{4,5}$	986.3 (0.1)		986.2 (0.2)		986.3 (0.1)	

Standard deviations are given in parentheses.

capacitance C to take into account a distributed capacitance due to surface roughness, variation in film thickness etc. resulting in an exponent $n < 1$. Overall there is a good agreement between the experimental and calculated spectra (**Figures 2**, **3**).

Examining the results of the adaption of the equivalent circuit to the experimental data (curve fitting procedure) given in **Tables 2**, **3** in more detail, it can be noted that the errors associated to the ohmic resistance R_Ω are generally lower than 10%. The film resistance R_{film} in the phosphate buffer solutions (**Table 2**) is very low (in the range of 1–4 kΩ cm^2), the associated error is between 20 and 50%. The error in the charge transfer resistance R_{ct} is generally below 25%.

Dissolution Mechanism of Brass Alloys

In this section the dissolution mechanism of the brass alloys in the two solutions is discussed combining the results of electrochemical impedance spectroscopy with the results of the surface analysis.

Electrochemical Impedance Spectroscopy

The analysis and interpretation of the impedance spectra recorded on the brass alloys after 1, 3, and 16 h of exposure to the phosphate buffer solution and to artificial saliva allowed determining the film resistance R_{film} and the charge transfer resistance, R_{ct}. R_{ct} provides information on the rate of the anodic dissolution reaction of the brass alloy whereas the film resistance R_{film} indicates to what extent the actual corrosion rate is limited by the surface film that was formed as a result of the alloy dissolution.

Plotting both parameters for the artificial saliva solution (**Figure 7A**) and for the phosphate buffer solution (**Figure 7B**) as a function of the open circuit potential, a net result is obtained:

o In the *artificial saliva solution* $R_{film} >> R_{ct}$, thus the dissolution reaction is controlled by the surface film in

agreement with the results of the DC polarization resistance measurements where an anodic control was found (Cocco et al., 2016a). The charge transfer resistance does not vary with the zinc content of the alloy and with immersion time whereas the film resistance increases with time of immersion from 3 to 16 h.

o In the *phosphate buffer* solution $R_{ct} >> R_{film}$, thus the dissolution reaction of the alloy is controlled by the charge transfer reaction. The film resistance remains constant at 4 ± 2 kΩcm^2 independent of the zinc content in the alloy or of the exposure time. The charge transfer resistance increases with time for all alloys from about 20–100 kΩcm^2, the difference between the alloys is a slight shift in the OCP values with the zinc content—a trend already found in the DC measurements (Cocco et al., 2016a).

In conclusion, in the phosphate buffer solution the dissolution rate is charge transfer controlled, in the artificial saliva the film resistance governs the dissolution rate.

Surface analysis

The dissolution mechanism of the brass alloys in the two solutions could be well-established based on the EIS results. What has to be discussed further is the link to the results of the XPS/XAES surface analysis, in other words how does the composition of the surface film influence the dissolution rate.

o In the *artificial saliva solution* a thick film is formed after 3 and 16 h of immersion (**Figure 1**) showing a surface morphology with numerous crystallites. No signals from the metal could be detected for all the alloys as it could be seen from the XAES spectra of both Cu LMM and Zn LMM (**Figure 4**) even after 1 h of immersion the film thickness thus is much higher than the escape depth of the photoelectrons. First results revealed, based on the Wagner chemical state plot (Cocco
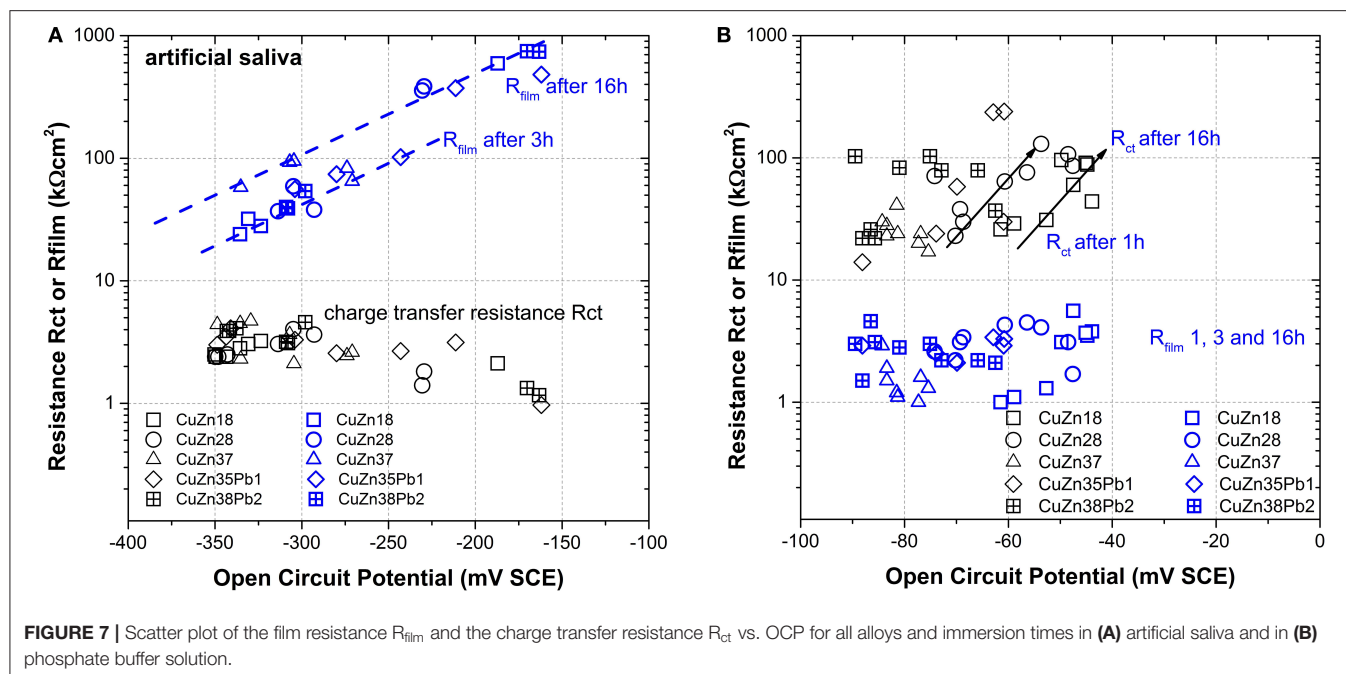
FIGURE 7 | Scatter plot of the film resistance R_{film} and the charge transfer resistance R_{ct} vs. OCP for all alloys and immersion times in **(A)** artificial saliva and in **(B)** phosphate buffer solution.

et al., 2016a) the presence of copper thiocyanate (CuSCN) and zinc phosphate. Quantitative analysis of the surface film in this work indicated 22 ± 3 at % zinc, 14 ± 3 at % phosphorus and about 64 ± 5 at % oxygen, thus the presence of $Zn_3(PO_4)_2$ is confirmed. The increase of the film resistance with time can be interpreted as an increase in the film thickness or the formation of a more compact film; this is also reflected in the decrease of the film capacitance (**Table 2**).

o In the *phosphate buffer solution* no visible film is formed, the morphology is similar to the mechanically polished surface (**Figure 1**). For all the brass alloys even after 16 h of immersion the presence of the metallic component of both Cu and Zn was detected in the high-resolution XAES signals of Cu LMM (**Figure 5**) and in the Zn LMM spectrum (**Figure 5**) respectively, qualitatively indicating the presence of a surface film in the order of some nano-meters only. This is in agreement with studies on the effect of phosphate ions on copper dissolution and passivation (Drogowska et al., 1992; Antonijevic and Petrovic, 2008; Valcarce and Vázquez, 2010; Deyab et al., 2015). In phosphate solution of pH 8 cyclic voltammetry showed that the phosphate ions were involved in the reaction. The thickness of the anodic film was estimated (based on the reduction charge) to 40–48 A when a film composition of CuO or Cu(OH)$_2$ was assumed (Cocco et al., 2016a). In an earlier work of Strehblow and Titze (1980) the surface film of copper exposed to phosphate solution was studied. In addition to Cu_2O and $Cu(OH)_2$ the presence of a copper phosphate compound, most probably $Cu_3(PO_4)_2$, was indicated as possible explanation of the traces of phosphorus revealed by XPS.

In the context of the nature of these surface films containing phosphates the detailed analysis of the P2p$_{3/2}$ binding energy

(given in **Table 4**) is interesting. As is shown in **Figure 8**, the P2p$_{3/2}$ BE in artificial saliva is found at 133.8 ± 0.2 eV with a slight trend toward high values at higher zinc contents. These binding energy values well-agree with previously measured compounds of zinc orthophosphate glass (Crobu et al., 2012). The presence of $Zn_3(PO_4)_2$ was determined on the brass samples immersed in artificial saliva with the help of the chemical state plot (Cocco et al., 2016a). On brass samples immersed in phosphate buffer solutions the binding energy of P2p$_{3/2}$ is found at 133.0 ± 0.2 eV for all alloys and immersion times (**Figure 8**), clearly lower than in saliva solution. Thus, the presence of pure zinc phosphate can be ruled out. The binding energy of pure $Cu_3(PO_4)_2$ on the other hand was found at 133.9 ± 0.15 eV (Biesinger, 2017) and the presence of pure copper phosphate can also be excluded. A possible explanation of the low binding energy of P2p$_{3/2}$ signal (BE 132.9 ± 0.1 eV, **Figure 8**) might be that in the thin surface film mainly composed of Cu_2O, ZnO, and $Cu(OH)_2$, the concentration of phosphate is low and the film is hydrated, copper hydrogen phosphate might be present. The binding energy of Na_2HPO_4 was reported at 133.0 eV.

Implications for the Interior Corrosion of Brass Wind Instruments

The motivation for this research project was based on the idea to use period brass musical instruments of the nineteenth and twentieth century for today concerts in the context of historically informed musical practice (Butt, 2002)[1]. Main problem is the corrosion inside the instruments due to the high humidity formed immediately during playing. From the point of view of museum conservators this can—in principle—not be tolerated in the very old, precious instruments, so the corrosion rate and mechanism of corrosion of the brass alloys had to be investigated.
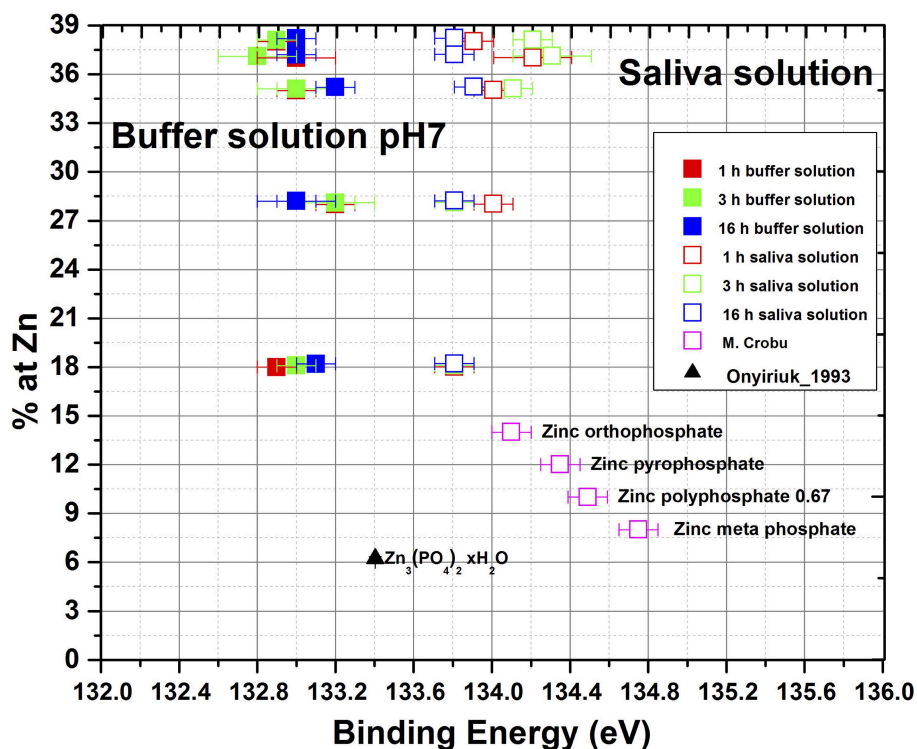
FIGURE 8 | P2p$_{3/2}$ binding energy of surface films formed on brass alloys in artificial saliva and in phosphate buffer solution together with phosphate compounds.

In a series of works it could be established using a dedicated electrochemical sensor that the highest corrosion rates of more than 20 μm/year were observed on freshly polished brass surfaces (Elsener et al., 2016a,b). Brass alloys or parts of old instruments covered with an oxide film showed much lower corrosion rates.

In this work freshly polished CuZn37 brass alloys was exposed to artificial saliva solution, a situation that could be encountered when playing brass wind instruments: measurements showed a high relative humidity inside the instruments after short playing time that remained for several days afterwards (Von Steiger et al., 2015). When analyzing the instrument with neutron computer tomography during playing (simulated with a flux of wet air) even condensation of solution was found (Von Steiger et al., 2015)—thus "artificial saliva" might be a severe but realistic environment inside the tuning slides. The possible formation of a protective surface film as reported in this work might contribute to markedly reduce the corrosion attack. In addition a drying treatment of the interior parts of the instrument with a fan was found to reduce the corrosion rate at least by a factor of two. The average corrosion rates measured after drying were lower than 3 μm/year and thus acceptable for playing the precious historic instruments in concerts (Von Steiger et al., 2018).

CONCLUSIONS

This work combining XPS surface analysis and electrochemical impedance spectroscopy in studying brass alloys with 18–37% of zinc in neutral phosphate buffer or saliva solution allows drawing the following conclusions:

Electrochemical impedance spectroscopy (EIS) allowed revealing the dissolution mechanism of the alloys in the two solutions studied:

- In the phosphate buffer solution the dissolution rate is charge transfer controlled, prolonged exposure time up to 16 h had only a minor influence on the corrosion rate.
- In the artificial saliva solution, the dissolution rate of the brass alloys is controlled by the resistance of the protective film formed on the surface, the corrosion rate decreased with prolonged exposure time. The charge transfer resistance was found at about 3 ± 1 kΩcm^2 for all alloys and exposure times.

Quantitative analysis of the surface films formed on the brass alloys in artificial saliva solution by XPS/XAES spectroscopy indicated 22 ± 3 at % zinc, 14 ± 3 at % phosphorus and about 64 ± 5 at % oxygen, thus the presence of $Zn_3(PO_4)_2$ indicated in the chemical state plot is confirmed. The increase of the film resistance with time can be interpreted as an increase in the film thickness and/or the formation of a more compact film.

The surface film formed in the phosphate buffer solution on all the brass alloys and even after 16 h of immersion shows a thickness of some nanometres only as the presence of the metallic component of both Cu and Zn was detected in the high-resolution XAES spectra. This can explain the charge

transfer controlled dissolution mechanism of the brass alloys in this solution.

DATA AVAILABILITY STATEMENT

The raw data supporting the conclusions of this article will be made available by the authors, without undue reservation, to any qualified researcher.

AUTHOR CONTRIBUTIONS

FUNDING

ACKNOWLEDGMENTS

SUPPLEMENTARY MATERIAL

The Supplementary Material for this article can be found online at: https://www.frontiersin.org/articles/10.3389/fchem.2020.00272/full#supplementary-material

REFERENCES

Aldakov, D., Chappaz-Gillot, C., Salazar, R., Delaye, V., Welsby, K. A., Ivanova, V., et al. (2014). Properties of electrodeposited CuSCN 2D layers and nanowires influenced by their mixed domain structure. *J. Phys. Chem. C* 118 16095–16103. doi: 10.1021/jp412499f

Antonijevic, M. M., and Petrovic, M. B. (2008). Copper corrosion inhibitors. a review. *Int. J. Electrochem. Sci.* 3, 31–28.

Barsoukov, E., and Macdonald, J. R. (2018). *Impedance Spectroscopy: Theory, Experiment, and Applications*, 3rd Edn. Hoboken, NJ: Wiley & Sons, Inc.

Biesinger, M. C. (2017). Advanced analysis of copper X-ray photoelectron spectra. *Surf. Int. Analy.* 49, 1325–1334. doi: 10.1002/sia.6239

Briggs, D., and Grant, J.T. (2003). *Surface Analysis by Auger and X-Ray Photoelectron Spectroscopy.* West Sussex: IM Publications and Surface Publication Data.

Butt, J. (2002). *Playing with History - The Historical Approach to Musical Performance.* Cambridge: Cambridge University Press.

Cocco, F., Fantauzzi, M., Elsener, B., Atzei, D., and Rossi, A. (2016a). Dissolution of brass alloys naturally aged in neutral solutions – an electrochemical and surface analytical study. *RSC Adv.* 6, 90654–90665. doi: 10.1039/C6RA18200C

Cocco,. F., Fantauzzi, M., Elsener, B., Atzei, D., and Rossi, A. (2016b). Nanosized surface films on brass alloys by XPS and XAES. *RSC Adv.* 6, 31277–31289. doi: 10.1039/C5RA23135C

Crobu, M., Rossi, A., Mangolini, F., and Spencer, N. D. (2012). Chain-length-identification strategy in zinc polyphosphate glasses by means of XPS and ToF-SIMS. *Analyt. Bioanalyt. Chem.* 403, 1415–1432. doi: 10.1007/s00216-012-5836-7

Deyab, M. A., Essehlib, R., and El Balic, B. (2015). Inhibition of copper corrosion in cooling seawater under flowing conditions by novel pyrophosphate. *RSC Adv.* 5, 64326–64334. doi: 10.1039/C5RA08119J

Drogowska, M., Brossard, L., and Ménard, H. (1992). Effects of phosphate ions on copper dissolution and passivation. *J. Electrochem. Soc.* 139 2787–2793.

Elsener, B., Alter, M., Lombardo, T., Ledergerber, M., Wörle, M., Cocco, F., et al. (2016a). A non-destructive *in-situ* approach to monitor corrosion inside historical brass wind instruments; *Microchem. J.* 124, 757–764, doi: 10.1016/j.microc.2015.10.027

Elsener, B., Cocco, F., Fantauzzi, M., and Rossi, A. (2016b). Determination of the corrosion rate inside historical brass wind instruments – proof of concept. *Mater. Corros.* 67, 1336–1343. doi: 10.1002/maco.201608996

Fantauzzi, M., Pacella, A., Fournier, J., Gianfagna, A., Andreozzi, G. B., and Rossi, A. (2012). Surface chemistry and surface reactivity of fibrous amphiboles that are not regulated as asbestos. *Analy. Bioanaly. Chem.* 404, 821–833. doi: 10.1007/s00216-012-6190-5

Onyiriuka, E. C. (1993). Zinc phosphate glass surfaces studied by XPS. *J. Non Crystalline Solids* 163, 268–273.

Passiu, C., Rossi, A., Bernard, L., Paul, D., Hammond, J., Unger, W. E. S., et al. (2017). Fabrication and microscopic and spectroscopic characterization of planar, bimetallic, micro- and nanopatterned surfaces. *Langmuir* 33, 5657–5665. doi: 10.1021/acs.langmuir.7b00942

Pattanasattayavong, P., Ndjawa, G. O. N., Zhao, K., Wei Chou, K., Yaacobi-Gross, N., O'Regan, B. C., et al. (2013). Hole-transporting transistors and circuits based on the transparent inorganic semiconductor copper(I) thiocyanate (CuSCN) processed from solution at room temperature. *Chem. Commun.* 49 4154–4156. doi: 10.1002/adma.201202758

Reilman, R.F., Msezane, A., and Manson, S.T. (1976). Relative intensities in photoelectron spectroscopy of atoms and molecules. *J. Electr. Spectrosc. Relat. Phenomena* 8, 389–394.

Rossi, A., and Elsener, B. (1992). XPS analysis of passive films on the amorphous alloy Fe70Cr10P13C7: effect of the applied potential. *Surf. Interface Anal.* 18, 499–504.

Scofield, J.H. (1976). Hartree-Slater subshell photoionization cross-sections at 1254 and 1487 eV. *J. Electr. Spectrosc. Relat. Phenomena* 8, 129–137. doi: 10.1016/0368-2048(76)80015-1

Shirley, D.A. (1972). High-resolution X-ray photoemission spectrum of the valence bands of gold. *Phys. Rev. B* 5, 4709–4714. doi: 10.1103/PhysRevB.5.4709

Strehblow, H.H., and Titze, B. (1980). The investigation of the passive behaviour of copper in weakly acid and alkaline solutions and the examination of the passive film by ESCA and ISS. *Electrochim. Acta* 25, 839–850.

Tani, G., and Zucchi, F. (1967). Electrochemical measurement of the resistance to corrosion of some commonly used metals for dental prosthesis. *Minerva Stomatol.* 16, 710–713.

Tanuma, S., Powell, C. J., and Penn, D. R. (2003). Calculation of electron inelastic mean free paths (IMFPs) VII. Reliability of the TPP-2M IMFP predictive equation. *Surf. Interface Analy.* 35, 268–275. doi: 10.1002/sia.1526

Valcarce, M.B., and Vázquez, M. (2010). Phosphate ions used as green inhibitor against copper corrosion in tap water. *Corros. Sci.* 52, 1413–1420. doi: 10.1016/j.corsci.2009.12.015

Von Steiger, A., Allenbach, D., Elsener, B., Ledergerber, M., Lombardo, T., Mannes, D., et al. (2015). To play versus to display – Historische Blasinstrumente aus

Messing im Spannungsfeld zwischen Konservierung und Nutzung. *Glareana* 2, 4–18. doi: 10.24451/arbor.6953

Von Steiger, A., Allenbach, D., Ledergerber, M., Elsener, B., Mannes, D., Lombardo, T., et al. (2018) New insights into the conservation of brass instruments: brass instruments between preventive conservation and use in historically informed performance, *Hist. Brass Soc. J.* 30, S. 85–101. doi: 10.2153/0120180011005

Von Steiger, A., Senn, M., Tuchschmid, M., Leber, H. J., Lehmann, E., and Mannes, D. (2013). Looking through the windows of French brasswind instrument workshops. *Historic Brass Soc. J.* 25, 21–38. doi: 10.2153/01201300 11002

Multi-Spectroscopic Approach for the Non-invasive Characterization of Paintings on Metal Surfaces

Monica Albini[1]*, Stefano Ridolfi[2], Chiara Giuliani[1], Marianna Pascucci[1], Maria Paola Staccioli[1] and Cristina Riccucci[1]

[1] Institute for the Study of Nanostructured Materials, National Research Council, Rome, Italy, [2] Ars Mensurae, Rome, Italy

The aim of this study is to propose a non-invasive multi-spectroscopic approach for the characterization of oil painting artworks that use a copper plates as substrate in place of a canvas. Indeed, in the last decade, many studies have been conducted on artworks made of single materials (e.g., paintings, stones, metals). However, the characterization and conservation of composite artifacts has never be fully investigated even though many masterpieces were created using this particular technique. In this work, several spectroscopic techniques such as Infrared Spectroscopy (FTIR), Energy-Dispersive X-Ray Fluorescence spectroscopy (EDXRF), and high spatial resolution Field Emission Scanning Electron Microscopy coupled with Energy Dispersive X-ray Spectroscopy (EDS), and Optical Microscopy (OM) were performed. The obtained results allowed to fully characterize the micro-chemical and microstructural features of the painted surfaces and of the metal plate. Particularly effective was the use of MA-XRF, resulting in the chemical map of the painted surfaces. Furthermore, traces of the mechanical preparation of the plate were found under the painted layers. Finally, the interface area between the paint film and the metallic support was characterized at a micro scale. This was particularly important in order to identify the degradation products formed by the interaction between the fatty acids of the binder and copper-based substrates.

Keywords: painting, metal, spectroscopy, FTIR, SEM-EDS, MA-XRF, imaging

INTRODUCTION

The technique of oil painting on a metal plate is not renowned by the public and the full potential of these artworks is not yet exploited. The practice of painting on metallic surfaces, in particular iron and copper, originated in Europe. An extraordinary example of this technique is the oil painting on copper supports, that started in the 16th century and had a huge growth in Europe during the 17th and 18th century (Graaf, 1972; Horovitz, 1986, 2017; Komanecky et al., 1998; Wadum, 2017). Magnificent artists like Rembrandt, Guido Reni, Diego Velasquez, and Peter Paul Rubens among others, created masterpieces using such a peculiar technique. More than two-thousand extant paintings on metals are exhibited in European and American museums, excluding the far larger production of portraits miniatures on copper (Komanecky, 1990). Indeed, the Galleria degli Uffizi in Florence has, in its collection, more than 500 portrait miniatures using a copper plate as support. The conservation of these artifacts is, thus, extremely important. Nevertheless, few data are available about this painting technique and about the conservation methodology to adopt to preserve them (Thistlewood and Northover, 2009; Pitarch et al., 2014; Veiga et al., 2014, 2015; Fuster-Lopez and Mecklenburg Marion, 2017; Colantonio et al., 2018).

The interesting challenge about these incredible artifacts is their composite nature. In fact, conservation activities have to deal with multiple materials and different degradation processes related to the metallic substrate, the organic paint film, and their interface interactions (Catalano et al., 2019; Keune et al., 2019; Rosi et al., 2019). Furthermore, an additional obstacle to the characterization of these objects is the impossibility to analyze the stratigraphy of the painting. In fact, because of their artistic value, cross-section destructive analyses are precluded on these artifacts. Thus, it is important to develop a systematic approach that exploit non-invasive analytical techniques for the study and characterization of oil paint on a metal substrate.

This work aims to propose a good analytical practice based on a multi-spectroscopic approach to characterize the microchemical and microstructural composition of these artworks and of their degradation products as it is done for painting on canvas (Miliani et al., 2010; Pitarch et al., 2014). This approach will allow to minimize and, in most cases, to make unnecessary the use of destructive analyses. A miniature portrait on a copper-based substrate (**Figure 1**) was analyzed by the means of multispectral imaging methods (UV, IR, and IRFC) (Cosentino, 2014), optical microscopy (OM), scanning electron microscopy coupled with energy-dispersive X ray spectrometry (SEM–EDS) (Haswell et al., 2006; Ingo et al., 2013), Fourier-transform infrared spectroscopy (FTIR) (Spring et al., 2005; Van der Weerd et al., 2005; Miliani et al., 2007) and macro X ray fluorescence (MA-XRF) (Cesareo et al., 2016; Iorio et al., 2019).

FIGURE 1 | Picture of the painting on metal plate under investigation.

MATERIALS AND METHODS

Artifact

The artwork under investigation belongs to a private collector and it is an oil painting representing the portrait of a nobleman painted on a metal plate as substrate (**Figure 1**). Unfortunately, it is not possible to attribute the painting to a specific artist as well as to a specific age, but due to the composition, the technique and the pigments used it is possible to presume that it was produced between the end of the 17th and the beginning of 18th century.

Multispectral Imaging Methods
Ultraviolet-Visible Fluorescence Photography (UV)
Pictures of ultraviolet fluorescence of the painting were collected by a Canon EOS 500D camera equipped with 18–55 mm lens by illuminating the artifact with a Wood's lamp (E27, 160W).

Infrared (IR) and Infrared False Color Reflectography (IRFC)
Infrared pictures (IR) were acquired in the range 400–1,100 nm using a MICRO IR 20 camera charge-coupled device with a silicon detector CCD equipped with 12.5 mm lens (f 1.3) and a VIS and IR80 filters.

Optical Microscopy (OM)
Investigations were performed by using Leica MZFLIII and Leica LAS multi-focus stereo microscopes equipped with a digital camera (Leica DFC 320).

Field-Emission Scanning Electron Microscopy Coupled With Energy-Dispersive X Ray Spectrometry (FE-SEM–EDS)
The artifact was positioned inside the analytical chamber of the microscope without any surface preparation. The metal part of the artifact (verso) was connected with the microscopy stub using copper wires. For the investigation, a high-brilliance and high-spatial-resolution LEO Gemini 1530 (Zeiss, Germany) field emission scanning electron microscope (FE-SEM) was used. The instrument was equipped with an INCA 450 (Oxford Instruments Analytical, U.K.) energy-dispersive X-ray spectrometer (EDS) and four-sector back-scattered electron (BSE) detectors. Images were recorded at an acceleration voltage of 20 kV. The EDS was calibrated using RXS-36M commercial metals reference standard.

Fourier Transform Infrared Spectroscopy (FTIR)
FTIR analyses were performed on the painting surface without any preparation using a Thermo Scientific Nicolet™Continuμm Infrared Microscope operating in reflectance mode. The FTIR microscope is equipped with an MCT-A (Mercury Cadmium Telluride) detector cooled by liquid nitrogen and a 15× Thermo—Electron Infinity Reflachromat objective with a tube
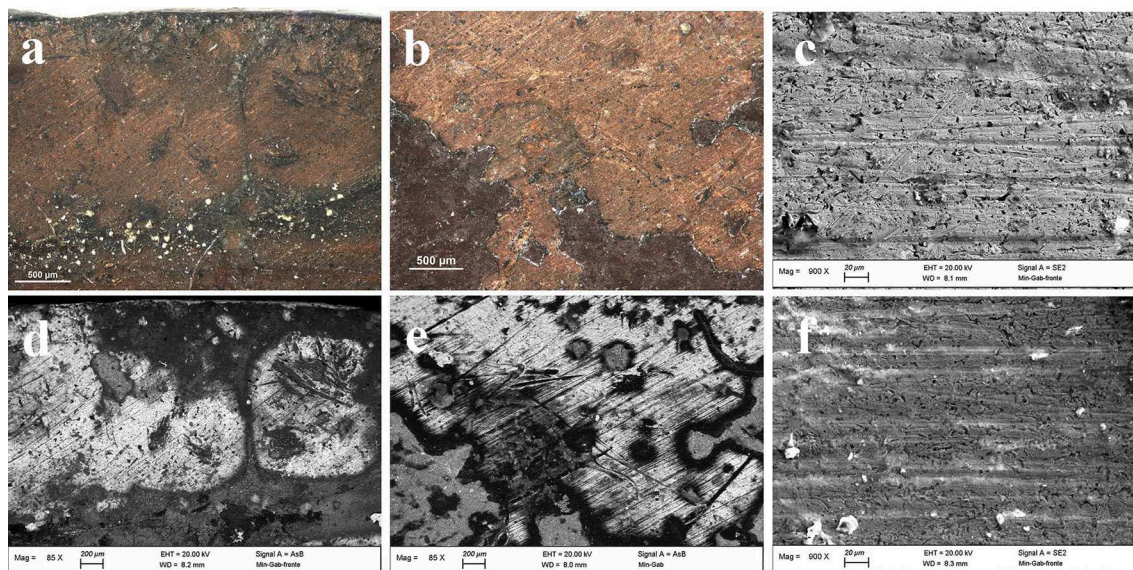
FIGURE 2 | OM **(a,b)** and FE-SEM **(c–f)** images of painting failures showing the underlying metal plate with working marks.

factor of 10×. All spectra were acquired in the range 4,000–650 cm^{-1}, at a spectral resolution of 4 cm^{-1}. A total of 32 scans were recorded and the resulting interferograms averaged. Data collection and post-run processing were carried out using Omnic^{TM} software.

Macro X-Ray Fluorescence (MA-XRF)

MA-XRF analyses were performed by a scanner prototype built by the INFN Roma TRE division and Ars Mensurae (Iorio et al., 2019). The scanner has an exchangeable head attached to a motorized x-y stage. The head is made of a low-power Moxtek$^®$ tube with a Ta target and collimated to 1 mm, a silicon drift detector (SDD), and a twin-laser focusing system. The images resolution is about 1 mm^2 per pixel. The tube operated at 37 kV and 17 μA with a dwell-time of 1 s. The XRF scanner was calibrated using SRM 1115—Commercial Bronze Standard for Optical Emission and X-ray Spectroscopic Analysis (NIST standard reference material) with the following composition expressed as % of mass fraction: Copper 87.96, Zinc 11.73, Lead 0.013, Iron 0.13, Tin 0.10, Nickel 0.074, and Phosphorus 0.05.

RESULTS AND DISCUSSION

Metal Substrate

The metal plate used as substrate was investigated on both sides of the painting. The back side was easily reachable because of the absence of a painted layer. However, the accessibility of the front side was limited to those areas where painting failures exposed the metal surface underneath. Therefore, only few area of the front side were investigated. The first visual characterization of both sides was performed by optical microscopy. The main difference between the two sides is the presence of parallel lines engraved on the front of the plate (**Figures 2a,b**), that are not
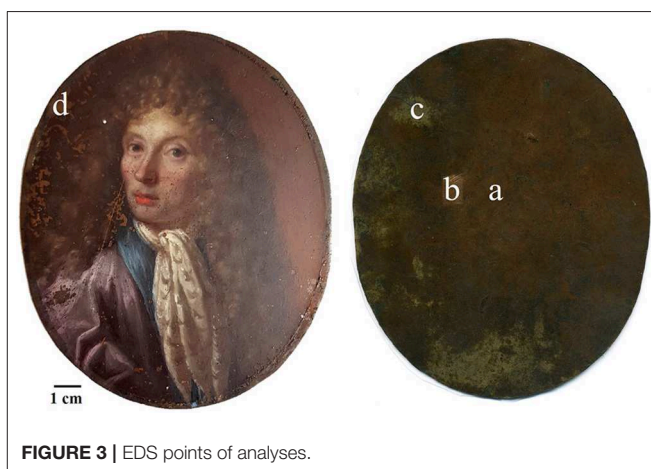
FIGURE 3 | EDS points of analyses.

present on the back. In order to characterize these lines and due to its limited dimensions, the artwork was positioned inside an FE-SEM chamber and analytical measurements were performed directly on its surface. The FE-SEM images (**Figures 2c–f**) allowed to measure the width of this marks that can be grouped into 3 different ranges: a large one of 7.56 ± 0.45 μm, a medium one of 4.64 ± 0.35 μm and a small one of 2.82 ± 0.35 μm. Because of the consistency in width and direction, these lines seem to be intentional working marks made by the artist using a specific tool. Previous studies (Horovitz, 1986; Komanecky, 1990; Vega, 2016) suggested that, for this particular painting technique, artists used to prepare the metal surface in order to allow a better hold of the oil paint. The presence of these marks confirms these studies, revealing the intention of increase the surface roughness of the substrate to enable the adhesion of the paint layers to it. The two

sides were also investigated by EDS in order to characterize the elemental composition of the metal plate. Three different area of the back side and one of the front side were analyzed (**Figure 3** and **Table 1**).

On the back, the analyses were performed on one area with the original red patina, one area with the bare metal exposed after a mechanical cleaning by scalpel, and also one area showing a whitish patina. In particular, analyses on the bare metal were performed in order to obtain an indication about the original chemical composition of the plate. Indeed, without cleaning, the original alloy signal could be attenuated by the presence of corrosion products on the metal surface resulting in the underestimation of minor elements. In **Table 1**, EDS results show that the metal substrate is made of a ternary bronze (Cu, Sn, Pb) with the presence of impurity such as Al, S, Cl, Fe, Ni, and As. The presence of these elements is quite common in ancient copper-based alloys and it is due to the smelting and uncompleted purification processes of copper from its ores (Craddock, 1976, 1977, 1978). The composition of the plate resulted to be similar on both patinated sides, with a higher contribution of those elements coming from the external environment and interacting with the metal. However, the content of tin appears to be significantly different. This result, paired with the composition of the whitish area on the back mainly containing tin corrosion products, may suggest a phenomenon of differential corrosion and surface enrichment in Sn at the back of the plate. Indeed, the back side was constantly exposed to the environment while the front was protected by the paint film that acted as a "coating." Therefore, it is possible that the measured composition is the result of Sn concentration gradient that increases moving from the center toward the surface of the plate. Since the front side is partially protected from corrosion phenomena, the concentration of Sn has not increased there. To confirm this hypothesis, it would be interesting to analyze a cross-section of the metal substrate that would allow a better characterization of the chemical composition of the plate. Unfortunately, due to the general good conservation state of the painting, it was not possible to perform this supplementary investigation without jeopardizing the integrity of the artifact.

Paint Layers

A first characterization of the painted layers was performed by multispectral imaging techniques as UV fluorescence, IR and IR false color (IRFC) photography on the entire surface of the painting (**Figure 4**). This allowed to determine the possible presence of an underlying preparatory layer as well as underdrawings, pentimenti or alterations. Also, these techniques can detect the presence of protective layers, retouches above and/or below the varnish and any other restoration intervention. Furthermore, it was possible to obtain preliminary informations about the pigments used in the upper layers (Cosentino, 2014). From the UV picture it is possible to observe, on the left edge, the presence of a blue fluorescence due to some residues from an old protective varnish. This evidence indicates an almost complete intervention of cleaning of the varnish that was most probably oxidized. The small dark spots with no

TABLE 1 | Elemental composition of the metal plate by EDS analyses.

Analised area	C	O	Al	Si	S	Cl	K	Ca	Fe	Ni	Cu	As	Sn	Pb
Back side—No Patina	12.80 ± 4.14	5.24 ± 1.13	0.05 ± 0.07	ND	0.57 ± 0.08	0.45 ± 0.05	ND	ND	0.15 ± 0.21	0.07 ± 0.10	77.29 ± 5.68	0.18 ± 0.14	3.09 ± 0.14	0.13 ± 0.18
Back side—White Patina	9.75 ± 0.88	11.05 ± 7.26	0.10 ± 0.13	0.11 ± 0.16	0.68 ± 0.68	0.60 ± 0.49	ND	ND	0.19 ± 0.26	ND	65.03 ± 9.11	ND	12.35 ± 1.22	ND
Back side—Red Patina	29.28 ± 0.17	15.32 ± 0.55	0.17 ± 0.01	0.38 ± 0.04	1.18 ± 0.08	0.96 ± 0.12	ND	0.15 ± 0.21	0.51 ± 0.01	0.05 ± 0.07	48.23 ± 0.54	0.05 ± 0.06	3.50 ± 0.29	0.44 ± 0.06
Front side	37.26 ± 8.38	11.34 ± 8.38	0.24 ± 0.03	0.58 ± 0.10	0.31 ± 0.04	0.29 ± 0.05	0.17 ± 0.06	ND	0.08 ± 0.11	ND	49.00 ± 7.98	0.05 ± 0.07	0.09 ± 0.12	0.62 ± 0.04

Results are showed in wt%. ND, not detected.

FIGURE 4 | Painting images by imaging techniques: **(A)** visible; **(B)** UV-induced visible fluorescence; **(C)** IR Reflectography. **(D)** IR false-color images.

fluorescence are due to non-retouched failures of the painting, while the areas on the face and on the neckcloth seem to be re-painted areas. This hypothesis is supported by the IR pictures results, where the different transparency of the pigments to the radiation showed the unevenness of the trait due to small retouches. Furthermore, the investigation by IR radiation did not show pentimenti or other modification to the composition as well as no underlying preparatory drawing. However, it is important to highlight here that the absence of a light-colored preparatory layer pose some limitations to the technique and does not allow to observe the high chromatic contrast that would results from a dark trait on a light background. Therefore, it is not possible to fully exclude the existence of a preparatory drawing even though no evidence of its presence were found. The final imaging technique applied to this painting was the IRFC photography, that allows to suggest the possible use of some pigments from its chromatic response. The red pigments from the lips, the skin, the eyes inner corner and part of the brown background resulted as a yellow tone which is usually due to the presence of cinnabar. Also, the red-purple resulting color of the collar, the eyes and partially of the blouse, might indicate the presence of lapis lazuli pigment. It is of uppermost importance to underline that, although IRFC results are reliable and of great importance for painting characterization as non-invasive technique, they only give an indication about the possible pigments used and cannot be substitute to chemical analyses. Therefore, to confirm IRFC results, the characterization of the

pigment needs to be done through complementary chemicalbr analysis techniques.

In order to identify pigments and binder, EDS, MA-XRF and μFTIR were performed. In **Figure 5** results from EDS analyses for each color are summarized. The white pigment used for the neckcloth and the skin contains mainly Pb suggesting the use of lead white [$(PbCO_3)_2 \cdot Pb(OH)_2$]. Furthermore, a high content of Pb was found on the entire painting surface but mainly in the bright areas. This is due to its use in mixture with other pigments to brighten them and create a chiaroscuro effect in the composition. Concerning the skin color, in addition to Pb, the presence of S and Hg indicated the use of cinnabar or vermillion (HgS) in combination with lead white. Cinnabar and vermillion are red pigments that have the same chemical composition and differ only for their origin, being a natural mineral the first and an artificial synthetic product the latter. The two forms of this red pigments are not distinguishable using this analytical technique. The presence of cinnabar was also detected in the lower lip of the figure, while, in the upper lip, this pigment was not found. The disappearing of Hg and S corresponded to a relevant increase in the content of C suggesting the use of a red organic pigment that resulted in a darker red color. The blue pigment used for the eye iris and for the collar of the blouse contained Si, Al, Na, S, that indicate the use of lapis lazuli pigment (Na_{8-10} $Al_6Si_6O_{24}S_{2-4}$). This pigment was one of the most refined and expensive among all pigments and during the Renaissance it coasted even more than gold (Roy, 1993; Eastaugh et al., 2007). Therefore, the use of this pigment was exclusively devoted to refined and high-quality paintings. Lapis lazuli was also probably used to paint the blouse in mixture with the organic red pigment already detected in the upper lip in order to create the purple color. The brown background contains at the same time Fe, Al, and Ca that are the main component of brown ocher as well as a Hg and S, suggesting a mixture of the ocher with cinnabar, to enhance the red tone. The brown shade of the hair, on the contrary, was made using only the ocher. From this first chemical analysis, it is worth to notice that the indications given by the IRFC characterization were confirmed.

A combined chemical and visual characterization of the pigments was performed by MA-XRF, which resulted in the elemental distribution map of the painting. The main elements identified in each pigment can be used to map the white (Pb), the red (Hg), and the brown (Fe) color, as showed in **Figure 6**. However, due to the instrumental set-up, light elements as Na, Al, Si, and S that are present in the lapis lazuli could not be detected and, thus, this pigment was not mapped. In addition to the signals of the main pigments components, it is interesting to look at the Cu signal coming from the metal support, that can provide insights about both the thickness and the characteristics of the superposing pigments. In fact, the decrease of Cu signal corresponds to those areas where Pb is present and the higher is the Pb signal the lower is the Cu one. This is explained by the fact that Pb has shielding properties toward X-rays and therefore, the higher are its concentration and thickness the higher will be its shielding effect. In general terms, the use of this technique is comparable to EDS, giving the same analytical results, made exception for the lighter elements detection. However, EDS
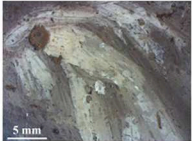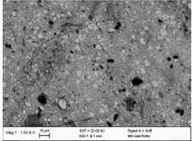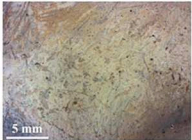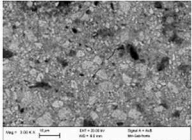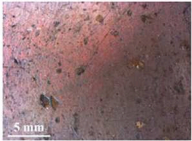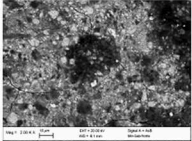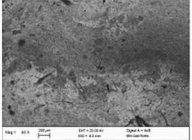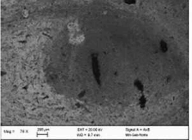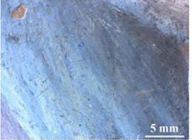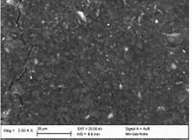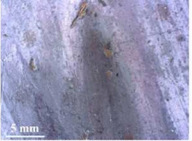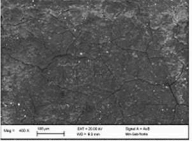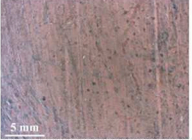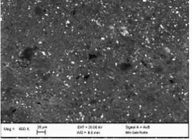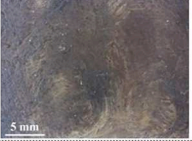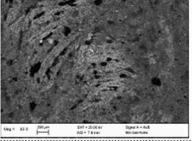
Color /area	OM	FE-SEM	Elements	Pigment attribution
White - Neckcloth			**Pb**, *Cu, Cl*, Na, Ca	Lead white
Skin – Forehead			**Pb**, *Cl*, Si, Ca	Lead white
Skin - Cheek			**Pb**, *Cl, Cu*, Al, Si, S, Ca, Hg	Lead White; Cinnabar
Red-Lips			Upper: **C**, *Pb, Al, Ca, Cu*, Si, Cl Lower: **Pb, Hg,** *S, Cu, Cl*, Si, Al	Upper: Organic Red Lower: Cinnabar; Lead white
Blue- eye			**Pb**, *Si, Al*, Na, Ca, *Cu, Cl*, S, K	Lapis lazuli ultramarine; Lead white
Blue - Collar			**Pb**, *Si, Al*, Na, Ca, S, *Cu*, Cl, K	Lapis lazuli ultramarine; Lead white
Violet -			**C,** Pb, *Si, Al*, Na, Ca, S, *Cu*, Cl, K	Lapis lazuli ultramarine; Lead white; Organic red
Brown - Background			**Pb**, *Al, Si, S, Ca, Fe, Cu, Hg*, Na, P, Cl, K	Red Ocher; Cinnabar; Carbon Black
Brown - Hair			**Pb**, *Si, Al*, Ca, *Fe, Cu*, Cl, P, K	Red Ocher; Lead white

FIGURE 5 | OM and FE-SEM pictures for each color shade of the painting. EDS results are showed in element wt% concentration range: higher than 10% (bold), between 10 and 1% (*italic*) and lower than 1% (regular). The C and O content is omitted, although always present, since their presence do not provide an indication for the pigment attribution. The pigment attribution is proposed based on the detected element.

analyses cannot be performed on large objects, due to the limited analytical chamber dimensions. Furthermore, most of the time it is mandatory to perform *in-situ* measurements, making XRF the best techniques for such situations. Moreover, this technique combines the advantages of a single spot chemical analyses, as EDS or classic XRF, with the more straightforward visual
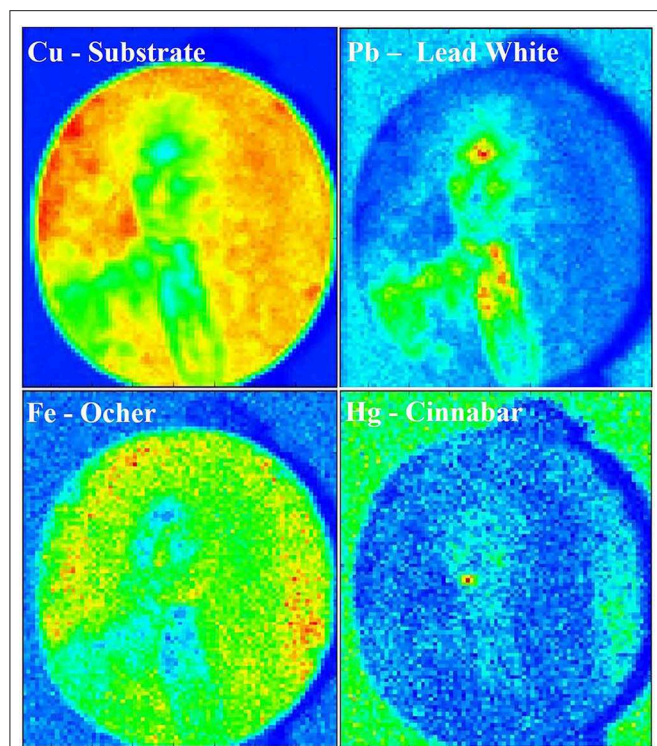
FIGURE 6 | MA-XRF chemical map of the painting showing the distribution of Cu, Pb, Fe, and Hg. The intensity scale goes from blue (no detection of the element) to red (highest concentration of the element).
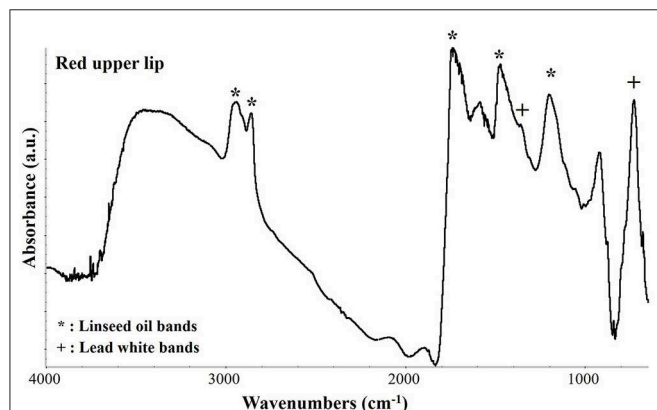

FIGURE 7 | μFTIR absorbance spectrum collected on the upper lips in correspondence of a dark red pigment. The characteristic peaks of linseed oil and of lead white are indicated by an asterisk (*) and a cross (+), respectively.

FIGURE 8 | OM and μFTIR absorbance spectrum picture of the green degradation products found at the paint-metal interface. The spectrum of the product (black) is compared with the reference spectrum of copper oleate (gray). The asterisks indicate the corresponding copper oleate peaks in the green degradation product spectrum.

interpretation given by imaging techniques as UV, IR, and IRFC. If needed, the use of this technique would allow to detect hidden paintings below the outermost surface, due to the difference in composition between pigments used in different time of history (Saverwyns et al., 2018). Therefore, even if time consuming, the application of MA-XRF for the study of this kind of artifact allows to have many information by a non-invasive approach and to

have an easier discussion of the results between scientist and conservators or art-historians.

The characterization of the organic materials of the painting, such as the organic medium and the red pigment of the upper lips, was performed by μFTIR analysis (Vetter and Schreiner, 2011). In **Figure 7** the resulting spectrum acquired on the upper lips is shown. The peaks at 2,963, 2,937, 2,858, and 1,465 cm^{-1} are characteristic of C-H vibrational modes while the wide and asymmetric peak at 1,737 cm^{-1} indicates the C=O bond. All these peaks are characteristic of an aged linseed oil that was most probably used as binder of this painting. Regarding the red pigment, the FTIR spectra were not conclusive since the only other peaks present were those of lead white at 1,400, 1,358, and 7,60 cm^{-1}. On the bases of all the investigation performed, it can be possible to presume that the red pigment could be a red lake. Indeed, because of the low content of dyestuff in traditional red lake pigments it would be very difficult to detect it in a mixture with lead white. In fact, the μFTIR spectrum would be easily

dominated by the bands of the inorganic white pigment and of the binder.

Finally, μFTIR spectroscopy was used to analyze some characteristic green corrosion products that were found at the interface between the paint layers and the copper plate (**Figure 8**). These products were only visible in those areas with painting failures and their presence resulted in a very brittle paint film. The corrosion product was identified as copper oleate, with its characteristic bands at 2,960, 2,930, 2,855, 1,592, 1,509, a broad band between 1,469, and 1,410, 1,316, 1,281, and 1,114 cm^{-1} (Robinet and Corbeil, 2003; Deng et al., 2014). The presence of metal soaps at the paint/copper interface is due to the interaction between the fatty acid of the binder and the metal ions of the substrate. Therefore, as suggested by other authors (Low et al., 1967; Pavlopoulou and Watkinson, 2006; Casadio et al., 2019), the formation of this corrosion product has to be expected in this kind of artifacts and possibly monitored in order to avoid brittleness of the paint film.

CONCLUSIONS

In this work, a non-invasive analytical approach for the characterization of a painting on metal plate was proposed and performed. These kind of artworks present typical issues of composite artifacts made of two different materials. The use of a wide range of spectroscopic analytical techniques allowed to tackle both the paint film and the metal plate as well as new products originated from the metal/paint interaction. The micro-chemical and microstructural approach allowed to characterize the metal substrate, its composition and its preparation that the artist performed in order to obtain the best outcome for the painting. Furthermore, the full characterization of the painting with its pigments and binder, the preparatory layer and the conservation-restauration interventions was performed. Finally, it was possible to identify newly formed compounds resulting from the interaction between the metal plate and the painting binder. As future perspective,

it would be interesting to further investigate a cross-section of the metal plate. This would allow to better characterize its composition as well as to look at the nano and microstructure of the metal bulk in order to obtain useful information about the working processes used to produce the plate. To conclude, the non-invasive multi-spectroscopic approach used on this artifact can be proposed as a good analytical practice to be adopted for the study of oil paintings on metal plates as it is already made for oil on canvas. The analyses allowed to obtain valuable information about the painting technique and the conservation state of the artwork that can be used by the conservator-restorers to propose the best conservation method and materials for the conservation-restoration on these artifacts.

DATA AVAILABILITY STATEMENT

The datasets generated for this study are available on request to the corresponding author.

AUTHOR CONTRIBUTIONS

MA designed the experiments and prepared the manuscript. CR and MP performed the FE-SEM characterization. SR carried out imaging and MAXRF characterization. MA, CG, and MPS performed FTIR characterization.

FUNDING

REFERENCES

Casadio, F., Keune, K., Noble, P., Van Loon, A., Hendriks, E., Centeno, S. A., et al. (2019). *Metal Soaps in Art*. Amsterdam: Springer.

Catalano, J., Murphy, A., Yao, Y., Zumbulyadis, N., Centeno, S. A., and Dybowski, C. (2019). "Understanding the dynamics and structure of lead soaps in oil paintings using multinuclear NMR," in *Metal Soaps in Art. Cultural Heritage Science,* eds F. Casadio, et al. (Cham: Springer), 69–84.

Cesareo, R., Jordan, R. F., Fernandez, A., Bustamante, A., Fabian, J., Zambrano, S., et al. (2016). Analysis of the spectacular gold and silver from the Moche tomb 'Señora de Cao.' *X-Ray Spectro.* 45, 138–154. doi: 10.1002/xrs.2680

Colantonio, C., Pelosi, C., D'Alessandro, L., Sottile, S., Calabrò, G., and Melis, M. (2018). Hypercolorimetric multispectral imaging system for cultural heritage diagnostics: an innovative study for copper painting examination. *Eur. Phys. J. Plus* 133:526. doi: 10.1140/epjp/i2018-12370-9

Cosentino, A. (2014). Identification of pigments by multispectral imaging; a flowchart method. *Herit. Sci.* 2:8. doi: 10.1186/2050-7445-2-8

Craddock, P. T. (1976). The composition of the copper alloys used by the Greek, Etruscan and roman civilizations 1. The Greeks before the archaic period. *J. Archaeol. Sci.* 3, 93–113. doi: 10.1016/0305-4403(76)90079-0

Craddock, P. T. (1977). The composition of the copper alloys used by the Greek, etruscan and roman civilisations: 2. The archaic, classical and hellenistic greeks. *J. Archaeol. Sci.* 4, 103–123. doi: 10.1016/0305-4403(77)90058-9

Craddock, P. T. (1978). The composition of the copper alloys used by the Greek, Etruscan and roman civilizations: 3. The origins and early use of brass. *J. Archaeol. Sci.* 5, 1–16. doi: 10.1016/0305-4403(78)90015-8

Deng, D., Qi, T., Cheng, Y., Jin, Y., and Xiao, F. (2014). Copper carboxylate with different carbon chain lengths as metal–organic decomposition ink. *J. Mater. Sci.* 25, 390–397. doi: 10.1007/s10854-013-1599-y

Eastaugh, N., Walsh, V., Chaplin, T., and Siddall, R. (2007). *Pigment Compendium: A Dictionary of Historical Pigments*. Oxford: Routledge.

Fuster-Lopez, L., and Mecklenburg Marion, F. (2017). "A look into some factors influencing the film forming properties of oil paint films in copper paintings and the effects of environment in their structural behaviour," in *Paintings on Copper and Other Metal Plates. Production, Degradation and Conservation Issues*, eds L. Lopez-Fuster, et al. (Valencia: Universidad Politécnica de Valencia), 95–102.

Graaf, J. A. (1972). Development of oil-paint and the use of metal-plates as a support. *Stud. Conservat.* 17, 139–151. doi: 10.1179/sic.1972.17.s1.004

Haswell, R., Carlyle, L., and Mensch, K. T. J. (2006). Van gogh's painting grounds: quantitative determination of bulking agents (Extenders) using SEM/EDX. *Microchim. Acta* 155, 163–167. doi: 10.1007/s00604-006-0536-7

Horovitz, I. (1986). Paintings on copper supports: techniques, deterioration and conservation. *Conservator* 10, 44–48. doi: 10.1080/01410096.1986.9995017

Horovitz, I. (2017). "Paintings on copper: a brief overview of their conception, creation and conservation," in *Paintings on Copper and Other Metal Plates. Production, Degradation and Conservation Issues*, eds L. Lopez-Fuster, et al. (Valencia: Universidad Politécnica de Valencia), 17–26.

Ingo, G. M., Guida, G., Angelini, E., Di Carlo, G., Mezzi, A., and Padeletti, G. (2013). Ancient mercury-based plating methods: combined use of surface analytical techniques for the study of manufacturing process and degradation phenomena. *Acc. Chem. Res.* 46, 2365–2375. doi: 10.1021/ar300232e

Iorio, M., Graziani, V., Lins, S., Ridolfi, S., Branchini, P., Fabbri, A., et al. (2019). Exploring manufacturing process and degradation products of gilt and painted leather. *Appl. Sci.* 9:3016. doi: 10.3390/app9153016

Keune, K., Kramer, R. P., Stangier, S., and van Eikema Hommes, M. H. (2019). "Impact of lead soaps on the formation of age craquelure," in *Metal Soaps in Art. Cultural Heritage Science,* eds F. Casadio, et al. (Cham: Springer), 107–121.

Komanecky, M. K. (1990). *Copper as Canvas: Two Centuries of Masterpiece Paintings on Copper, 1575-1775*. Oxford: Oxford University Press, Inc.; Phoenix Art Museum.

Komanecky, M. K., Horovitz, I., and Eastaugh, N. (1998). Antwerp artists and the practice of painting on copper. *Stud. Conservat.* 43, 136–139. doi: 10.1179/sic.1998.43.Supplement-1.136

Low, M. J. D., Brown, K. H., and Inoue, H. (1967). The reaction of oleic acid with copper surfaces. *J. Col. Inter. Sci.* 24, 252–257. doi: 10.1016/0021-9797(67)90228-7

Miliani, C., Rosi, F., Brunetti, B. G., and Sgamellotti, A. (2010). *In situ* noninvasive study of artworks: the MOLAB multitechnique approach. *Acc. Chem. Res.* 43, 728–738. doi: 10.1021/ar100010t

Miliani, C., Rosi, F., Burnstock, A., Brunetti, B. G., and Sgamellotti, A. (2007). Non-invasive in-situ investigations versus micro-sampling: a comparative study on a renoirs painting. *Appl. Phys. A* 89, 849–856. doi: 10.1007/s00339-007-4222-3

Pavlopoulou, L.-C., and Watkinson, D. (2006). The degradation of oil painted copper surfaces. *Stud. Conservat.* 51, 55–65. doi: 10.1179/sic.2006.51.Supplement-1.55

Pitarch, A., Ramón, A., Álvarez-Pérez, A., Castro, K., Madariaga, J. M., and Queralt, I. (2014). Multispectroscopic characterization of oil on copper painting. *Spectro. Lett.* 47, 38–51. doi: 10.1080/00387010.2013.782319

Robinet, L., and Corbeil, M.-C. (2003). The characterization of metal soaps. *Stud. Conservat.* 48, 23–40. doi: 10.1179/sic.2003.48.1.23

Rosi, F., Cartechini, L., Monico, L., Gabrieli, F., Vagnini, M., Butiet, D., et al. (2019). "Tracking metal oxalates and carboxylates on painting surfaces by non-invasive reflection Mid-FTIR spectroscopy," in *Metal Soaps in Art. Cultural Heritage Science*, eds F. Casadio, et al. (Cham: Springer,), 173–193.

Roy, A. (1993). *Artists' Pigments: A Handbook of their History and Characteristics, v. 2*. Washington, DC: Oxford University Press; National Gallery of Art,.

Saverwyns, S., Currie, C., and Lamas-Delgado, E. (2018). Macro X-ray fluorescence scanning (MA-XRF) as tool in the authentication of paintings - sciencedirect. *Microchem. J.* 137, 139–147. doi: 10.1016/j.microc.2017.10.008

Spring, M., Higgitt, C., and Saunders, D. (2005). Investigation of pigment-medium interaction processes in oil paint containing degraded smalt. *Nat. Gallery Tech. Bull.* 26, 56–70.

Thistlewood, J., and Northover, P. (2009). Corrosion analysis and treatment of two paintings on zinc supports by frederick preedy. *J. Ins. Conservat.* 32, 137–148. doi: 10.1080/19455220903059933

Van der Weerd, J., Van Loon, A., and Boon, J. J. (2005). FTIR studies of the effects of pigments on the aging of oil. *Stud. Conservat.* 50, 3–22. doi: 10.2307/25487713

Vega, D. E. (2016). *Oil painting on copper: characterization of the copper support and the feasibility of using pigmented wax-resin infills for paint loss reintegration* (Ph.D. thesis). Faculdade de Ciências e Tecnologia da Universidade Nova de Lisboa, Lisbon, Portugal.

Veiga, A., Mirão, J., Candeias, A. J., Rodrigues, P. S., Teixeira, D. M., Muralha, V. S. F., et al. (2014). Pigment analysis of portuguese portrait miniatures of 17th and 18th centuries by raman microscopy and SEM-EDS. *J. Raman Spectro.* 45, 947–957. doi: 10.1002/jrs.4570

Veiga, A., Teixeira, D. M., Candeias, A. J., Mirão, J., Manhita, A., Miguel, C., et al. (2015). Micro-analytical study of two 17th century gilded miniature portraits on copper. *Microchem. J.* 123, 51–61. doi: 10.1016/j.microc.2015.05.015

Vetter, W., and Schreiner, M. (2011). Characterization of pigment binding media systems comparison of non invasive *in situ* reflection FTIR with transmission FTIR microscopy. *e-PRESERVATIONScience* 8, 10–22.

Wadum, J. (2017). "The Spanish connection. The making and trade of antwerp paintings on copper in the 17th century," in *Paintings on Copper and Other Metal Plates. Production, Degradation and Conservation Issues*, eds L. Lopez-Fuster, et al. (Valencia: Universidad Politécnica de Valencia), 27–42.

On-Demand Release of Protective Agents Triggered by Environmental Stimuli

Chiara Giuliani[1], Elena Messina[1], Maria Paola Staccioli[1], Marianna Pascucci[1], Cristina Riccucci[1], Leonarda Francesca Liotta[2], Luca Tortora[3,4], Gabriel Maria Ingo[1] and Gabriella Di Carlo[1*]

[1] Institute for the Study of Nanostructured Materials (ISMN), National Research Council (CNR), Rome, Italy, [2] Institute for the Study of Nanostructured Materials (ISMN), National Research Council (CNR), Palermo, Italy, [3] Surface Analysis Laboratory, Istituto Nazionale di Fisica Nucleare (INFN) - Sezione di Roma Tre, Rome, Italy, [4] Department of Sciences, Roma Tre University, Rome, Italy

The aim of this study was to develop smart materials with stimuli-responsive properties for the long-term protection of steel. The idea was to obtain a tailored and controlled release of protective agents in response to the environment stimuli. First, the protective efficacy of three inhibitors containing a carboxylic moiety, such as *p*-aminobenzoic (pAB), succinic (SA), and caffeic (CA) acids, was investigated in alkaline chloride solutions. The results revealed that pAB is the most effective protective agent, significantly better than SA and CA. It is surprising that the steel surface in the pAB solution remains unchanged even after 5 months of corrosion treatment, whereas the formation of degradation products in the SA and CA solutions was observed after only 6 days. Based on these findings, pAB was selected and used for the functionalization of silica nanoparticles and layered double hydroxides (LDHs) that can act as delivery vehicles and as an inhibitor reservoir. Specifically, pAB was chemisorbed on silica amino groups *via* an amide bond, and this makes possible a gradual inhibitor release induced by an alkaline environment. The intercalation of pAB in its anionic form into the LDHs structure is responsible for a completely different behavior since the release is induced by chloride ions and occurs by an anionic exchange reaction. Thus, these materials play a dual role by acting as an inhibitor reservoir and by capturing chlorides. These findings reveal that it is possible to create a reservoir of corrosion inhibitors gradually released on demand based on the chemical environment. The stimuli-responsive properties and the complementary protective action of inhibitor-loaded silica and LDHs make them attractive for the long-term protection of steel and open the way for innovative solutions in the preservation of concrete cultural heritage.

Keywords: nanocarriers, inhibitors, corrosion, stimuli responsive, steel

INTRODUCTION

Chloride-induced corrosion of reinforcing steel is one of the major causes of degradation in concrete structures. During the past decades, the search for new protective materials has received considerable attention in order to hinder the degradation processes which can be responsible for irreversible damages (Bertolini et al., 2004; Goyal et al., 2018). The inhibition of steel corrosion

is mandatory to increasing the service life of reinforced concrete structures and is particularly relevant to avoiding the loss of reinforced concrete monuments that are recognized as part of a cultural heritage. To face these issues, an attractive strategy is to develop novel solutions that can provide a long-lasting protection by considering safety and aesthetic aspects. The latter are necessary especially in cultural heritage applications.

Several approaches have been explored to prevent or slow down the corrosion processes of metals and their alloys (Bertolini et al., 2004; Rani and Basu, 2012; Yang et al., 2013; Saremi and Yeganeh, 2014; Giuliani et al., 2018; Goyal et al., 2018). Among them, the use of corrosion inhibitors is one of the most attractive since it can offer a simple and cost-effective prevention technique (Ormellese et al., 2009; Yang et al., 2016). In the last decades, organic inhibitors mainly based on mixtures of alkanolamines, amines, organic acids, or amino acids have received great interest since they represent an effective and safe alternative to common inorganic inhibitors (Jamil et al., 2003; Söylev and Richardson, 2008; Gartner et al., 2016). However, their efficiency may be reduced by certain factors, such as the evaporation of the volatile components (Elsener et al., 1999; Tritthart, 2003). Moreover, due to increasing awareness of the health and ecological risks, the search for environment-friendly inhibitors for steel represents an open issue. Further efforts are necessary to explore new interesting compounds, improve the efficacy of protective agents, and develop systems able to provide long-term action against corrosion.

A promising approach is to develop smart materials that can act as a reservoir of inhibitors and release them under external stimuli, thus prolonging their protective action. Due to their versatility, silica and layered double hydroxides (LDHs) have great potential to be used for the storage and controlled release of corrosion inhibitors (Yang et al., 2013, 2016; Saremi and Yeganeh, 2014; Rahsepar et al., 2017; Salzano de Luna et al., 2018). According to the literature, silica nanocontainers were studied, for example, as a host of molybdate ions or a mercaptobenzothiazole corrosion inhibitor (Saremi and Yeganeh, 2014; Rahsepar et al., 2017). Layered double hydroxides were intercalated with different inhibitor molecules, including organic acids (Yang et al., 2016). Several substances of potential interest have also been investigated for the corrosion inhibition of steel, among them organic acids and their derivatives, such as p-aminobenzoic (pAB), succinic (SA), and caffeic (CA) acids (Giacomelli et al., 2004; Amin et al., 2007; de Souza and Spinelli, 2009; Yang et al., 2016).

The novelty of this study is in selecting an environment-friendly organic corrosion inhibitor containing at least a carboxylic moiety and using the same molecule for the functionalization of both silica and the LDH nanocarrier. Moreover, the stimuli-responsive properties of the inhibitor-loaded nanocarriers were investigated in alkaline chloride solutions. To the best of our knowledge, a direct comparison between silica and the LDH nanocarriers loaded with the same inhibitor has not been reported so far.

The presence of a carboxylic group was preferred since it is suitable for chemisorption on silica and for the intercalation

into the LDH structures. To select the protective agent, three corrosion inhibitors, pAB, SA, and CA, were compared and their protective efficacy was investigated in alkaline chloride solutions. The alkaline pH simulates the typical environment of steel reinforcement in concrete structures, whereas chloride ions promote the corrosion processes, thus assessing the protective efficacy in a short time. The best-performing candidate, pAB, was chemisorbed into silica nanoparticles and intercalated into a layered double hydroxide. The challenge was to develop stimuli-responsive materials able to release the inhibitor under pH variations and in the presence of chloride ions. In particular, pAB chemisorption on silica *via* amide bonds is aimed at a pH-dependent release, whereas the intercalation into LDHs is of interest for a chloride-induced release. Silica nanoparticles and LDHs functionalized with pAB were characterized by using complementary techniques and their stimuli-responsive properties were explored in the alkaline chloride solutions.

MATERIALS AND METHODS

Materials

Silica nanoparticles with an average diameter of 5–15 nm and specific surface area of 540 m^2/g, 3-aminopropyl)-triethoxysilane (APTES), 1-(3-(dimethylamino)propyl)-3ethylcarbodiimide (EDC), N-hydroxysuccinimide (NHS), p-aminobenzoic acid, 4-morpholineethanesulfonic acid (MES), ninhydrin, ethanol, and toluene were purchased from Sigma-Aldrich. Magnesium nitrate hexahydrate, aluminum nitrate non-ahydrate, and succinic acid were purchased from Carlo Erba.

Preparation of Silica and LDHs With Inhibitor

Silica Nanoparticles With Inhibitor

Preparation of amino-functionalized silica nanoparticles (SiO₂-NH₂)

Amino-functionalized silica nanoparticles (SiO_2-NH_2) were prepared by dissolving 0.5 g of commercial silica nanoparticles (SiO_2-NPs-15) in 30 ml of anhydrous toluene. Then, 1.3 ml of APTES was slowly added to the silica suspension under vigorous stirring. The resulting solution was refluxed at 120°C under stirring for 24 h. The nanoparticles were separated by centrifugation (10,000 rpm, 10 min; Thermo Scientific IEC CL31R Multispeed Centrifuge) and then purified by five cycles of centrifugation–dispersion in ethanol (50 ml), followed by vacuum drying at 60°C for 12 h.

Preparation of p-aminobenzoic-functionalized silica nanoparticles (SiO₂-NH-pAB)

The carboxylic groups of pAB were activated with EDC in the presence of NHS. The use of water-soluble EDC and NHS avoids the use of organic toxic solvents in the synthesis. EDC (150 mg) and NHS (111 mg) were added to a solution of pAB (133 mg) in 8 ml of MES buffer (0.1 M, pH 5.5). The reaction was allowed to proceed under stirring at room temperature for 1 h. Subsequently, a suspension of 400 mg of amino-functionalized silica (SiO_2-NH_2) in 20 ml of MES buffer

was added to the pAB solution. The mixture was kept in the dark, at room temperature, under stirring for 24 h. The obtained nanoparticles were separated by centrifugation (10,000 rpm, 10 min; Thermo Scientific IEC CL31R Multispeed Centrifuge), purified by repeated cycles of centrifugation and dispersion in water (two cycles) and ethanol (four cycles), and dried in air at room temperature for 24 h.

Layered Double Hydroxides With Inhibitor

MgAl-pAB was prepared by a pH-controlled co-precipitation synthetic method (Meyn et al., 1990; Aisawa et al., 2001; Kuang et al., 2010), which is the most common preparative technology for LDHs. This method is based on the hydrolysis of M^{2+} and M^{3+} hydroxide ions in the presence of pAB (Wang and O'Hare, 2012).

The Mg/Al ratio chosen for the synthesis was 1:1 to obtain stable layered compounds. Typically, 200 ml of a mixed solution of 0.25 M $Mg(NO_3)_2 \cdot 6H_2O$ and 0.25 M $Al(NO_3)_2 \cdot 9H_2O$ was slowly added dropwise to 200 ml of 0.125 M of the pAB solution at room temperature, with stirring under a nitrogen atmosphere to avoid contamination by atmospheric CO_2 (He et al., 2004). The free organic acid was previously dissolved in a freshly prepared solution of NaOH (0.4 M) and the resulting solution stirred for 1 h under nitrogen.

The solution pH of the moisture remained fairly constant at 10 by dropwise addition of 1 M NaOH. The slurry was aged at 65°C for 24 h and then the resulting precipitate was washed extensively with water, centrifuged, and dried at 70°C under vacuum for a further 24 h. The product was labeled as LDH-pAB.

Mg–Al–MHT–NO$_3$ was also synthesized by using the co-precipitation method, where an aqueous solution containing M^{2+} and M^{3+} ions was slowly added to a basic aqueous solution (NaOH). The precipitate was then filtered in a vacuum process and washed with deionized water in order to remove the excess nitrate. The solid was dried at 100°C in an oven for 12 h. The so-obtained material was labeled as LDH-NO$_3$ and used as a comparison during the characterizations.

Characterization

X-Ray Powder Diffraction

The measurements were performed in a Siemens 5000 X-ray powder diffractometer with a CuKα radiation ($\lambda = 1.5418$ Å) filtered by a nickel window. Angular values with a step size of 0.05° and a sampling time of 2 s were the experimental parameters used for data acquisition. In order to identify the crystalline phases, analysis of the X-ray diffraction patterns was carried out by using electronic databases.

FTIR Spectroscopy

The spectra were recorded using a Nicolet iS50 (Thermo Fisher) spectrometer equipped with an attenuated total reflectance (ATR) accessory. The measurements were recorded using a diamond crystal cell ATR using typically 32 scans at a resolution of 4 cm^{-1}. No ATR correction has been applied to the data. The samples were investigated under the same mechanical force pushing the samples in contact with the diamond crystal.

Scanning Electron Microscopy

Morphological characterizations were performed by a high-brilliance and high-spatial-resolution LEO Gemini 1530 (Zeiss, Germany) field-emission scanning electron microscope (FE-SEM) equipped with an INCA 450 energy-dispersive X-ray spectrometer (EDS) and a four-sector backscattered electron detector (BSD).

Analysis of Amino Groups on Silica

The amino groups grafted on the silica nanoparticle surface were qualitatively detected and quantitatively determined by using the ninhydrin assay. Initially, ninhydrin in ethanol (2 ml, 25 mM) was reacted with APTES in ethanol at various known concentrations (0.2–0.85 mM). Ruhemann's Blue, with its characteristic intense absorption band at 584 nm, was formed by the selective reaction of ninhydrin with the primary amine groups. The absorbance at 584 nm of the above samples was recorded to establish the calibration curve by plotting the absorbance vs. the molarity of APTES. Thereafter, 10 mg of SiO$_2$-NH$_2$ was added to 2 ml of the ninhydrin ethanol solution (25 mM) and the mixture was heated at 90°C for 15 min. After cooling and centrifugation (10,000 rpm, 10 min; Thermo Scientific IEC CL31R Multispeed Centrifuge), the absorbance of the supernatant was measured at 584 nm against a blank reference (SiO$_2$-NH$_2$) by using a UV–Vis double-beam spectrophotometer (JASCO V 660). The supernatant was diluted in order to maintain the absorbance in the range 0.1–1. The concentration of the amine groups of SiO$_2$-NH$_2$ was determined by using the calibration curve of APTES.

TGA Analysis

SiO$_2$-NH$_2$ and SiO$_2$-NH-pAB were characterized by thermogravimetric analyses (TGA) to evaluate the organic content of the surface-modified silica nanoparticles. SiO$_2$-NPs-15 was used as a reference. TGA characterization was performed with a TGA/DSC1 STAR system from Mettler Toledo. The sample (15 mg) was treated under airflow (30 ml min^{-1}) heating from 25 to 1,100°C (ramp rate, 10°C min^{-1}).

Corrosion Tests in Simulated Concrete Pore Solutions

Steel disks were immersed in a simulated concrete pore solution prepared by dissolving 0.001 wt% Ca(OH)$_2$ in deionized water and fixing the pH at 10.5 using KOH (Gartner et al., 2016). In order to study the anti-corrosion performance of the three inhibitors selected (pAB, SA, and CA), an amount of 0.01 wt% of chloride ions was added to the solutions with a determined amount of inhibitor so as to reach a concentration of 50 mM. The disks were left in the simulated concrete pore solutions, and they were analyzed by means of optical microscopy after 40 h, 6 days, 20 days, and 5 months of immersion. The steel surface was also characterized by ATR-Fourier transform infrared (FTIR) spectroscopy after 6 days of corrosion tests.

Tests of Inhibitor Release

p-Aminobenzoic Acid Release Experiments

The inhibitor release was investigated in alkaline solutions at a pH of 12.65, which represents the typical value for concrete pore solutions (Ormellese et al., 2006; Garcés et al., 2011). Initially, alkaline solutions (pH 12.65) of pAB at various known concentrations ($1.75–4.25 \times 10^{-5}$ M) were prepared and their absorbance was recorded. The absorbance of the above samples at 266 nm was plotted vs. the molarity of pAB to establish the calibration curve of pAB at pH 12.65. Thereafter, pAB-functionalized silica nanoparticles (20 mg) were placed in an Eppendorf tube containing 1.5 ml of aqueous solution at neutral and alkaline pH (pH 12.65). The suspensions were kept in the dark at 30°C under stirring for 552 h (23 days). At predetermined intervals of time, i.e., 3, 24, 48, 144, and 552 h, the mixtures were centrifuged for 10 min at 10,000 rpm (Thermo Scientific IEC CL31R Multispeed Centrifuge) and the collected supernatants were analyzed by UV–Vis spectroscopy (JASCO V 660 UV–Vis double-beam spectrophotometer). An alkaline solution (pH 12.65) of pAB was used as the control. After that, the original nanoparticles were redispersed with the corresponding supernatant. The molar concentration (in moles per liter) of the released pAB was evaluated as a function of time by the absorption at 266 nm using a calibration curve for pAB.

The stimuli-responsive properties of LDH-pAB were investigated by using a similar procedure and by monitoring the inhibitor release in solutions at neutral pH, at alkaline pH, and at alkaline pH in the presence of chloride ions. The amount of pAB released into the solutions was measured at different times by UV–Vis spectroscopy considering the absorbance at 266 nm.

RESULTS AND DISCUSSION

Selection of Protective Molecules

In order to select the protective molecule to be confined into stimuli-responsive carriers, three corrosion inhibitors were compared, namely, pAB, SA, and CA. All these molecules contain at least a carboxylic group, but they differ for the other functional groups and their steric hindrance, as shown in **Figure 1**, and this can have an effect on the protective performance. These inhibitors were identified based on literature data since they were recognized as effective in corrosion inhibition (Giacomelli et al., 2004; de Souza and Spinelli, 2009; Yang et al., 2016). However, the tests assessing inhibitor efficacy are usually carried out in experimental conditions that are sometimes difficult to compare. Therefore, in this study, pAB, SA, and CA were tested by using the same procedure.

The protective efficacy of these inhibitors was evaluated by accelerating the corrosion of steel with chloride ions. Specifically, steel disks with a composition similar to commonly used rebars were immersed in simulated concrete pore solutions at pH 10.5 in the presence of chloride ions. The tests were conducted without any corrosion inhibitor (REF) and by adding equimolar amounts of pAB, SA, and CA to the solutions. The occurrence of modifications on the steel surface was evaluated by optical microscopy after immersion in the testing solutions for certain times, such as 20 h, 6 days, 20 days, and 5 months. The

micrographs in **Figure 2** clearly show that all the three molecules are able to protect the steel surface after treatment in solution for 20 h, whereas the formation of degradation products was observed in the disk used as the reference. By prolonging the corrosion tests up to 6 days, it was found that pAB is the most effective in steel protection. The optical micrographs in **Figure 2** show that pAB is able to prevent alterations on the steel surface even after 5 months. On the contrary, the formation of degradation products starts to be detected after 6 days of treatment in the presence of SA and CA (**Figure 2**). These results suggest that pAB is the most promising among the selected molecules for steel protection.

The surface of the steel disks after the corrosion tests was also investigated by FTIR spectroscopy, with the aim of obtaining information about alteration products and possible interaction with the protective molecules. The results in **Figure 3A** suggest the formation of a typical iron degradation product, such lepidocrocite (γ-FeOOH) (Veneranda et al., 2018). This could be ascribed to the presence of a broad band at about 1,027 cm^{-1} and to the signals at 1,158 and 871 cm^{-1}, which are usually assigned to the lepidocrocite phase. When the treatments are conducted in solutions containing pAB, the FTIR spectrum showed the presence of some weak signals (i.e., in the range from 1,700 to 1,600 cm^{-1}), which could be due to inhibitor molecules interacting with the steel surface (**Figures 3B,C**). This is in agreement with optical micrographs since a chemical interaction between pAB and steel can hinder substrate degradation, preventing surface modifications. No relevant signals were detected in the spectra recorded on the steel surface treated in the presence of SA and CA (data not shown).

These findings clearly show that pAB is significantly more effective than SA and CA in steel protection. Therefore, it was selected as the best candidate to be loaded into silica and LDH containers for the development of stimuli-responsive materials.

Stimuli-Responsive Systems for a Controlled Release

The pAB inhibitor was used for the functionalization of silica nanoparticles and LDH materials by using two different types of interaction and, consequently, different stimuli-responsive properties. In the case of silica nanoparticles, the inhibitor was chemisorbed through a reaction between the pAB carboxylic group and the amino reactive groups at the silica surface. In the case of LDH, the inhibitor in its anionic form was intercalated into the positively charged lamellar structure.

pH-Responsive Materials Based on Silica

Functionalization of silica nanoparticles with chemisorbed pAB

Commercial silica nanoparticles SiO_2-NPs-15, with an average diameter of about 5–15 nm and a high specific surface area of 540 m^2/g, were first functionalized at their surface with amino reactive groups able to bond pAB protective molecules. According to the literature (Kishor and Ghoshal, 2015), the functionalization with the amino groups (SiO_2-NPs-15–NH_2) was carried out by post-grafting the silica surface with organosilanes.
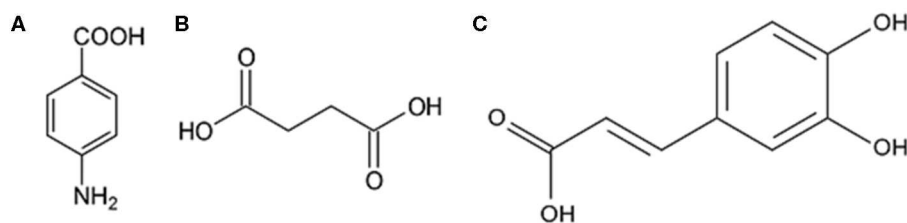
FIGURE 1 | Structural formula of **(A)** p-aminobenzoic acid (pAB), **(B)** succinic acid (SA), and **(C)** caffeic acid (CA).

The functionalization success was evaluated by ATR-FTIR spectroscopy. As shown in the spectra of SiO$_2$-NPs-15–NH$_2$ in **Figure 4**, the presence of the amino propyl functionalities was confirmed by the absorption band at 1,550 cm^{-1}, assigned to NH$_2$ bending vibrations, and by the weak band at 1,470 cm^{-1}, assigned to the symmetric –NH$_3^+$ deformation mode. The presence of the latter suggests that, when the sample is exposed to air, water molecules are weakly bonded to the amine groups, allowing their protonation. The broad bands in the range 2,500–3,500 cm^{-1} associated with the band near 1,630 cm^{-1} are also evidence of the water molecules hydrogen bonded on the silica nanoparticles. The N–H stretching vibration at 3,300 cm^{-1} is more difficult to observe because of its weak dipole moment and the superposition of the absorption of OH groups. In addition, the CH$_2$ asymmetric and symmetric stretching modes of the propyl chain are clearly visible at 2,937 cm^{-1} and in the range 2,850–2,920 cm^{-1}. The presence of the CH$_3$ asymmetric stretching mode at 2,980 cm^{-1} suggests that some ethoxy groups have not been completely hydrolyzed and that, consequently, the chemical-bonded APTES exists in a monodentate and bidentate structure grafted on the silica surface (Pasternack et al., 2008).

The organic content grafted on the SiO$_2$-NPs-15–NH$_2$ surface was evaluated at about 8 wt% ($\sim$1.2 $\times$ 10^{-6} mol APTES/mg SiO$_2$-NPs-15–NH$_2$) by thermogravimetric analysis from 300 to 770°C (Qiao et al., 2015). In the case of SiO$_2$-NPs-15–NH$_2$, the thermogram (reported in **Figure 5**) shows that the weight loss comes from three contributions (Qiao et al., 2015). The first contribution, in the temperature range of 25–200°C, derives from the elimination of the water molecules adsorbed on the silica surface. At temperatures higher than 200°C, the second weight loss results from the physically adsorbed APTES after ethanol washing. As the boiling point of APTES is 217°C, it is assumed that physically adsorbed APTES is completely desorbed at 300°C. Thus, the third contribution from 300 to 770°C comes from the decomposition of chemically bonded APTES and was used to quantify the grafting.

The amino groups at the silica surface were also qualitatively and quantitatively characterized by the ninhydrin assay. The selective reaction of ninhydrin with primary amine leads to the formation of a Ruhemann's Blue by-product with its characteristic intense absorption band at λ_{max} = 570 nm, thus allowing to assess and quantify the presence of amine groups. The concentration of the amine groups was calculated from the absorption at 570 nm of the SiO$_2$-NPs-15–NH$_2$ sample by using a calibration curve. The obtained value of 5.8 $\times$ 10^{-7} mol APTES/mg SiO$_2$-NPs-15–NH$_2$ is roughly of the same order of magnitude as that of the TGA. The differences can be explained by some approximations in the calculation from the TGA data.

The functionalization of the silica nanoparticles with the pAB inhibitor was conducted by introducing amino groups at the silica surface and by using them to covalently bond the inhibitor carboxylic moieties (de Oliveira et al., 2016). Therefore, the formation of a pH-sensitive amide bond between the SiO$_2$-NPs-15–NH$_2$ nanoparticles and pAB was used to provide a tailored release of the corrosion inhibitor in alkaline conditions. The obtained product was labeled as SiO$_2$-NPs-15-NH-pAB and was characterized by TGA to evaluate the inhibitor loading. The chemisorbed pAB was estimated at about 2.1 wt% by comparing the weight loss of SiO$_2$-NPs-15-NH-pAB and SiO$_2$-NPs-15–NH$_2$ in the range 300–770°C (**Figure 5**).

pAB release from silica nanoparticles

With the aim of investigating the stimuli-responsive properties of the SiO$_2$-NPs-15-NH-pAB nanocarrier, this system was studied in neutral environment and alkaline conditions simulating the concrete pore liquid. Defined amounts of SiO$_2$-NPs-15-NH-pAB were dispersed in a proper volume of aqueous solution at neutral and alkaline pH, and the pAB release was monitored at different time intervals, up to 552 h (23 days). An alkaline pH of 12.65 was selected since it represents the typical value of the concrete pore solutions. As expected, the experiments show a pH-dependent behavior of the inhibitor release from the nanocarrier. In particular, the pAB concentration in the silica suspension increases with time, from 0 to 144 h, under alkaline pH conditions (pH 12.65), whereas no pAB release is observed at neutral pH. A representative plot of the pAB release trends vs. time at the selected pH conditions is reported in **Figure 6**. A further increase in the pAB concentration is not detected by prolonging the test up to 552 h (23 days), thus suggesting that the amide hydrolysis is completed after 144 h (6 days) under experimental conditions. It is worth noting that the maximum release of pAB corresponds to about 2 wt% of the SiO$_2$-NPs-15-NH-pAB, confirming the inhibitor loading evaluated by TGA.

The obtained results confirm the pH-responsive properties of the developed SiO2-NPs-15-NH-pAB system. It is also worth noting that pAB release continued up to 144 h, due to the gradual hydrolysis of the inhibitor–nanocarrier amide bond, highlighting the potential of this system as an inhibitor reservoir for the long-term protection of steel substrates.
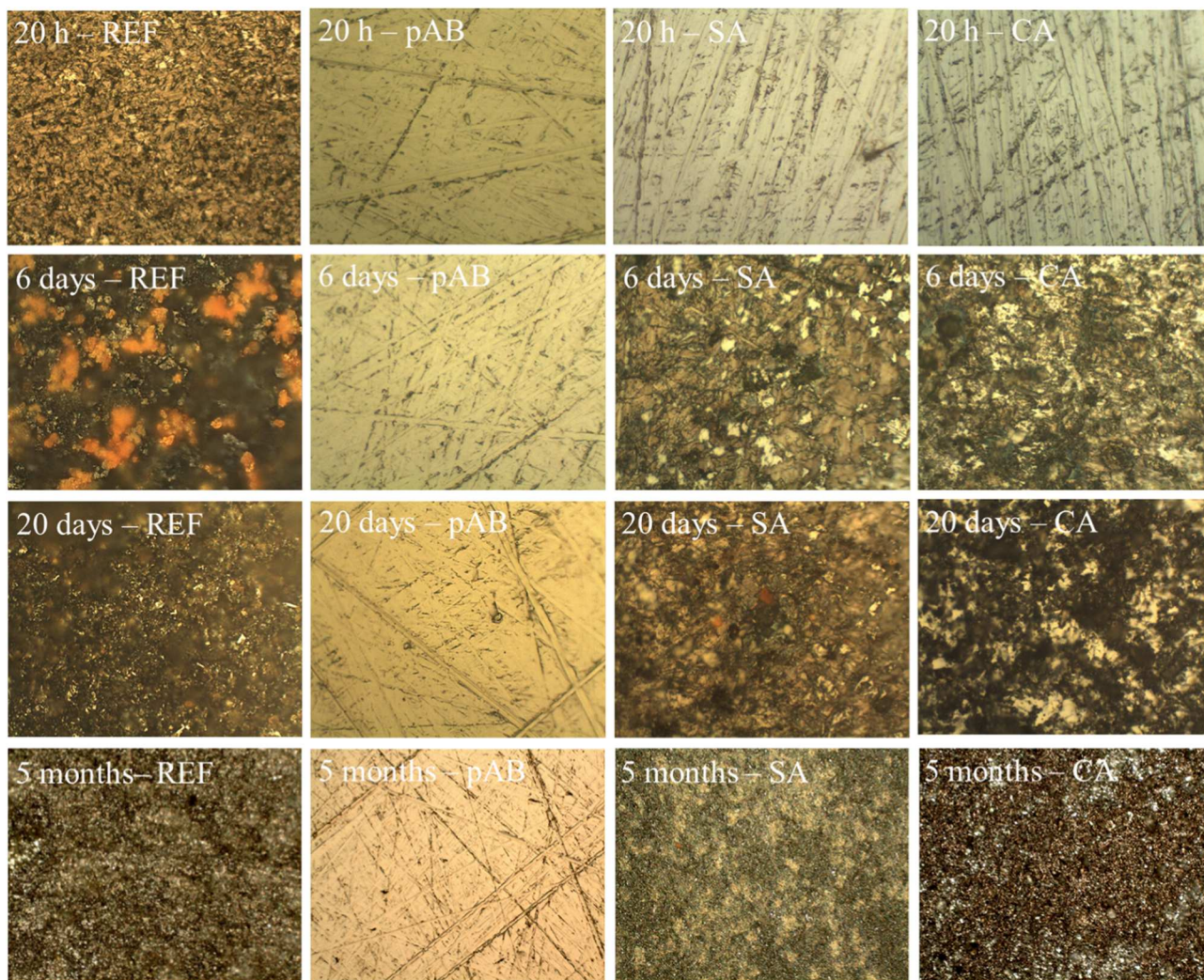
FIGURE 2 | Optical micrographs of the steel surface after corrosion treatment for 20 h, 6 days, 20 days, and 5 months in simulated concrete pore solutions containing chloride ions. The tests were conducted without inhibitor (*REF*) and with *p*-aminobenzoic acid (pAB), succinic acid (SA), and caffeic acid (CA).

Chloride-Responsive Materials Based on Layered Double Hydroxides

Intercalation of pAB into layered double hydroxides

The functionalization of LDH structures with pAB was achieved by using a co-precipitation method for their synthesis. The intercalation of pAB anions into the layered hydroxides was first evaluated by X-ray diffraction measurements. It is well-known that the basal *d*-spacings depend on the size of the intercalated guest anions and can be calculated from the (003) position using Bragg's law (Cavani et al., 1991). The X-ray powder diffraction (XRD) pattern of LDH-pAB is shown in **Figure 7**, and in order to confirm the intercalation of pAB anions, this profile was compared with LDH-NO$_3$. The diffraction pattern of LDH-NO$_3$ shows a typical layered structure with high crystallinity and a basal spacing *d*-value of 8.6 Å, comparable to those previously reported in the literature (Grover et al., 2010).

As expected, the pattern of LDH-pAB is rather different compared to LDH-NO$_3$. The basal reflections of LDH-pAB are broader and shifted at low angles, thus confirming the expansion of the crystalline structure, with a basal spacing *d*-value of 12.1 Å, due to the intercalation of the inhibitor guest molecules. The expanded interlayer separation is in good agreement with the results reported by Fischer and co-workers for LDHs loaded with pAB molecules (Yang et al., 2016).

The functional groups in LDHs intercalated with pAB and nitrates were investigated by ATR-FTIR spectroscopy, and their spectra are shown in **Figure 8**. Complete assignments of pAB bands require the application of an IR method supported by literature data (Samsonowicz et al., 2005). The relatively weak and broad band at around 3,500–3,100 cm^{-1} comes mainly from the O–H groups of the hydroxide layers and from the N–H stretching in the cases of the pAB-modified products (Yang et al., 2016). The peak at around 1,510 cm^{-1} corresponds to
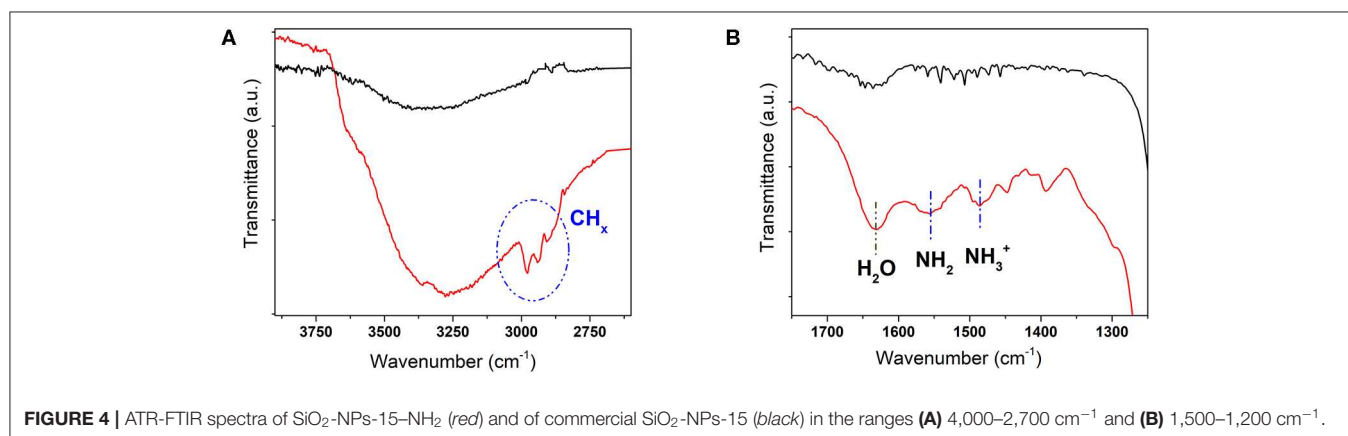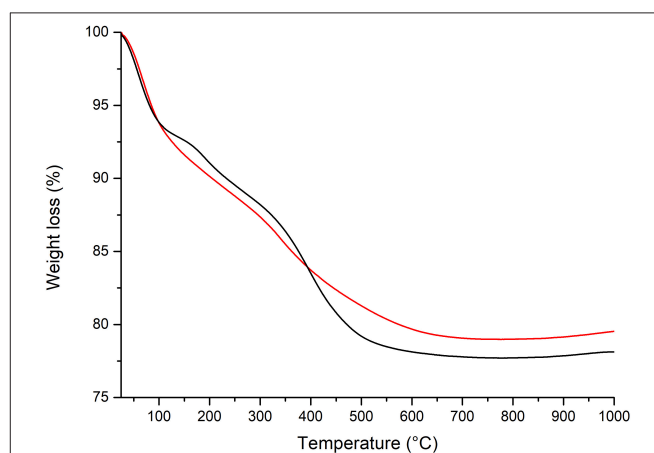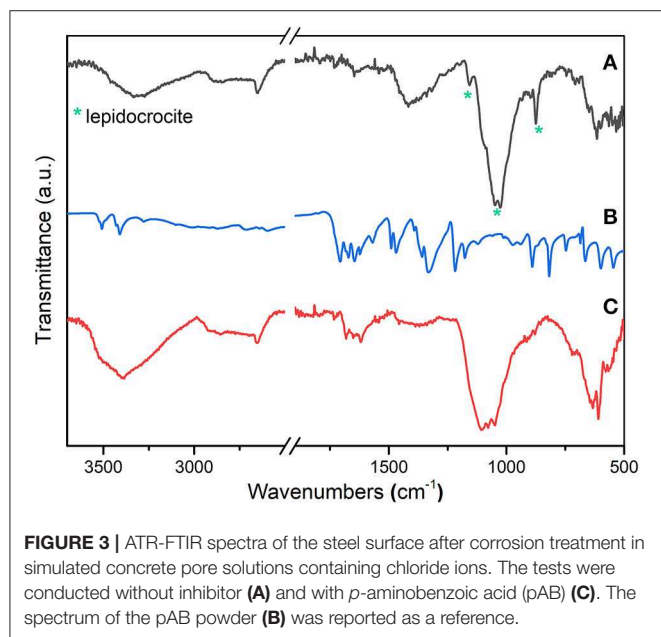
the asymmetric stretching vibrations associated with the –COO⁻ of pAB. Furthermore, other characteristic peaks of pAB are observed at around 1,602 cm^{-1} for the N–H bending mode, at around 1,587 cm^{-1} for the aromatic C=C stretching mode, and at around 1,284 and 1,179 cm^{-1} for the C–H bending vibrations of the benzene ring. The presence of these peaks is comparable to literature data for pAB-modified hydrotalcite (Yang et al., 2016) and indicates that pAB has been successfully intercalated into the interlayer space. The FTIR spectrum of LDH-NO$_3$ was reported in **Figure 8** for comparison. In this case, a peak occurring at 1,650 cm^{-1} can be ascribed to the bending mode of the interlayer water molecules. Additionally, an intense peak at about 1,350 cm^{-1} and a should near 1,400 cm^{-1} correspond to symmetric and asymmetric stretching modes of nitrate. The comparison between the FTIR spectra in **Figure 8** confirms that pAB molecules were successfully intercalated into the idrotalcite-like structure even if there was not a complete loss of interlayer nitrate anions
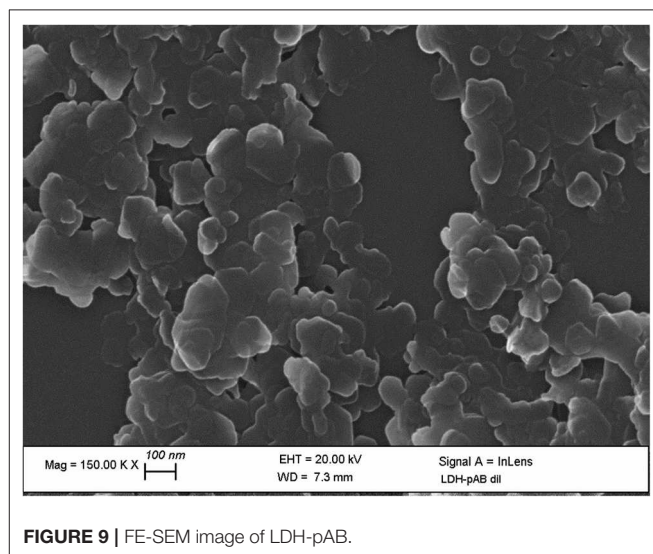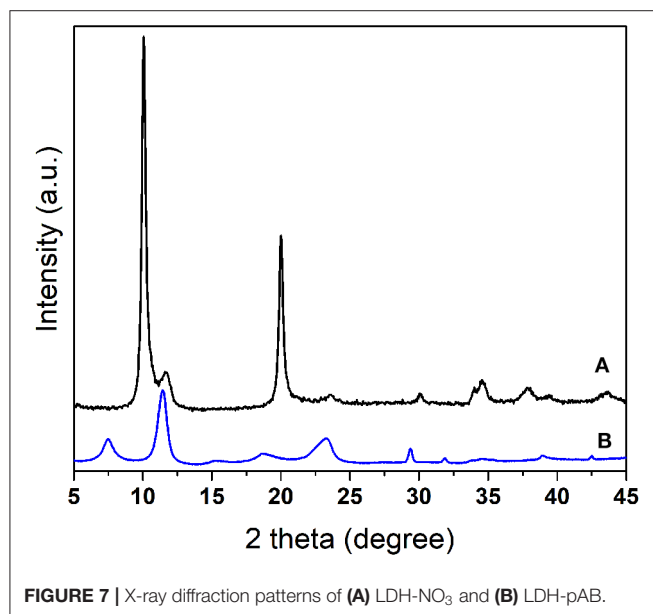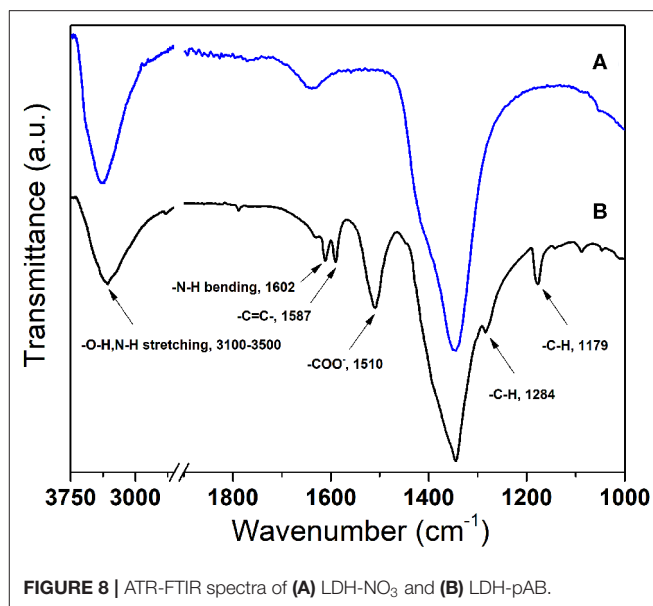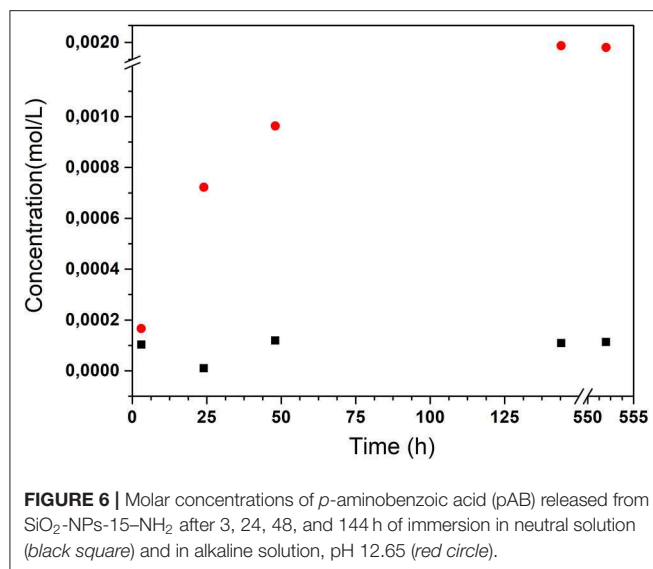
and bound water. This is indicated by the presence of a $\nu3$ stretching mode band of NO$_3^-$ at around 1,350 cm^{-1} and the O–H stretching band at 1,650 cm^{-1} for interlayer water molecules, although the intensity of both bands was much reduced.

The SEM images in **Figure 9** show that LDH-pAB particles are composed of round-edged hexagonal particles with a typical plate-like morphology. Probably, the presence of organic molecules in the interlamellar space has an effect on the aggregation between particles. In any case, the sizes of the LDH particles range from about 50 to 150 nm (Wang and Zhang, 2011).

pAB release from layered double hydroxides
In the LDHs, the organic anions can be exchanged by aggressive inorganic anions, such as chlorides present in the environment. Therefore, the release of pAB (in anionic form) from LDHs is expected to occur mostly by ion exchange. As such, LDHs play a dual role against chloride-induced corrosion, capturing chlorides as a chloride scavenger and providing corrosion inhibitors in
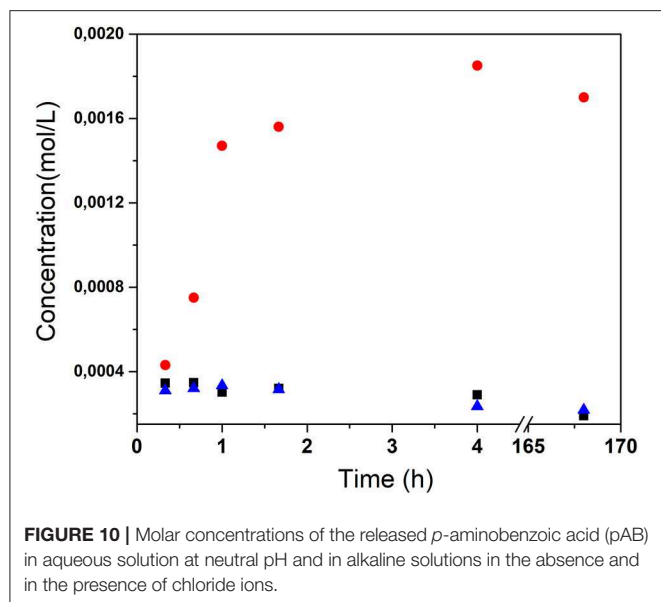

FIGURE 3 | ATR-FTIR spectra of the steel surface after corrosion treatment in simulated concrete pore solutions containing chloride ions. The tests were conducted without inhibitor **(A)** and with *p*-aminobenzoic acid (pAB) **(C)**. The spectrum of the pAB powder **(B)** was reported as a reference.

FIGURE 5 | Thermogravimetric (TG) curves in the N$_2$ flow of SiO$_2$-NPs-15-NH-pAB (*black line*) and SiO$_2$-NPs-15–NH$_2$ (*red line*).

FIGURE 4 | ATR-FTIR spectra of SiO$_2$-NPs-15–NH$_2$ (*red*) and of commercial SiO$_2$-NPs-15 (*black*) in the ranges **(A)** 4,000–2,700 cm^{-1} and **(B)** 1,500–1,200 cm^{-1}.

FIGURE 6 | Molar concentrations of *p*-aminobenzoic acid (pAB) released from SiO$_2$-NPs-15–NH$_2$ after 3, 24, 48, and 144 h of immersion in neutral solution (*black square*) and in alkaline solution, pH 12.65 (*red circle*).

FIGURE 8 | ATR-FTIR spectra of **(A)** LDH-NO$_3$ and **(B)** LDH-pAB.

FIGURE 7 | X-ray diffraction patterns of **(A)** LDH-NO$_3$ and **(B)** LDH-pAB.

FIGURE 9 | FE-SEM image of LDH-pAB.

parallel to an internal inhibitor reservoir. Thus, chloride ions can work as a trigger for the release of pAB on demand.

The stimuli-responsive properties were proven qualitatively and quantitatively by spectrophotometry, adding synthesized LDHs to distilled water, to an alkaline solution at pH 12.65 without and with chloride ions (0.3 M NaCl). The time-dependent release curves of pAB from LDHs are shown in **Figure 10**. The results clearly show that the concentration of pAB does not increase with time by treatments at neutral and alkaline pH solutions when chloride ions are not present. On the contrary, a selective pAB release by chloride ions was observed, confirming the stimuli-responsive properties of these materials. In this case, the cumulative content of the released inhibitor increases during the first hours of treatment. As shown in **Figure 10**, most of the

protective molecules were released after 4 h, thus leading to an overall released amount of pAB equal to 34.7% in loading.

CONCLUSIONS

This work was aimed at the development of protective materials able to release the loaded inhibitor depending on the chemical environmental conditions. First, the protective efficacy of three corrosion inhibitors containing a carboxylic moiety, namely, pAB, SA, and CA, was compared in simulated concrete pore solutions containing chloride ions. The results showed that, in alkaline chloride solutions, pAB is the most effective protective agent among the three inhibitors considered in this study. When the tests were performed without any inhibitor, the evident formation of degradation products was noted after only 20 h of

FIGURE 10 | Molar concentrations of the released *p*-aminobenzoic acid (pAB) in aqueous solution at neutral pH and in alkaline solutions in the absence and in the presence of chloride ions.

treatment, and the surface characterization by FTIR spectroscopy suggested mainly the presence of lepidocrocite among the iron corrosion products. When the tests were conducted in the presence of SA and CA inhibitors, corrosion processes on the steel surface were delayed and observed after only 6 days. It is surprising that, even after 5 months of corrosion treatments in alkaline chloride solutions containing pAB, the steel surface remains unchanged.

Based on the results from the corrosion tests, pAB was selected and used for the functionalization of silica nanoparticles and LDHs. The idea was to confine the protective agents into nanocarriers that can gradually release them on demand. Specifically, pAB was chemisorbed through its carboxylic moiety on silica nanoparticles with surface amino groups. Our findings confirm that pAB chemisorbed *via* an amide bond is gradually released at alkaline pH. It is worth noting that pAB release continued up to 144 h, highlighting the potential of this system as an inhibitor reservoir for the long-term protection of steel substrates.

Furthermore, pAB was intercalated in its anionic form into the LDH structure. In this case, the release mechanism is completely different since it is induced by the presence of chloride ions and occurs by an anionic exchange reaction. Thus, these materials play a dual role by acting as an inhibitor reservoir and by capturing chlorides. A gradual release of pAB was also observed for LDH-based materials, but, in this case, the release continued up to 4 h. However, an important advantage of LDH-pAB is the high inhibitor loading and release which corresponds to 34.7 wt%.

In summary, it is possible to create a reservoir of corrosion inhibitor which is released on demand based on the chemical environment. By selecting an appropriate nanocarrier, it is possible to tune the inhibitor release, which is triggered by alkaline environments for silica-based materials and by chloride ions for LDH-based materials. Our findings confirm that, by using different nanocarriers, it is possible to obtain stimuli-responsive materials with a complementary protective action. The gradual and tailored release of the pAB inhibitor is attractive since this can provide long-term protection of steel. These materials could be applied on the concrete surface or directly dispersed into the concrete matrix during the preparation, thus opening the way for innovative solutions in the preservation of concrete cultural heritage.

DATA AVAILABILITY STATEMENT

The datasets generated for this study are available on request to the corresponding author.

AUTHOR CONTRIBUTIONS

CG and EM contributed to the design of the work and to the material synthesis. MS and MP contributed to the corrosion tests and spectroscopic analysis. CR and LT contributed to the optical and SEM analysis. LL contributed to the TGA analysis. GI contributed to the revision and commented on the manuscript. GD designed the research and prepared the manuscript.

FUNDING

REFERENCES

Aisawa, S., Takahashi, S., Ogasawara, W., Umetsu, Y., and Narita, E. (2001). Direct intercalation of amino acids into layered double hydroxides by coprecipitation. *J. Solid State Chem.* 162, 52–62. doi: 10.1006/jssc.2001.9340

Amin, M. A., Abd El-Rehim, S. S., El-Sherbini, E. E. F., and Bayoumi, R. S. (2007). The inhibition of low carbon steel corrosion in hydrochloric acid solutions by succinic acid part I. weight loss, polarization, EIS, PZC, EDX, and SEM studies. *Electrochim. Acta* 52, 3588–3600. doi: 10.1016/j.electacta.2006.10.019

Bertolini, L., Elsener, B., Pedeferri, P., and Polder, R. (2004). *Corrosion of Steel in Concrete: Prevention, Diagnosis, Repair, 1st ed.* Weinheim: Wiley. doi: 10.1002/3527603379

Cavani, F., Trifirò, F., and Vaccari, A. (1991). Hydrotalcite-type anionic clays: preparation, properties and applications. *Catal. Today* 11, 173–301. doi: 10.1016/0920-5861(91)80068-K

de Oliveira, L. F., Bouchmella, K., de Almeida Gonçalves, K., Bettini, J., Kobarg, J., and Borba Cardoso, M. (2016). Functionalized silica nanoparticles as an alternative platform for targeted drug-delivery of water insoluble drugs. *Langmuir* 32, 3217–3225. doi: 10.1021/acs.langmuir.6b00214

de Souza, F. S., and Spinelli, A. (2009). Caffeic acid as a green corrosion inhibitor for mild steel. *Corros. Sci.* 51, 642–649. doi: 10.1016/j.corsci.2008.12.013

Elsener, B., Büchler, M., Stadler, F., and Böhni, H. (1999). Migrating corrosion inhibitor blend for reinforced concrete: part 1—prevention of corrosion. *Corrosion* 55, 1155–1163. doi: 10.5006/1.3283953

Garcés, P., Saura, P., Zornoza, E., and Andrade, C. (2011). Influence of pH on the nitrite corrosion inhibition of reinforcing steel in simulated concrete pore solution. *Corros. Sci.* 53, 3991–4000. doi: 10.1016/j.corsci.2011.08.002

Gartner, N., Kosec, T., and Legat, A. (2016). The efficiency of a corrosion inhibitor on steel in a simulated concrete environment. *Mater. Chem. Phys.* 184, 31–41. doi: 10.1016/j.matchemphys.2016.08.047

Giacomelli, F. C., Giacomelli, C., Amadori, M. F., Schmidt, V., and Spinelli, A. (2004). Inhibitor effect of succinic acid on the corrosion resistance of mild steel: electrochemical, gravimetric, and optical microscopic studies. *Mater. Chem. Phys.* 83, 124–128. doi: 10.1016/j.matchemphys.2003.09.013

Giuliani, C., Pascucci, M., Riccucci, C., Messina, E., Salzano de Luna, M., Lavorgna, M., et al. (2018). Chitosan-based coatings for corrosion protection of copper-based alloys: a promising more sustainable approach for cultural heritage applications. *Prog. Org. Coat.* 122, 138–146. doi: 10.1016/j.porgcoat.2018.05.002

Goyal, A., Sadeghi Pouya, H., Ganjian, E., and Claisse, P. (2018). A review of corrosion and protection of steel in concrete. *Arab. J. Sci. Eng.* 43, 5035–5055. doi: 10.1007/s13369-018-3303-2

Grover, K., Komarneni, S., and Katsuki, H. (2010). Synthetic hydrotalcite-type and hydrocalumite-type layered double hydroxides for arsenate uptake. *Appl. Clay Sci.* 48, 631–637. doi: 10.1016/j.clay.2010.03.017

He, Q., Yin, S., and Sato, T. (2004). Synthesis and photochemical properties of zinc–aluminum layered double hydroxide/organic UV ray absorbing molecule/silica nanocomposites. *J. Phys. Chem. Solids* 65, 395–402. doi: 10.1016/j.jpcs.2003.08.031

Jamil, H. E., Montemor, M. F., Boulif, R., Shriri, A., and Ferreira, M. G. S. (2003). An electrochemical and analytical approach to the inhibition mechanism of an amino-alcohol-based corrosion inhibitor for reinforced concrete. *Electrochim. Acta* 48, 3509–3518. doi: 10.1016/S0013-4686(03)00472-9

Kishor, R., and Ghoshal, A. K. (2015). APTES grafted ordered mesoporous silica KIT-6 for CO_2 adsorption. *Chem. Eng. J.* 262, 882–890. doi: 10.1016/j.cej.2014.10.039

Kuang, Y., Zhao, L., Zhang, S., Zhang, F., Dong, M., and Xu, S. (2010). Morphologies, preparations, and applications of layered double hydroxide micro-/nanostructures. *Materials* 3, 5220–5235. doi: 10.3390/ma3125220

Meyn, M., Beneke, K., and Lagaly, G. (1990). Anion-exchange reactions of layered double hydroxides. *Inorg. Chem.* 29, 5201–5207. doi: 10.1021/ic00351a013

Ormellese, M., Berra, M., Bolzoni, F., and Pastore, T. (2006). Corrosion inhibitors for chlorides induced corrosion in reinforced concrete structures. *Cement Concrete Res.* 133, 536–547. doi: 10.1016/j.cemconres.2005.11.007

Ormellese, M., Lazzari, L., Goidanich, S., Fumagalli, G., and Brenna, A. (2009). A study of organic substances as inhibitors for chloride-induced corrosion in concrete. *Corros. Sci.* 51, 2959–2968. doi: 10.1016/j.corsci.2009.08.018

Pasternack, R. M., Amy, S. R., and Chabal, Y. J. (2008). Attachment of 3-(aminopropyl)triethoxysilane on silicon oxide surfaces: dependence on solution temperature. *Langmuir* 24, 12963–12971. doi: 10.1021/la8024827

Qiao, B., Wang, T. J., Gao, H., and Jin, Y. (2015). High density silanization of nano-silica particles using γ-aminopropyltriethoxysilane (APTES). *Appl. Surf. Sci.* 351, 646–654. doi: 10.1016/j.apsusc.2015.05.174

Rahsepar, M., Mohebbi, F., and Hayatdavoudi, H. (2017). Synthesis and characterization of inhibitor-loaded silica nanospheres for active corrosion protection of carbon steel substrate. *J. Alloys Compd.* 709, 519–530. doi: 10.1016/j.jallcom.2017.03.104

Rani, B. E. A., and Basu, B. B. J. (2012). Green inhibitors for corrosion protection of metals and alloys: an overview. *Int. J. Corros.* 2012, 1687–9325. doi: 10.1155/2012/380217

Salzano de Luna, M., Buonocore, G. G., Giuliani, C., Messina, E., di Carlo, G., Lavorgna, M., et al. (2018). Long-lasting efficacy of coatings for bronze artwork conservation: the key role of layered double hydroxide nanocarriers in protecting corrosion inhibitors from photodegradation. *Angew. Chem. Int. Ed.* 57, 7380–7384. doi: 10.1002/anie.201713234

Samsonowicz, M., Hrynaszkiewicz, T., Swisłocka, R., Regulska, E., and Lewandowski, W. (2005). Experimental and theoretical IR, Raman, NMR spectra of 2-, 3-, and 4-aminobenzoic acids. *J. Mol. Struct.* 744–747, 345–352. doi: 10.1016/j.molstruc.2004.11.063

Saremi, M., and Yeganeh, M. (2014). Application of mesoporous silica nanocontainers as smart host of corrosion inhibitor in polypyrrole coatings. *Corros. Sci.* 86, 159–170. doi: 10.1016/j.corsci.2014.05.007

Söylev, T. A., and Richardson, M. G. (2008). Corrosion inhibitors for steel in concrete: state-of-the-art report. *Constr. Build. Mater.* 22, 609–622. doi: 10.1016/j.conbuildmat.2006.10.013

Tritthart, J. (2003). Transport of a surface-applied corrosion inhibitor in cement paste and concrete. *Cement Concrete Res.* 33, 829–834. doi: 10.1016/S0008-8846(02)01067-0

Veneranda, M., Aramendia, J., Bellot-Gurlet, L., Colomban, P., Castro, K., and Madariaga, J. M. (2018). FTIR spectroscopic semi-quantification of iron phases: a new method to evaluate the protection ability index (PAI) of archaeological artefacts corrosion systems. *Corros. Sci.* 133, 68–77 doi: 10.1016/j.corsci.2018.01.016

Wang, Q., and O'Hare, D. (2012). Recent advances in the synthesis and application of Layered Double Hydroxide (LDH) nanosheets. *Chem. Rev.* 112, 4124–4155. doi: 10.1021/cr200434v

Wang, Y., and Zhang, D. (2011). Synthesis, characterization, and controlled release anticorrosion behavior of benzoate intercalated Zn–Al layered double hydroxides. *Mater. Res. Bull.* 46, 1963–1968. doi: 10.1016/j.materresbull.2011.07.021

Yang, Z., Fischer, H., Cerezo, J., Mol, J. M. C., and Polder, R. (2016). Modified hydrotalcites for improved corrosion protection of reinforcing steel in concrete – preparation, characterization, and assessment in alkaline chloride solution. *Mater. Corros.* 67, 721–738. doi: 10.1002/maco.201508618

Yang, Z., Fischer, H., and Polder, R. (2013). Modified hydrotalcites as a new emerging class of smart additive of reinforced concrete for anticorrosion applications: a literature review. *Mater. Corros.* 64, 1066–1073. doi: 10.1002/maco.201206915

Synthesis and Characterization of TEOS Coating Added With Innovative Antifouling Silica Nanocontainers and TiO$_2$ Nanoparticles

Ludovica Ruggiero[1]*, Maria Rosaria Fidanza[1], Morena Iorio[2], Luca Tortora[1,2], Giulia Caneva[1], Maria Antonietta Ricci[1] and Armida Sodo[1]

[1] *Dipartimento di Scienze, Università degli Studi "Roma Tre", Rome, Italy,* [2] *Laboratorio Analisi Superfici, INFN Roma Tre, Rome, Italy*

We study the synthesis and characterization of an innovative TEOS-based composite coating, which could improve previous formulations used in the field of monument conservation. The proposed coating is composed by a tetraethoxyorthosilicate matrix (TEOS), containing an elasticiser [hydroxyl-terminated polydimethylsiloxane (PDMS-OH)] and a non-ionic surfactant (n-octylamine). The specific self-cleaning and antifouling properties are obtained by the addition of different kinds of nanofillers: the commercial TiO$_2$ nanoparticles, plus two different silica nanocontainers, loaded with the commercial biocide 2-mercaptobenzothiazole. Through a multi-analytical approach, we evaluate the effect of the nanoparticles concentration on the coatings drying rate, on the variation of their visual aspect and textural properties. Our results show that the addition of the silica nanocontainers at 0.05% (w/v) in sol does not change the color of the coating and reduces the formation of cracks after drying. Moreover, the coating charged with nanocontainers undergoes slower drying, thus improving its penetration into the pores of the treated surface. Further tests of photocatalytic and biocidal properties of this new product on different lithotypes and their potential interactions are in progress.

Keywords: multifunctional coating, TiO$_2$, SiO$_2$ nanocontainers, antifouling, biocide

INTRODUCTION

Most historical buildings and monuments, that are a seamless part of our urban landscape, employ natural and artificial stone materials, which are subject to deterioration processes, due to the interaction with the environment (Jackson et al., 2005; Bourges et al., 2008; Torraca, 2009; Doehne and Price Clifford, 2010). In particular, urban environment accelerates the deterioration and may cause crumble of outdoor surfaces (such as architectural elements and sculptures), due to pollution and high concentration of fine particulate. In addition, biotic factors, especially microorganisms, are among the main agents of stone damage (McNamara and Mitchell, 2005; Caneva et al., 2008; Scheerer et al., 2009). Given the large number and the different nature of the stone materials and the various related degradation processes, finding potential supporting solutions is a challenging issue.

Among the consolidant products used for stone, TEOS-based materials have relevant applications and properties (Kim et al., 2009; Zárraga et al., 2010). When these products are applied

on the decaying stone substrate, the tetraethoxysilane polymerizes into the porous structure, thus increasing the intragranular cohesion. Ideally, the TEOS matrix rebinds adjacent mineral grains (Zárraga et al., 2010), appreciably increasing the strength of the stone. However, although TEOS-based coatings are widely applied for consolidation interventions (Zárraga et al., 2010), it is well-known that during the drying phase these products undergo crack formation (Wen and Mark, 1995; Mosquera et al., 2003; Salazar-Hernández et al., 2009; Illescas and Mosquera, 2011; Xu et al., 2012; Pinho et al., 2013; Angulo-Olais et al., 2018).

Different authors have tested the effects of the addition of oxide nanoparticles. To quote a few of them, we mention that Milani et al. (2007) have investigated the realization of a new TEOS-based consolidant with colloidal silica particles. Kim et al. (2009) and the Mosquera's group (Mosquera et al., 2003) have also highlighted that the addition of nanoparticles into the TEOS matrix noticeably decreases the cracking during the drying phase.

Addition of TiO_2 nanoparticles, with antifouling and self-cleaning capabilities, seems a promising way in order to scale up the properties of TEOS based products; indeed titanium oxide properties have been widely tested in conservative treatments of stone surfaces (La Russa et al., 2012; Quagliarini et al., 2012, 2013; Kapridaki and Maravelaki-Kalaitzaki, 2013; Munafò et al., 2015; Gherardi et al., 2016; Xu et al., 2019). In the last years, self-cleaning and antifouling coatings have attracted the attention of many researchers in the field of stone conservation (Colangiuli et al., 2015; Lettieri et al., 2019). The self-cleaning properties of titanium oxide are due to its ability to photocatalyze the complete degradation of many organic contaminants and environmental toxins (Liu and Liu, 2016). Moreover, the photocatalytic activity of TiO_2 determines a collateral biocidal effect. The photocatalytic killing action by titania has been studied on a wide spectrum of organisms including bacteria, fungi, algae (Ruffolo et al., 2017). However, the structural properties of the target microorganism (e.g., the complexity and thickness of cell envelope) influence the microbiocidal efficacy of TiO_2: fungi, for instance, have a complex structure, which protects them from damage due to the radical species produced during the photocatalytic titania activities (Seven et al., 2004; Munafò et al., 2015).

In order to improve the antifouling effects, most coatings are prepared by dispersion of biocides molecules into the wet coating material (Omae, 2003; Almeida et al., 2007). This practice suffers from some drawbacks, such as poor control of the release rate of the antifoulants or degradation of the active substance. On the other hand, increasing the quantity of biocides into the coating, in order to extend its functionality over time is not economically, environmentally, and practically sustainable (Pinna et al., 2012; Fidanza and Caneva, 2019). Moreover, the high concentration of biocides into the coating may induce macroscopic damage of the film, detectable as a phase separation (Trojer et al., 2015).

Since several biocides are effective only for a short period of time after the application (between 6 months and 1 year), due to the cleaning of the surfaces after the treatments or due to the washing out of the compounds by rainfall, a frequent reapplication is needed (Jämsä et al., 2013). Thus, when indirect control methods are not possible (Almeida et al., 2007;

Caneva et al., 2008; Pinna et al., 2012; Fidanza and Caneva, 2019), improving the performance of the antifouling coating is necessary from both economical and environmental points of view.

Several biocides have been used in antifouling treatments for buildings conservation (Nugari and Salvadori, 2003; Caneva and Tescari, 2017; Pinna, 2017). A lot of active principles widely used in the past, such as organ-stannic or organotin compounds, have been excluded for toxicological reasons. The quaternary ammonium salts (Quats, e.g., benzalkonium chloride) are among the most used materials, despite their lower efficacy with respect others (Nugari and Salvadori, 2003; Caneva and Tescari, 2017; Pinna, 2017). Considering its chemical properties and the documented efficacy, we selected, as an active principle, 2-mercaptobenziothiazole (MBT), which can be easily encapsulated into silica based nanocapsules (Maia et al., 2015). In commercial products (e.g., Vancide 51, Vanderbilt Company) MBT is included in combination with dimethyldithiocarbamate (Nugari and Salvadori, 2003). Nevertheless, in order to improve the stability of our silica nanocontainers, we have encapsulated and confined only the 2-mercaptobenziothiazole (Ruggiero et al., 2019). The potential oxidation of the biocide induced by the TiO_2 nanoparticles is expected to decrease thanks to the confinement into the silica containers that "protect" the biocide against oxidation. In this contest, we tested the addition of two different kinds of nanofillers: the commercial TiO_2 nanoparticles and, for the first time, the silica nanocontainers (Si-NC and Si-MNP) loaded with MBT synthesized in our laboratory. The addition of these nanofillers to the TEOS-based coating formulation will improve the physic-chemical properties of the proposed product while providing a multifunctional composite coating with antifouling and self-cleaning properties.

In particular, TiO_2 nanoparticles provide self-cleaning properties, while the two silica nanocontainers (hereafter labeled as Si-NC and Si-MNP) loaded with 2-mercaptobenzothiazole (MBT) will contribute to the antifouling action through a controlled release of the biocide. The first silica nanocontainer (Si-NC) shows a core-shell structure, and thus is called NanoCapsule. The second one (Si-MNP) consists instead of Mesostructured NanoParticles. Si-NC and Si-MNP nanocontainers have different size and different textural properties, which affect the loading capability and, consequently, the release rate of the MBT, as measured in water for 120 days (Ruggiero et al., 2019).

This study presents the design and the characterization of a composite coating, which may have application on outdoor stone monuments, while planning the necessary further tests on different lithotypes and biological communities. The incorporation of TiO_2 and SiO_2 nanocontainers into coating matrices is supposed to increase the quality of a multifunctional composite coating, as it combines the self-cleaning and antibacterial properties of TiO_2, the antifouling and mechanical strength of SiO_2 nanocontainers, and the controlled release of the encapsulated biocide. In order to select the best composition from a physic-chemical point of view, we compare a series of coatings by mixing in the starting sols different concentrations of nanoparticles.

Coatings	Nanoparticles		
	TiO_2	SiO$_2$	
		NC	MNP
C			
C_1%Si-NC		0.1%	
C_2%Si-NC		0.2%	
C_TiO$_2$/Si-NC	0.05%	0.05%	
C_2_TiO$_2$/Si-NC	0.1%	0.1%	
C_1%_Si-MNP			0.1%
C_2%_Si-MNP			0.2%
C_TiO$_2$/Si-MNP	0.05%		0.05%
C_2_TiO$_2$/Si-MNP	0.1%		0.1%

MATERIALS AND METHODS

In order to overcome the drawbacks of cracking of conventional TEOS-based materials, the proposed coatings was synthesized by combining three different strategies: (i) the addition of nanofillers, (ii) the addition of an non-ionic surfactant (n-octylamina) (González-Rivera et al., 2018), (iii) the modification of the elastic properties of the gel with Poly(dimethylsiloxane) hydroxy terminated (PDMS-OH) (Tamayo and Rubio, 2010; Zhang et al., 2010).

Preparation of Coatings

The coating matrix has been prepared as described in a recent article (Xu et al., 2012). In short, a typical starting sol has been prepared by mixing TEOS with ethanol, then different amounts of the two nanoparticles have been added, as summarized in **Table 1**. Technical grade TiO_2 (by Sigma-Aldrich), with an average particle size of ∼21 nm, has been used as a photocatalytic element into the proposed coating. Two different SiO$_2$ nanocontainers (Si-NC and Si-MNP), synthesized in our laboratory, have been loaded with the 2-mercaptobenzothiazole (MBT, Sigma-Aldrich) and added to the coatings as antifouling agent. As reported in our previous work (Ruggiero et al., 2019), the Si-NC are core-shell structures with porous surface and a diameter of (128 ± 15) nm, while Si-MNP are mesoporous spherical nanoparticles with a diameter of (39 ± 4) nm.

In detail, the mixtures of TEOS and ethanol have been magnetically stirred (350 rpm) for 2 h at room conditions, prior to addition of the fillers (TiO_2 and Si-NC or Si-MNP). Afterwards, distilled water and PDMS-OH have been added under vigorous stirring (500 rpm). After 2 min of magnetic stirring, the mixture has been sonicated for 10 min. The n-octylamine has been added to each sol and the mixture has been magnetically stirred for further 20 min. The mole ratios of each mixture are 1 TEOS/16 ETOH/10H$_2$O/0.04 PDMS-OH/0.004 n-octylamine. TEOS (analytical grade reagent), n-octylamine and PDMS-OH (Mn = 550) have

been purchased from Sigma-Aldrich and used without further purification.

After completing the synthesis, 500 μL of each sol has been cast in plastic Petri dishes of 1.7 cm diameter and 0.7 cm height. Dried xerogels have been obtained by simple exposure of the sols to laboratory conditions (T = 25°C and RH = 60%). The xerogels are labeled according to **Table 1**.

Preparation of Colloidal Silica Nanofillers: Si-NC and Si-MNP

The silica nanocapsules (Si-NC) have been synthesized through the dynamic self-assembly of TEOS and CTAB (Ruggiero et al., 2018, 2019, 2020). After the dissolution of the cationic surfactant (CTAB) in deionized water, an ammonia aqueous solution (25–28% V) has been added. Then, the biocide (MBT) has been dissolved in the organic solvent (diethyl ether) and this second solution has been mixed to the aqueous solution under constant magnetic stirring. Once the miniemulsion stabilized, 2 mL of TEOS have been slowly dripped. The reaction has proceeded at room temperature for 24 h (Ruggiero et al., 2019). The obtained product has been finally filtered under vacuum, repeatedly washed and dried at laboratory conditions.

The silica nanoparticles (Si-MNP) have been obtained starting from the sonication of the CTAB water solution and MBT for 30 min. At the same time, 100 mL of deionized water have been basified by NaOH aqueous solution (2.0 M) and then added to the first solution. After reaching the temperature of 80°C, the silica precursor (TEOS = 1.25 mL) has been dripped and the final mixture is kept under fast stirring for an additional 2 h. Finally, the Si-MNP have been filtrated and washed several times with water (Knezevic et al., 2017; Ruggiero et al., 2019).

Characterization Procedures

The morphology of the nanosystems has been visualized by using a Field Emission Scanning Electron Microscope (FE-SEM, Sigma 300, Carl Zeiss SMT). Before the measurements, each sample has been sputtered with a thin layer of gold.

The BET surface area, the pore volume and pore size distribution have been characterized by the Nitrogen Physisoption at −196°C (Micromeritics Gemini V apparatus). Prior to the N$_2$ adsorption, the sample has been degassed in flowing He at 150°C by using a Micromeritics Flow Prep accessory.

The infrared (IR) spectra of the coatings have been collected using a ThermoFisher Nicolet iS50 FTIR instrument in Attenuated Total Reflection (ATR) mode. The spectra were recorded, on the powdered samples, from 4,000 to 400 cm^{-1} at 4 cm^{-1} of resolution; 132 scans have been recorded.

Possible changes in the color of each coating, over time, were evaluated by using a solid reflection spectrophotometer (Chroma-Meter CR-200 Konica Minolta), working with the illuminant D65 and the observer at 2°. For each coating, three spot areas were analyzed and each spot area was measured in triplicate. CIE L*a*b* color space has been used and the variations of color have been quantified by the total color difference ΔE*, defined as: $\Delta E^* = \sqrt{\Delta L^{*2} + \Delta a^{*2} + \Delta b^{*2}}$.

TABLE 2 | Hybrid coatings after drying under laboratory conditions for different concentration of Si-NC/Si-MNP and TiO$_2$.

C	C_1%TiO$_2$	C_2%TiO$_2$
C	**C_1%Si-NC**	**C_2%Si-NC**
C	**C_TiO$_2$/Si-NC**	**C_2TiO$_2$/Si-NC**
C	**C_1%Si-MNP**	**C_2%Si-MNP**
C	**C_TiO$_2$/Si-MNP**	**C_2_TiO$_2$/Si-MNP**
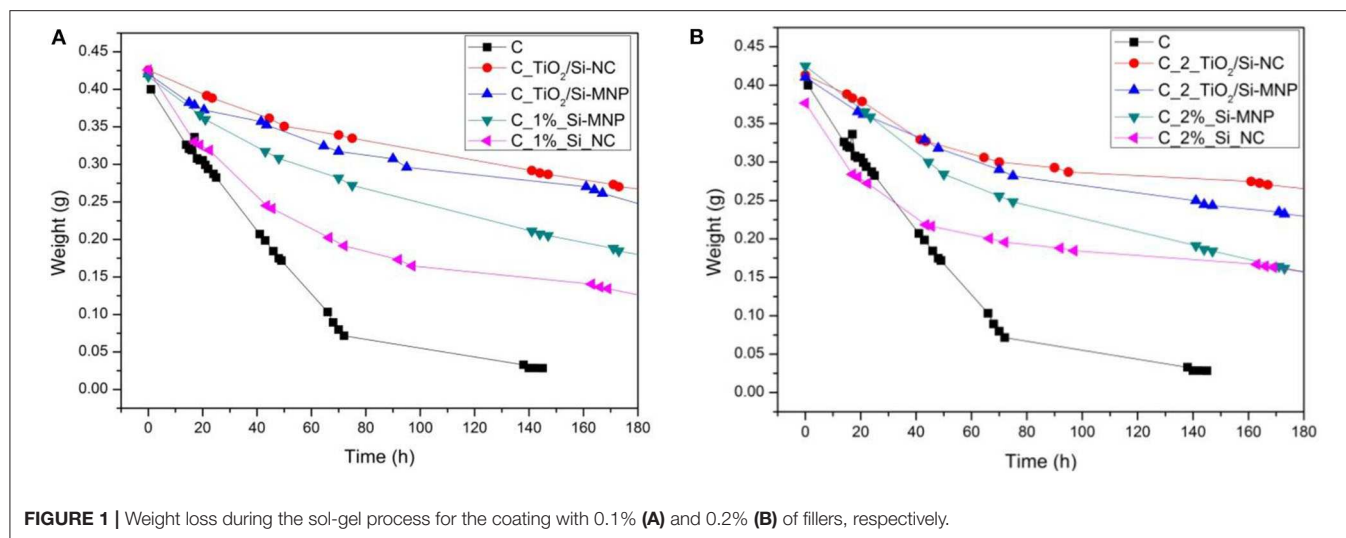
FIGURE 1 | Weight loss during the sol-gel process for the coating with 0.1% **(A)** and 0.2% **(B)** of fillers, respectively.

RESULTS AND DISCUSSION

The coatings have been cast on plastic Petri dishes and examined after drying. First of all, their transparency has been investigated. Within the series shown in **Table 2**, dry coating (C) without nanoparticles is colorless and transparent but presents cracks. The addition of nanofillers into the sol changes the chromaticity of the final coatings: we notice a whitening of the charged coatings, with intensity depending on the type of nanoparticle and on their concentration. In particular, the addition of TiO_2 nanoparticles induces a whitening of the coatings with decreased transparency (first raw of **Table 2**). The coatings with Si-MNP maintains a good level of transparency with a few cracks. From the optical point of view, the reasonable amount of nanoparticles is 0.1% (w/v) and the best systems seem to be the coatings added with Si-MNP. The smaller size of Si-MNP in comparison with Si-NC allows the dispersion of these nanofillers into the coating matrix, reducing the optical effects correlated with the formation of aggregates.

In order to evaluate the effect of the nanofillers on the drying time of the gel, the weight loss of each sample has been measured. **Figures 1A,B** show the weight loss for the sols obtained by the addition of 0.1 and 0.2% w/v nanoparticles, respectively, over time (from 0 to 180 h), showing different drying rates.

The sample without nanoparticles shows the faster drying rate: the weight reaches a plateau after 145 h. Generally, the addition of the nanofillers slows down noticeably the drying rate, indeed the coatings with 0.2% w/v of fillers show a lower weight loss than the coatings with 0.1% w/v of fillers.

Comparing the green and magenta curves in **Figures 1A,B**, we notice that the coating charged with the Si-NC has a faster drying rate compared to that charged with the smaller sized Si-MNP. This difference persists, although reduced, when also TiO_2 particles are added; moreover, the presence of TiO_2 particles makes the drying process even slower. These observations, in the light of what reported in the previous paragraph, suggest that the nanoparticles are stratified in the coating, according to
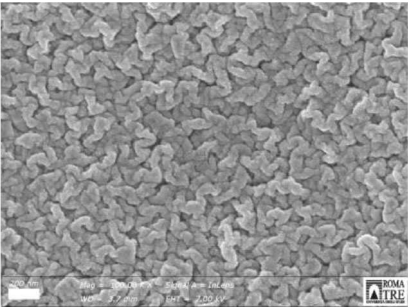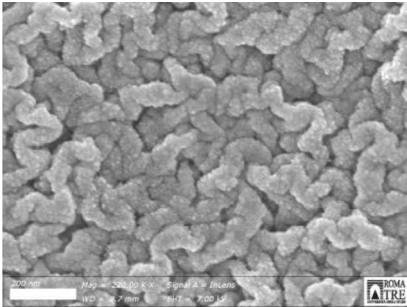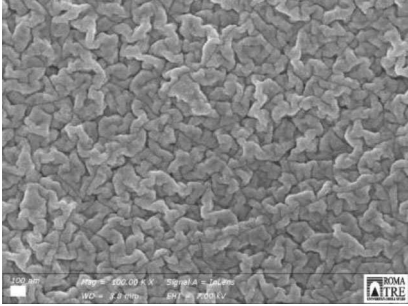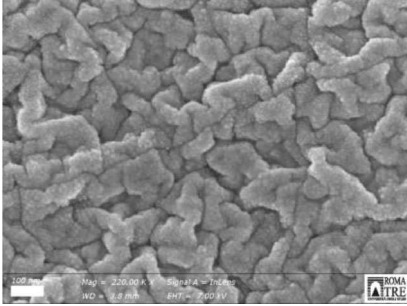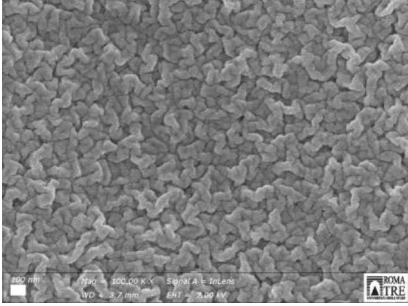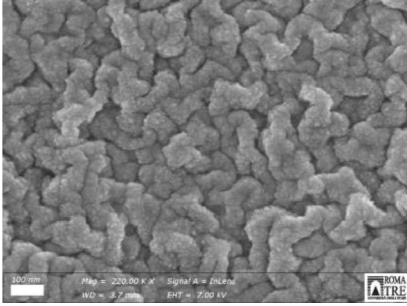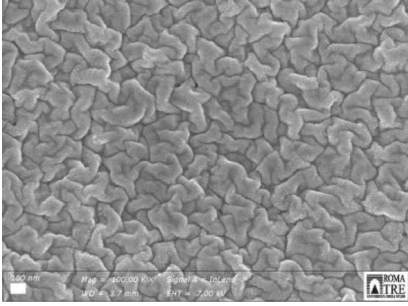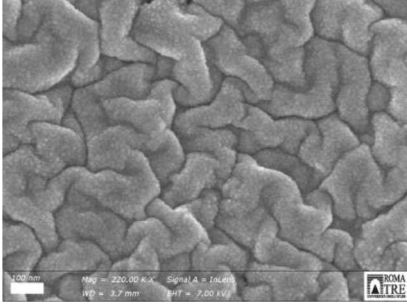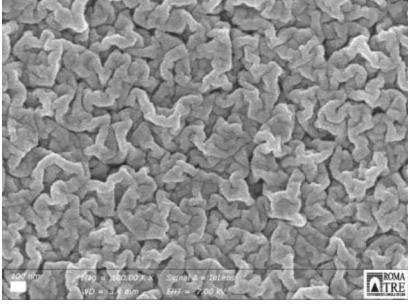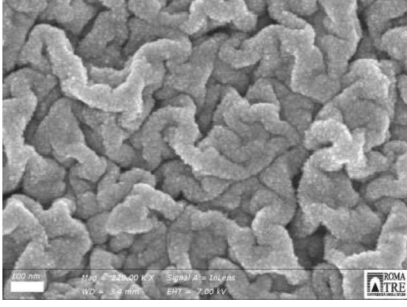
their average dimension, with the Si-NC occupying the bottom layers of it. As a matter of fact, it can be verified by naked eye that the Si-NC tend to deposit at the bottom of the coating and thus have a limited effect on the drying rate. On the contrary, the TiO_2 and/or Si-MNP, characterized by a smaller size than the Si-NC, seem to be more homogeneously dispersed in the coatings. This implies a slowing of the evaporation of the solvents and, consequently, a longer drying time of the coating. The presence of the nanofillers, distributed into the thickness of the coating, hinders this evaporation process by slowing the gelation and, consequently, the drying of the products. These results suggest that nanofillers interfere with the drying process. The coatings in this way penetrate into the porous substrate before the viscosity naturally increases upon the sol-gel transition (Milani et al., 2007). The most promising system seems to be once again the $C\_TiO_2/Si\text{-}MNP$.

SEM micrographs, collected with InLens detector on the upper surface of the coating, are compared in **Table 3**. All the coatings show a homogeneous morphology, consisting of microstructured folds, formed by uniform nanospheres of size of the order of 13–15 nm. These spherical microstructures do not depend on the size distribution and the morphology of the nanofillers. The SEM micrographs are quite similar one to each other and suggest that, during the deposition of the coatings into the petri dish, the nanofillers are preferably distributed through the thickness, or in some cases precipitate at the bottom and for these reasons are not visible on the surface.

In order to investigate the textural properties of the hybrid coatings, we have measured the N_2 adsorption-desorption isotherms of the most promising samples as the as far as the optical properties and drying rates are concerned, i.e., those containing 0.1% w/v of nanoparticles. The corresponding textural data are reported in **Table 4**.

All the analyzed coatings show type IV adsorption isotherms, with a H1 hysteresis loop (see **Figure 2A**). This loop is more evident for the coatings loaded with TiO_2 nanoparticles. These isotherm profiles suggest that the proposed coatings are a

TABLE 3 | SEM micrographs at different magnification of the samples added with silica nanoparticles and silica nanoparticles and TiO_2.

Sample	100 000 x	220 000 x
C_1%_Si-NC		
C_2%_Si-NC		
C_TiO_2/Si-NC		
C_2_TiO_2/Si-NC		
C_1%_Si-MNP		

(Continued)

TABLE 3 | Continued
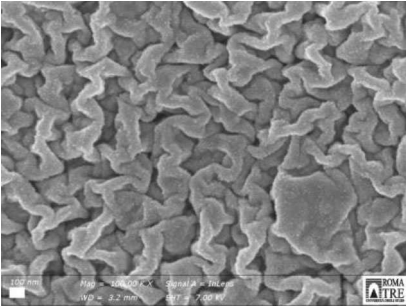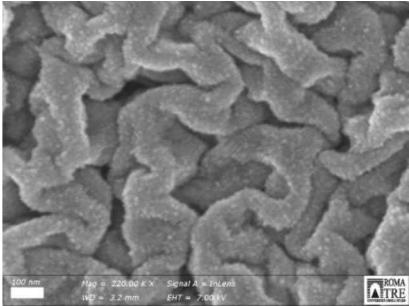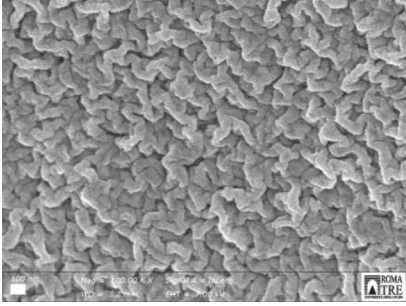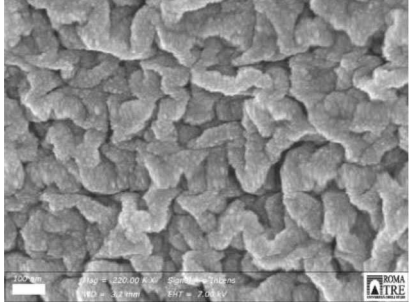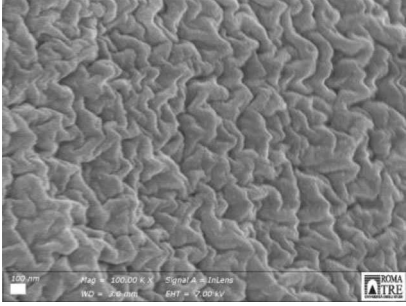
Sample	100 000 ×	220 000 ×
C_2%_Si-MNP		
C_TiO$_2$/Si-MNP		
C_2_TiO$_2$/Si-MNP		-

TABLE 4 | Surface area (S.A.), total pore volume (BJH P.V.), and pore size (BJH P.S.) of samples added with 0.1% of nanoparticles.

Sample	S.A (m^2g^{-1})	BJH P.V. (cm^3g^{-1})	BJH P.S. $P/P^0 < 0.60$ (nm)
C	440	0.70	8.4
C_1%Si-NC	481	0.75	5.9
C_1%_Si-MNP	475	0.76	6.4
C_1%_TiO$_2$/Si-NC	489	0.67	6.3
C_1%_TiO$_2$/Si-MNP	488	0.76	5.8

network of silica nanoparticles and that the fillers (Si-NC/Si-MNP and TiO$_2$) are embedded and integrated into the porous structures (Milani et al., 2007).

The BET surface area of the empty coating is 440 m^{2}g^{-1}, whereas for all sample with the addition of silica nanodevices and/or TiO$_2$ nanoparticles, the BET surface area is around 480 m^{2}g^{-1}. In **Figure 2B** the peak of sample C is centered at 8.4 nm (BJH P.S.): the addition of Si-NC/Si-MNP and/or TiO$_2$ reduces the pore size to a value between 5.8 and 6.4 nm, without substantially changing the total pore volume (0.67 ÷ 0.76 cm^{3}g^{-1}). These results suggest that the nanoparticles are integrated into the coating matrix, inducing an increase of BET surface area of about 10% and a decrease of the pore size of about 30% in comparison with the empty coating (C). The textural properties outline that the size of the two different silica fillers determines the properties of the coatings. When the TiO$_2$ nanoparticles are added into the coating formulations, the differences in surface area between the coating loaded with Si-NC and Si-MNP are reduced, as shown in **Table 4**. Moreover, TiO$_2$ nanoparticles induce an increase of the pore size in the coating loaded with Si-NC. This behavior suggests that the TiO$_2$ nanoparticles work in synergy with the Si-NC, positively shaping the network structure. The Si-NC, because of their diameter, tend to precipitate and agglomerate during the sol-gel process. Otherwise, the Si-MNP shape the network modifying the porosity of the coating in comparison with the empty coating. For this reason, when the TiO$_2$ nanoparticles are added to the coating with Si-MNP, the TiO$_2$ is embedded in the porosity created by the
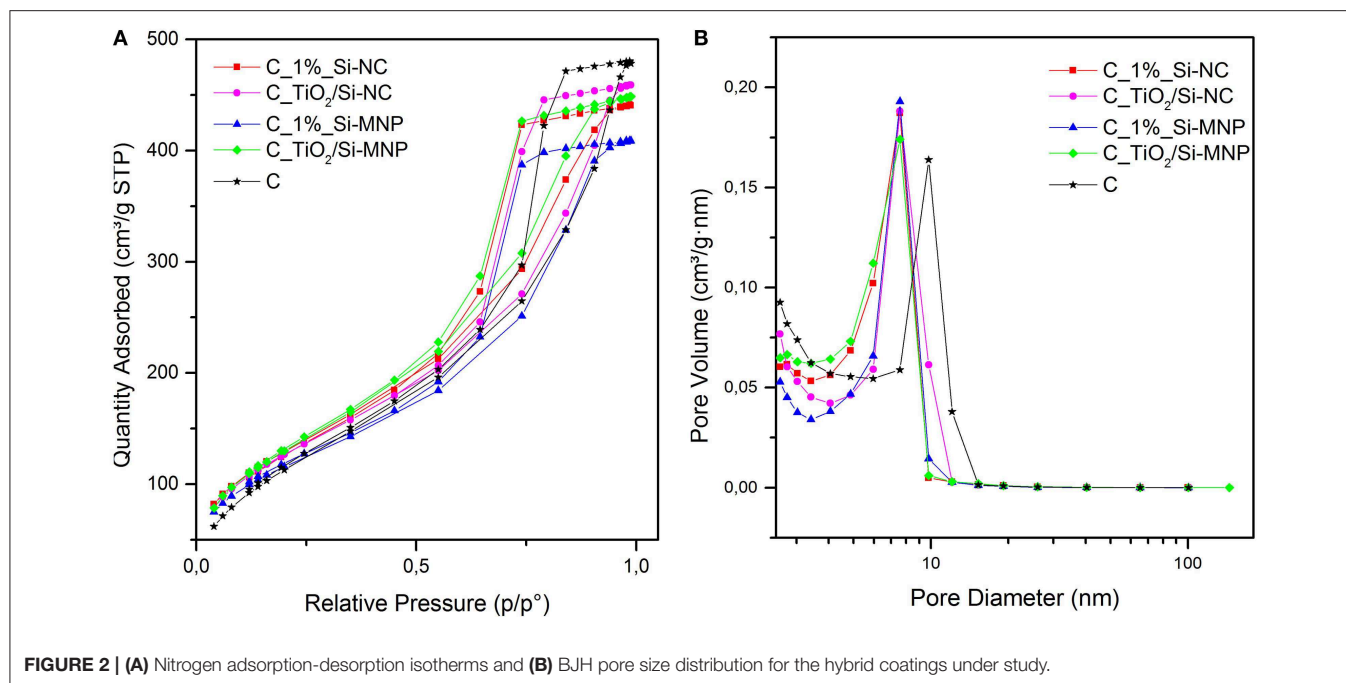
FIGURE 2 | (A) Nitrogen adsorption-desorption isotherms and **(B)** BJH pore size distribution for the hybrid coatings under study.
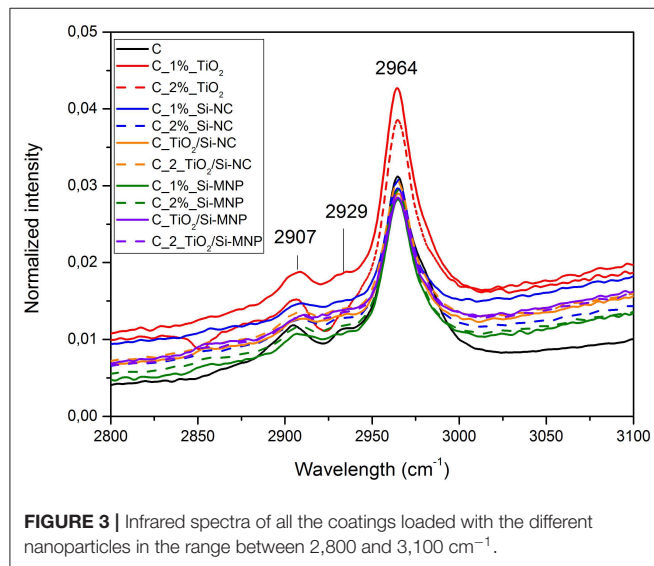

FIGURE 3 | Infrared spectra of all the coatings loaded with the different nanoparticles in the range between 2,800 and 3,100 cm^{-1}.
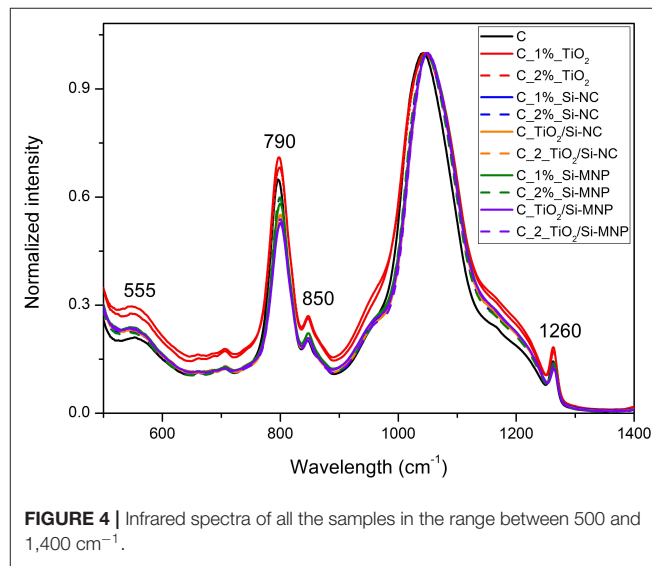

FIGURE 4 | Infrared spectra of all the samples in the range between 500 and 1,400 cm^{-1}.

Si-MNP, decreasing the pore diameter of the C_ TiO_2/Si-MNP (Pinho and Mosquera, 2011).

Structural characterization of dried coatings has been performed by means of Fourier Transformed Infrared Spectroscopy. **Figures 3–5** report the FTIR spectra of the coatings under study. The band corresponding to the Si–O–Si vibration ($\sim$1,050 cm^{-1}), being the most intense, has been used for the normalization of the infrared spectra. The spectra (**Figure 3**) show a few bands that are unequivocally assigned to vibrations of an organic fraction, namely PDMS-OH. In particular, the band at 2,907 cm^{-1} corresponds to the symmetric stretching vibration of the C-H bonds, whereas the bands at

2,929 and 2,964 cm^{-1} are assigned to the asymmetric stretching vibration of the C-H bonds in CH_2 and CH_3 groups, respectively (Tamayo and Rubio, 2010; González-Rivera et al., 2018).

The symmetric bending vibration of CH_3 groups in PDMS-OH contributes to a sharp band centered around 1,260 cm^{-1} (Zhang et al., 2010; Goffredo et al., 2019) in **Figure 4**. The band at $\sim$790 cm^{-1} is related to the rocking modes of methyl groups and to the Si-C stretching in Si-$(CH_3)_n$, as reported in **Figure 4** (Fidalgo et al., 2005; Johnson et al., 2013).

The copolymerization of Si-OH group of hydrolyzed TEOS and Si-OH of PDMS-OH is suggested by the band at 850 cm^{-1} (Tellez et al., 2003), as reported in **Figure 4**. This implies that
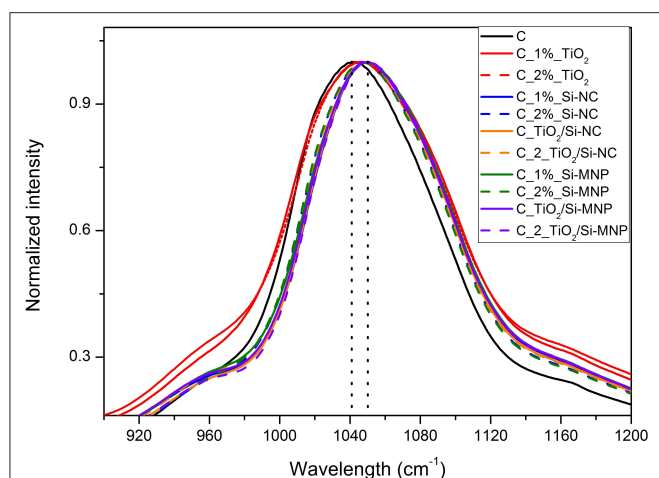
FIGURE 5 | Detail of the Si-O-Si infrared band for the all coatings. The dot lines highlight the shift in the principal component from the empty coating to the coating with nanoparticles.

TABLE 5 | Shift and assignments of the bands observed in the spectra of the coatings.

Sample	δ Si-O-Si in SiO$_4$ (nm)	ν_{as} Si-O-Si in SiO$_4$ and SiO$_6$ (nm)
C	555	1,042
C_1%_TiO$_2$	550	1,046
C_2%_TiO$_2$	552	1,047
C_1%_Si-NC	550	1,046
C_2%_Si-NC	550	1,050
C_TiO$_2$/Si-NC	543	1,050
C_2_TiO$_2$/Si-NC	549	1,050
C_1%_Si-MNP	550	1,046
C_2%_Si-MNP	552	1,050
C_TiO$_2$/Si-MNP	550	1,048
C_2_TiO$_2$/Si-MNP	552	1,051

during the synthesis PDMS-OH and TEOS interact, producing a homogeneous hybrid coating.

Several vibration modes of siloxane bonds contribute to the most intense band of the infrared spectra, in the region between 1,000 and 1,250 cm^{-1}. In detail, the large band centered at 1,050 cm^{-1} is related to the asymmetric ν(Si–O–Si) stretching of the Si-O-Si network and it can be deconvoluted in four components: two longitudinal (LO) and two transverse (TO) optic modes. These components correspond to the four-membered (SiO)$_4$ and the six-membered (SiO)$_6$ arrangement of siloxane rings (Fidalgo and Ilharco, 2004). The position and the relative intensities of the LO and TO modes, according to the literature, change when chemical groups or organic molecules modify the silica network (Fidalgo and Ilharco, 2004).

In this contest, a shift of the Si-O-Si asymmetric stretching bands toward higher wavelengths in comparison with the empty coating is observed (from 1,042 to ~1,050 cm^{-1}, **Figure 5**). These shifts are ascribed to the network deformation needed to accommodate the nanoparticles within the hybrid coating

matrix, as summarized in **Table 5**. This phenomenology outlines that the distance between interacting species (e.g., the matrix and the nanoparticles) is reduced by the increase of the long-range Coulomb interactions. This finding is in agreement with the porosity decrease, suggested by N$_2$ adsorption-desorption measurements (Li et al., 2013; Xu and Li, 2013).

As reported in **Table 5**, the position of the band at ~555 cm^{-1} (**Figure 4**), assigned to a coupled mode in four-member siloxane rings (SiO)$_4$, moves from a maximum of 555 cm^{-1} to a minimum of 543 cm^{-1}, depending on the species and concentration of dispersed nanoparticles (Tamayo and Rubio, 2010).

In order to evaluate the chromatic stability of the coating over time, the total color variation (ΔE^*) of the samples has been measured at $t = 0$[1] and after 20, 40, and 60 days. All the coatings show a ΔE^* below the perceivable threshold. The chromatic feature of the coating does not change over time, regardless of the type and quantity of nanoparticles added as filler. Such absence of chromatic variation will be further tested in direct application of these coatings on outdoor building surfaces, following the standards in the field. Future plans also include investigating the photocatalytic activity of the commercial TiO$_2$ nanoparticles added to the coating, and the long-time effects on the stone properties after the treatment (e.g., color, porosity, and permeability changes).

CONCLUSIONS

In this work, we report the synthesis and the multi-analytical characterization of an innovative TEOS-based composite coating with the addition of two different silica nanofillers with antifouling properties. The best results in terms of optical properties (e.g., visual aspect and transparency), porosity and absence of cracking are obtained with the following nanofiller concentrations: 0.05% w/v of TiO$_2$ and 0.05% w/v of Si-MNP or Si-NC loaded with MBT. The coatings with Si-MNP as filler show better properties than the coatings with Si-NC: indeed, the size of the filler shapes the behavior of the coatings, modifying not only the visual aspect, but also the drying rate. Further tests are in progress to check the interaction of this new coating with the most common substrates of interest for conservation of buildings and Cultural Heritage, as for instance its photocatalytic and biocidal activities and long-lasting efficacy on different lithotypes.

DATA AVAILABILITY STATEMENT

The datasets generated for this study are available on request to the corresponding author.

AUTHOR CONTRIBUTIONS

LR made the synthesis, some characterizations, and drafted the manuscript. MI and LT made FT-IR analysis. MF made the colorimetric measurements. GC, MR, and AS coordinated the project and participated in the discussion of the results.

---

[1]It has been considered as time 0, when the coating reached a constant weight.

All authors contributed to write the article and approved the submitted version.

REFERENCES

Almeida, E., Diamantino, T. C., and De Sousa, O. (2007). Marine paints: The particular case of antifouling paints. *Prog. Org. Coat.* 59:2. doi: 10.1016/j.porgcoat.2007.01.017

Angulo-Olais, R., Illescas, J. F., Aguilar-Pliego, J., Vargas, C. A., and Haro-Pérez, C. (2018). Gel point determination of TEOS-based polymeric materials with application on conservation of cultural heritage buildings. *Adv. Condens. Matter Phys.* 2018:5784352. doi: 10.1155/2018/5784352

Bourges, A., Fehr, K. T., Simon, S., and Snethlage, R. (2008). Correlation between the micro-structure and the macroscopic behaviour of sandstones. *Restor. Build. Monum. Int. J.* 14, 157–166. doi: 10.1515/rbm-2008-6214

Caneva, G., Nugari, M. P., and Salvadori, O. (2008). *Plant Biology for Cultural Heritage.* Los Angeles, CA: Getty Conservation Institute.

Caneva, G., and Tescari, M. (2017). "Stone biodeterioration: treatments and preventive conservation," in *Proceedings of International Symposium of Stone Conservation, Conservation Technologies for Stone Cultural Heritages: Status and Future Prospects* (Seoul).

Colangiuli, D., Calia, A., and Bianco, N. (2015). Novel multifunctional coatings with photocatalytic and hydrophobic properties for the preservation of the stone building heritage. *Constr. Build. Mater.* 93, 189–196. doi: 10.1016/j.conbuildmat.2015.05.100

Doehne, E., and Price Clifford, A. (2010). *Stone Conservation: An Overview of Current Research.* Technical Report. Getty Conservation Institute, Los Angeles, CA.

Fidalgo, A., Ciriminna, R., Ilharco, L. M., and Pagliaro, M. (2005). Role of the alkyl-alkoxide precursor on the structure and catalytic properties of hybrid sol-gel catalysts. *Chem. Mater.* 17, 6686–6694. doi: 10.1021/cm051954x

Fidalgo, A., and Ilharco, L. M. (2004). Chemical tailoring of porous silica xerogels: local structure by vibrational spectroscopy. *Chem. Eur. J.* 10, 392–398. doi: 10.1002/chem.200305079

Fidanza, M. R., and Caneva, G. (2019). Natural biocides for the conservation of stone cultural heritage: a review. *J. Cult. Herit.* 38, 271–286. doi: 10.1016/j.culher.2019.01.005

Gherardi, F., Colombo, A., D'Arienzo, M., Di Credico, B., Goidanich, S., Morazzoni, F., et al. (2016). Efficient self-cleaning treatments for built heritage based on highly photo-active and well-dispersible TiO$_2$ nanocrystals. *Microchem. J.* 126, 54–62. doi: 10.1016/j.microc.2015.11.043

Goffredo, G. B., Accoroni, S., and Totti, C. (2019). "Nanotreatments to inhibit microalgal fouling on building stone surfaces," in *Nanotechnology in Eco-efficient Construction*, 2nd Edn (Woodhead Publishing), 619–647. doi: 10.1016/B978-0-08-102641-0.00025-6

González-Rivera, J., Iglio, R., Barillaro, G., Duce, C., and Tinè, M. R. (2018). Structural and thermoanalytical characterization of 3D Porous PDMS foam materials: the effect of impurities derived from a sugar templating process. *Polymers* 10:616. doi: 10.3390/polym10060616

Illescas, J. F., and Mosquera, M. J. (2011). Surfactant-synthesized PDMS/silica nanomaterials improve robustness and stain resistance of carbonate stone. *J. Phys. Chem. C*, 115, 14624–14634. doi: 10.1021/jp203524p

Jackson, M. D., Marra, F., Hay, R. L., Cawood, C., and Winkler, E. M. (2005). The judicious selection and preservation of tuff and travertine building stone in ancient Rome. *Archaeometry* 47, 485–510. doi: 10.1111/j.1475-4754.2005.00215.x

Jämsä, S., Mahlberg, R., Holopainen, U., Ropponen, J., Savolainen, A., and Ritschkoff, A.-C. (2013). Slow release of a biocidal agent from polymeric microcapsules for preventing biodeterioration. *Progress Organic Coat.* 76, 269–276. doi: 10.1016/j.porgcoat.2012.09.018

Johnson, L. M., Gao, L., Shields, C. W., Smith, M., Efimenko, K., Cushing, K., et al. (2013). Elastomeric microparticles for acoustic mediated bioseparations. *J. Nanobiotechnol.* 11:22. doi: 10.1186/1477-3155-11-22

Kapridaki, C., and Maravelaki-Kalaitzaki, P. (2013). TiO$_2$-SiO$_2$-PDMS nano-composite hydrophobic coating with self-cleaning properties for marble protection. *Progress Organ. Coat.* 76, 400–410. doi: 10.1016/j.porgcoat.2012.10.006

Kim, E. K., Won, J., Do, J.-y., Kim, S. D., and Kang, Y. S. (2009). Effects of silica nanoparticle and GPTMS addition on TEOS-based stone consolidants. *J. Cult. Herit.* 10, 214–221. doi: 10.1016/j.culher.2008.07.008

Knezevic, N. Z., Mauriello Jimenez, C., Albino, M., Vukadinovic, A., Mrakovic, A., Illes, E., et al. (2017). Synthesis and characterization of core-shell magnetic mesoporous silica and organosilica nanostructures. *MRS Adv.* 2, 1037–1045. doi: 10.1557/adv.2017.69

La Russa, M. F., Ruffolo, S. A., Rovella, N., Belfiore, C. M., Palermo, A. M., Guzzi, M. T., et al. (2012). Multifunctional TiO$_2$ coatings for cultural heritage. *Prog. Org. Coat.* 74, 186–191. doi: 10.1016/j.porgcoat.2011.12.008

Lettieri, M., Colangiuli, D., Masieri, M., and Calia, A. (2019). Field performances of nanosized TiO$_2$ coated limestone for a self-cleaning building surface in an urban environment. *Build. Environ.* 147, 506–516. doi: 10.1016/j.buildenv.2018.10.037

Li, D., Xu, F., Liu, Z., Zhu, J., Zhang, Q., and Shao, L. (2013). The effect of adding PDMS-OH and silica nanoparticles on sol–gel properties and effectiveness in stone protection. *Appl. Surf. Sci.* 266, 368–374. doi: 10.1016/j.apsusc.2012.12.030

Liu, Y., and Liu, J. (2016). Design of multifunctional SiO$_2$-TiO$_2$ composite coating materials for outdoor sandstone conservation. *Ceramics Int.* 42, 13470–13475. doi: 10.1016/j.ceramint.2016.05.137

Maia, F., Silva, A. P., Fernandes, S., Cunha, A., Almeida, A., Tedim, J., et al. (2015). Incorporation of biocides in nanocapsules for protective coatings used in maritime applications. *Chem. Eng. J.* 270, 150–157. doi: 10.1016/j.cej.2015.01.076

McNamara, C. J., and Mitchell, R. (2005). Microbial deterioration of historic stone. *Front. Ecol. Environ.* 3, 445–451. doi: 10.1890/1540-9295(2005)003[0445:MDOHS]2.0.CO;2

Milani, C., Velo-Simpson, M. L., and Scherer, G. W. (2007). Particle-modified consolidants: a study on the effect of particles on sol-gel properties and consolidation effectiveness. *J. Cult. Herit.* 8, 1–6. doi: 10.1016/j.culher.2006.10.002

Mosquera, M. J., Bejarano, M., De la Rosa-Fox, N., and Esquivias, L. (2003). Producing crack-free colloid-polymer hybrid gels by tailoring porosity. *Langmuir* 19, 951–957. doi: 10.1021/la0265981

Munafò, P., Goffredo, G. B., and Quagliarini, E. (2015). TiO$_2$-based nanocoatings for preserving architectural stone surfaces: an overview. *Constr. Build. Mater.* 84, 201–218. doi: 10.1016/j.conbuildmat.2015.02.083

Nugari, M. P., and Salvadori, O. (2003). "Biocides and treatment of stone: limitations and future prospects," in *Art, Biology, and Conservation: Biodeterioration of Works of Art*, eds R. J. Koestler, V. H. Koestler, A. Elena Charola, and F. E. Nieto-Fernandez (New York, NY: The Metropolitan Museum of Art), 518–535.

Omae, I. (2003). General aspects of tin-free antifouling paints. *Chem. Rev.* 103:3431. doi: 10.1021/cr030669z

Pinho, L., Elhaddad, F., Facio, D. S., and Mosquera, M. J. (2013). A novel TiO$_2$-SiO$_2$ nanocomposite converts a very friable stone into a self-cleaning building material. *Appl. Surf. Sci.* 275, 389–396. doi: 10.1016/j.apsusc.2012.10.142

Pinho, L., and Mosquera, M. J. (2011). Titania-silica nanocomposite photocatalysts with application in stone self-cleaning. *J. Phys. Chem. C* 115, 22851–22862. doi: 10.1021/jp2074623

Pinna, D. (2017). *Coping With Biological Growth on Stone Heritage Objects: Methods, Products, Applications, and Perspectives.* New York, NY: Apple Academic Press.

Pinna, D., Salvadori, B., and Galeotti, M. (2012). Monitoring the performance of innovative and traditional biocides mixed with consolidants and water-repellents forthe prevention of biological growth on stone. *Sci. Total Environ.* 423, 132–141. doi: 10.1016/j.scitotenv.2012.02.012

Quagliarini, E., Bondioli, F., Goffredo, G. B., Licciulli, A., and Munafò, P. (2012). Smart surfaces for architectural heritage: preliminary results about the application of TiO$_2$-based coatings on travertine. *J. Cult. Herit.* 13, 204–209. doi: 10.1016/j.culher.2011.10.002

Quagliarini, E., Bondioli, F., Goffredo, G. B., Licciulli, A., and Munafò, P. (2013). Self-cleaning materials on architectural heritage: compatibility of photo-induced hydro-philicity of TiO$_2$ coatings on stone surfaces. *J. Cult. Herit.* 14, 1–7. doi: 10.1016/j.culher.2012.02.006

Ruffolo, S. A., De Leo, F., Ricca, M., Arcudi, A., Silvestri, C., Bruno, L., et al. (2017). Medium-term *in situ* experiment by using organic biocides and titanium dioxide for the mitigation of microbial colonization on stone surfaces. *Int. Biodeteriorat. Biodegrad.* 123, 17–26 doi: 10.1016/j.ibiod.2017.05.016

Ruggiero, L., Bartoli, F., Fidanza, M. R., Zurlo, F., Marconi, E., Gasperi, T., et al. (2020). Encapsulation of environmentally-friendly biocides in silica nanosystems for multifunctional coatings. *Appl. Surf. Sci.* 514:145908. doi: 10.1016/j.apsusc.2020.145908

Ruggiero, L., Crociani, L., Zendri, E., El Habra, N., and Guerriero, P. (2018). Incorporation of the zosteric sodium salt in silica nanocapsules: synthesis and characterization of new fillers for antifouling coatings. *Appl. Surf. Sci.* 439, 705–711. doi: 10.1016/j.apsusc.2017.12.228

Ruggiero, L., Di Bartolomeo, E., Gasperi, T., Luisetto, I., Talone, A., Zurlo, F., et al. (2019). Silica nanosystems for active antifouling protection: nanocapsules and mesoporous nanoparticles in controlled release applications. *J. Alloys Compd.* 798, 144–148. doi: 10.1016/j.jallcom.2019.05.215

Salazar-Hernández, C., Zárraga, R., Alonso, S., Sugita, S., Calixto, S., and Cervantes, J. (2009). Effect of solvent type on polycondensation of TEOS catalyzed by DBTL as used for stone consolidation. *J. Sol Gel Sci. Technol.* 49, 301–310. doi: 10.1007/s10971-008-1879-9

Scheerer, S., Ortega Morales, O., and Gaylarde, C. (2009). Microbial deterioration of stone monuments-an updated overview. *Adv Appl Microbiol.* 66, 97–139. doi: 10.1016/S0065-2164(08)00805-8

Seven, O., Dindar, B., Aydemir, S., Metin, D., Ozinel, M., and Icli, S. (2004). Solar photocatalytic disinfection of a group of bacteria and fungi aqueous suspensions with TiO$_2$, ZnO and Sahara Desert dust. *J. Photochem. Photobiol. Chem.* 165, 103–107. doi: 10.1016/j.jphotochem.2004.03.005

Tamayo, A., and Rubio, J. (2010). Structure modification by solvent addition into TEOS/PDMS hybrid materials. *J. Non Crystalline Solids* 356, 1742–1748. doi: 10.1016/j.jnoncrysol.2010.04.025

Tellez, L., Rubio, J., Rubio, F., Morales, E., and Oteo, J. L. (2003). Synthesis of inorganic-organic hybrid materials from TEOS, TBT and PDMS. *J. Mater. Sci.* 38:1773. doi: 10.1023/A:1023240129477

Torraca, G. (2009). *Lectures on Materials Science for Architectural Conservation.* Los Angeles, CA: Getty Conservation Institute.

Trojer, M. A., Nordstierna, L., Bergek, J., Blanckc, H., Holmberg, K., and Nydén, M. (2015). Use of microcapsules as controlled release devices for coatings. *Adv. Coll. Interface Sci.* 222, 18–43. doi: 10.1016/j.cis.2014.06.003

Wen, J., and Mark, J. E. (1995). Sol-Gel preparation of composites of poly(dimethylsiloxane) with SiO$_2$ and SiO$_2$/TiO$_2$, and their mechanical properties. *Polymer J.* 27, 492–502. doi: 10.1295/polymj.27.492

Xu, F., and Li, D. (2013). Effect of the addition of hydroxyl-terminated polydimethylsiloxane to TEOS-based stone protective materials. *J. Sol Gel Sci. Technol.* 65, 212–219. doi: 10.1007/s10971-012-2926-0

Xu, F., Li, D., Zhang, Q., Zhang, H., and Xu, J. (2012). Effects of addition of colloidal silica nanoparticles on TEOS-based stone protection using n-octylamine as catalyst. *Progress Organ. Coat.* 75, 429–434. doi: 10.1016/j.porgcoat.2012.07.001

Xu, F., Zeng, W., and Li, D. (2019). Recent advance in alkoxysilane-based consolidants for stone. *Progress Organ. Coat.* 127, 45–54. doi: 10.1016/j.porgcoat.2018.11.003

Zárraga, R., Cervantes, J., Salazar-Hernandez, C., and Wheeler, G. (2010). Effect of the addition of hydroxyl-terminated polydimethylsiloxane to TEOS-based stone consolidants. *J. Cult. Heritage* 11, 138–144. doi: 10.1016/j.culher.2009.07.002

Zhang, X., Ye, H., Xiao, B., Yan, L., and Jiang, B. (2010). Sol–Gel preparation of PDMS/silica hybrid antireflective coatings with controlled thickness and durable antireflective performance. *J. Phys. Chem. C* 114, 19979–19983. doi: 10.1021/jp106192z

Microchemical Investigation of Long-Term Buried Gilded and Silvered Artifacts From Ancient Peru

Gabriel M. Ingo[1]*, Monica Albini[1], Angel D. Bustamante[2],
Sandra del Pilar Zambrano Alva[2], Arabel Fernandez[3], Chiara Giuliani[1], Elena Messina[1],
Marianna Pascucci[1], Cristina Riccucci[1], Paola Staccioli[1], Gabriella Di Carlo[1] and
Luca Tortora[4]

[1] Institute for the Study of Nanostructured Materials, National Research Council, Rome, Italy, [2] Departamento Académico de Física del Estado Sólido, Universidad Nacional Mayor de San Marcos, Lima, Peru, [3] Museo Señora de Cao and Fundacion Wiese, Trujillo, Peru, [4] Surface Analysis Laboratory, Istituto Nazionale di Fisica Nucleare (INFN) & Department of Mathematics and Physics, Roma Tre University, Rome, Italy

A large number of metal artifacts with exceptional artistic value of the Moche culture have been found in the tombs of the Lords of Sipán (Lambayeque, Peru) and of the Lady of Cao (El Brujo, Peru) characterized by different burial conditions. Some of the objects, dated around 300–400 AD, are constituted by substrates of Cu- or Ag-based alloys coated by uniformly distributed thin films of precious metal (1–4 microns) that create also polymetallic bicolored surfaces with "gold" and "silver" areas. In order to investigate the corrosion product structure and composition as well as to identify the techniques used to give the gold or silver appearance, an integrated analytical approach has been adopted. The selected complementary methodologies were scanning electron microscopy (SEM) coupled with energy-dispersive spectroscopy (EDS), X-ray diffraction (XRD), X-ray photoelectron spectroscopy (XPS), and optical microscopy (OM). The findings reveal that the substrates are mainly composed of Cu-Ag-Au alloys that at the site of Sipán have been almost completely corroded during the burial. Furthermore, the results show that the main aggressive agent is Cl^- coming from the soil and that the degradation phenomena were likely enhanced by the galvanic coupling between the precious metal layer and the less noble substrate. The degradation products have formed mainly layered structures containing chloroargyrite (AgCl), cuprite (Cu_2O), nantokite (CuCl), and atacamite [$CuCl_2 \cdot 3Cu(OH)_2$] polymorphs. These latter species warn that dangerous copper cyclic corrosion is occurring, a harmful phenomenon, commonly defined as "bronze disease," which must be firmly mitigated. Finally, the findings reveal that the Moche metal workers used the depletion gilding to selectively modify the surface chemical composition of the artifacts to produce the Ag or Au thin films. According to this subtractive method, the surface of the Cu-Au-Ag alloys was enriched with a layer of precious metal by means of cycles of thermal treatments and removal of Cu or both Cu and Ag from the outermost region by using pickling solutions.

Keywords: Cu-Ag-Au ternary alloys, long-term burial soil corrosion, surface analytical techniques, metal surface chemical modification, galvanic coupling, tumbaga

INTRODUCTION

In 1987, great treasures composed of spectacular metal artifacts were discovered in the unlooted tombs of the Lords of Sipán (Huaca Rajada, Lambayeque, Peru), and in 2006, in the tomb of the Lady of Cao (El Brujo, Trujillo, Peru). These sites are characterized by different burial conditions that have influenced the long-term corrosion behavior. Indeed, the artifacts found at Sipán are extensively corroded, while the objects found at El Brujo are generally in a good state of preservation. The extraordinary artifacts found there, mainly jewels and ceremonial ornaments, were produced by the metal smiths of the Moche culture that flourished on the northern coast of present-day Peru between about 0 and 600 AD. The discovery of these amazing artifacts confirms that the Moche metal workers were sophisticated pre-Columbian producers of unequaled metal objects. Some of them show a bicolored aspect since characterized by a polymetallic surface with thin "gold" and "silver" areas likely achieved by using manufacturing methods able to precisely manipulate the surface chemical composition at a nanoscale dimension.

In order to investigate the microchemical surface and bulk structure and the degradation products formed during the long-term burial, we have adopted an integrated analytical approach by using complementary methodologies such as scanning electron microscopy (SEM) combined with energy-dispersive spectroscopy (EDS), X-ray photoelectron spectroscopy (XPS), X-ray diffraction (XRD), and optical microscopy (OM).

It is worth noting that the interaction between these polymetallic (Ag-Cu-Au) artifacts and the soil constituents has lasted many hundred years, and the information on the resulting products could be of great interest in the study of long-term environmentally driven degradation phenomena of polymetallic materials, phenomena that until now have been investigated by few authors (Scott, 1986, 1998; Hörz and Kallfass, 2000; Ingo et al., 2013a,b).

Our effort was also aimed to gain further insights into methods used by the Moche metallurgists to modify the surface chemical composition (Lechtman, 1971, 1979; Lechtman et al., 1982; Lechtman, 1984a,b; Scott, 1986, 1998, 2000; Hörz and Kallfass, 1998, 2000). We point out that the selected artifacts were not objects of common use but ornaments for an elite exhibiting power and rank. They include high-status ceremonial objects and spectacular nose ornaments, i.e., the narigueras, large jewels to be hooked to the nostrils. These artifacts clearly demonstrate the outstanding virtuosity of the Moche artisans and the impressive quality of their metal production as well as reflect the most sophisticated metal production techniques of that period in the New World.

EXPERIMENTAL DETAILS

Archeological Artifacts

The archeological artifacts to be analyzed have been selected by the archeologists. The samples are mainly fragments detached from the artifacts likely being crushed by pressure from the soil sediments during the long-term burial or small parts accidentally broken during the cleaning and conservation procedures. For XRD measurements, low quantities of patina have been also carefully removed from the objects and properly ground. The samples were subjected to metallographic, microchemical, and structural investigations in as-received conditions by means of the abovementioned analytical techniques. Furthermore, some fragments also have been cross-sectioned to study the structure of the corrosion products and of the thin Ag or Au surface layers. In order to prepare the cross sections, representative shards have been embedded in a suitable two-component resin (curing time: 1 day) and sectioned by using a diamond saw able to retain the outermost layer's features and the bulk microchemical structure (Ingo et al., 2013a). The polishing procedure was performed by using silicon carbide papers until 1,200 grit, while the final treatment was carried out with diamond pastes up to 0.1 μm.

Scanning Electron Microscopy – Energy-Dispersive Spectroscopy Analysis

The surface morphology and microchemical structure have been investigated by means of a thermionic scanning electron microscope (SEM) Stereoscan 360 (Cambridge, United Kingdom) and a high-spatial resolution LEO 1530 field emission scanning electron microscope (FE-SEM). SEM and FESEM instruments are equipped with an INCA 250 and INCA 450 energy-dispersive spectrometer (EDS), respectively, and back-scattered electron (BSE) detectors. SEM investigations were performed by using both secondary (SE) and BSE electrons and selecting an acceleration voltage of 20 kV, while the FE-SEM characterizations were carried out by varying the acceleration voltages from 1 to 20 kV in order to better disclose the micromorphological features.

In order to investigate the powered materials, a suitable double-faced adhesive carbon tape was used to collect and fix the matter. These carbon tapes are commonly and conveniently used for SEM-EDS microchemical investigations (Ingo et al., 2001). In order to avoid charging effects induced on the sample by the electron beam, the surfaces of the samples were coated with a thin layer of Cr or C, deposited by using a Bal-Tech SCD 500 equipment at a pressure of about 5×10^{-3} mbar to achieve a conductive and uniform film, a few nanometers thick.

X-Ray Diffraction Investigation

XRD investigations were carried out by analyzing directly the artifact surfaces or the small amount of powdered patina by using a Siemens 5000 X-ray powder diffractometer with Ni-filtered Cu K_α radiation (λ = 0.154056 nm). The following experimental parameters were selected: angular values between 10 and 90° in additive mode, step size 0.05°, and sampling time of 20 s. XRD patterns were analyzed by using specific electronic databases and compared with the literature information.

Optical Microscopy Study

OM morphological studies were performed by using a Leica MZFLIII and a Leica Application Suite (LAS) multifocus stereo microscope. Furthermore, at the Museum of the Lady of Cao, a

Zeiss optical microscope equipped with a digital camera was used for *in situ* morphological investigation. The metallurgical features of the cross-sectioned artifacts have been studied by means of a Leica MEF IV optical microscope.

X-Ray Photoelectron Spectroscopy

The XPS technique has been used to ascertain the surface possible presence of alloying elements such as As or Sn (Lechtman and Klein, 1999). Measurements were carried out by using an ESCALAB Mk II spectrometer equipped with a hemispherical electron energy analyzer and a twin anode X-ray source emitting not monochromatized Al Kα and Mg Kα radiations, 1,486.6 and 1,253.6 eV, respectively. The binding energy (BE) accuracy has been measured to be $\pm$ 0.1 eV. The values of the BEs of the Au $4f_{7/2}$ signal from Ar^+-cleaned Au 99.99%, of the Zr $3d_{5/2}$ peak from zirconia, and of Sn $3d_{5/2}$ peak from cassiterite (SnO_2) were 84.0, 182.3, and 487.0 eV, respectively (Paparazzo et al., 1988; Ingo et al., 1992; Ingo and Padeletti, 1994; Curulli et al., 2005). In order to avoid, or reduce, any eventual sample damage potentially provoked by the x-ray irradiation during the XPS measurements, short acquiring times were imposed and a copper sample holder cooled by liquid N_2 was used (Schlesinger et al., 2000). Other experimental details are reported elsewhere (Ingo et al., 2000, 2002).

RESULTS AND DISCUSSION

The paper presents some highlighting cases of study describing the microchemical features of long-term buried Cu-Ag-Au alloy artifacts whose outermost chemical composition was intentionally modified to achieve a local accentuated Ag or Au surface amount. This latter in some cases formed polymetallic bicolored surfaces with "gold" and "silver" areas likely for symbolic, shamanic, or religious reasons.

The aim of the ancient goldsmiths was to give to the objects the appearance of solid precious metal or to create an elaborate and fascinating specific visual effect combining the color of different metals (Oddy, 1981, 1990; Raub, 1986a,b; Schorsch, 1988; Bray, 1993; Merkel et al., 1995; Hörz and Kallfass, 1998, 2000; Grimwade, 1999; Centeno and Schorsch, 2000; Ingo et al., 2013a).

The first case describes the surface and bulk microchemical and morphological features of a gilded semicircular diadem, an owl crown, almost completely mineralized) found in the tomb T15 at Sipán (Peru) where a young warrior was interred.

The OM images and the XRD pattern reported in **Figure 1** show areas of the bare original gilded surface embedded in light green-blue corrosion products, i.e., the patina. This structure suggests to the conservators to pay a great deal of attention during the cleaning procedure to avoid the loss of the thin gold layer that could be peeled away (Scott, 1990, 1991, 2002; Ingo et al., 2013b).

The results reveal that the corrosion products are mainly constituted by atacamite and its polymorph paratacamite [basic copper oxy-chloride, $Cu_2Cl(OH)_3$], thus demonstrating that the main aggressive agent coming from the burial environment is chlorine. Furthermore, the findings show the presence of a layer

or randomly scattered particles of reddish cuprite (Cu_2O) and yellow-orange nantokite (CuCl) inside the patina.

Since the presence of atacamite corrosion products in bronze archeological objects is a symptom of the detrimental "bronze disease" degradation phenomenon, great attention must be paid to avoid its insurgence and development. This relentless and cyclic corrosion process is caused by the presence of chlorine in the burial environment that corrodes copper forming nantokite (Scott, 1990, 1991, 2002; Bastidas et al., 2010). When this latter specie is exposed to moisture and oxygen, it gives rise to the formation of atacamite or its polymorphs [$2Cu_2(OH)_3Cl$] and hydrochloric acid which in turn reacts with copper to form new nantokite in a cyclic and self-sustaining process that converts copper in atacamite.

As a consequence of this phenomenon, the surface of the object is transformed into a light greenish powder, thus inducing the progressive loss of its original form and integrity (Ingo et al., 2013b). At present, different conservation materials and methods are used to hinder the degradation process. Unfortunately, some of these procedures are based on the use of toxic inhibitors (Stupnišek-Lisac et al., 1998; Antonijevic and Petrovic, 2008) but tailored innovative solutions based on nanostructured materials are emerging for bronze conservation and cleaning similar to those used to stop degradation of other classes of ancient works of art (Chelazzi et al., 2014; Baglioni et al., 2015; Poggi et al., 2016).

In order to monitor the presence of Pb, Sn, or As also as surface enrichment (Lechtman and Klein, 1999) from the Cu-Ag-Au substrate caused by corrosion phenomena, we have used the XPS technique (Ingo et al., 2002, 2013b; Hayez et al., 2004). The results (not shown) reveal that neither Pb nor As is present in the metallic state or as oxides and further exclude the presence in the corrosion products of cassiterite (SnO_2) or romarkite (SnO) (Paparazzo et al., 1988; Ingo et al., 1992), thus suggesting the absence of As, Pb, and Sn in the Cu-Ag-Au alloy.

Other information is given by the SEM images and EDS spectra of the cross-sectioned fragment shown in **Figure 1** that describe the microchemical structure of the artifact (~0.2 mm thick). The object is almost completely mineralized, and the only survived pristine metal is the thin gold layer originally on the surface and now almost entirely embedded in the Cu corrosion products.

The gold layer (2–3 μm thick; **Figure 1** and **Supplementary Figure S1**) contains a low amount of silver and copper and is uniformly distributed over the entire surface on both sides of the hammered sheet substrate marking the original surface of the object.

The presence of Au and Ag is well documented also in the inner part of the object as shown by the BSE SEM images and the EDS spectra of the light gray areas scattered everywhere inside the mineralized substrate. These local enrichments of precious metals indicate the use of a "tumbaga" Cu-based ternary alloy containing an appreciable content of gold and a small amount of silver.

As a consequence of the long-term interaction with the surrounding environment, silver has reacted with chlorine from the soil and it has been transformed in chlorargyrite (AgCl), while gold has formed small metallic nanoparticles distributed in the mineralized substrate. Furthermore, EDS spectra confirm the
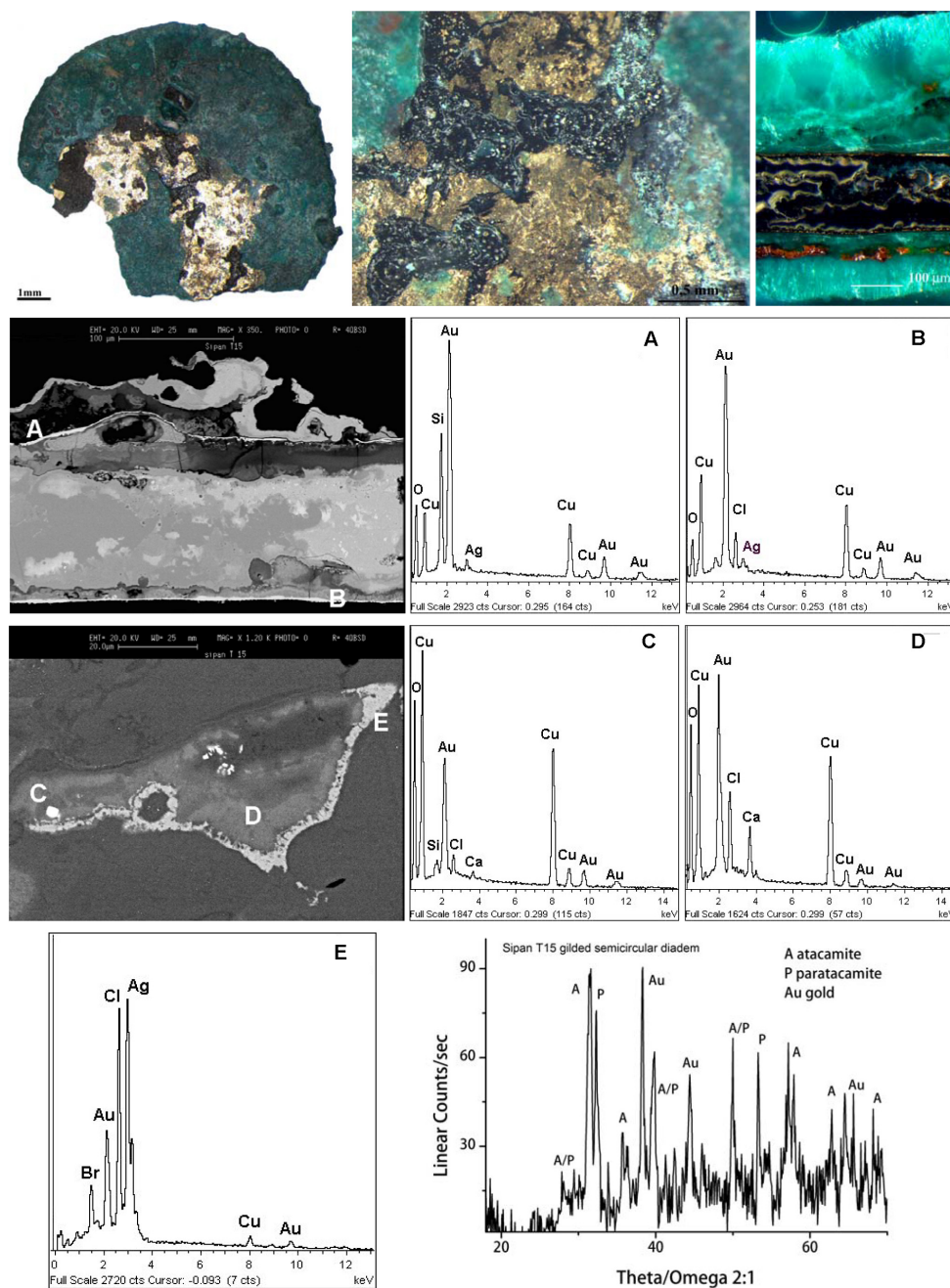
FIGURE 1 | SEM, EDS (spectrum **A–E**), OM and XRD results describing the micro-chemical of a fragment of a gilded semicircular diadem (tomb T15 of a young warrior, Sipán). OM images and XRD pattern show the green patina composed of acicular atacamite [$Cu_2Cl(OH)_3$] with areas of the bare original gilded surface. The OM image discloses also layered particles of reddish cuprite (Cu_2O) and yellow-orange nantokite (CuCl).

absence of Pb, As, and Sn in the substrate as already documented by XPS for the external surface (Lechtman and Klein, 1999).

The severe corrosion process occurring during the long-term burial does not allow determining precisely the chemical composition of the tumbaga Ag-Cu-Au ternary alloy (Twilley and Boyles, 1981). Therefore, it cannot be possible to determine the relative proportions of metals which constitute the alloy substrate. However, the gold content may be estimated to be around 10–15 weight percent (hereafter wt%).

It is worth noting that the corrosion of copper is likely enhanced by the presence of the precious metal layer since a relevant degradation driving force could be the difference between the electrochemical potentials of Cu and Au or Ag along with the soil characteristics

(pH, humidity, presence of aggressive ions) that could increase the transformation of Cu and Ag into minerals (Ingo et al., 2013a,b).

The severe alteration phenomena could have been probably exacerbated by the galvanic corrosion, also known as dissimilar metal corrosion or bimetallic corrosion. This latter destructive reaction is an electrochemical process occurring when two or more metals are in contact in the presence of an electrolyte and a corrosive environment.

Under these conditions, the less noble metal acts as an anode and is preferentially corroded at an accelerated rate if compared with the uncoupled condition (Ingo et al., 2013a,b). On the contrary, the other more noble metal acts as a cathode and remains protected until the less noble metal is completely transformed in corrosion products. As mentioned above, the extent of corrosion depends on the difference between the electrochemical potentials of the involved metals and makes gilded-metal artworks particularly unstable from a chemico-physical and structural point of view.

Our findings suggest that the electrochemical oxidation–reduction process could have enhanced the degradation of these polymetallic objects having created a galvanic cell formed by the precious metal layer connected to the substrate with water and dissolved ions that provide a means for ion and electron migration (Ingo et al., 2013a,b).

Concerning the manufacturing techniques used by the Moche metallurgists, the above shown results exclude the application of a thin gold film *via* mechanical or metallurgical methods and suggest the use of the gilding process to remove copper from a tumbaga substrate to create an Au-looking surface. According to this bottom-up subtractive method, an artifact appearance could be substantially modified, rendering the objects golden or silvery even if the amount of Au or Ag in the alloy was relatively low.

As described by other scholars, the depletion gilding is based first on the surface oxidation of Cu from the near-surface region that is favored as compared to Au or Ag (Lechtman, 1971, 1979; Forty, 1979; Forty and Durkin, 1980; Lechtman et al., 1982; Lechtman, 1984a,b; Scott, 1986, 1998, 2000; Hörz and Kallfass, 1998, 2000; Sáenz-Samper and Martinón-Torres, 2017).

The removal of Cu oxides was carried out by immersing the oxidized artifact in a poultice of an acid plant juice containing likely other appropriate corrosive chemical compounds that progressively dissolved copper oxides from the surface and created a fine outermost layer of precious metal. In this way, an Ag or Au spongy crust on the surface was formed and then burnished, leaving a brilliant finish.

The success of the process depends mainly on the skill of the artisans that empirically selected not only the alloy chemical composition but also the pickling solutions (Forty, 1979; Forty and Durkin, 1980; Lechtman et al., 1982; Hultquist, 1985; Guisbiers et al., 2014).

The artifacts found at Sipán and Trujillo demonstrate that the Moche artisans were able to effectively control the selective removal of copper oxides (and sometimes silver) from the surface, creating a homogeneous distribution of Au or Ag along the surface (Ingo et al., 2013a,b). This ability was based only on the long-term cognitive skill of the Moche metal workers who

realized that an alloy surface could be modified by empirically optimized treatments and that unique symbolic and esthetic features could be achieved.

It is worth pointing out that the aim of the Moche metallurgists was not fraudulent as frequently observed in the Old World (Lins and Oddy, 1975; Lechtman, 1979, 1984a,b; Scott, 1986, 1998, 2000; Schorsch, 1988; Oddy, 1991; La Niece, 1993; Zwicker et al., 1993; Cooke et al., 2008; Ingo et al., 2013b). Their aim was only finalized to modify color and esthetic appearance of an object combining different metals as Cu, Au, and Ag on the artifact surface, thus stimulating the development of sophisticated methods acting on a nanoscale as the electrochemical replacement plating discovered by Lechtman (1971, 1979, 1984a,b) and Lechtman et al. (1982). Other techniques were also developed to alter the surface chemical composition such as the foil gilding or the fusion gilding the use of which can be determined only by examining the ancient gilt surfaces *via* microchemical investigations (Scott, 1986, 1998, 2000; Cooke et al., 2008).

The second case study is a gilded plaque, completely mineralized, found in the tomb T16 of a warrior found with a "Pututo," i.e., a ceremonial trumpet produced by using a great seashell.

The high-spatial resolution SEM images shown in **Figure 2** (first row) describe the morphology of the surface gold-enriched layer present on both sides, while the other SEM and EDS results allow to evaluate the internal corroded structure of the artifact.

The high-spatial resolution SEM images (first row) reveal the presence of not uniformly distributed micro and nano pitlike pores on the surface of the gilding layer. The development of this morphological feature could be related to the procedures adopted for the formation and removal of oxides such as temperature and duration of thermal treatments as well as to the pickling conditions.

The thickness of the gilding layer is not uniform and ranges from about 2–4 μm and is mainly composed of Au with a consistent presence of Ag and Cu. Also for this object the Moche metalworkers used a tumbaga Cu-based alloy with gold and some silver as documented by the BSE SEM images and the EDS spectra of the cross-sectioned fragment. These results also reveal the presence of consistent amounts of Ag and Au in the light gray areas of the completely mineralized substrate and of chlorine as main degrading agent.

Another interesting object found at Sipán is a silver-plated nariguera found in the tomb T16 of the warrior with a Pututo. The SEM-EDS results shown in **Figure 3** reveal that the artifact is constituted by an Ag-based alloy whose surface was deliberately enriched in silver. The SEM and OM images and EDS spectra show that it is almost completely mineralized and describe the microchemical structure of the surface silver-enriched layer as well as show the internal corroded structure of the artifact. The XRD pattern of the green copper corrosion product (third row, **Figure 3**) also in this artifact reveals the presence of harmful atacamite that is present also inside the artifact (see the OM image shown in the third row of **Figure 3**), thus confirming the role of chlorine in the corrosion process.
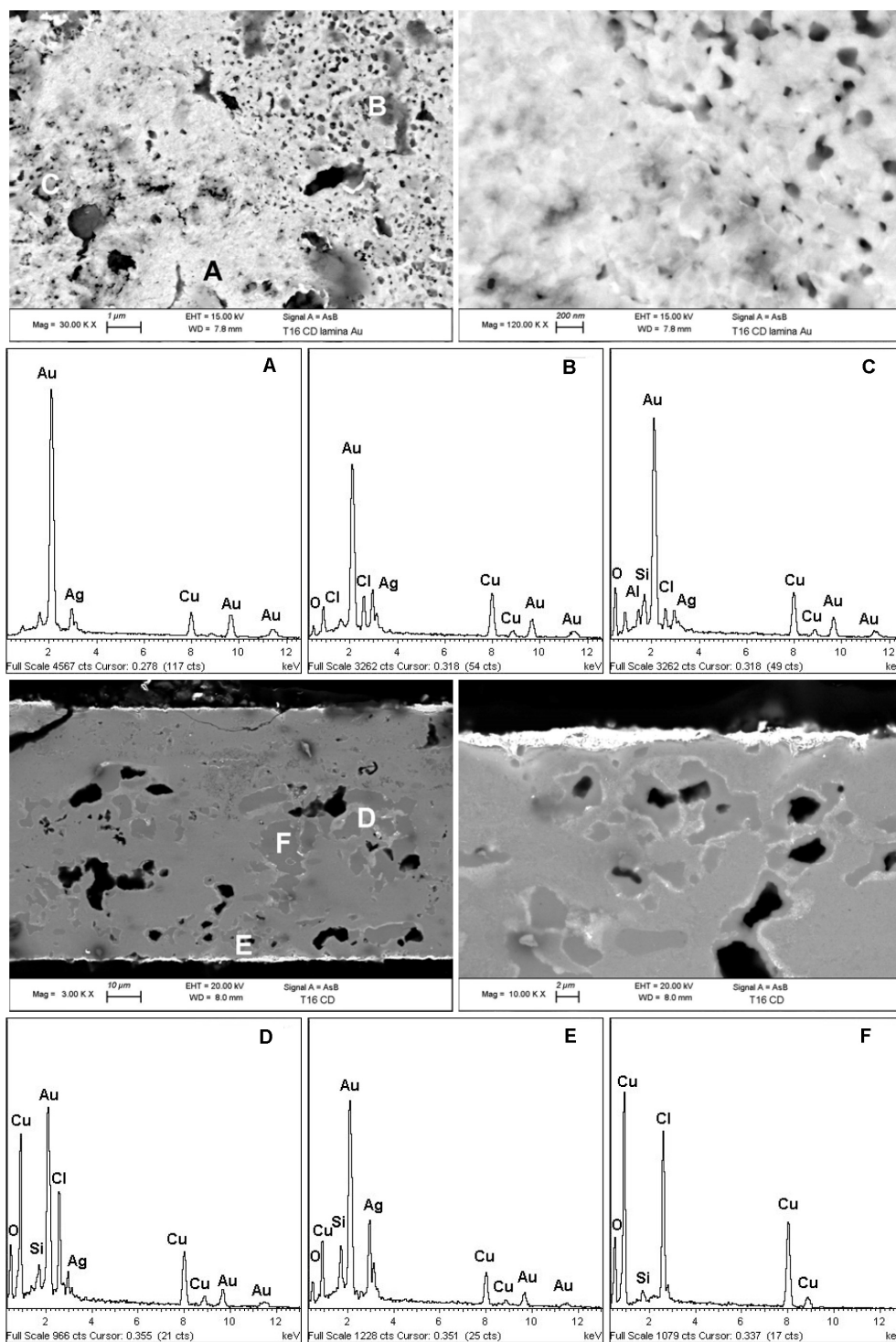
FIGURE 2 | SEM images and the EDS spectra **(A–F)** of a fragment of a gilded plaque completely mineralized found in the tomb T16 of the warrior with a ceremonial trumpet called Pututo. The results describe the microchemistry and the morphology of the surface gold-enriched layer present on both sides as well as show the internal corroded structure of the artifact.

Unfortunately, the conditions of the investigated artifacts found at Sipán do not allow the determination of detailed information on the chemical composition and metallurgical features of the Ag-Cu-Au alloys used by the Moche metallurgists; therefore, our investigations have been focused also on the well-preserved artifacts found in the tomb of the lady of Cao
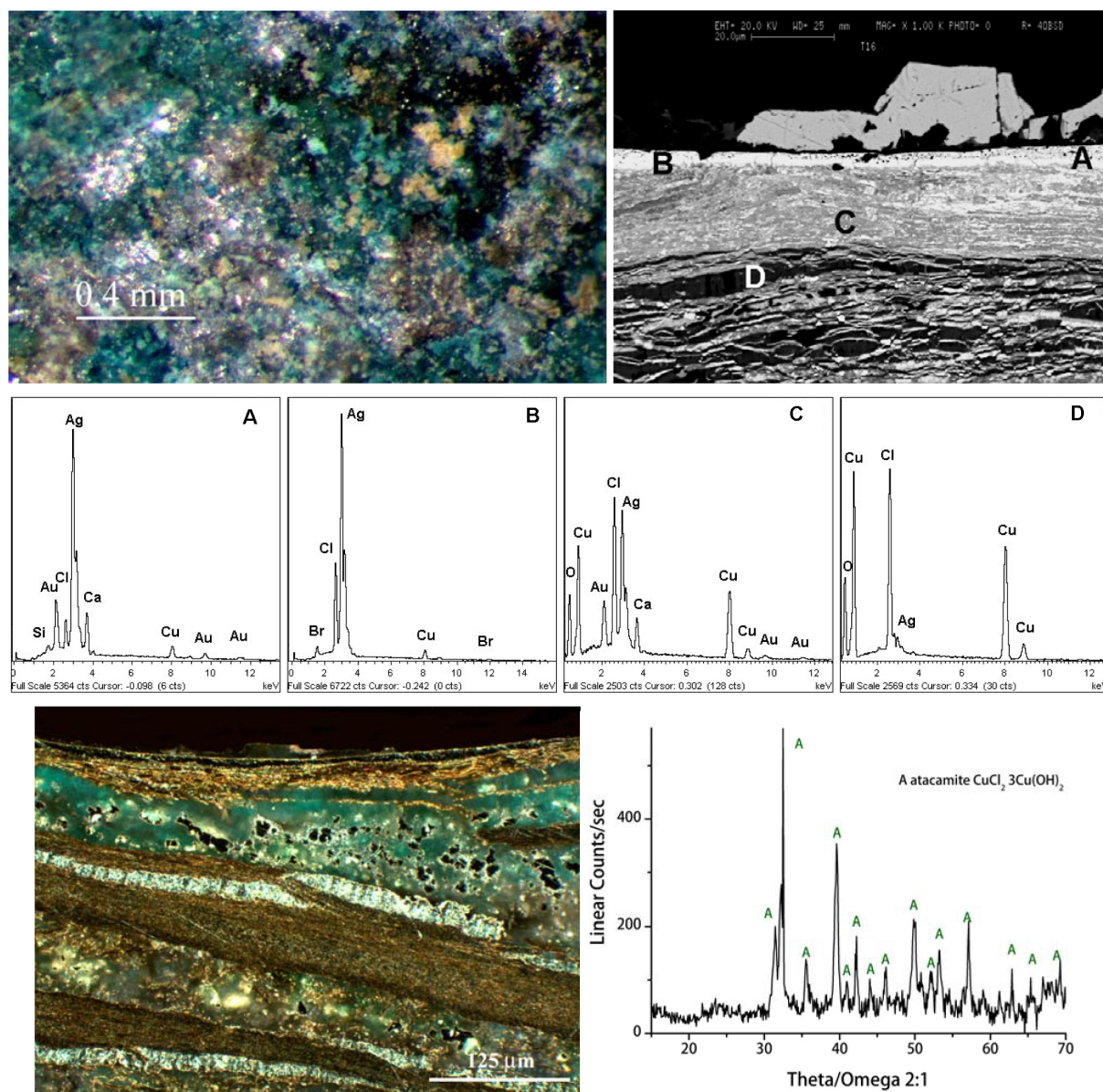
FIGURE 3 | SEM and OM images and EDS spectra (A–D) of a fragment of a silver plated nariguera almost completely mineralized found in the tomb T16 of the warrior with a ceremonial trumpet called Pututo. The results describe the micro-chemical structure of the surface silver-enriched layer as well as show the internal corroded structure of the artifact. The XRD pattern of the green copper corrosion product (third row) reveals the presence of harmful atacamite that is present also inside the artefact (see the OM image shown in the third row).

whose environment was different with respect to that of Sipán being desert-arid.

In particular, we have investigated some narigueras, i.e., large jewels to be hooked to the nostrils, that have been found with the mummy of the Lady of Cao; she was also well-preserved by the arid burial condition.

The narigueras are generally in a very good state of conservation and are generally characterized by well-evident "silver" and "gold" surfaces as depicted in **Figures 4**, **5** where the front and back of the nariguera F4-22, F4-24, and F4-03 are shown.

Some morphological details are shown by the optical images reported in **Figures 4**, **5** that disclose the smooth interface between the "gold" and the "silver" areas characterized by a color change variation quite sharp without a morphological variation.

We have had the possibility to investigate in detail a small fragment detached from the "silver" area of the head of the animal on the left of the narigeura F4-03 (**Figure 5**). The FE-SEM images and the EDS spectra of the cross-sectioned fragment shown in **Figures 5**, **6** and **Supplementary Figure S2** reveal the metallurgical features of the single sheet constituting the nariguera while in **Table 1**
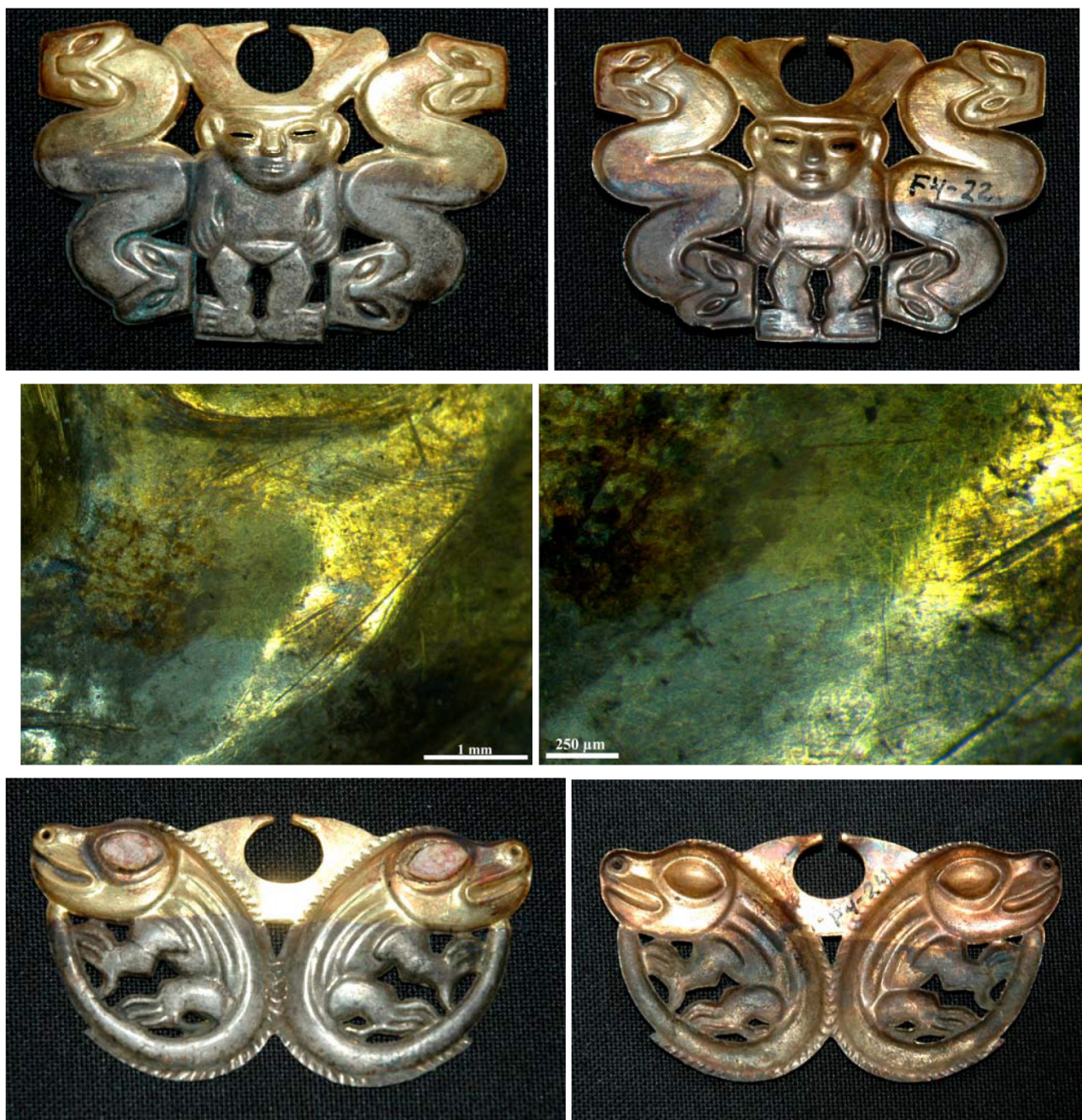
FIGURE 4 | The front and back of the nariguera F4-22 from the tomb of the Lady of Cao and optical images of the interface between the gold- and the silver-enriched areas, on the first and second rows, respectively. In the third row is shown the front and back of the nariguera F4-24. The images of the narigueras clearly reveal the color change from the "silver" and "gold" surface.

are reported the EDS elemental semiquantitative compositions expressed as weight percent (wt%). These latter data reveal the use of a deliberate ternary alloy of Ag, Cu, and Au to produce the narigeura F4-003.

The BSE SEM and the EDS results of the cross-sectional view through the nariguera show a lamellar-fibrous structure with an array of periodical alternating light and gray semi-aligned layers quite parallel to the surface.

This structure is similar to that observed in the nariguera found at Sipán in the tomb 16 and shown by the SEM and OM images reported in **Figure 3**; therefore, from the comparisons between these structures, we can evaluate the effect of the long-term corrosion phenomena that occurred in the soil to the buried Ag-Cu-Au artifacts.

As evidenced by the EDS results reported in **Figure 6** and **Tables 1**, **2**, the alternated layers of the bulk structure are
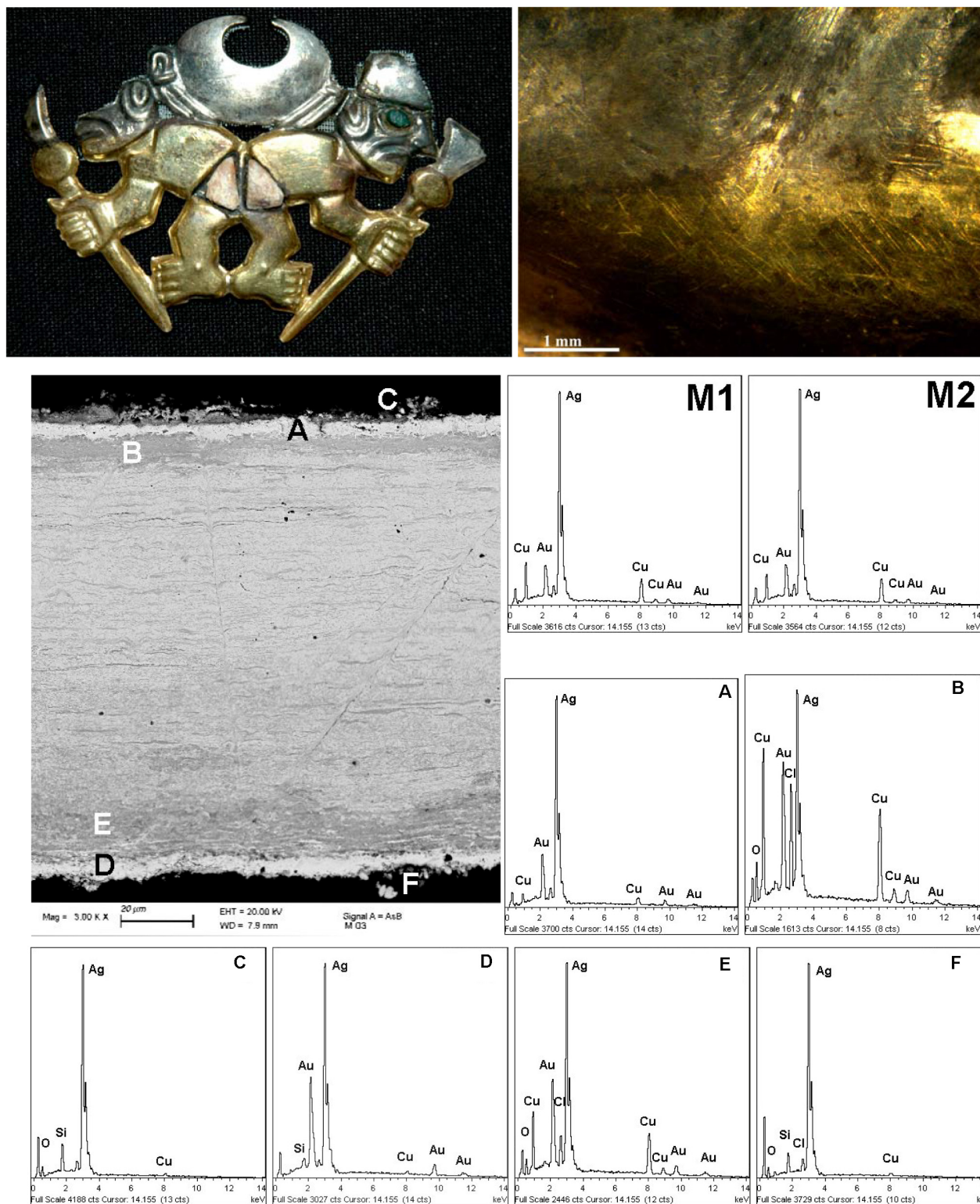
FIGURE 5 | The nariguera F4-03 from the tomb of the Lady of Cao and an optical image the interface between the "gold" and the "silver" areas, on the left and right side of the first raw, respectively. SEM images and EDS spectra (M1, M2, **A–F**) of the different areas of a cross-sectioned fragment of the nose ornament taken in the silvered area of the head of the animal on the left, second and third raw, respectively. The EDS elemental semi-quantitative composition (expressed as wt%) are reported in **Table 1**.
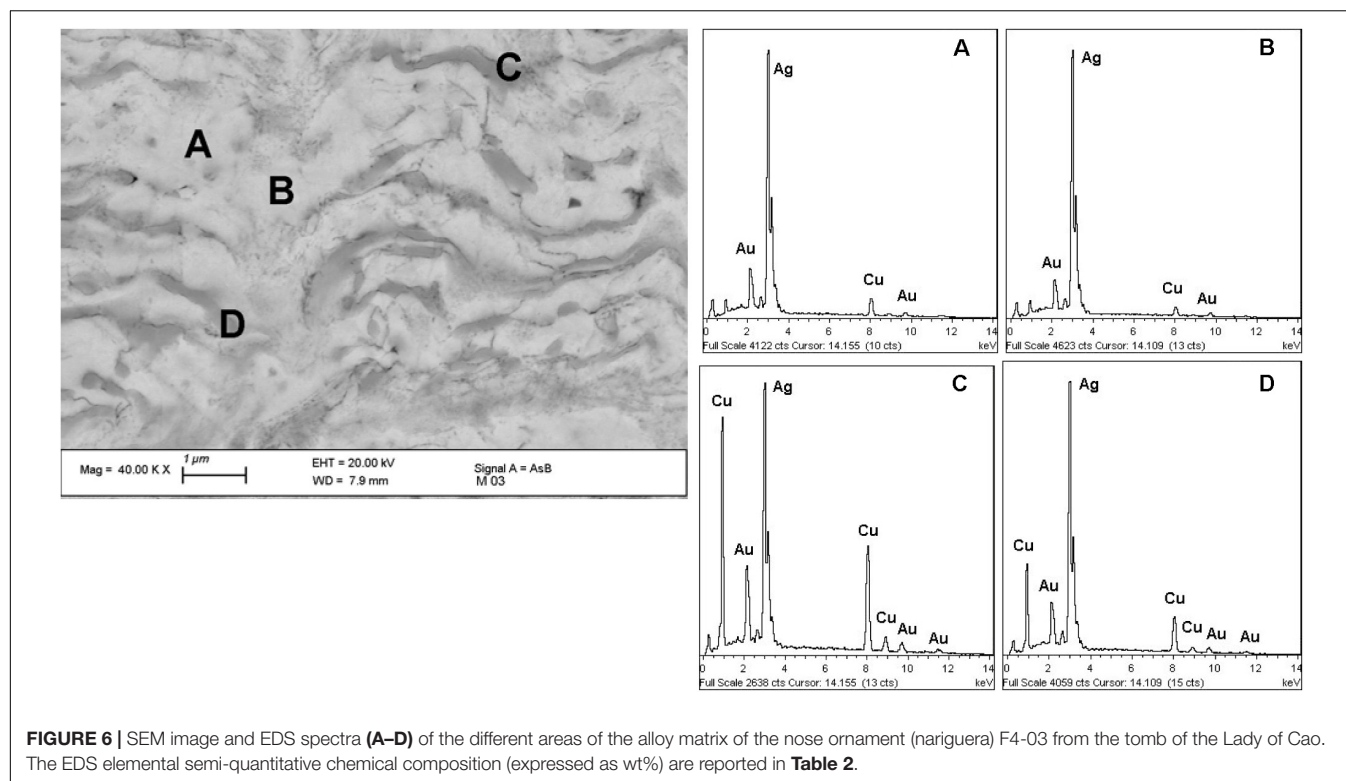
FIGURE 6 | SEM image and EDS spectra **(A–D)** of the different areas of the alloy matrix of the nose ornament (nariguera) F4-03 from the tomb of the Lady of Cao. The EDS elemental semi-quantitative chemical composition (expressed as wt%) are reported in **Table 2**.

TABLE 1 | Energy-dispersive spectroscopy (EDS) elemental composition [expressed as weight percent (wt%)] of the different areas of the cross-sectioned fragment of the nariguera F4-03 from the tomb of the Lady of Cao.

Spectrum	O	Si	S	Cl	Cu	Ag	Au
M1-alloy matrix*	–	–	–	–	18.18	70.41	11.40
M2-alloy matrix*	–	–	–	–	17.96	70.08	11.96
A-white thin layer	–	–	–	–	6.07	77.06	16.88
B-gray areas under the white thin layer	10.20	–	–	6.15	31.66	32.75	19.24
C-small white particles	10.70	3.88	0.25	–	2.30	82.87	–
D-white thin layer	1.73	–	3.43	–	2.10	68.83	23.91
E-gray areas under the white thin layer	7.41	0.44	–	2.37	20.56	49.19	20.03
F-small white particles	3.75	0.98	11.64	1.36	–	83.63	–

The EDS spectra are shown in **Figure 4**. *Analyzed area 100 μm × 100 μm.*

characterized by different amounts of Au, Cu, and Ag being the bright areas Ag-enriched, while the gray ones are Cu-enriched.

The data reported in **Tables 1**, **2** are in agreement with the information achieved by Cesareo et al. (2016, 2017) and Cesareo (2019), private communication during an *in situ* investigation carried out at the Museum of the Lady of Cao by using a portable X-ray fluorescence (XRF) apparatus. The reliability and utility of this analytical approach have been already largely demonstrated in the study of cultural heritage artifacts being a rapid and useful method to evaluate the elemental surface content of metals and degraded surfaces (Angelini et al., 2006; Figueiredo et al., 2010; Galli et al., 2011; Trojek and Hlozek, 2012).

SEM images shown in **Figures 5**, **6** also reveal that the metallurgical structure reasonably has been

originated by the drastic deformation of a heterogeneous material where segregation areas have been formed. This phenomenon presumably occurred during the solidification of the cast Ag-based alloy (Hörz and Kallfass, 1998, 2000) and has given rise to the formation of Cu-enriched areas in the melt containing more precious metals and less Cu.

SEM images clearly show that the material was subjected to heavy deformation by mechanical working carried out to reduce the thickness of the sheet and by the embossing and punching during the manufacture of the nariguera. The intense hammering process have elongated the Cu-enriched areas to form thin parallel layers whose shape was slightly modified by the thermal treatment of annealing carried out to restore ductility before the final depletion gilding process.

TABLE 2 | Energy-dispersive spectroscopy (EDS) elemental composition of the different areas present in the alloy matrix of the nariguera F4-03 from the tomb of the Lady of Cao.

Spectrum	Cu	Ag	Au
A-white areas	11.98	76.07	11.95
B-white areas	6.71	83.27	10.02
C-gray elongated phases	40.61	45.50	13.89
D-gray elongated phases	20.79	67.54	11.67

The EDS spectra are shown in **Figure 5**. *It is worth noting that the presence of Cu in the Ag-based alloy gives some practical advantages to the nose ornament because it increases the mechanical features of the alloy with respect to the pure silver.*

After repeated cycles of hammering and annealing treatments of a single Ag-based alloy sheet, the depletion gilding finally removed Cu or Cu and Ag from the near-surface region forming an outermost silver- or gold-enriched layer, respectively. The formation of a "gold" or a "silver" surface was achieved likely by tuning the pickling procedures and agents.

The presence of these inhomogeneous structures has clearly influenced the environmentally driven alteration phenomena, thus giving rise to the formation of peculiar corrosion products and structures.

Our results provide some other interesting information on the pickling procedures. The images shown in **Figure 4** reveal that the narigueras have been dipped up to half its height in a solution or wrapped in a poultice that removed, in a targeted manner, copper and silver from different areas of the object to achieve a seemingly bicolored metallic surface characterized by a spectacular dual esthetic effect.

As shown by the OM images of the front and the back of the nariguera F4-24 (**Figure 4** and **Supplementary Figure S3**), the color change from the "silver" and "gold" surface is quite sharp and the interface smooth without any morphological variation.

The reasons of combining gold and silver surfaces in these nose ornaments, sometimes rarely also with copper, with a typical duality, could be presumably ascribed to a symbolic and spiritual meaning, perhaps to be related to an astral or religious rationale. Some scholars believe that Au was considered to be the rain or the sweat of the sun and Ag the rain or the tears of the moon (Lechtman et al., 1982; Jones and Heidi, 2002; Cooke et al., 2008) or that gold could be related to the masculinity and the right side of the humans while silver could be associated to the femininity and the left side (Hörz and Kallfass, 1998, 2000). However, it seems that gold and silver were associated in some way to the sun and the moon, respectively, with a religious symbolism likely related to the nature duality.

However, the production of bicolored polymetallic surfaces was made possible by the local availability of metal resources and mainly by the sophisticated ability of the Moche metallurgists in the alloying and surface chemical manipulation processes. By means of empirically optimized methods, they modified at a nanoscale dimension the surface chemical composition of Cu-Au-Ag ternary alloys often containing only small percentages of precious metals to give them locally an accentuated appearance up to change their aspect where this desired specific effect was required.

This advanced skill was employed to produce elaborate artifacts with polymetallic surfaces and complex shapes of spectacular beauty with symbolic, shamanic, or religious values to be worn by an elite of the highest status, exhibiting power and rank.

CONCLUSION

This study highlights the analytical ability of micro-destructive surface and bulk techniques in providing a detailed information on the long-term interaction between polymetallic artifacts and surrounding environment that has caused at the Sipán site the almost complete mineralization of the objects.

The integrated analytical approach based on the use of complementary techniques such as SEM-EDS, XPS, OM, and XRD allows to describe the naturally grown degradation products resulting from interactions between soil species and Ag-Cu-Au ternary alloys and disclose that the main aggressive agent is Cl^- from the burial soil.

The microchemical information suggests also that the degradation phenomena were probably enhanced by the galvanic coupling between the precious metal layer and the less noble substrate.

The corrosion process formed mainly layered structures containing chloroargyrite (AgCl), cuprite (Cu_2O), nantokite (CuCl), and atacamite [$CuCl_2 \cdot 3Cu(OH)_2$] polymorphs. This information is useful to select tailored conservation materials and procedures for a long-term reliable conservation since the presence of atacamite warns that the dangerous copper cyclic corrosion is occurring and must be firmly mitigated to transmit these fascinating artifacts to future generations.

Finally, the combined use of different investigation methodologies has given information useful to identify the manufacturing methods used by the Moche goldsmiths to chemically modify the surface of Cu-Au-Ag alloys in some case achieving the contemporaneous presence of "gold" and "silver" areas. The depletion gilding was the method used by the Moche metallurgists to create these amazing esthetic effects by manipulating the surface of Cu-Au-Ag ternary alloys at a nanoscale dimension for creating adherent precious metal layers with a thickness ranging from one to a few micrometers.

DATA AVAILABILITY STATEMENT

All datasets generated for this study are included in the article/**Supplementary Material**.

AUTHOR CONTRIBUTIONS

GI designed the research and wrote the manuscript. GI, MA, AB, SZ, AF, CG, EM, MP, CR, PS, GD, and LT equally contributed to preparing the samples, performing the research,

analyzing the artifacts, discussing the data, and critically giving a substantial intellectual contribution. All authors contributed to the article and approved the submitted version.

SUPPLEMENTARY MATERIAL

The Supplementary Material for this article can be found online at: https://www.frontiersin.org/articles/10.3389/fmats.2020.00230/full#supplementary-material

REFERENCES

Angelini, E., Ingo, G. M., Grassini, S., Corbellini, S., De Caro, T., Riccucci, C., et al. (2006). Potentialities of XRF and ELS portable instruments for the characterisation of ancient artefacts. *Appl. Phys. A Mat. Sci. Process.* 83, 643–649. doi: 10.1007/s00339-006-3546-8

Antonijevic, M. M., and Petrovic, M. B. (2008). Copper corrosion inhibitors. a review. *Int. J. Electrochem. Sci.* 3, 1–28.

Baglioni, P., Bonelli, N., Chelazzi, D., Chevalier, A., Dei, L. G., Domingues, J., et al. (2015). Organogel formulations for the cleaning of easel paintings. *Appl. Phys. A-Mat. Sci. & Process.* 121, 857–868. doi: 10.1007/s00339-015-9364-0

Bastidas, D. M., Criado, M., Fajardo, S., La Iglesia, V. M., Cano, E., and Bastidas, J. M. (2010). Copper deterioration: causes, diagnosis and risk minimisation. *Int. Mat. Rev.* 55, 99–127. doi: 10.1179/095066009X12506721665257

Bray, W. (1993). "Techniques of gilding and surface-enrichment in pre-Hispanic American metallurgy," in *Metal Plating and Patination*, eds P. T. Craddock, and S. La Niece, (Butterworth-Heinemann), 174–192.

Centeno, S. A., and Schorsch, D. (2000). "The characterisation of gold layers on copper artifacts from the Piura Valley (Peru) in the early intermediate period," in *Gilded Metals: History, Technology and Conservation*, ed. T. Drayman-Weisser (London: Archetype Publications Ltd).

Cesareo, R. (2019). Gold, gildings and tumbaga from the Moche tomb of the Lady of Cao: an EDXRF test for the internal ratio method. *X Ray Spectrom.* 48, 202–207. doi: 10.1002/xrs.3021

Cesareo, R., Bustamante, A. D., Azeredo, S., Lopes, R. T., Jordan, R. F., Fernandez, A., et al. (2017). Radiography and transmission measurements on gold and silver from the Moche tomb "Señora de Cao". *Radiogr. Diagn. Imaging* 2017, 1–6. doi: 10.15761/RDI.1000106

Cesareo, R., Jordan, R. F., Fernandez, A., Bustamante, A. D., Fabian, J., Zambrano, S. D., et al. (2016). Analysis of the spectacular gold and silver from the Moche tomb "Señora de Cao". *X Ray Spectrom.* 45, 138–154. doi: 10.1002/xrs.2680

Chelazzi, D., Chevalier, A., Pizzorusso, G., Giorgi, R., Menu, M., and Baglioni, P. (2014). Characterization and degradation of poly(vinyl acetate)-based adhesives for canvas paintings. *Polym. Degradation Stabil.* 107, 314–320. doi: 10.1016/j.polymdegradstab.2013.12.028

Cooke, C. A., Abbott, M. B., and Wolfe, A. P. (2008). "Metallurgy in Southern South America," in *Encyclopaedia of the History of Science, Technology, and Medicine in Non-Western Cultures*, ed. H. Selin (Cham: Springer), 1658–1662. doi: 10.1007/978-1-4020-4425-0_9628

Curulli, A., Valentini, F., Padeletti, G., Cusmà, A., Ingo, G. M., Kaciulis, S., et al. (2005). Gold nanotubules arrays as new materials for sensing and biosensing: synthesis and characterisation. *Sens. Actuators B* 111, 526–531. doi: 10.1016/j.snb.2005.03.084

Figueiredo, E., Silva, R. J. C., Araújo, M. F., and Senna-Martinez, J. C. (2010). Identification of ancient gilding technology and late bronze age metallurgy by EDXRF, Micro-EDXRF, SEM-EDS and metallographic techniques. *Microchim. Acta* 168, 283–291. doi: 10.1007/s00604-009-0284-6

Forty, A. J. (1979). Corrosion micromorphology of noble metal alloys and depletion gilding. *Nature* 282, 597–598. doi: 10.1038/282597a0

Forty, A. J., and Durkin, P. (1980). A micromorphological study of the dissolution of silver-gold alloys in nitric acid. *Philos. Mag. A* 42, 295–318. doi: 10.1080/01418618008239360

Galli, A., Bonizzoni, L., Sibilia, E., and Martini, M. (2011). EDXRF analysis of metal artefacts from the grave goods of the Royal Tomb 14 of Sipan, Peru. *X Ray Spectrom.* 40, 74–78. doi: 10.1002/xrs.1298

Grimwade, M. (1999). "The surface enrichment of carat gold alloys- depletion gilding," in *Proceedings of the Thirteenth Santa Fe Symposium 16-19 May, 1999*, Albuquerque, NM, 293–318.

Guisbiers, G., Mejia-Rosales, S., Khanal, S., Ruiz-Zepeda, F., Whetten, R. L., and José-Yacaman, M. (2014). Gold–copper nano-alloy, "Tumbaga", in the era of nano: phase diagram and segregation. *Nano Lett.* 14, 6718–6726. doi: 10.1021/nl503584q

Hayez, V., Franquet, A., Hubin, A., and Terryn, H. (2004). XPS study of the atmospheric corrosion of copper alloys of archaeological interest. *Surf. Interf. Anal.* 36, 876–879. doi: 10.1002/sia.1790

Hörz, G., and Kallfass, M. (1998). Pre-columbian metalworking in peru - ornamental and ceremonial objects from the royal tombs of Sipan. *JOM J. Min. Met. Mat. Soc.* 50, 8–16. doi: 10.1007/s11837-998-0298-2

Hörz, G., and Kallfass, M. (2000). The treasure of gold and silver artifacts from the Royal Tombs of Sipán, Peru - a study on the Moche metalworking techniques. *Mat. Character.* 45, 391–420. doi: 10.1016/S1044-5803(00)00093-0

Hultquist, G. (1985). Surface enrichment of low gold alloys. *Gold Bull.* 18, 53–57. doi: 10.1007/BF03214686

Ingo, G. M., Angelini, E., Bultrini, G., De Caro, T., Pandolfi, L., and Mezzi, A. (2002). Contribution of surface analytical techniques for the microchemical study of archaeological artefacts. *Surf. Interf. Analysis* 34, 328–336. doi: 10.1002/sia.1311

Ingo, G. M., Bultrini, G., De Caro, T., and Del Vais, C. (2000). Microchemical study of the black gloss on red and black-figured Attic vases. *Surf. Interf. Anal.* 30, 101–105. doi: 10.1016/0169-4332(92)90326-S

Ingo, G. M., Bustamante, A. D., Alva, W., Angelini, E., Cesareo, R., Gigante, G. E., et al. (2013a). Gold coated copper artifacts from the Royal Tombs of Sipán (Huaca Rajada, Perù): manufacturing techniques and corrosion phenomena. *Appl. Phys. A Mat. Sci. Process.* 113, 877–887. doi: 10.1007/s00339-013-7711-6

Ingo, G. M., Giorgi, L., Zacchetti, N., and Azzerri, N. (1992). Electrochemical and XPS studies on lacquer-low tinplated steel adhesion. *Corr. Sci.* 33, 361–377. doi: 10.1016/0010-938X(92)90066-C

Ingo, G. M., Guida, G., Angelini, E., Di Carlo, G., Mezzi, A., and Padeletti, G. (2013b). Ancient mercury-based plating methods: combined use of surface analytical techniques for the study of manufacturing process and degradation phenomena. *Acc. Chem. Res.* 46, 2365–2375. doi: 10.1021/ar300232e

Ingo, G. M., and Padeletti, G. (1994). Segregation aspects at the fracture surfaces of 8 wt% yttria-zirconia thermal barrier coatings. *Surf. Interf. Anal.* 21, 450–454. doi: 10.1002/sia.740210623

Ingo, G. M., Riccucci, C., Bultrini, G., Dirè, S., and Chiozzini, G. (2001). Thermal and microchemical characterization of sol-gel SiO_2, TiO_2 and x SiO_2-(1-x) TiO_2 powders. *J. Therm. Anal. Calorim.* 66, 37–46. doi: 10.1023/A:1012471112566

Jones, J., and Heidi, K. (2002). *Gold of the Americas*. New York: Metropolitian Museum of Art.

La Niece, S. (1993). "Silvering," in *Metal Plating and Patination*, eds P. T. Craddock, and S. La Niece (Oxford: Butterworth-Heinemann), 201–210.

Lechtman, H. (1971). "Ancient methods of gilding silver: examples from the old and the. new worlds," in *Science and Archaeology*, ed. R. H. Brill (Cambridge, MA: MIT press), 2–30.

Lechtman, H. (1979). Pre-Columbian technique for electrochemical replacement plating of gold and silver on copper objects. *J. Metals* 31, 154–160. doi: 10.1007/BF03354479

Lechtman, H. (1984a). Andean value systems and the development of prehistoric metallurgy. *Technol. Cult.* 25, 1–36. doi: 10.2307/3104667

Lechtman, H. (1984b). Pre-Columbian surface metallurgy. *Sci. Am.* 250, 56–63. doi: 10.1038/scientificamerican0684-56

Lechtman, H., Erlij, A., and Barry, E. J. (1982). New perspective on Moche metallurgy - techniques of gilding copper at Loma-Negra, Northern Peru. *Amer. Antiquity* 47, 3–30. doi: 10.2307/280051

Lechtman, H., and Klein, S. (1999). The production of copper-arsenic alloys (arsenic bronze) by cosmelting: modern experiment, ancient practice. *J. Archaeol. Sci.* 26, 497–526. doi: 10.1006/jasc.1998.0324

Lins, P. A., and Oddy, W. A. (1975). The origins of mercury gilding. *J. Archaeol. Sci.* 2, 365–373. doi: 10.1016/0305-4403(75)90007-2

Merkel, J. F., Seruya, A. I., Griffiths, D., and Shimada, I. (1995). Metallography and microanalysis of precious metalobjectsfrom the middle Sican elite tombs at batan Grande, Peru. *Mat. Res. Soc. Symp. Proc.* 352, 105–126.

Oddy, W. A. (1981). Gilding through the Ages. *Gold Bull.* 14, 75–79. doi: 10.1007/BF03214601

Oddy, W. A. (1990). Gilding: an outline of the technological history of the plating of gold on to silver or copper in the Old World. *Endeavour* 15, 29–33. doi: 10.1016/0160-9327(91)90085-P

Oddy, W. A. (1991). Gilding: an outline of the technological history of the plating of gold on to silver or copper in the Old World. *Endeavour* 5, 29–33. doi: 10.1016/0160-9327(91)90085-P

Paparazzo, E., Fierro, G., Ingo, G. M., and Zacchetti, N. (1988). XPS studies on the surface thermal modifications of tin oxides *Surf. Interf. Anal.* 12, 438–439. doi: 10.1002/sia.740120720

Poggi, G., Toccafondi, N., Chelazzi, D., Canton, P., Giorgi, R., and Baglioni, P. (2016). Calcium hydroxide nanoparticles from solvothermal reaction for the deacidification of degraded waterlogged wood. *J. Coll. Interf. Sci.* 473, 1–8. doi: 10.1016/j.jcis.2016.03.038

Raub, C. J. (1986a). Gold-plating in the early history. *Metall* 40, 1029–1032.

Raub, C. J. (1986b). The development of gilding from antiquity to the middle ages, Materials Australasia, 18 (9), November/December. 7–11.

Sáenz-Samper, J., and Martinón-Torres, M. (2017). Depletion gilding, innovation and life-histories: the changing colours of Nahuange metalwork. *Antiquity* 91, 1253–1267. doi: 10.15184/aqy.2017.97

Schlesinger, R., Klewe-Nebenius, H., and Bruns, M. (2000). Characterization of artificially produced copper and bronze patina by XPS. *Surf. Interf. Anal.* 30, 135–139. doi: 10.1002/1096-9918(200008)30:1<135::aid-sia720>3.0.co;2-v

Schorsch, D. (1988). Silver- and gold- Moche artifacts from Loma Negra, Peru. *Metropol. Museum J.* 33, 109–136. doi: 10.2307/1513009

Scott, D. A. (1986). Gold and silver alloy coatings over copper: an examination of some artefacts from Ecuador and Colombia. *Archaeometry* 28, 33–50. doi: 10.1111/j.1475-4754.1986.tb00372.x

Scott, D. A. (1990). Bronze disease: a review of some chemical problems and the role of relative humidity. *J. Am. Instit. Conserv.* 29, 193–206. doi: 10.2307/3179583

Scott, D. A. (1991). *Metallography and Microstructure of Ancient and Historic Metals*. Malibu: The J. Paul Getty Conservation Institute.

Scott, D. A. (1998). Technical examination of ancient South American metals: some examples from Colombia, Peru and Argentina. *Boletín Museo del Oro N* 44, 79–105.

Scott, D. A. (2000). "A review of gilding techniques in South America," in *Gilded Metals: History, Technology and Conservation*, ed. T. Drayman-Weisser (London: Archetype Publications Ltd), 203–222.

Scott, D. A. (2002). "Corrosion and environment," in *Copper and Bronze in Art*, ed. T. Paul (Malibou, CA: Getty Conservation Institute), 10–80.

Stupnišek-Lisac, E., Lonèariæ Božiæ, A., and Cafuk, I. (1998). Low-toxic copper corrosion inhibitors. *Corrosion* 54, 713–720. doi: 10.5006/1.3284890

Trojek, T., and Hlozek, M. (2012). X-ray fluorescence analysis of archaeological finds and art objects: recognizing gold and gilding. *Appl. Radiat. Isot.* 70, 1420–1423. doi: 10.1016/j.apradiso.2012.03.033

Twilley, J. W., and Boyles, J. (1981). Compositional analysis of columbian Tumbaga by X-ray fluorescence spectroscopy. *Revue d'Archéométrie* 1, 303–312. doi: 10.3406/arsci.1981.1160

Zwicker, U., Oddy, W. A., and La Niece, S. (1993). "Roman techniques of manufacturing silver-plated coins," in *Metal Plating and Patination*, eds P. T. Craddock, and S. La Niece (Oxford: Butterworth-Heinemann), 223–246. doi: 10.1016/b978-0-7506-1611-9.50024-8

Advantages of publishing in Frontiers

OPEN ACCESS
Articles are free to read
for greatest visibility
and readership

FAST PUBLICATION
Around 90 days
from submission
to decision

HIGH QUALITY PEER-REVIEW
Rigorous, collaborative,
and constructive
peer-review

TRANSPARENT PEER-REVIEW
Editors and reviewers
acknowledged by name
on published articles

Frontiers
Avenue du Tribunal-Fédéral 34
1005 Lausanne | Switzerland

Visit us: www.frontiersin.org
Contact us: info@frontiersin.org | +41 21 510 17 00

REPRODUCIBILITY OF RESEARCH
Support open data
and methods to enhance
research reproducibility

DIGITAL PUBLISHING
Articles designed
for optimal readership
across devices

FOLLOW US
@frontiersin

IMPACT METRICS
Advanced article metrics
track visibility across
digital media

EXTENSIVE PROMOTION
Marketing
and promotion
of impactful research

LOOP RESEARCH NETWORK
Our network
increases your
article's readership